Flow Through and Around Groups of Bodies

University College London

Department of Mechanical Engineering

Author:
Andre Nicolle

Supervisor:
Dr. Ian Eames

Doctor of Philosophy

Submitted in partial fulfilment of the requirements for the Degree of

Doctor of Philosophy in Mechanical Engineering

October 2, 2009

Abstract

Fluid flows often consist of multiple bodies either filling most of the flow domain (for instance, porous media) or grouped in localized regions. Flow through localized groups containing many bodies has, hitherto, had little detailed study. The primary objective was to develop and trial new numerical and experimental procedures that make possible detail studies of complex multibody flows. The research investigates flow through a circular array of fixed size and populated by different numbers of equally spaced cylinders, allowing the void fraction (ϕ) to be varied.

The main contribution is a detailed fully-resolved two-dimensional numerical calculation of flow past arrays containing from 1 to 133 cylinders, where the array Reynolds number is 2100. To produce this, a parallel computational code has been written, specifically for a supercomputer, in general object-orientated language using late binding and high performance numerical libraries (PETSc, MKL and ParaMETIS). New diagnostics were applied to understand the array's influence on the flow through and around the array. A linear model was used to interpret the results.

An experimental apparatus was designed to measure and vizualize the flow field and force contributions from an array fixed in a uniform flow. The design concept (including the flume, instrument array and electronics) was tested and optimized using CFD and FEA. The experimental results provide insight into the difference between two- and three-dimensional flow patterns.

Case studies and experiments have generated data and graphical images at a level of resolution not previously possible. Three distinct regimes have been identified. For low ϕ, the interaction between the individual cylinders is weak. For intermediate ϕ, a shear layer is created and stabilized by the bleed flow through the group, resulting in steady forces on the group. For high ϕ, strong blocking occurs and the array acts like a solid cylinder.

Declaration

I hereby declare that the work presented in this thesis is solely my own work and that to the best of my knowledge the work is original except where otherwise indicated by reference to other authors. No part of this work has been submitted for any other degree or diploma.

Andre Nicolle

May 2009

Acknowledgements

The diverse nature of this PhD has required a commitment of resources and time on many separate fronts.

Special thanks to my supervisor, Dr Ian Eames, who has given me boundless encouragement and facilitated the most exciting project that I could hope for. He has found, and made available, the considerable resources needed. Ian's appetite and enthusiasm for research has driven me forward and introduced me to a fascinating research field. He has always been ready to discuss and advise, as well as being very understanding about my dyslexia.

Legion, UCL's supercomputer, has been instrumental in this research and I would like to thank Dr Jeremy Yates and his team who have supported and made available such an important resource. Thanks to Dr Mark Landeryou, who introduced me to the world of high performance supercomputers. The initial steps into a new field are often the most difficult and this was greatly facilitated by Mark's enthusiasm and patience.

Thanks to Phil Jeavons who helped in the design and manufacture of the experminental apparatus, with assistance from John Inns. The apparatus took over a year to manufacture and their dedication to the project and high quality workmanship meant that it performed perfectly first time. I would also like to thank my department, in particular Dr Kevin Drake who supported this experimental endeavour with advice, materials and instrumentation, and also Christian Klettner with whom I have worked over several years.

I am severely dyslexic and received substantial help from the local council and the very dedicated team of teachers in the Isles of Scilly. They gave me huge encouragement and support in realizing my potential and in particular I would like to thank Linda Wornes, my special needs teacher and mentor at school. I hope this work will be an inspiration to others who have dyslexic difficulties and an encouragement not to give up on their education.

Almost all PhD's are an uphill struggle. I could not have done this work without the forbearance, encouragement and support of my parents, which has motivated me right through my education. Thanks to them and to my partner Erika who has similarly supported me and waited patiently for this study to be completed.

Contents

List of Figures

List of Tables

List of Symbols

Chapter 1

Introduction

In practice, many fluid flows consist of multiple bodies. These either fill most of the flow domain (for instance, porous media Bhattacharyya et al. [2006]) or are grouped in localized regions. While the flow through porous media has been studied extensively, the problem of localized groups of bodies has not, and this is the focus of research in this thesis.

To give one example of a practical application: wind turbines are located in the atmospheric boundary layer and are used to generate energy by extracting momentum from the wind. They are often grouped together in wind farms, as seen in Figure 1.1. In such situations, it is critical to understand the interaction between the turbines and to assess any potential negative impact this may have on turbine efficiency (Crespo et al. [1999]). This requires large-scale analysis of the turbine farm as a whole.

At present, computational models can only be used to accurately analyze a single turbine blade, with strictly prescribed domain conditions. This can take account of the complex three-dimensional contouring of the blade and, with the use of a turbulence model, can partially resolve the boundary and vortex interactions induced on a heavily loaded blade (Vermeera et al. [2003]).

Modelling the complete turbine with many blades and in a moving frame of reference is considerably more difficult, because of the range of lengthscales. A more common method is to use blade element momentum theory (BEM) which is still primarily based on the data from a single blade. This method also has substantial limitations in engineering terms, as it relies upon having a steady predictable flow

Figure 1.1: Large off-shore wind farm in Denmark – Picture from Elsam.

and predetermined aerofoil characteristics.

As farms become larger, with numerous clusters of turbines, such analysis requires understanding of interactions, not just between individual turbines in a cluster, but also between clusters (Frandsen et al. [2004]).

The available models are still in their infancy; UPMWAKE, for instance, which has been shown to produce reasonable results using the $k - \epsilon$ closure model for the Navier-Stokes equations and actuated disc models which imitate the drag force on the fluid in place of the turbine. These models still, however, do not capture and deal with vorticity annihilation and inviscid blocking, processes which are believed to be important in multibody flows (Eames et al. [2007]).

In considering the flow past a localized group of two-dimensional bodies, it is useful to have a conceptual picture of the problem being considered. Figure 1.3 shows a schematic of the changing properties between a single body (with a characteristic size D) – from one extreme – to when there are a large number of bodies N_C, which are grouped in a region of size D_G. The fraction of bodies within the group is $\phi \sim N_C D^2/D_G$ for a two-dimensional group of bodies. It is relevant to describe the two limits of $N_C < 5$ and $N_C \to \infty$. To accurately capture the flow past small numbers of bodies ($N_C < 5$), the flow needs to be fully resolved. Only recently has

Figure 1.2: Illustration of a complex urban terrain – New York City.

this been possible with DNS in three dimensions. For more practical engineering circumstances, turbulence models have been the only option. These rely on tuning to account for the convection and diffusion of turbulent energy. At the limit of $N_C \to \infty$, it is not practical to fully resolve the individual bodies. Instead, it is usual to apply a distributed drag approach, which is widely employed for studying the urban terrain (Figure 1.2) and plant canopies (Batchelor [1967]). The intermediate limit of $N_C \sim 5 - 100$ has not been studied in detail.

Distributed drag models have been adopted in urban and plant canopy modelling as illustrated at the NATO Ukraine Conference on Urban and Plant Modelling, 2004. As contributions to this conference made clear, the distributed drag models tend to flag up significant questions in terms of parameters that are often ill-defined or difficult to define – like geometrical shape and drag coefficient. In fact, these distributed drag models tend to assume an unrealistically high average drag coefficient of about $C_D \approx 3$ (Eames et al. [2007]). They do not again take account of vorticity or wake annihilation and inviscid blocking, which are thought to be important in multibody flows.

With increased computer processing power, it has become feasible to reliably

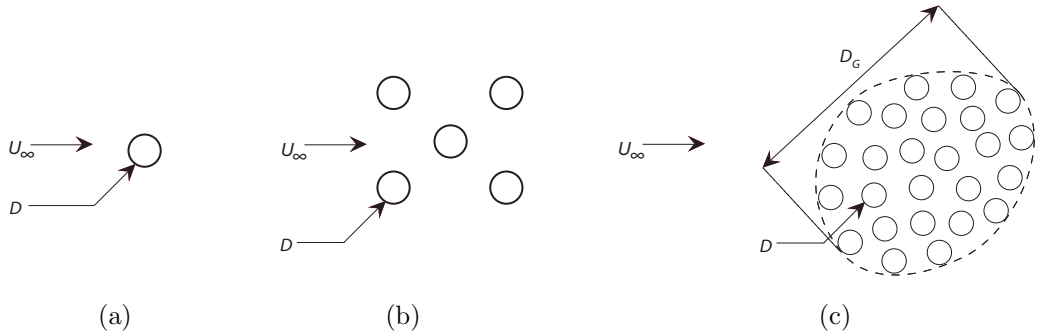

Figure 1.3: Schematic showing the change in structure of the group of bodies as N_C increases from (a) $N_C = 1$, (b) $N_C < (\approx 5)$, (c) $N_C >> (\approx 5)$.

analyze simple engineering fluid problems, often with tools such as computational fluid dynamics (CFD). However, many everyday problems (such as off-shore structures, marine effluent dispersal, wind turbine farms and urban terrains) are sufficiently complex that they have not easily lent themselves to using computational techniques.

A common theme in the above examples is the need to interpret the velocity field. This is often turbulent due to the scales, complex geometry and interactions between different facets. All approaches rely on models which attempt to impose a simplified interpretation onto the flow field, covering the factors which are believed to be most influential. It is difficult, though, in many cases, to determine which parameters are important, especially when turbulent sources interact.

Engineers are often required to apply knowledge derived from fundamental research to the more complex engineering issues in everyday environmental and industrial applications. This needs to take account of the fluid flows and turbulent environments induced by the structures and boundaries involved. In these cases, vorticity annihilation and accumulation become significant, and their effects on the flow field need to be accurately quantified and understood, in order to determine the effect of inviscid blocking.

1.1 Objectives of the research

This research investigates complex inertial flow interactions, induced by a localized group of bodies. As later shown (Chapter 2), this is an area which, until now, has had limited detailed and dedicated research. There is very little numerical and experimental data available. The understanding of the flow processes is also weak. Therefore, the aims of this thesis are to:

1. Quantify properties of a group of bodies and consider factors which influence the flow field around them.
2. Develop tools and frameworks to emulate the flow field of a group of bodies in a measurable environment.
3. Conduct a study which will allow measurement of the group properties of the flow field, in both the near and the very far-field.
4. Conduct a study which can take account of varying flow conditions, more commonly seen in the engineering environment.
5. Study the impact of inter-relationships and coupling of individual bodies making up a group and how individual wakes contribute to a group's wake.
6. Produce high-quality results that can be used for comparison in future work.
7. Identify useful diagnostic techniques and tools which are available to help with the measurement and analysis of flow field properties, through and around a group of bodies.
8. Compare the numerical results against a mathematical model to help interpret the data.

1.2 Limitations of the research

When investigating flow through and around groups of bodies, there are three defining geometric features specific to any case:

1. Shape and size of individual bodies making up the group.
2. Distribution of bodies within the group.
3. Overall shape and size of the group.

For a given flow regime, the behaviour of the resultant flow field through and round a group of bodies are expected to be similar, even if the geometry of the individual bodies differs. Likewise, the overall group is expected to exhibit behaviour similar to that of a bluff body at high void fractions, and at low void fractions the behaviour in no longer expected to depend on the overall shape of the group. This can be examined by reviewing the simplest case. This work, therefore, concentrates on the well-understood geometry of a cylinder for both the shape of the individual bodies making up the group and the shape of the overall group array. Additionally, this work was confined to evenly distributed bodies and tries to minimize the anticipated effect of boundedness.

1.3 Organization of the thesis

This research thesis has the following structure:

Chapter 2 provides a detailed assessment of the present state of research knowledge concerning flow through and around groups of bodies. The complex flow patterns around an isolated body and different regimes are reviewed. It includes an analysis of the general limitations of previous work. The latter part of this chapter outlines how the present research is targeted, identifying two substantially different approaches and what limitations are imposed.

Chapter 3 defines the numerical techniques, which are employed in this thesis to study the flow past individual bodies and groups of bodies. The mathematical framework, which underpins a CBS (Characteristic Based Split)formulation of FEM, is described. The implementation of the FEM scheme, including the programme code development, and its use on a large supercomputer, is discussed. The numerical scheme is tested against commercial and open-source CFD codes, using the standard lid-driven cavity (to test steady state solutions), and flow past a symmetrically and asymmetrically placed cylinder (to test unsteady solutions). Purely for the purpose

of demonstrating the flexibility and scalability of the new code, the code is run for the lid-driven three-dimensional cavity and validated.

Chapter 4 describes the design methodology for the experimental component of the work. The purpose of the experimental study is to provide a comparison with the numerical calculations, to enable the results to be reliably extended to higher Reynolds numbers. The experiments use a water flume with a confined group of instrumented cylinders. The design aspect combines CAD design, simulating the instrumented cylinders using SolidWorks and refinement of the flow field (to reduce unsteadiness) using Fluent. The requirements and limitations of the experiments are considered and taken into account in a final experimental design.

Chapter 5 describes the numerically investigated case studies and explains the domain and mesh parameters. Diagnostic techniques are defined and the comparative mathematical model introduced. These results and the comparison with the mathematical model are discussed.

Chapter 6 presents the newly-finished experimental apparatus and describes the experimental procedure used to validate and commission its design. The experimental results for group force and dye imaging are discussed.

Chapter 7 summarizes the conclusions of both the numerical and experimental work. Suggestions are made for the refinement of the experimental apparatus and future work, in both numerical and experimental areas.

Chapter 2

Literature Review

2.1 Introduction

In this thesis, the flow and forces acting on localized groups of bodies fixed in an uniform flow are examined. The literature on flow past multiple bodies in a bounded domain is extensive, for instance, in the context of tubes in a heat exchanger. The effect of boundedness is critical – in the context of boiler tubes, the average flow between the tubes is increased (by blocking), while in the context of unbounded flows, the average flow between the bodies is decreased (both by the effect of blocking by the entire group and drag). To relate the research to practical engineering problems, the individual bodies which form the localized group are taken to be cylinders. Whilst a circular cylinder is one of the simplest geometries, it exhibits a surprising range of flow regimes, some of which have still not been fully resolved (Zdravkovich [1997]). To help describe the characteristics of flow around an individual cylinder and the forces which act on them, a number of standard diagnostics and measures are introduced in §2.2. These definitions have previously been applied to isolated cylinders and some are applicable in multibody situations.

In §2.3, the different regimes for flow around an isolated cylinder (for $N_C = 1$) are reviewed. There is substantial literature describing the total and individual drag on small numbers of cylinders ($N_C < 4$). This is mainly experimental and very little is available in the way of numerical calculations. In the context of off-shore risers, there has been experimental work done on square/circular arrangements of

groups of cylinders of both varying and fixed diameters (Taylor [1991]) but there does not appear to be a consensus, or fundamental description, of the mean flow. As much of the fundamental work was undertaken in wind tunnels, there has been no attempt to analyze the near wake behind or attached to the group, or the flow far downstream, because visualization in air is challenging. For large numbers of bodies ($5 < N_C < 100$), there is hardly any fundamental work on the flow through and around a group of bodies. Interestingly, and partly in recognition of the importance of multibody flows, a number of new diagnostics have been developed to study the flow through and around bodies and the forces acting on them (described in §2.5). These diagnostics were developed for steady, inviscid flows or have been applied to flows where the number of bodies is small ($N_C \leq 4$).

When the number of bodies increases $N_C \to \infty$, but the void fraction of bodies in the array ($\phi = N_C D^2/D_G^2$) is finite, the array of bodies begins to resemble a porous media. In this limit, it is not important to fully resolve the flow around individual bodies whose effect on the ambient fluid can be represented in terms of a distributed drag force. This approach is well-known, particularly in the context of flow through the urban terrain and over plant canopies (Finnigan and Belcher [2004]).

The concluding remarks (§2.6) highlight the new aspects of the research which will be undertaken.

2.2 Force and flow characteristics: definitions

Due to the relevance of cylinders in this work, precise terminology is presented in this section, such as is typically used for discussing cylinder behaviour. An isolated cylinder of diameter D fixed in a uniform stream of speed U_∞ is considered. A series of definitions and measurable parameters are introduced and described in order to provide a framework to describe and interpret the force and flow.

The Reynolds number, characterizing the ratio of inertial to viscous forces, Re, is defined by

$$Re = \frac{U_\infty D}{\nu}, \tag{2.1}$$

where $\nu = \mu/\rho$ is the kinematic viscosity of the fluid (Massey [1998, p. 174]). The

Newtonian flow past a rigid body is described by the Navier-Stokes equation

$$\rho \frac{\mathrm{D}\boldsymbol{u}}{\mathrm{D}t} = -\boldsymbol{\nabla} p + \boldsymbol{\nabla} \boldsymbol{\tau}, \tag{2.2}$$

where p is pressure (Batchelor [1967, p. 174]). The stress tensor, $\boldsymbol{\tau}$, expressed in tensor notation, is

$$\tau_{ij} = \mu \left(\frac{\partial u_i}{\partial x_j} + \frac{\partial u_j}{\partial x_i} \right). \tag{2.3}$$

For a rigid body, two boundary conditions are applied to the flow at its surface. The kinematic boundary condition requires

$$\boldsymbol{u} \cdot \hat{\boldsymbol{n}} = 0, \tag{2.4}$$

so that the normal flux through the body, surface is zero where $\hat{\boldsymbol{n}}$ is the unit vector pointing out of the flow domain. This boundary condition is applied to both viscous and inviscid flows. The finite viscosity of the fluid requires a no-slip condition to be applied

$$\boldsymbol{u} \times \hat{\boldsymbol{n}} = \boldsymbol{0}, \tag{2.5}$$

on the surface of the body. In relation to the numerical calculations where $\hat{\boldsymbol{n}}$ is the unit vector pointing out of the flow domain and into the body. An upstream uniform velocity and a downstream pressure condition are also applied.

The force on a rigid body is defined by

$$\boldsymbol{F}(t) = \int_{S_b} (p\boldsymbol{I} - \boldsymbol{\tau}) \cdot \hat{\boldsymbol{n}} \mathrm{d}S, \tag{2.6}$$

where S_b is the surface of the body (Zienkiewicz et al. [2005, p. 392]). To interpret the force on the body, it is usual to express it in dimensionless terms of drag and lift coefficients . When the mean ambient flow is parallel to the x-axis, the drag coefficient is defined by

$$C_D(t) = \frac{\boldsymbol{F} \cdot \hat{\boldsymbol{x}}_1}{\frac{1}{2}\rho D U_\infty^2}, \tag{2.7}$$

where $\hat{\boldsymbol{x}}_1$ is the unit vector in the x-direction. The drag coefficient is time dependent and it is usual to calculate the time-average drag coefficient. For a time interval T , the time average drag coefficient is

$$\langle C_D \rangle = \frac{1}{T} \int_0^T C_D \, \mathrm{d}t. \tag{2.8}$$

The lift coefficient is defined as

$$C_L(t) = \frac{\boldsymbol{F} \cdot \hat{\boldsymbol{x}}_2}{\frac{1}{2}\rho D U_\infty^2}, \tag{2.9}$$

where $\hat{\boldsymbol{x}}_2$ is the unit vector in the y-direction . The average lift coefficient on a cylinder in free stream or symmetric arrangement is zero. The maximum lift coefficient C_{Lmax} is defined as

$$C_{Lmax} = \max_{0 \le t \le T} C_L(t). \tag{2.10}$$

For unsteady flows, the lift is periodic (i.e. below a critical Reynolds number) and the period of oscillation T_p is defined through

$$C_L(t + T_p) = C_L(t). \tag{2.11}$$

The Strouhal number (St) characterizes the periodicity of the lift coefficient (and wake shedding) and is defined as the ratio of the period of oscillation to a characteristic advective time-scale U_∞/D:

$$St = \frac{T_p}{U_\infty/D} \tag{2.12}$$

(Massey [1998, p. 342]). For cylinders moving impulsively from rest, the initial creation of the wake tends to be chaotic and leads to a gradual growth in the lift coefficient. The drag coefficient tends to considerably overshoot its steady or average value. In this case, the time period over which the drag coefficient is averaged (and the maximum lift coefficient determined) is over a period T, long after the cylinder

has been set in motion.

The pressure at the wake stagnation point (base pressure) has been used in many papers as a method of identifying changes in the flow regime around a cylinder. It is preferred because it is simpler to measure and more sensitive to changes in the wake regimes downstream of the cylinder than either C_D or C_L. The base-pressure coefficient is defined by

$$C_{pb} = \frac{p - p_\infty}{\frac{1}{2}\rho U_\infty^2} \tag{2.13}$$

(Zdravkovich [1997, p. 20]). Pressure difference at stagnation points is measured on the surface of the cylinder perpendicular to the flow on the upstream and downstream points of the cylinder surface by

$$C_{pb} = \frac{p(r = D/2, \theta = 0) - p(r = D/2, \theta = \pi)}{\frac{1}{2}\rho U_\infty^2}. \tag{2.14}$$

2.3 Isolated cylinder

The literature review on the flow past an isolated cylinder is described in this section, because the bodies which form the array are cylinders and the effect of the group of bodies on an incident flow is similar to that of a bluff body. Much of the research has been focused on the flow induced by and around a circular cylinder, and the resulting wake regimes. This has been conducted in engineering as well as scientific work, as it has always been seen as useful in furthering a better general understanding of boundary layer separation, vortex formation and interaction, turbulent wakes etc. The circular cylinder is considered to be a bluff body and, as a result, the influence it projects onto a flow field is determined by the Reynolds number (Re) and the far field effect of boundaries. The effect of the flow being bounded by channel walls is discussed in §2.3.5. The flow regime (as discussed in §2.3.1), in which the cylinder is studied, has to be considered to ensure that the investigation produces definitive results and does not merely reflect apparently different bluff body characteristics caused by regime switching.

A review into the different flow behaviour of a two-dimensional isolated cylinder is conducted in §2.3.4. The induced force on an isolated cylinder is separately discussed in §2.3.3.

Cylinder flow regimes			
State		Regime	Re ranges
Laminar	L1	No-separation	0 to 4-5
	L2	Closed wake	4-5 to 30-48
	L3	Periodic wake	30-48 to 180-200
Transition in wake	TrW1	Far-wake	180-200 to 220-250
	TrW2	Near-wake	220-250 to 350-400
Transition in shear layers	TrSL1	Lower	350-400 to 1k-2k
	TrSL2	Intermediate	1k-2k to 20k-40k
	TrSL3	Upper	20k-40k to 100k-200k
Transition in boundary layers	TrBL0	Pre-critical	100k-200k to 300k-340k
	TrBL1	Single bubble	300k-340k to 380k-400k
	TrBL2	Two-bubble	380k-400k to 500k-1M
	TrBL3	Supercritical	500k-1M to 3.5M-6M
	TrBL4	Post-critical	3.5M-(unknown)
Fully turbulent	T1	Invariable	(unknown) to ∞
	T2	Ultimate	

Table 2.1: Cylinder flow regimes as collated in Zdravkovich [1997].

2.3.1 Flow regimes

There are presently fifteen separately identifiable flow regimes (shown in Table 2.1) for flow past a circular cylinder which are categorized by changes in such parameters as St and $\langle C_D \rangle$ over a range of Re.

The main problem with the previous studies of flow regimes is that they have focused on distinguishing between two regimes and, necessarily, focused on one or two regimes at most. Many authors, including Posdziech and Grundmann [2001] and Williamson [1988] have noted this fragmented research over the range $Re = 1 - 10^4$. With recent improvements in computer processing power, there has been a development of two-dimensional calculations and, most recently, three-dimensional DNS. This is now being applied to Reynolds numbers in excess of $Re = 10^4$ (Dong and Karniadakis [2005]). In the following section, there is a focus on the flow regimes associated with an unbounded flow (or very wide channel) past a rigid circular cylinder.

Regime L1

The first regime, (L1), more commonly referred to as the 'creeping flow' regime,

is found to operate in the range $0 \leq Re \approx 5$. In this range, the flow is laminar, symmetric and there is no recirculating wake region, as illustrated in Figure 2.1a. The flow is symmetric about the center line (Henderson [1995]) and can be fully explained by Stokes flow. The lift force on the cylinder is zero because the flow is symmetric. At such low Re, the force is viscously dominated and the velocity field decays slowly with distance, on either side and upstream of the cylinder. White [1956] illustrated this when he discovered that a channel width of $500D$ still influenced the flow field around the cylinder.

Regime L2

The second regime, (L2), occurs in the range $5 \leq Re \approx 46$ and is shown by a reduction in viscous drag force, and an enhanced boundary layer which separates from the cylinder and converges downstream to form a parallel shear layer in the wake, as illustrated in Figure 2.1b. Theoretically, it has been shown that the boundary separation originates from the downstream stagnation point on the cylinder at 180° and, with increasing Re, initially moves quickly around the cylinder towards the shoulders. Experimentally, this has not been proven and separation at around 150° is more common (Zdravkovich [1997]). This is likely to be due to the experimental difficulties in measuring the flow near a stagnation point, because of the very slow flow rates in this region. Inside the separated boundary shear layer, oppositely signed eddies are induced which grow with Re. It should be noted (as explained by Zdravkovich [1997]) that when dye is released upstream into the cylinder's boundary layer, it can enter the circulating eddies. In this class of flows, the dye does not diffuse in the same way as vorticity and can enter and accumulate in the closed recirculating regions. The boundary layer itself is swept over the eddies. Williamson [1995] showed, using numerical calculations (DNS), that this regime stayed stable up to $Re = 46$.

Regime L3

The transition to L3 (shown in Figure 2.1c) is first observed with the periodic downstream oscillation of the wake. This oscillation starts downstream and propagates towards the cylinder. The transition to this oscillatory state is at $Re = 46$ (Williamson [1995]). Although the existence of the transition was well-known as far back as 1927 (see Camichel et al. [1927]), its value was previously difficult to determine. It is very sensitive to bounding geometry, surface properties, etc. and cannot be reliably

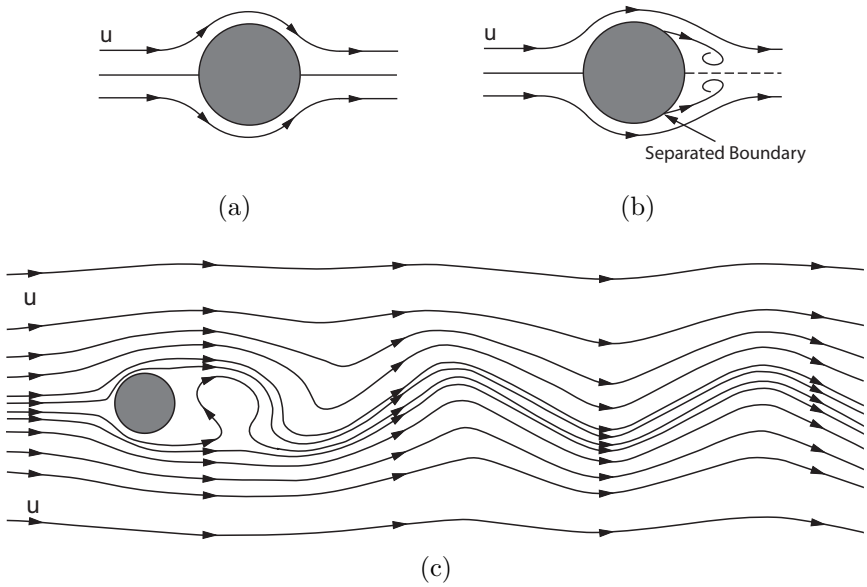

Figure 2.1: Schematic of the flow regimes around a cylinder: (a) L1, (b) L2 and (c) L3.

measured experimentally. The transition from steady to unsteady flows undergoes a supercritical Hopf bifurcation, which results in the formation of the von Karman vortex street, where the trailing, entrapped, attached vortices periodically become unstable and detached. In this regime, all regions of the wake remain laminar up to $Re = 188 \pm 1.0$ (found using DNS by Barkley and Henderson [1996]).

The oscillating wake induces a lift force on the cylinder with a frequency denoted by St. It would be expected that, with the simplistic two-dimensional geometry of a cylinder and a symmetric laminar wake, two- and three-dimensional measurements of St would be similar. However, as illustrated in Figure 2.2a, there seem to be two St values for any single Re up to $Re = 64$, which was discovered Tritton [1959]. Tritton measured the deflection of quartz crystal fibres (used to represent the cylinder) in the streamwise direction to measure the drag force at low Re. He also photographed vortex shedding from the fibres in two axial planes, which revealed bending in the previously two-dimensional vortex shedding at $Re \approx 78$. He observed oblique slantwise vortices being shed, which is clearly a three-dimensional phenomenon.

He concluded that multiple St numbers existed along the span of the cylinder for the same Re. Tritton believed that this was probably caused by two instabilities, one in the wake and the other caused by the cylinder itself. Several other researchers have found the same phenomenon, albeit at different Re. Much discussion has ensued on the cause of the oblique shedding. It has even been suggested that cylinder vibrations or non-uniformities in the flow could be responsible (Gaster [1969], Gaster [1971]). Williamson [1988] conducted in-depth work into the phenomenon, and concluded that the effect was not due to cylinder vibrations, but was the result of cylinder-end effects. He carried out a sequence of experiments in an open water tunnel for different cylinder diameters, and established that oblique vortex shedding occurred at a given Re, irrespective of the diameter of the cylinder. From the formation of the parallel Von Karman vortex street, until $Re = 64$, Williamson proved that different vortex shedding frequencies (St) were present for any given Re. He explained this in terms of the three vortex elements shown in Figure 2.2. The central vortex element was parallel at the primary St number, while at each end of the cylinder a vortex element at lower frequency was generated and was responsible for the second St values measured. At above $Re = 64$, he showed that a 'chevron' type vortex is produced (Figure 2.2(b)) which has angle $\pm\theta$ to the line parallel to the cylinder. Williamson used the following equation $St = St_\theta \cos\theta$ to correct measured experimental St, so that it could be accurately compared with St data for parallel shedding, e.g. two-dimensional data. In this equation, θ is the vortex angle, St_θ is the experimentally determined Strouhal number, and St is the corrected parallel St number. Gerich and Eckelmann [1982] also measured the oblique shedding frequency for different length cylinders to be $10-15\%$ less than the parallel shedding frequency for a cylinder length $< 6D$.

Williamson believed this effect was only visible up to $Re = 190$ and that above this, three-dimensional effects became dominant. As later shown by Williamson [1989], the oblique vortex shedding was not present in the ideal case of an infinitely long cylinder in a turbulent free stream. This was also shown by Norberg [1994]. Later numerical research by Mittal [2001] carried out high accuracy, three-dimensional simulations on the formation of oblique and parallel vortex sheets at $Re = 100, 300$ and 1000. Mittal used no-slip walls at the ends of the cylinders to represent a typical experimental

configuration. He measured the oblique shedding angle at 25°, which compared well with Williamson's experimental studies. In other three-dimensional numerical work, using slip wall conditions, only parallel shedding was observed (Henderson [1997]). This was taken to indicate that the wall condition is the cause of the oblique shedding. As already assumed, this indicates that the cylinder ends are responsible for the oblique vortex shedding.

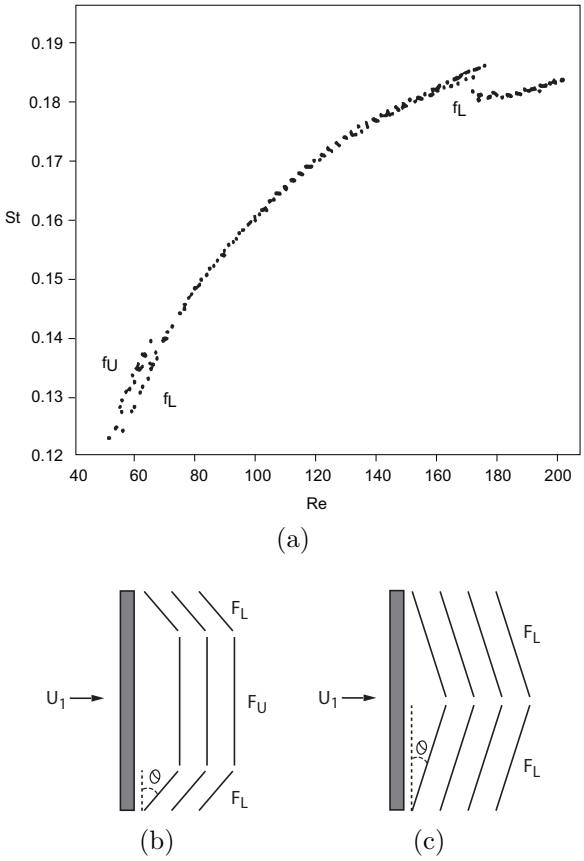

Figure 2.2: The variation of St with Re is shown in (a) (reproduced from Williamson [1988]). The different types shedding (fU and fL) are indicated in (b) and (c) respectively for the range of $46 < Re < 64$ and $100 < Re < 188$.

Regime TRW including three-dimensional wake transition

Roshko [1954] discovered, and Williamson [1998] later confirmed, that there was a discontinuity in St in the range $Re = 150 - 250$, in which St could switch between two different values. This showed that the transition to Mode A was hysteretic,

with the sudden formation of Mode A vortices. The later transition to Mode B was a gradual change with the low frequency vortices from Mode A being absorbed into higher frequency Mode B vortices. There has been some argument over the process involved in this Mode B transition but it is now generally accepted that the different St numbers reflect a switching between Mode A and B (Williamson [1996]). The transition into Mode A is characterized by oppositely signed vortices in the free stream direction, distributed spanwise along from the cylinder at 3.96 ± 0.2 cylinder diameters. They are wrapped into the primary vortex street. During Mode B, vortices have a shorter wavelength of 0.22 cylinder diameters, and are now believed to be scaled with the braid shear layer.

Barkley and Henderson [1996] showed that the only accurate way to calculate the transitional Re was numerically and the transition to Mode A occurred at $Re = 188.5 \pm 1$ and that Mode B was dominant by $Re = 259$ for an infinitely long cylinder in a turbulent free stream. Experimentally, it has been shown that oblique vortex shedding and dislocations can be generated by end effects of the cylinder and can prematurely trigger Mode A at a lower Re.

Regime TRW Transition in Shear Layers

The first sign of turbulence in free flow about a cylinder takes place at $Re > 350$ (Gerrard [1978]). This is,however,situation dependent and difficult to measure, as shown in the scatter of data reviewed in Prasad and Williamson [1997]. In this latter work, data is cited which varies over the range from $Re = 350$ to 3000, and it points out that the spanwise end conditions control the primary mode of vortex shedding, which affects the onset of turbulence within the shear layer. This instability in the shear layer forms after separation from the laminar boundary layers downstream, progressively moving towards the cylinder as Re increases. The turbulence is a result of eddies rolling up in the shear layer which is often referred to as a 'transitional wave along the free shear layer' (Zdravkovich [1997]). The turbulent shear layer is then wrapped into the transverse wake trailing the cylinder, resulting in the formation of turbulent eddies. Bloor [1964] conducted hot wire experiments and deduced that the frequency of the turbulent eddies within the unstable shear layer was $f_{Tr} \propto Re^{1/2}$. Later, Prasad and Williamson [1997] conducted an in-depth review of available

research (including Bloor), and suggested that a better fit for this data was

$$\frac{f_{SL}}{f_k} = 0.0235 \times Re^{0.67}. \tag{2.15}$$

Also of note is that these new turbulent wakes still result in a negative/positive vortex ejection from the wake, which is now formed closer to the cylinder.

2.3.2 Two-dimensional flow regime for an isolated cylinder

As already discussed, three-dimensional wake structures appear as early as flow regime L3, but two-dimensional numerical studies can still be a useful tool in measuring certain cylinder flow properties. Both coefficients of lift and drag in two-and three-dimensional simulations exhibit similar values, even though the former does not show the three-dimensional structure.

Experimentally, the closest analogy to a two-dimensional flow past a cylinder would be the two-dimensional soap film experiments of Wen et al. [2004]. These did not show the Mode A and B transition present in three-dimensional experiments, thus confirming what had already been found by Barkley and Henderson [1996] in his computational two-dimensional comparison. Soap film experiments are useful for visualization of ideal two-dimensional flows. However, as pointed out by Wen et al. [2004] important qualities such as drag coefficient can only be interpreted to an accuracy of $\pm$ 10%. This is because they rely on the momentum deficit method, computing the drag coefficient from the velocity field.

Because of the additional three-dimensional wake structures, St (which is highly dependent on downstream wake) can be substantially changed. Figure 2.3 by Barkley and Henderson [1996] shows these differences, which mainly result from regime changes caused in the three-dimensional wake. Henderson, R.D., in private correspondence with Williamson, determined the St for a two-dimensional cylinder in free stream. Henderson deduced that a very good approximation for a two-dimensional cylinder was

$$St = 0.2417 - 0.8328Re^{-0.4808} \exp\left(-0.001895Re\right). \tag{2.16}$$

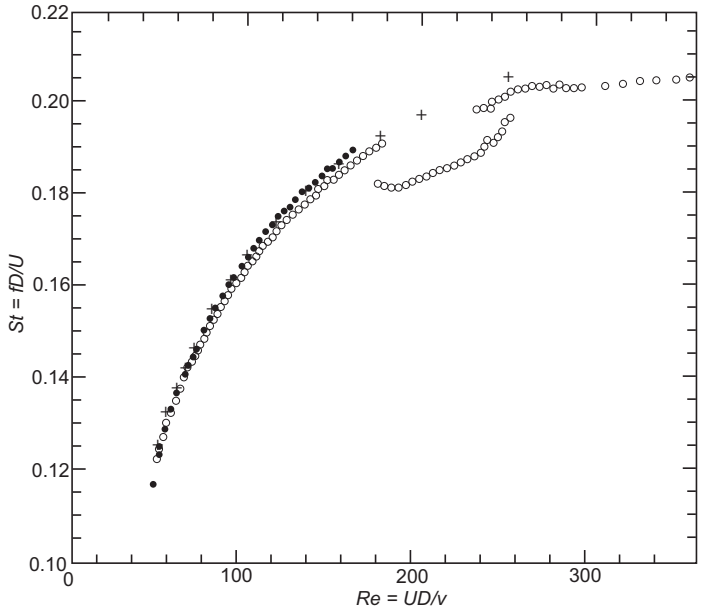

Figure 2.3: The variation of the Strouhal number St with Re is shown (reproduced from Barkley and Henderson [1996]). The experimental measurements and computer simulations of two-dimensional flow correspond to : ∘, Williamson (1989); •, Hammache and Gharib (1991); +, Barkley and Henderson [1996].

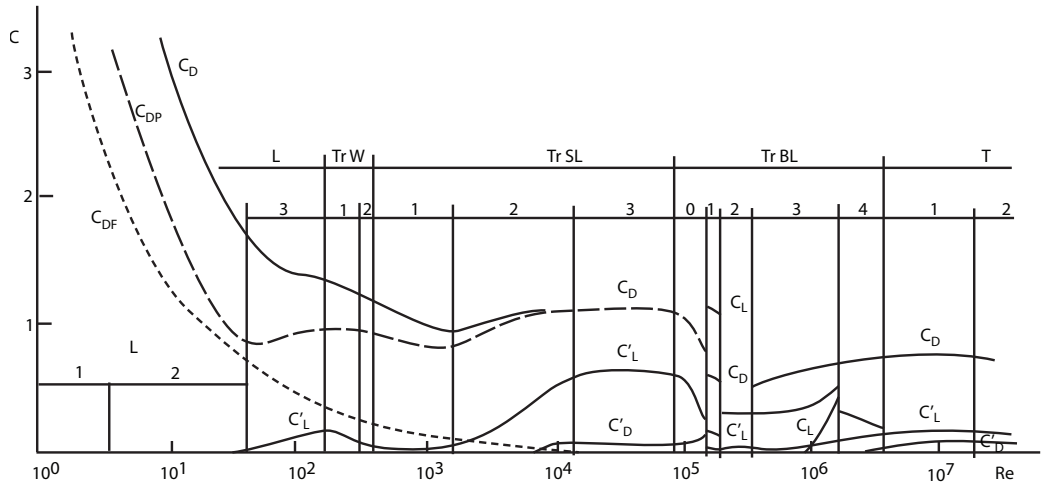

Figure 2.4: Force drag and lift coefficient plotted against Re, reproduced from Zdravkovich [1997].

As can be seen in Figure 2.3, three-dimensional flows exhibit similar two-dimensional values of St up to $Re \approx 170$. Above this, three-dimensional effects take over and two-dimensional analysis of a three-dimensional St ceases to be valid.

2.3.3 Forces on an isolated cylinder

In this research, an understanding of the individual bodies' contributions to the group's overall drag force is investigated. This helps to explain the importance of the front perimeter cylinders of a group compared with their interior or downstream counterparts. The force on an individual cylinder results from the relative fluid motion around it. This force comprises two components: the first is due to the pressure variation over the cylinder surface (S_b) and the second is due to the viscous stresses on the cylinder surface. The equation for the pressure component is

$$F_{p1} = \int_{S_b} pn_1 \mathrm{d}S, \qquad F_{p2} = \int_{S_b} pn_2 \mathrm{d}S, \tag{2.17}$$

and viscous component is

$$F_{\nu 1} = -\int_{S_b} (\tau_{11} n_1 + \tau_{12} n_2) \mathrm{d}S, \qquad F_{\nu 2} = -\int_{S_b} (\tau_{21} n_1 + \tau_{22} n_2) \mathrm{d}S. \tag{2.18}$$

The resultant force will, depending on the flow regime, have lift and drag contributions. The drag contribution acts in the free stream direction, whereas the lift contribution acts at 90° to the free stream. These two forces are usually reported in a non-dimensionalized form, such as shown in equation 2.7 and 2.9 respectively.

Figure 2.4 shows both total drag coefficient and total lift coefficient with their contributions over a full range of Re, in disturbance free flow. This Figure also shows the regimes in which these values occur. It can be seen that the drag and lift coefficients are not just a reflection of the flow regimes in which they operate, even though some regime changes are hysteretic. This explains why Williamson [1996] and others prefer to use a base suction coefficient measure when reviewing regime changes. However, when looking at wake signatures, it is useful to compare this against the drag and lift forces. Engineering applications are typically concerned with induced forces which are not easily deduced from the base suction coefficient.

The lift and drag coefficient history (illustrated in Figure 2.4) shows a progressive reduction in $\langle C_D \rangle$ in L1 and L2 regimes, with an almost equal contribution from both viscous and pressure components of drag. Regime L3 shows the first sign of C_L' , predominantly due to an increased pressure component, while the viscous drag contribution continues to reduce as the pressure component increases.

The TRW regime has little influence on the drag contribution, which continues to reduce; but the lift contribution also now substantially reduces. By TrSL3, the viscous contribution has become zero and the lift contribution has increased to approximately 50% of drag. In the further regimes, drag and lift go through several transition steps, which are more regime dominated, reflecting the onset of a fully turbulent flow field.

The values of the lift and drag coefficients which have been described here, have been collected over time from many different research contributions and reflect the difficulty in collecting accurate and comparable data where experimental conditions do not influence the results.

2.3.4 Flow field around an isolated cylinder

The flow field around an isolated body is less complex than that around a group of bodies, irrespective of the void fraction. However, many characteristics are likely to be common to both. Flow past a cylinder can be analyzed by studying different

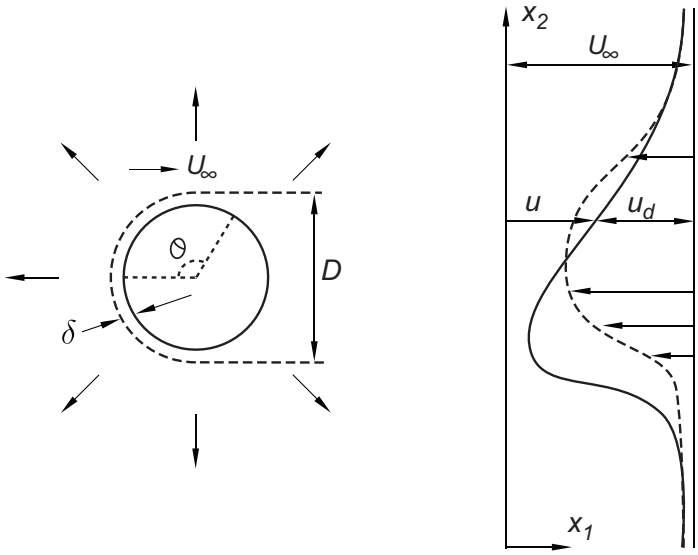

Figure 2.5: Flow field schematic showing the wake profile and boundary layer.

regions of the flow. Upstream of the cylinder, the incident flow is irrotational. On the cylinder surface, a boundary layer develops from the upstream stagnation point and grows proportionally as

$$\delta \sim (\nu s/U_\infty)^{\frac{1}{2}}, \tag{2.19}$$

where

$$s = \frac{D\theta}{2} \tag{2.20}$$

and θ is the angle from the upstream stagnation point to the boundary layer separation point and the flow separates roughly at an angle of 110° from the incident flow (Acheson [1990, p. 50]). Far downstream of the cylinder, the wake flow generates an instantaneous velocity deficit

$$u_d(x_1, x_2, t) = U_\infty - u_1. \tag{2.21}$$

The time-averaged velocity deficit profile, at a fixed distance downstream, is

$$\langle u_d(x_1, x_2)\rangle = \frac{1}{T}\int_0^T (U_\infty - u_1)\mathrm{d}t. \tag{2.22}$$

For unbounded flows, the volume flux associated with the wake deficit is

$$Q = \int_{-\infty}^{\infty} \langle u_d\rangle \mathrm{d}x_2. \tag{2.23}$$

As demonstrated by Betz [1925], Batchelor [1967], the volume flux tends to a constant far downstream of the body, and is related to the mean drag force on the body through

$$\langle \boldsymbol{F}\cdot\hat{\boldsymbol{x}}_1\rangle = \rho Q U_\infty. \tag{2.24}$$

The volume flux deficit drives fluid towards the cylinder. As a consequence, there is a source flow whose strength is Q in the far field. The flow downstream of a rigid body can be interpreted in terms of the vorticity field it generates. A two-dimensional body generates positive and negative vorticity on its bottom and top surfaces (with the flow orientated right-to-left). Near the body, the intermingling and cancelling of positive and negative components of vorticity initially leads to the maximum vorticity decaying rapidly with distance downstream (as $\omega_{max} \sim 1/x_1$). This is a process described as vorticity annihilation and analyzed by Hunt and Eames [2002] and Eames [2008]. When Re is sufficiently small that the von Karman vortex street is not created, the maximum vorticity magnitude decays at a slower rate and persists downstream. When the von Karman vortex street is present, the positive and negative vorticity are alternately shed. This creates isolated vortices whose maximum vorticity decreases slowly as the vorticity diffuses from them (i.e. vorticity annihilation is suppressed). The concept of vorticity annihilation has been used by Hunt and Eames [2002] to explain how wakes decay rapidly in complex flows and is useful in multibody flows.

2.3.5 The effect of a bounding channel

It is often of most interest to study flows around bluff bodies when in an unbounded flow. This is difficult to achieve either experimentally or numerically, as there will invariably be a boundary which may have a substantial effect on the flow regime. In

order to design experimental apparatus to study the forces on a group of bodies, it is important to understand the effect of a bounding channel on these measurements. Numerically, it is often desirable to minimize the computational domain and the size of the problem, which can be done by keeping the channel boundaries as small as possible. A measure of the effect of the bounding channel on the flow past an isolated cylinder is D/L, where L is the channel width. The other parameters which could have an influence are the upstream and downstream distance from the inlet and outlet respectively. Blackburn [2006] investigated the effect on upstream and downstream boundaries at different flow rates, and compared St and Re changes for the critical transition from laminar to periodic wake. He found that this boundary had little effect on St but did have a small influence on the transition Re. These discussions focus on the case when the effect of the inlet and outlet distances are negligible.

For $Re < 180$, blocking ratios in the range of $D/L > 0.001$ (Zdravkovich [2003]) still affect the transition between T and TrW. In flow regimes TrSL, TrBL and T, the effect of blocking above $D/L < 0.1$ can be ignored. Between $0.1 > D/L > 0.6$, some sort of correction is necessary. For $D/L > 0.6$, the flow regime is substantially altered and bears little resemblance to the unbounded flow case.

For laminar flows, several experimental investigations by White [1956], Taneda [1964] and others have produced numerical solutions for different ranges of Re. In turbulent wake regimes, the most successful correction models were derived from theoretical potential flow theory as produced by Fage [1929] and formulated in Rankines' work on potential flow around an oval. Successive work used two-dimensional inviscid theory Lock [1929], but it was not until Modi and El-Sherbiny [1977] used higher order terms that limited success was found. In reality, as stated by Blackburn [1994] all these correction models have limited use when flow separation occurs on a bluff body, generating large wake deficits. This has led to several numerical and experimental investigations into different aspects of blocking ratio effects. Two parameters influence the flow regime which are varied independently of each other to ascertain their effect on the flow. Blackburn [2006] carried out an in-depth investigation to determine how blocking D/L affected Re, when the flow regime switched between L2 and L3. This work demonstrates how St is highly influenced by D/L up until $D/L > 0.01$. Beyond this value, its influence is negligible. Blackburn's work also demonstrates how other

work, which uses limited boundary data, is heavily influenced by the boundary and cannot be reliably compared with the presented data. Blocking has an effect due to the effective narrowing of the channel accelerating the flow around the body, which results in larger forces on the body.

Anagnostopoulos and Iliadis [1996] looked at the effect of $Re = 106$ for three different $D/L = 0.05$, 0.15 and 0.25. They demonstrated that for $D/L = 0.05$ $St = 0.1658$ and for $D/L = 0.25$ $St = 0.2239$. For the same D/L's, there was a 0.377 drag coefficient difference. This shows the difficulty in choosing boundary conditions.

Experimentally, research by West and Apelt [1982] shows similar influences from the boundary as measured from wall pressure on the cylinder. However, this report also seemed to suffer from spanwise effect which, while considered, may prove impossible to decouple from the two-dimensional blocking effect. It is clear from these and other reviews that blocking is a substantial issue which much literature has addressed. Results from experiments and numerics must be put in a clear context of domain dimensions or calibrated corrections to free stream data.

The literature review indicates that, for blocking ratios of $D/L > 0.1$, the effect of blocking on the St is important and possibly changes it by a factor of 10%. The effect of blocking clearly affects the two-dimensional flow far downstream of the cylinder. In the near field, the drag and lift coefficients on the individual bodies are weakly affected by blocking, until $D/L > 0.33$.

2.4 Groups of a moderate number of cylinders ($2 < N_C < 10$)

The lack of research on small groups of interacting cylinders is not due to an absence of practical engineering applications. Local groups of cylinders are regularly found and an understanding of their interaction and the effect on their induced wake field is essential. This was well-illustrated by the collapse of a power station cooling tower stack at Ferrybridge in 1967. This stack was situated within a group, and a failure at the design stage to properly identify the possible interaction between the stacks and the potential problems caused by wakes from upstream stacks was responsible for the catastrophic failure.

Cylinder interaction can be broken into two sections. The simplest and most reviewed is the interaction between two cylinders. The more complex and less understood is the interaction where there are many cylinders together. The only experimental variables for the two cylinder arrangement are: Re, separation, ratio of diameters and inclination of the line between them and the incident flow. The arrangement of cylinders in relation to one another is simplified into three categories and illustrated in Figure 2.6 – the two extreme cases are tandem and side-by-side.

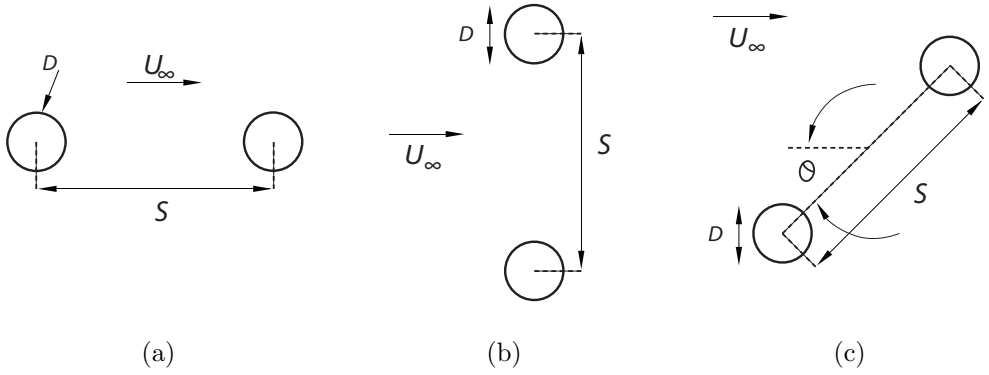

(a) (b) (c)

Figure 2.6: Schematic of the arrangement of two cylinders configured as (a) tandem, (b) side-by-side and (c) staggered.

Figure 2.6a is a tandem arrangement, where the second cylinder is downstream from the first and the critical parameter is the distance apart. Figure 2.6b illustrates side-by-side cylinders and again distance apart S/D is critical. The staggered arrangement shown in Figure 2.6c is more complex, where the distance between cylinder S/D is important but a second variable α measures the offset of the second cylinder and the exposure to free stream which can also be critical.

The literature on the tandem cylinder arrangement still contends with the complexities of single flow regimes, but additionally must take into account the effect of cylinder positioning. As a result, research has emerged where different cylinder positions are investigated in a defined flow regime. Most of this research is experimental, as it has not been possible theoretically and numerically to explain what is substantially more complex flow behaviour. An attempt by Rosenhead [1931] did produce a vortex wake model for cylinders based on the symmetry of cylinders when placed side

by side. More recently, three-dimensional numerical models have been attempted for low Re (Carmo et al. [2008]) and, as they did for a single cylinder, they reveal more of the flow field behaviour, particularly at regime switch stages. Experimentally, the effects of wake interactions have shown criteria in different regimes, which can have an input on one or both the cylinders.

In the arrangements shown in Figure 2.6b, it can be seen that as S/D reduces, the oppositely signed vortices produced on the inside edges of the cylinders weaken. Eventually, a single eddy street regime appears, as if the two cylinders at this point form a single bluff body. This occurs when $S/D < 1.2$.

For the arrangement shown in Figure 2.6a, when $S/D > 4$, both cylinders produce an eddy street, which is in phase and synchronized in frequency. At $S/D < 4$, the upstream cylinder detached shear layer attaches to the downstream cylinder's boundary. The upstream cylinder's wake stabilizes and only a wake from the downstream cylinder is detectable. When $S/D < 3$, the downstream cylinder becomes enveloped by the wake of the upstream cylinder.

The arrangements in Figure 2.6c can show both side by side and tandem behaviours. It is notable that, as the cylinders are brought together, there is a magnified C_L induced by the downstream cylinder deflecting the upstream cylinder's wake. The onset of all these effects is determined by Re.

More complex arrangements of cylinders have been experimentally investigated, typically for off-shore risers. These are summarized in Zdravkovich [1997]. In these experiments, different arrangements have been investigated but predominantly in either square or circular arrays and revolving around determining the effect of different angles of free stream on the group.

Much of this research is concerned with the induced forces on the group but Pearcey et al. [1982] also carried out measurements on the individual cylinders forming a group. In this work, they reviewed a square arrangement of 3×3 cylinders at three different angles to the flow stream. Ball and Hall [1980] investigated larger square arrays of cylinders up to 9×9 for different angles, but only related this to the total group drag. Both of these investigations did show how the effect of blocking could reduce the drag from downstream cylinders. However, from this work, it is not possible to deduce any fundamental description of the flow field, nor of the effect of

different blocking ratios on the free stream around the group.

2.5 Groups of a large number of cylinders ($N_C > 10$)

For large numbers of bodies ($N_C > 10$) in localized groups, the published research is limited. Interestingly, and partly in recognition of the importance of multibody flows, a number of new diagnostics have been developed to study the flow through and around bodies and the forces acting on them (described in §2.5.1 and 2.5.2). These diagnostics were developed for steady, inviscid flows, or have been applied to flows where the number of bodies is small ($N_C \leq 4$). The review below emphasizes the diagnostics which have been developed and applied to groups of bodies.

As the number of bodies increases $N_C \to \infty$, but the void fraction of bodies in the array ($\phi = N_C D^2/D_G^2$) is finite, the array of bodies begins to resemble a porous media. At this limit, it is not important to fully resolve the flow around individual bodies whose effect on the ambient fluid can be represented in terms of a distributed drag force. This approach is well-known and has been applied by Taylor [1991]. But the main difficulty, which is also widely recognized, is choosing a closure for the drag force. This is generally addressed by undertaking laboratory experiments.

2.5.1 Forces within groups of bodies

There is less research on localized groups of bodies. The previously defined characteristic equations for a single cylinder extend the metrics (described in previous section) to multiple bodies. Consider a group of bodies $i = 1, ..., N_C$ which lie in a localized group. The i-th body experiences a force

$$\boldsymbol{F}_i = \int_{S_{bi}} (p\boldsymbol{I} - \boldsymbol{\tau}) \cdot \hat{\boldsymbol{n}} \mathrm{d}S. \tag{2.25}$$

The drag and lift force is usually defined in terms of the local relative slip velocity. For a group of bodies, the local slip velocity will be different for each body and, indeed, may not be possible to calculate (for closely packed bodies). It is more relevant to define drag and lift coefficients based on the flow far upstream of the array:

$$C_{Di}(t) = \frac{\boldsymbol{F}_i \cdot \hat{\boldsymbol{x}}}{\frac{1}{2}\rho D U_\infty^2}, \qquad C_{Li}(t) = \frac{\boldsymbol{F}_i \cdot \hat{\boldsymbol{y}}}{\frac{1}{2}\rho D U_\infty^2}. \tag{2.26}$$

Following the described methodology, the time average drag and lift coefficients can be defined. For groups of bodies, the individual bodies experience mean forces due to wake separation, the effect of a mean shear and strain, unsteady components due to wake shedding and the interaction with vorticity shed from neighbouring bodies. A new approach to studying the force on a body within a large group was recently proposed by Chang et al. [2008].

2.5.2 Mean flow through and around groups of bodies

Most of the current work on the mean flow through and around groups of bodies is based on an inviscid description by Eames et al. [2004] of the *steady potential flow* past localized groups of bodies. While the framework they developed is general, it was applied to potential flows, and has yet to be tested for viscous flows past rigid bodies. Their analysis distinguishes between different processes which occur within, around and downstream of the group. The important point they addressed was the subtle distinction between average velocities based on an Eulerian mean (spatial average) and a mean velocity based on a Lagrangian mean (based on the average travel time of fluid parcels). It is certainly of interest to determine whether these results carry across to viscous flows. For bubbly flows at high void fraction (5 - 20% by void fraction), the experimental measurements by Roig and Tournemine [2007] appear to support the inviscid treatment. The major reason is that the conditionally averaged measurements by Roig and Tournemine [2007] are dominated by the kinematic blocking caused by the bubbles and are only weakly dependent on their wakes. A variety of mechanisms have been suggested, including wakes intermingling and the alternate positive/negative straining of wake vortical signatures to explain the weak effect of the wakes.

The definitions in Eames et al. [2004] are introduced to enable the flow to be studied and the notation is shown in Figure 2.7. Time averaged velocity is defined by

$$\langle \boldsymbol{u} \rangle = \frac{1}{T} \int_0^T \boldsymbol{u}. \tag{2.27}$$

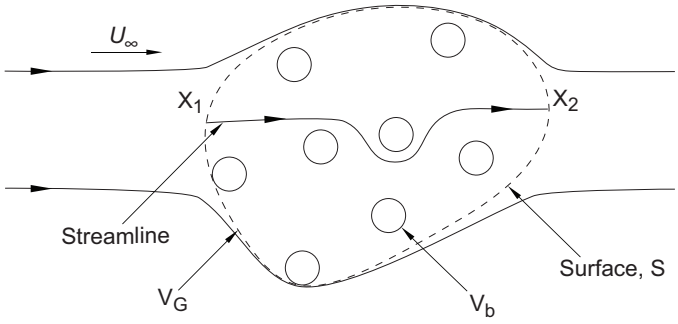

Figure 2.7: Schematic showing the notation for the Eulerian formulation, Eames et al. [2004].

The Eulerian mean of the velocity within the array of bodies is

$$\langle u_1 \rangle_E = \frac{1}{V_G - V_B} \int_V \langle \boldsymbol{u} \rangle \mathrm{d}V, \tag{2.28}$$

where V_G is the volume of the group and

$$V_B = \sum_{i=1}^{N_C} V_b \tag{2.29}$$

is the sum of the volumes of the bodies in the array. Eames et al. [2004] introduced a number of different measures of the Lagrangian velocity. Probably the most relevant here is the Lagrangian velocity based on the average travel time. Consider a fluid particle released at a point on the upwind side of the group, which later emerges at a downstream part of the array. Fluid particle released at $\boldsymbol{X}_1$ is transported to $\boldsymbol{X}_2$ in time t, where

$$\frac{\mathrm{d}\boldsymbol{X}}{\mathrm{d}t} = \boldsymbol{u}(\boldsymbol{x}, t). \tag{2.30}$$

The travel time between the two points is T_r and downstream distance L_r. The average Lagrangian velocity is

$$\langle u_1 \rangle_L = \left\langle \frac{L_r}{T_r} \right\rangle. \tag{2.31}$$

Eames et al. [2004] showed that there were subtle differences between the Eulerian and Lagrangian velocities, and that they were also sensitive to the shape of the group of bodies. For a wide high-aspect ratio rectangular array, the mean Eulerian velocity is increased because the flow tends to pass through the array, leading to $\langle u_1 \rangle_E = U_\infty/(1-\phi)$; for a thin, low-aspect ratio rectangular array, $\langle u_1 \rangle_E$ decreases (as $\langle u_1 \rangle_E = U_\infty(1-\phi C_m)$, where $C_m = 1$ is the added-mass coefficient of a cylinder). For a circular array, the mean Eulerian velocity is unchanged from the free stream velocity ($\langle u_1 \rangle_E = U_\infty$), while the Lagrangian is decreased (as $\langle u_1 \rangle_L = U_\infty(1-\phi C_m)$). To date, there have been no numerical studies of the Eulerian and Lagrangian mean flow in the context of localized groups of bodies.

2.6 Conclusion

The literature review has shown that considerable research effort has been concentrated on understanding the behaviour of individual bodies within various flow regimes. This has been extended to reviewing the complex interactive effects of coupled bodies but going beyond this point, work on multiple bodies has been limited to applications in specific situations, notably off-shore structures.

The new aspect of the work conducted here extends previous research by investigating how clearly defined groups of bodies interact and measuring the effect on the upstream and downstream flow for different void fractions of the groups. Within the groups, the Eulerian and Lagrangian average velocities were compared and the forces on individual bodies and the overall groups were measured. This was accomplished using two approaches.

The first approach was a numerical study conducted at high resolution and processed on the newly installed University College London supercomputer. This required a two-dimensional study of six different void fraction cases, which allowed accurate flow field measurements to be made and compared against measurements of the cylinder boundary forces. This is expanded in Chapter 3.

The complementary approach required the development of experimental techniques to extend the numerical work in a more general three-dimensional environment, with the capacity to investigate higher Re. This is expanded in Chapter 4.

Chapter 3

Numerical formulation

3.1 Numerical considerations

CFD (computational fluid dynamics) is a general description of a set of numerical techniques, models and tools to analyse fluid flows in complex situations. Broadly, the widely used technique has four interrelated aspects: mesh generation, formulation, solution and post-processing. Many commercial and open source programmes are available for each aspect or are combined together into single packages. In most cases, the use and interrogation of commercial packages (such as Fluent or CFX), for bespoke programming, requires writing additional modules to interface with the opaque internal coding which is generally not released.

Such commercial codes give rapid solutions to complex geometrical problems. This is, however, achieved by employing poorly resolved sub grid scales. This said, when correctly applied, these are practical engineering tools such as – Fluent (with a $k-\epsilon$ formulation solver) which can be used to assist in the design of the experimental apparatus in Chapter 4. Even open source software (e.g. Gerris, OpenFoam) requires the searching of their internal structure and tend to render post-processing (and the setting up of the geometry) rather difficult. Except for the simple case of internally bounded geometry (e.g. the cavity flow problem) and a small number of nodes (e.g. FEMLAB, less than 40k nodes), this tends to preclude their application to multibody flows.

In this chapter, the steps involved in formulating a general two-dimensional Navier-Stokes solver to study multibody flows are covered. The formulation includes how the structure of the code can be optimized to ensure efficient data interfacing specifically for the case of multibody analysis. This will also allow parallelization to be optimized, so that individual bodies are maintained and solved on dedicated processing nodes. This minimizes the handicap imposed by data swapping and becomes essential when dealing with a number of irregularly arranged bodies, as in this study. In such a programme, the generality of the coding is expressed in an object orientated form (using C++) and specific calls to dedicated solvers (such as PETSc or MKL libraries) allow the code to work for multiple dimensions with little change (Nithiarasu et al. [2004]).

At a general level, the inertia of most practical engineering fluid dynamics problems ensures that, on some level, the interior flow or boundary layers are small compared to the overall geometric lengthscale of the problem. This leads to a cascade of approximations which have been applied to study such problems. Working from the computationally most intensive (and the most accurate) to the fastest (and least intensive), we have at one extreme DNS (Direct Numerical Simulations) where the entire flow field is fully resolved. For the attached boundary layers (discussed in Chapter 2), this usually requires approximately $6-8$ points across the thin boundary layer on the upstream portion of the rigid body (Zienkiewicz et al. [2005]). At the next level of approximation - LES (Large Eddy Simulations) – the small-scale structure in the flow (the subgrid scale, which is smaller than the grid scale) is approximated as an increase in the fluid stress. This class of solutions tend to be tuned for specific problems. At the lowest level of approximation ($k-\epsilon$), the Reynolds-averaged Navier-Stokes equation is modelled by two evolution equations, one for the mean flow (coupled to the average turbulent kinetic energy and dissipation) and a second, which is introduced to model the coupling. $k-\epsilon$ models are well-known to poorly resolve wake shedding (Zienkiewicz et al. [2005]). This chapter describes an approach where the whole flow field is resolved.

Once the system of equations which represent or model the Navier-Stokes equation have been chosen, how the system of equations are coupled together and solved follow broadly the same principles. In the first instance, the computational domain needs to be discretized in some form and this tends to be related to the type of approximation

used and ultimately controls how quickly it will be solved. In the case of a DNS technique, the flow is discretized either as linear, triangular or tetrahedron elements for one, two and three-dimensional flows for complex arbitrary geometries. To speed up such calculations, many users use a Fourier decomposition (in two or three directions) depending on whether there is double or single periodicity in the computational domain. This approach significantly improves the computational speed of calculating the numerical solutions but tends to preclude their application to complex geometrical problems. A number of techniques employ Cartesian griding to exploit a banded structure of the matrix or to ensure easy regriding in areas of interest. The technique applied here uses a fixed triangular mesh, described in §3.4.1. Higher order polynomial approximations or curvilinear coordinates can be applied to elements which ensure that they are larger, but sometimes at a sacrifice to computational flexibility.

Following on from this, there are many computational techniques which can be applied to solve the resulting set of complex equations. A major question here is computational stability. The approach to dealing with the inertia of the flow in the FEM (finite element method) formulations, is the CBS (characteristic based scheme) technique which is applied to the inertial terms. Traditionally for engineering flows a checker-board pressure-velocity technique is employed.

The approach developed here was derived from six months of initial trials using Fluent as a means of evaluating the computational approaches to solving multibody flows, as described § 3.2. From this it was decided that a purpose-designed code would best address the problem, since it combines the best attributes of numerical techniques. In keeping with this, a FEM approximation was employed in the flow domain using a CBS scheme which is described in detail by Zienkiewicz and Codina [1995], Zienkiewicz et al. [1995], Codina et al. [1998] and reviewed below in § 3.3. This formulation enabled the computational technique to be kept general, facilitating application to the complex arbitrarily shaped domains found in multibody flows.

A major part of the numerical research conducted in this study was targeted at achieving an efficient implementation of the FEM approach. In the literature, the subtle features of writing and running such a code are largely ignored. These aspects are described in the implementation § 3.4, where they are broken down into domain

discretization (§ 3.4.1), code implementation and optimization (§ 3.4.2), and post-processing (§ 3.4.7).

New computational codes require validation which here is done against established test cases as presented in § 3.5. The first case, (§ 3.5.1), is used to test the steady state solution. The second case, (§ 3.5.3), deals with both steady and transient states and the third, (§ 3.5.4), deals with transient states. An in-depth analysis of the effect of mesh resolution on the unsteady parameters is also described.

3.2 Preliminary investigation

Initial investigations used a commercial finite volume code called Fluent. This code can be extended through a UDF interface which allows users to add functionality to the programme. In the work done here, this was used to impose a drag force in the shape of a cylinder on the flow field to quantify the required $\langle C_{DG} \rangle$ to induce a similar wake to that which would be expected behind a cylinder. Figures 3.1a and 3.1b show the variation of x_1 and x_2 components of velocity, while figure 3.1c shows the vorticity magnitude. The drag force value for each node was set in the cylinder region, so the velocity magnitude would be reduced to zero. This initial investigation found limitations in the practicability of writing the interfaces necessary to use Fluent for multi-body research. This was because of the uncertainty involved in interfacing with the underlining code of Fluent (which is not released) and limitations imposed by using the integrated compiler.

3.3 Finite element method

The main numerical technique applied in this thesis will now be discussed. This utilizes the finite element method which is described in detail by Zienkiewicz et al. [2005]. Consider a general partial differential equation described by

$$\mathcal{L}(T) = 0, \tag{3.1}$$

which is satisfied in a domain Ω where $\mathcal{L}$ is an operator and T is the unknown function (or a vector of functions). The approximate solution to T, $\overline{T}$ is represented in terms

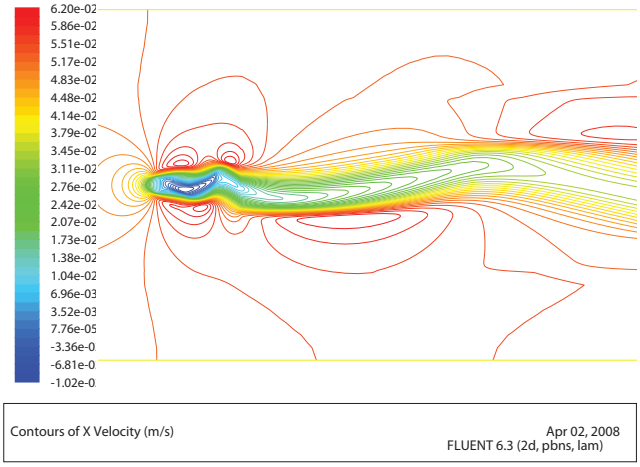

(a)

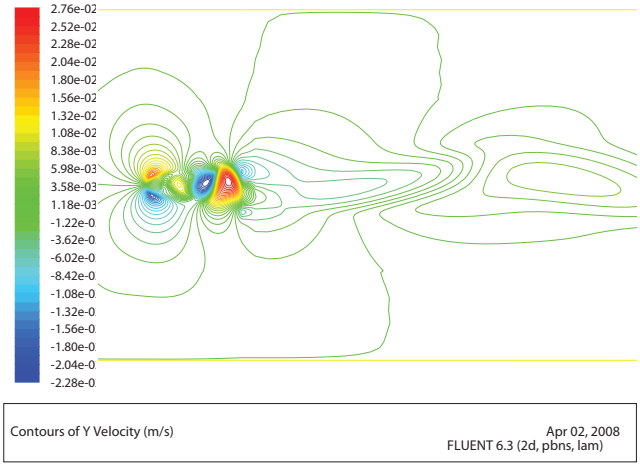

(b)

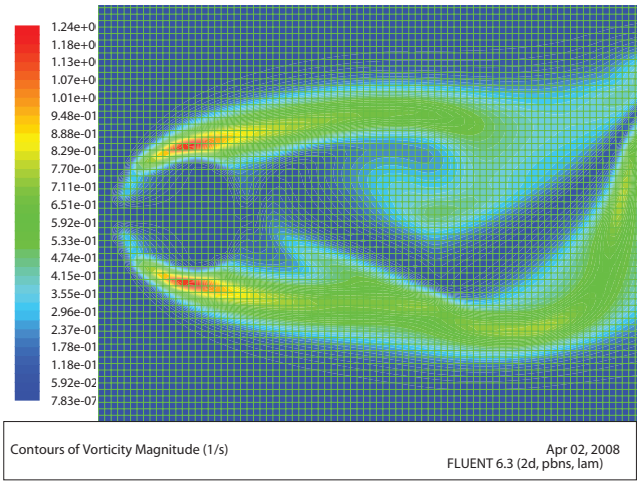

(c)

Figure 3.1: Flow field generated by Fluent using a circular drag source (a) u_1 velocity contour, (b) u_2 velocity contour, (c) vorticity.

of a series of basis functions,

$$T \approx \overline{T} = \sum_{i=1}^{N} a_j N_j(\boldsymbol{x}), \tag{3.2}$$

where N is the number of nodes in the approximation. A measure of the (residual) error in this approximation to the partial differential equation is

$$R = \mathcal{L}(\overline{T}). \tag{3.3}$$

The method of weighted residuals requires that the unknown coefficient a_i are calculated to satisfy $\int_\Omega w_i(\boldsymbol{x}) R \mathrm{d}\Omega = 0$ for specified weighting functions w_i for $i = 1, ..., N$. The Galerkin method requires the weighting functions to be the basis functions, ie. $w_i = N_i$, and it is required to determine the unknowns a_j so that

$$\int_\Omega N_i \mathcal{L}(\overline{T}) \mathrm{d}\Omega = 0. \tag{3.4}$$

In terms of applying this technique to solving the Navier-Stokes equation, a series of (coupled) partial differential equations is formulated where one is solving the velocity components (u_1, u_2) and pressure (p). Since two-dimensional flows are explicitly dealt with, the position vector is $\boldsymbol{x} = (x_1, x_2)$ and the integration is taken over the computational domain. As a starting point, there are a number of different choices for the basis functions, depending on the degree of approximation that is permitted. Curvilinear elements tend to be applied when the computational domain does not change; parallelogram elements give improved accuracy (with 4, 6 or 8 nodes) with a computational expense in setting up the system of equations – triangle elements (with 3 nodes) are employed for simplicity.

Consider a triangular element with the edge points labeled as i, j and k, whose positions are (x_{1i}, x_{2i}), (x_{1j}, x_{2j}) and (x_{1k}, x_{2k}) respectively. The linear basis functions for the triangle element shown in figure 3.2 are:

$$N_i = \frac{1}{2A}(a_i + b_i x_{1i} + c_i x_{2i}), \quad N_j = \frac{1}{2A}(a_j + b_j x_{1j} + c_j x_{2j}), \quad N_k = \frac{1}{2A}(a_k + b_k x_{1k} + c_k x_{2k}), \tag{3.5}$$

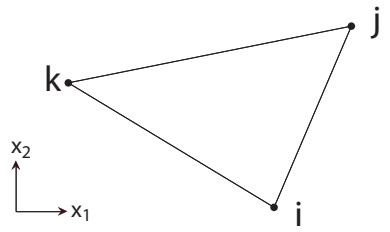

Figure 3.2: Schematic of a triangular element used in the study. The labels i, j and k are cyclic in the anticlockwise direction sense, so that the area A, defined by (3.9) is positive.

where

$$a_i = x_{1j}x_{2k} - x_{1k}x_{2j}, \quad b_i = x_{2j} - x_{2k}, \quad c_i = x_{1k} - x_{1j} \tag{3.6}$$

$$a_j = x_{1k}x_{2i} - x_{1i}x_{2k}, \quad b_j = x_{2k} - x_{2i}, \quad c_j = x_{1i} - x_{1k} \tag{3.7}$$

$$a_k = x_{1i}x_{2j} - x_{1j}x_{2i}, \quad b_k = x_{2i} - x_{2j}, \quad c_k = x_{1j} - x_{1i}. \tag{3.8}$$

The vector $[\mathbf{N}]$ is defined as $[\mathbf{N}] = [N_i, N_j, N_k]$. The area of the triangular element is

$$A = \begin{vmatrix} 1 & x_{1i} & x_{2i} \\ 1 & x_{1j} & x_{2j} \\ 1 & x_{1k} & x_{2k} \end{vmatrix}. \tag{3.9}$$

The gradient vectors of the linear shape functions are:

$$\boldsymbol{b} = \frac{\partial[\mathbf{N}]}{\partial x_1} = \frac{1}{2A}[b_i, b_j, b_k], \qquad \boldsymbol{c} = \frac{\partial[\mathbf{N}]}{\partial x_2} = \frac{1}{2A}[c_i, c_j, c_k]. \tag{3.10}$$

In setting out the FEM formulation, a standard result describing the weighted integral of the basis functions over the triangular element is used:

$$\int_\Omega N_i^a N_j^b N_k^c \, \mathrm{d}\Omega = \frac{a!b!c!2A}{(a+b+c+2)!}. \tag{3.11}$$

The defining equations which are being solved are continuity and momentum, where

$$\frac{\partial u_1}{\partial x_1} + \frac{\partial u_2}{\partial x_2} = 0 \tag{3.12}$$

$$\frac{\partial u_i}{\partial t} + u_1 \frac{\partial u_i}{\partial x_1} + u_2 \frac{\partial u_i}{\partial x_2} = -\frac{1}{\rho}\frac{\partial p}{\partial x_i} + \nu \left(\frac{\partial^2 u_i}{\partial x_1^2} + \frac{\partial^2 u_i}{\partial x_2^2} \right), \tag{3.13}$$

where $i = 1, 2$. The velocity $\boldsymbol{u} = (u_1, u_2)$. These are solved in three steps, over the period t_n to $t_{n+1} = t_n + \Delta t$. The superscript n or $n+1$ refer to evaluation at t_n or t_{n+1} respectively.

Step 1

The Navier-Stokes equations are solved by a characteristic based split (CBS) algorithm based on the projection method of Chorin [8] as described in Zienkiewicz and Codina [20] and Zienkiewicz and Taylor [21]. In this method, an auxiliary velocity field is introduced to uncouple the momentum and continuity equations; a characteristic method is used to stabilize the non self-adjoint operators in the CBS formulation of (3.13) can be written as

$$\begin{aligned} \frac{\tilde{u}_i - u_i^n}{\Delta t} = -u_1 \frac{\partial u_i^n}{\partial x_1} - u_2 \frac{\partial u_i^n}{\partial x_2} + \nu \left(\frac{\partial^2 u_i}{\partial x_1^2} + \frac{\partial^2 u_i}{\partial x_2^2} \right)^n \\ + u_1 \frac{\Delta t}{2} \frac{\partial}{\partial x_1} \left[u_1 \frac{\partial u_i^n}{\partial x_1} + u_2 \frac{\partial u_i^n}{\partial x_2} \right] + u_2 \frac{\Delta t}{2} \frac{\partial}{\partial x_2} \left[u_1 \frac{\partial u_i}{\partial x_1} + u_2 \frac{\partial u_i}{\partial x_2} \right]^n, \end{aligned} \tag{3.14}$$

for $i = 1, 2$. The intermediate velocity $\tilde{\boldsymbol{u}}$.

Step 2

Taking the divergence of the momentum equation one has:

$$\boldsymbol{\nabla}^2 p = -\rho \frac{\partial \boldsymbol{\nabla} \cdot \boldsymbol{u}}{\partial t}. \tag{3.15}$$

Integrating (3.15) from time t_n to $t_n + \Delta t$, gives

$$\Delta t \boldsymbol{\nabla}^2 p = -\rho \left[\boldsymbol{\nabla} \cdot \boldsymbol{u}^n - \boldsymbol{\nabla} \cdot \tilde{\boldsymbol{u}} \right] = \rho \boldsymbol{\nabla} \cdot \tilde{\boldsymbol{u}}. \tag{3.16}$$

(Using the continuity equation, $\boldsymbol{\nabla} \cdot \boldsymbol{u}^n = 0$.) The pressure correction is chosen to force the intermediate solution $\tilde{\boldsymbol{u}} = (\tilde{u}_1, \tilde{u}_2)$ to be solenoidal, i.e. from (3.16),

$$\frac{\partial^2 p}{\partial x_1^2} + \frac{\partial^2 p}{\partial x_2^2} = \frac{\rho}{\Delta t}\left(\frac{\partial \tilde{u}_1}{\partial x_1} + \frac{\partial \tilde{u}_2}{\partial x_2}\right). \tag{3.17}$$

Step 3

The pressure calculated in Step 2 is used to correct the intermediate velocity so that it is sinusoidal, i.e.

$$\frac{u_1^{n+1} - \tilde{u}_1}{\Delta t} = -\frac{1}{\rho}\frac{\partial p^n}{\partial x_1}, \qquad \frac{u_2^{n+1} - \tilde{u}_2}{\Delta t} = -\frac{1}{\rho}\frac{\partial p^n}{\partial x_2}. \tag{3.18}$$

3.3.1 Spatial discretization

To solve the three-step problem, a spatial discretization of the data is introduced where $[\boldsymbol{N}] = [N(x_1, x_2)_i, N(x_1, x_2)_j, N(x_1, x_2)_k]$ is a 1×3 vector of basis functions which depends on x_1 and x_2 and $\{\boldsymbol{u}_1\}$, $\{\boldsymbol{u}_2\}$ and $\{\boldsymbol{p}\}$ are 3×1 vectors of unknowns (e.g. $\{\boldsymbol{u}_1\} = [u_{1_i}, u_{1_j}, u_{1_k}]^T$). Within the triangular element, the velocity components and pressure are approximated by

$$u_1 = [\boldsymbol{N}]\{\boldsymbol{u}_1\}, \quad u_2 = [\boldsymbol{N}]\{\boldsymbol{u}_2\}, \quad p = [\boldsymbol{N}]\{\boldsymbol{p}\}. \tag{3.19}$$

Each term in the momentum equation was considered. The first term is

$$\int_{\Omega_e} \frac{[\boldsymbol{N}]^T[\boldsymbol{N}](\{\tilde{\boldsymbol{u}}_1\} - \{\boldsymbol{u}_1\}^n)}{\Delta t} \mathrm{d}\Omega = \frac{\boldsymbol{M}(\{\tilde{\boldsymbol{u}}_1\} - \{\boldsymbol{u}_1\}^n)}{\Delta t}, \tag{3.20}$$

where the local mass matrix is

$$[\boldsymbol{M}] = \frac{A}{12}\begin{bmatrix} 2 & 1 & 1 \\ 1 & 2 & 1 \\ 1 & 1 & 2 \end{bmatrix}. \tag{3.21}$$

The convective term is

$$\int_{\Omega_e} [\boldsymbol{N}]^T[\boldsymbol{N}]\left(\{\boldsymbol{u}_1\}\frac{\partial[\boldsymbol{N}]}{\partial x_1} + \{\boldsymbol{u}_2\}\frac{\partial[\boldsymbol{N}]}{\partial x_2}\right)\{\boldsymbol{u}_1\}^n \mathrm{d}\Omega = [\boldsymbol{C}]\{\boldsymbol{u}_1\}^n, \tag{3.22}$$

where

$$[\boldsymbol{C}] = \frac{[\boldsymbol{M}]}{2A}\left(\{\boldsymbol{u}_1\}^n \boldsymbol{b} + \{\boldsymbol{u}_2\}^n \boldsymbol{c}\right). \tag{3.23}$$

The viscous term is

$$\begin{aligned}\nu \int_{\Omega_e} [\boldsymbol{N}]^T \left(\frac{\partial^2 u_1}{\partial x_1^2} + \frac{\partial^2 u_1}{\partial x_2^2}\right)^n \mathrm{d}\Omega = \\ \nu \int_{\Gamma_e} \left([\boldsymbol{N}]^T \frac{\partial [\boldsymbol{N}]}{\partial x_1} + [\boldsymbol{N}]^T \frac{\partial [\boldsymbol{N}]}{\partial x_2}\right) \mathrm{d}\Gamma \{\boldsymbol{u}_1\}^n - \\ \nu \int_{\Omega_e} \left(\frac{\partial [\boldsymbol{N}]^T}{\partial x_1}\frac{\partial [\boldsymbol{N}]}{\partial x_1} + \frac{\partial [\boldsymbol{N}]^T}{\partial x_2}\frac{\partial [\boldsymbol{N}]}{\partial x_2}\right) \mathrm{d}\Omega \{\boldsymbol{u}_1\}^n \\ = \{\boldsymbol{f}_1\} - \nu [\boldsymbol{K}] \{\boldsymbol{u}_1\}^n, \end{aligned} \tag{3.24}$$

where

$$\{\boldsymbol{f}_1\} = \frac{\nu}{2A} \int_{\Gamma_e} \left(\boldsymbol{N}^T n_1 \mathrm{d}\Gamma \boldsymbol{b} + \int_{\Gamma_e} \boldsymbol{N} n_2 \mathrm{d}\Gamma \boldsymbol{c}\right) \{\boldsymbol{u}_1\}^n, \tag{3.25}$$

and

$$[\boldsymbol{K}] = \frac{1}{4A}\left(\boldsymbol{b}^T \boldsymbol{b} + \boldsymbol{c}^T \boldsymbol{c}\right). \tag{3.26}$$

The forcing vector can be expressed explicitly as

$$\{\boldsymbol{f}_i\} = \frac{1}{4A} \begin{bmatrix} n_{1,ij}\mathrm{d}\Gamma_{ij} + n_{1,ki}\mathrm{d}\Gamma_{ki} \\ n_{1,ij}\mathrm{d}\Gamma_{ij} + n_{1,jk}\mathrm{d}\Gamma_{jk} \\ n_{1,jk}\mathrm{d}\Gamma_{jk} + n_{1,ki}\mathrm{d}\Gamma_{ki} \end{bmatrix} \boldsymbol{b}\{\boldsymbol{u}_i\}^n + \frac{1}{4A} \begin{bmatrix} n_{2,ij}\mathrm{d}\Gamma_{ij} + n_{2,ki}\mathrm{d}\Gamma_{ki} \\ n_{2,ij}\mathrm{d}\Gamma_{ij} + n_{2,jk}\mathrm{d}\Gamma_{jk} \\ n_{2,jk}\mathrm{d}\Gamma_{jk} + n_{2,ki}\mathrm{d}\Gamma_{ki} \end{bmatrix} \boldsymbol{c}\{\boldsymbol{u}_i\}^n \tag{3.27}$$

$$= \frac{1}{4A} \begin{bmatrix} 1 & 0 & 1 \\ 1 & 1 & 0 \\ 0 & 1 & 1 \end{bmatrix} \left(\begin{bmatrix} n_{1,ij}\mathrm{d}\Gamma_{ij} \\ n_{1,jk}\mathrm{d}\Gamma_{jk} \\ n_{1,ki}\mathrm{d}\Gamma_{ki} \end{bmatrix} \boldsymbol{b} + \begin{bmatrix} n_{2,ij}\mathrm{d}\Gamma_{ij} \\ n_{2,jk}\mathrm{d}\Gamma_{jk} \\ n_{2,ki}\mathrm{d}\Gamma_{ki} \end{bmatrix} \boldsymbol{c} \right) \{\boldsymbol{u}_i\}^n, \tag{3.28}$$

for $i = 1, 2$

The stabilization matrix is

$$[\boldsymbol{K}_e] = \int_{\Omega_e} [\boldsymbol{N}]^T [\boldsymbol{N}] \{\boldsymbol{u}_1\} \frac{\Delta t}{2} \left[\frac{\partial [\boldsymbol{N}]}{\partial x_1} \{\boldsymbol{u}_1\} \frac{\partial [\boldsymbol{N}]}{\partial x_1} + \frac{\partial [\boldsymbol{N}]}{\partial x_1} \{\boldsymbol{u}_2\} \frac{\partial [\boldsymbol{N}]}{\partial x_2} \right] \mathrm{d}\Omega +$$
$$+ \int_{\Omega_e} [\boldsymbol{N}]^T [\boldsymbol{N}] \{\boldsymbol{u}_2\} \frac{\Delta t}{2} \left[\frac{\partial [\boldsymbol{N}]}{\partial x_2} \{\boldsymbol{u}_1\} \frac{\partial [\boldsymbol{N}]}{\partial x_1} + \frac{\partial [\boldsymbol{N}]}{\partial x_2} \{\boldsymbol{u}_2\} \frac{\partial [\boldsymbol{N}]}{\partial x_2} \right] \mathrm{d}\Omega \tag{3.29}$$
$$= \frac{[\boldsymbol{M}]\{\boldsymbol{u}_1\}\Delta t}{8A^2} \left[\boldsymbol{b}\{\boldsymbol{u}_1\}\boldsymbol{b} + \boldsymbol{b}\{\boldsymbol{u}_2\}\boldsymbol{c} \right] + \frac{[\boldsymbol{M}]\{\boldsymbol{u}_2\}\Delta t}{8A^2} \left[\boldsymbol{c}\{\boldsymbol{u}_1\}\boldsymbol{b} + \boldsymbol{c}\{\boldsymbol{u}_2\}\boldsymbol{c} \right]. \tag{3.30}$$

Noting that $\boldsymbol{b}\{\boldsymbol{u}_1\} = \{\boldsymbol{u}_1\}^T \boldsymbol{b}^T$, then the stabilization matrix is

$$[\boldsymbol{K}_e] = \frac{[\boldsymbol{M}]\{\boldsymbol{u}_1\}\Delta t}{8A^2} \left[\{\boldsymbol{u}_1\}^T \boldsymbol{b}^T \boldsymbol{b} + \{\boldsymbol{u}_2\}^T \boldsymbol{b}^T \boldsymbol{c} \right] + \frac{[\boldsymbol{M}]\{\boldsymbol{u}_2\}\Delta t}{8A^2} \left[\{\boldsymbol{u}_1\}^T \boldsymbol{c}^T \boldsymbol{b} + \{\boldsymbol{u}_2\}^T \boldsymbol{c}^T \boldsymbol{c} \right]. \tag{3.31}$$

To ensure the velocity estimate at t_{n+1} is solenoidal, we update by

$$\boldsymbol{u}_{n+1} - \tilde{u} = -\frac{\Delta t \boldsymbol{\nabla} p}{\rho}. \tag{3.32}$$

The kinematic condition $\hat{\boldsymbol{n}} \cdot \boldsymbol{u} = 0$ is on the boundaries and this must be taken into account in dealing with the pressure equation. From (3.16),

$$\int_{\Omega_e} [\boldsymbol{N}]^T \boldsymbol{\nabla}^2 p \mathrm{d}\Omega = \int_{\Omega_e} \frac{\partial}{\partial x_1} \left([\boldsymbol{N}]^T \frac{\partial p}{\partial x_1} \right) + \frac{\partial}{\partial x_2} \left([\boldsymbol{N}]^T \frac{\partial p}{\partial x_2} \right) \mathrm{d}\Omega \tag{3.33}$$
$$- \int_{\Omega_e} \left(\frac{\partial [\boldsymbol{N}]^T}{\partial x_1} \frac{\partial p}{\partial x_1} + \frac{\partial [\boldsymbol{N}]^T}{\partial x_2} \frac{\partial p}{\partial x_2} \right) \mathrm{d}\Omega \tag{3.34}$$
$$= -[\boldsymbol{K}]\{\boldsymbol{p}\} + \{\boldsymbol{f}_3\}, \tag{3.35}$$

and

$$\{\boldsymbol{f}_3\} = \frac{1}{2A} \left(\int_{\Gamma_e} \boldsymbol{N}^T n_1 \mathrm{d}\Gamma \boldsymbol{b} + \int_{\Gamma_e} \boldsymbol{N}^T n_2 \mathrm{d}\Gamma \boldsymbol{c} \right) \{\boldsymbol{p}\}. \tag{3.36}$$

The forcing term is

$$\{\boldsymbol{f}_3\} = \frac{1}{4A}\begin{bmatrix} 1 & 0 & 1 \\ 1 & 1 & 0 \\ 0 & 1 & 1 \end{bmatrix}\left(\begin{bmatrix} n_{1,ij}\mathrm{d}\Gamma_{ij} \\ n_{1,jk}\mathrm{d}\Gamma_{jk} \\ n_{1,ki}\mathrm{d}\Gamma_{ki} \end{bmatrix}\boldsymbol{b} + \begin{bmatrix} n_{2,ij}\mathrm{d}\Gamma_{ij} \\ n_{2,jk}\mathrm{d}\Gamma_{jk} \\ n_{2,ki}\mathrm{d}\Gamma_{ki} \end{bmatrix}\boldsymbol{c}\right)\{\boldsymbol{p}\}. \tag{3.37}$$

Note that the contribution to the boundary sides to the boundary elements is zero as a consequence of the kinematic boundary conditions. The divergence of the velocity field is

$$\int_{\Omega_e}\left([\boldsymbol{N}]^T\frac{\partial\tilde{u}_1}{\partial x_1} + [\boldsymbol{N}]^T\frac{\partial\tilde{u}_2}{\partial x_2}\right)\mathrm{d}\Omega = \boldsymbol{G}_1\{\tilde{\boldsymbol{u}}_1\}^n + \boldsymbol{G}_2\{\tilde{\boldsymbol{u}}_2\} \tag{3.38}$$

where the gradient vectors are

$$[\boldsymbol{G}_1] = \frac{1}{6}\begin{bmatrix} 1 \\ 1 \\ 1 \end{bmatrix}\boldsymbol{b}, \qquad [\boldsymbol{G}_2] = \frac{1}{6}\begin{bmatrix} 1 \\ 1 \\ 1 \end{bmatrix}\boldsymbol{c}. \tag{3.39}$$

To summarize

Step 1: momentum calculations

$$[\boldsymbol{M}]\frac{\Delta\{\tilde{\boldsymbol{u}}_i\}}{\Delta t} = -[\boldsymbol{C}]\{\boldsymbol{u}_i\}^n - \nu[\boldsymbol{K}]\{\boldsymbol{u}_i\}^n - [\boldsymbol{K}_e]\{\boldsymbol{u}_i\}^n + \{\boldsymbol{f}_i\}, \tag{3.40}$$

for $i = 1, 2$

Step 2: pressure calculation

$$[\boldsymbol{K}]\{\boldsymbol{p}\}^n = -\frac{1}{\Delta t}[[\boldsymbol{G}_1]\{\tilde{\boldsymbol{u}}_1\} + [\boldsymbol{G}_2]\{\tilde{\boldsymbol{u}}_2\}] + \{\boldsymbol{f}_3\} \tag{3.41}$$

Step 3: velocity correction

$$[\boldsymbol{M}]\{\boldsymbol{u}_i\}^{n+1} = [\boldsymbol{M}]\{\tilde{\boldsymbol{u}}_i\} - \Delta t[\boldsymbol{G}_i]\{\boldsymbol{p}\}^n. \tag{3.42}$$

The above equations are solved for $i = 1, 2$.

3.3.2 Critical time step Δt

The CBS formulation can be written either implicitly, explicitly or semi-implicitly. The latter is used in this work. For flow regimes which do not change with time after an initial settling time, such as the lid-driven cavity problem, a local time step could be calculated at each node, which will greatly improve processing time. This method of calculating the time step has not been used, however, as this investigation primarily examines the unsteady nature of high Re flows about a circular cylinder. To investigate unsteady flow behaviour, a global time step is used which is based on the minimum time step at any node in the domain. Therefore, there are two time steps calculated at each node to take account of both diffusion and convection. To ensure stability, the minimum of either of these is used, with an additional safety factor which varies. In this work, a safety factor, $Sf = 0.5$, was found to give good stability. Thus, the local time step for each node is

$$\Delta t = Sf \times \min(\Delta t_{diffusion}, \Delta t_{convection}). \tag{3.43}$$

The time steps for convection and diffusion are calculated using

$$\Delta t_{convection} = \frac{h_n}{u}, \quad \Delta t_{diffusion} = \frac{h_n^2}{\nu}, \tag{3.44}$$

where

$$u = \sqrt{u_1^2 + u_2^2}.vv \tag{3.45}$$

h_n is a characteristic lengthscale (as shown in Figure 3.3) which is unique to each element and node combination. The measure h_n is isotropic because there is no preferential direction to the flow. The lengthscale does not change with a fixed mesh unless the mesh is refined. To speed up calculation, it can be simply calculated using

$$h_n = \min \left(\frac{2 \times \text{element area}}{\text{opposite side length}} \right)_e, \tag{3.46}$$

where $(e = element_1, element_2, \ldots)$. For example, in the case of figure 3.3, h_n is defined as

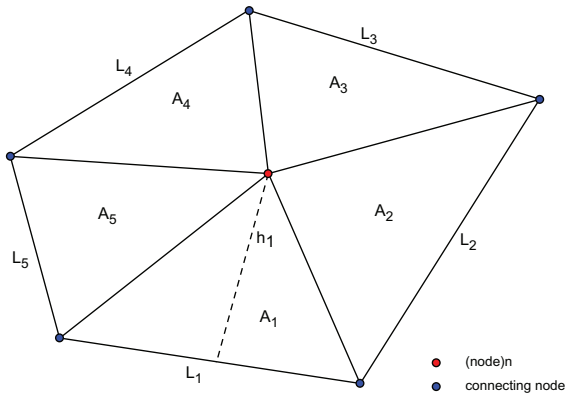

Figure 3.3: Schematic showing how the local characteristic lengthscale, h_n, used to define the limits for the time step (3.44), is defined.

$$h_n = \min\left(\frac{2A_1}{L_1}, \frac{2A_2}{L_2}, \frac{2A_3}{L_3}, \frac{2A_4}{L_4}, \frac{2A_5}{L_5}\right). \tag{3.47}$$

More elaborate methods can be employed to maximize the value of Δt, which use the flow in the stream-wise direction at every node, as described by Shakib [1988]. When resolving boundary layers, small elements are employed and, as the element size determines Δt, it was found that run times are considerably increased. Figure 3.4 shows how Δt varies with the element size used to resolve the very fine boundary layer induced on a cylinder wall. This imposes a stringent restraint on the speed at which a solution can be found (see Zienkiewicz et al. [2005] and Massarotti et al. [2006]). Therefore, typically, an artificial time step is employed as described by Nithiarasu and Liu [2005]. There is still an open question as to whether this can be used in this research.

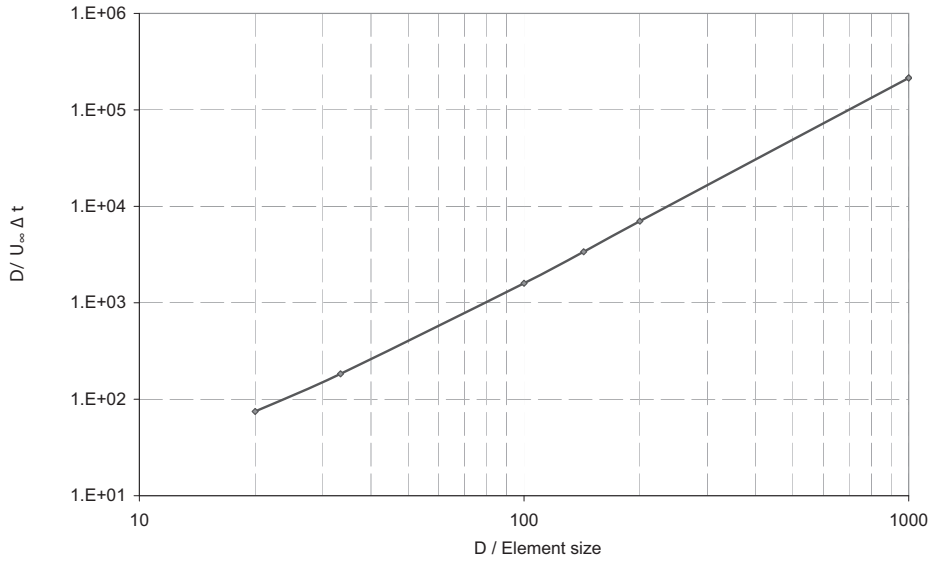

Figure 3.4: Variation of $D/U_\infty \Delta t$ with element size normalized by D.

3.3.3 Calculating the vorticity field

From Acheson [1990, p. 186] the two-dimensional flow vorticity field is given by:

$$\omega = \frac{\partial u_2}{\partial x_1} + \frac{\partial u_1}{\partial x_2}. \tag{3.48}$$

To calculate the vorticity field at each node, we solve the equation

$$\omega - \frac{\partial u_2}{\partial x_1} + \frac{\partial u_1}{\partial x_2} = 0. \tag{3.49}$$

The vorticity field is expressed as

$$\omega = [\boldsymbol{N}]\{\boldsymbol{\omega}\}. \tag{3.50}$$

The FEM formulation involves weighting (3.49) against a basis function and integrating over the whole domain, to give

$$\int_{\Omega_e} \left([\boldsymbol{N}]^T [\boldsymbol{N}]\{\boldsymbol{\omega}\} - [\boldsymbol{N}]^T \frac{\partial u_2}{\partial x_1} + [\boldsymbol{N}]^T \frac{\partial u_1}{\partial x_2} \right) \mathrm{d}\Omega = 0. \tag{3.51}$$

This reduces to

$$[\boldsymbol{M}]\{\boldsymbol{\omega}\} = \boldsymbol{G}_1\{\tilde{\boldsymbol{u}}_2\}^n - \boldsymbol{G}_2\{\tilde{\boldsymbol{u}}_1\}. \tag{3.52}$$

The other gradients of the velocity are dealt with in the same manner. Equation 3.52 is solved in the same way as step one in the CBS scheme.

3.4 Implementation

3.4.1 Meshing

An FEM formation starts by defining the domain and boundary conditions. Typically, there are two methods in which this is accomplished. The first, which is becoming less popular due to its inflexibility, is to define the problem in terms of simple parameters which the code then discretizes into a solution. This is normally used for regular simple geometric problems which use structured meshes.

The second method, which has been employed in this study, is to split parameterization and domain discretization through meshing into two parts. This work did not attempt to investigate the optimum meshing method or approach. Instead, in common with commercial software, purpose-built, well-tested, unstructured meshing programmes were used to discretize the domain into triangles and tetrahedrons. Many such programmes are available commercially such as GAMBIT (used elsewhere in this study for the flume design) formerly from Fluent now ANSYS, Triangle and others.

These commercial packages are costly and unnecessarily complex for the two-dimensional domains presented here. A very good and freely available open source programme called Gmsh was therefore chosen. Gmsh produces high-quality meshes and has post-processing facilities. The programme was designed Christophe Geuzaine (University of Liege) and Jean-Franois Remacle (Catholic University of Louvain) and released under the GNU general public license. Effectively, this package pulls together lots of freely available and powerful libraries. Of particular note is Triangle (produced by Jonathan Shewchuk) which produces high-quality exact Delaunay triangulations, constrained Delaunay triangulations, conforming Delaunay triangulations and Voronoi diagrams. These combine to ensure high-quality triangular meshes,

where every triangle is as close as possible to an ideal isosceles shape.

The post-processor in Gmsh uses GLZPS, also written by Christophe Geuzaine, which gives very high-quality open GL to PostScript conversions and has been implemented with considerable success. Gmsh uses a script file definition of a domain to define the domain geometry. This is a simple language, in which points are defined in three-dimensional space, linked together by lines and arcs which are then grouped to form surfaces and, in turn, volumes. On the points, mesh resolution is set at that point and all elements inherit from it, using a linear interpolation between different resolved areas. A short illustration of the code, which forms the geometry in Figure 3.5b, is shown in Figure 3.5a.

```
Point (1) = {0,0,0,0.1};
Point (2) = {1,0,0,0.1};
Point (3) = {1,1,0,0.1};
Point (4) = {0,1,0,0.1};
Line (1) = {1,2};
Line (2) = {2,3};
Line (3) = {3,4};
Line (4) = {4,1};
Line Loop (5) = {1,2,3,4};
Plane Surface (6) = {5};
```

(a)

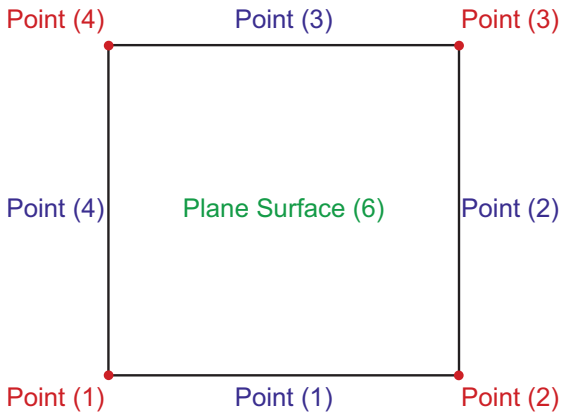

(b)

Figure 3.5: Example of the Gmsh scripting language in (a) which generates the geometry and is shown in (b).

The Gmsh programme then meshes the domain and saves the nodal element lists in a mesh file. This can be either binary or ASCII format. The order of this file starts by listing the nodes with their coordinates. After this, all elements forming the domain or on a boundary are listed in an integer reference to the nodes which form them. All elements also contain the highest level boundary condition necessary for the solver to form an understanding of the problem domain.

3.4.2 Solvers

The primary role of the solver is to conduct matrix operations and to solve large arrays of linear equations. Historically, there has been no single approach to how the solver is best implemented, partly because each application is different, as is the technical expertise of the person implementing. This may be because of natural inertia in the face of the speed of change in technology and also the lack of a consistent approach to computer architecture and standards.

The code has been developed considering the following:

1. Allowing cross-compiler support to ensure platform independence.
2. Utilizing object oriented techniques to simplify and reduce coding complexity.
3. Making use of readily available numerical libraries to reduce development time.
4. Optimizing code for performance, with particular attention to avoiding bottlenecks.
5. Parallelizing where significant benefits are found.
6. Allowing the programme to be driven using externally set parameters and scripts.

Below, the development is mapped out with the overall objective of simplifying and optimizing both the development of the code itself and also its eventual user application.

3.4.3 Programme Structure and Language

Traditionally, high performance codes are written in Fortran, which is an efficient, fast but basic language. Fortran's performance results from highly optimized compilers, which are often written with a specific platform in mind. Previously, this was unachievable in more complex languages, but now C and C++ can perform equally well when compiled with new optimized libraries and compilers. In this case, C++ was chosen as it has become well supported by numerical libraries and offers the benefits

of a much more structured approach with object oriented methods which simplifies code development and helps with code reuse.

To ensure maximum flexibility in running the code, it was written using the standard ANSI-C++ which allows the code to be compiled and run on most operating systems – e.g. Linux or Windows which support a standard C++ compiler.

Objects are an abstract concept which has become popular in modern programming. In effect, it allows variables and operating functions to exist as one item. When properly used, code can be tested and reused, without adversely affecting other components in the system. This code has been implemented, so that each aspect is broken into an object and only linked where necessary.

The programme utilizes a simple executable when starting which has no bearing on the application. The executable has the ability to load in other executable fragments to give it functionality. This is controlled through macro-specific commands, either from the script files or on the command prompt. An example of the command script is printed in Appendix A.1. These commands have the ability to set variables and instruct the programme to construct or destroy objects in a safe manner, at any time, through the life of the executable.

Examples of just two important objects in the code are described here: the element object is fundamental and is an abstract base class which can take the form of any element within the mesh, for example it can be a node, line, triangle or tetrahedron. It can be treated by the rest of the code in an identical manner. All the elements which inherit the element class are polymorphic, but only store local data which is relevant to their type. For instance, the tetrahedron stores its volume, the line stores its forming nodes and a node stores its coordinates. Nodes are also required to store the properties of the flow which ensures that flow field data is available from a unified point throughout the programme's hierarchy.

The mesh class stores all the elements and ensures proper linkage. This is done in a staged manner where the object is instantiated through the class constructor. The first stage reads the mesh file, then subsequent linking is processed through a cached bullion search facility which ensures minimum searching of non-relevant elements and thus optimizes efficiency of the code. The final linkage is structured so that every element is aware of other elements which are used to form it or are formed from it.

For example, a line element knows from which nodes it is derived but is also aware of any triangle edge which it forms. This is achieved via a pointer to the element's abstract base class.

The ultimate requirement of the mesh class is to ensure that boundary element look-ups are performed in an optimum manner. This is achieved by local boundary object caching. Thus, when a search is done on the internal mesh for a type of element on a boundary, a very reliable and fast result is returned. For instance, if one needs to find all the line elements on the boundary of a cylinder, a function call (such as below) would return a pointer to the first element in a list of pointers which identify line elements on that boundary. This saves looping through all the line elements to determine if they lie on the boundary.

```
int error = domain->ElementFind(1, list , size ,*m);
```

where '1' = line elements type tag, 'list' = boundary tag, 'size' = number of elements returned, 'm' is the pointer to the first element in the returned list and 'domain' is the mesh class object.

3.4.4 Parallelization

Parallelization in numerical code is essential, especially as technology is moving towards multiple core processors. Consideration was given to the method of parallelization that should be adopted.

The main choices were:

1. POSIX threads or Pthreads.
2. Win Threads.
3. Intel threaded building blocks.
4. MPI.
5. Open MP.

The decision as to which threading technology to use is largely driven to accord with the numerical libraries adopted and this is primarily decided depending on the

architecture of the computers on which the programmes are to be installed. The two main contenders for the numerical libraries which were considered are MPI and Open MP and they are primarily designed for different types of architecture.

Open MP is designed for shared memory resources, where all the processors use the same memory addressing space. This would be typical on a desktop and on facilities such as an ALTEX supercomputer. Open MP is a compiler directive applied approach which effectively makes it clear to an Open MP compliant compiler what sequences of code can be run concurrently. The user is, therefore, responsible for ensuring that memory deadlocks do not occur between different threads. In this manner, a new thread can be started and released whenever the compiler spots an optimization opportunity to speed up the code.

MPI is a well-established parallelization technology which is designed around clusters of discrete nodes in which a high latency interconnect, such as Mirrornet, or Infiniband, allows updating between processing nodes. There is no reason for MPI not to be run on shared memory resources and specific distributions have been made available for this which reduces interconnect latency using Pthreads.

MPI is substantially different from Open MP in its approach to managing threads. On start-up, the programme distributes an executable to each linked node which runs identical code using local resources. Special MPI functions are made available through the MPI libraries which facilitate synchronization and communication generally over an IP protocol or over local memory buses. Both approaches have been used and tested but the final selection is based on the numerical libraries discussed below.

3.4.5 Numerical Libraries

Existing numerical libraries are used in this work as there is little point rewriting already highly optimized and accepted techniques for matrix and vector operations. Numerical libraries have been developed over decades and generally use the latest mathematics to optimize performance with different platforms. The FEM formulation adopted here requires numerical libraries which can work efficiently and in parallel while performing large matrix/vector operations and solves.

Initial code development was conducted using dense matrices which meant that LAPACK (Linear Algebra PACKage) was used. The LAPACK version used was

Library Differences		
Numerical Library	**PETSc**	**Intel MKL**
Parallelization	MPI	Open MP
Matrix Storage Format	CSD Native to node	CSD
Implementation	Open Source	Compiled DLL's
Sparse Solver	Iterative	Direct Pardiso
Matrix operations	Local to node with Blas	Blas level 3
Lower Level Library	Any Blas and Lapack	Intel Blas and Lapack
Operating system	Windows, Linux and others	Windows and Linux
Support	Open community	Intel
Produced by	Argonne National Labs	Intel
Source Code	Open Source	Closed
Licensed	Copyright by Argonne	Licensed by Intel
Cost	Free	Pounds 400 per node

Table 3.1: Comparison between the PETSc and MKL numerical libraries.

ACML 2.6, distributed by Advanced Microdevices Limited which is a highly optimized library including Blas level 1, 2 and 3. This library is designed to perform optimally on Opteron processors and is tuned to use SSE, SSE2, SSE3 and multithreaded open MP. For initial testing, this library offers a very stable, widely adopted and simple interface with which to verify code behaviour. For more practical solutions above 3,000 nodes, a sparse matrix capable numerical library was employed.

PETSc and Intel MKL libraries were used to allow both MPI and Open MP to be compared. To simplify code adaptation between the two libraries, an interface class model was used which allows the main body of code to be unchanged irrespective of the numerical library adopted. The numerical libraries can therefore be loaded at run-time, making it easy to switch between them. PETSc is a complete numerical package which handles the data structure internally.

MKL is a fast, efficient implementation of Blas and LAPACK and makes available highly-optimized functions such as Pardiso. The two libraries are substantially different. Table 3.1 shows the main differences. The choice of library is a matter of optimization, taking account of run times, memory usage and availability.

3.4.6 High-performance processing on a supercomputer

The aims and objectives of this numerical study have become progressively more ambitious and demanding as new computer resources have come on stream to allow analysis of increasingly complex fluid dynamic problems. The code used here anticipated the additional computational power made available by the new UCL Legion supercomputer. The code, written for this study, was used during the acceptance trials and commissioning of Legion, when several increments of processing capacity were made available as they came on stream.

The numerical work focuses on conducting accurate and detailed numerical studies of a problem made complex by the range of lengthscales involved. The flow around a single simple body can now be numerically simulated to a high degree of accuracy. The challenge here was to maintain this accuracy and to extend its application to multiple bodies. This difficulty was compounded by the fact that solutions are asymmetric and there is an overall lengthscale that is lineally proportional to the number of bodies simulated. As a result, simulations at DNS resolutions need very long processing runs to fully resolve all lengthscales. The computations in this work are characterized by highly coupled memory and processor intensive calculations, which have a large footprint in the system's random access memory.

The rapid development of computer hardware over the last twenty years has made possible resolving these sorts of problems. With new supercomputers planned to break the 10 PFLOPS barrier, within the next few years more and more complex fluids problems will become resolvable.

One of the largest limitations for CFD work is the memory intensive nature of I/O communications between RAM and processors. On a single processor, the memory is directly hard-wired to the processor. In a parallelized form, this type of architecture is classed as Shared Memory Processing (SMP), and relies on virtual address mapping to ensure continuity across the entire platform. This is a very expensive form for a supercomputer but was, at one time, the only computer architecture with adequate I/O bandwidth for conducting CFD work.

The more modern supercomputer approach is to couple very large numbers of processing nodes together, using a high-speed communication network. This was initially very costly, but recent reductions in hardware costs (90% in some cases) have

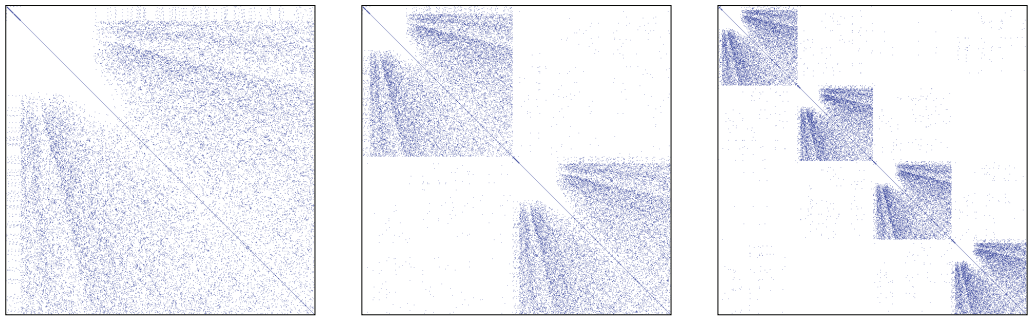

(a) (b) (c)

Figure 3.6: Scatter plot of the non-zero elements in the sparse global mass matrix M after reordering by ParaMETIS, for (a) one, (b) two and (c) four processors. The number of nodes is $N = 1 \times 10^4$.

meant that the number of medium sized supercomputers has significantly increased. The new Legion supercomputer is based on such a cluster architecture.

Legion is formed from 640 1U servers, each housing two dual processor Xeon 3.0MHz processors, with 4GB of memory per core. These are arranged in ten computational units, with bi-directional InfiniPath chip to chip connectivity, with a bandwidth of 1.9 GB/S within computational units. The operating system in each node uses Scientific Linux 4.1 and there is a Lustre Cluster file system which supports 192TB of data, at a bandwidth of 2GB/S.

Legion was the proposed target for this numerical code, which has been specifically designed to make use of its distributed memory processing (DMP) architecture. This was done by efficiently distributing the numerical problem amongst each computational node and minimizing the amount of inter-processor communication to maintain the code in sync. In effect, the flow domain is split into regions as illustrated in Figure 3.7. This was done using ParaMETIS, which uses graph partitioning to efficiently load-balance elements between each processing core, whilst minimizing connected nodes and regions in the domain. This produces a highly-optimized sparse matrix (illustrated in Figure 3.6 for different number of cores), where distinctive regions form for each processor along the diagonal. Values which fall outside these regions are shared and this is where numerical libraries such as PETSc become useful, as they

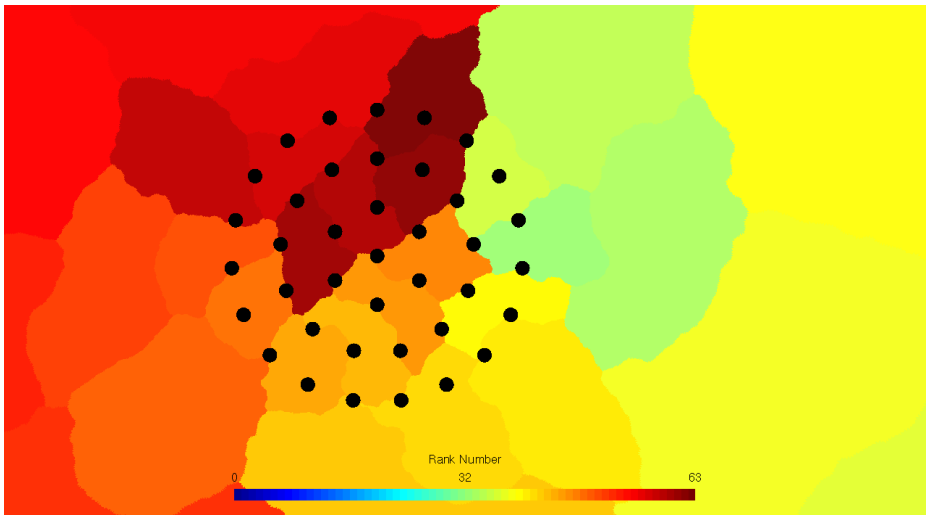

Figure 3.7: Domain decomposition for case C_{39} showing the region near to the array. Each colour represents the region allocated to a different processor core.

maintain concurrency between these values. PETSc was used to maintain and operate vector and matrix operations within the code, with some specific optimizations used to help with mapping values between boundaries. This only forms one aspect of the code and much development focuses upon efficient matrix filling element ordering routines. In general, the parallelization of the code is handled within class objects. This produces a clean interface, within which there is no sign of parallelization and results in a non-centralized code implementation, where there is no head node and all nodes perform the same function calls and operations. This is a very important feature of parallelization and illustrated by the simple fact that, at no point within the programme, does any processing node need (or even know without calculating) the total number of nodes within the whole domain.

Legion is not a single operating environment, but relies on management programmes (Moab and Torque), which control and synchronize independent processing nodes. To best utilize Legion's resources, jobs are scheduled to start running when processing nodes become free. To improve performance, each processing job in this work is restricted to an individual processing unit and does not share nodes with other jobs. If jobs shared nodes, this would be a problem as MPI codes generally run at the speed of the slowest processing thread. Legion's workload manager Moab

schedules jobs according to their duration and resource requirement, which is set with the use of flags in the job submission script file. Each investigated case requires a dedicated submission file, which will automatically start and restart the job over the 20+ day run period. As with all newly-commissioned and complex systems, failure of any system component tends to kill the job, so it was important to have an automatic backup procedure to minimize lost processing time. This was set at six hours and was initially frequently used, as there were several node failures during the acceptance period.

Legion is a shared resource and, as such, limits were imposed on the available processing resources at any time. This project was finally allowed a very generous 256 processors in any 48 hour period. To make the most efficient use of these resources/periods, 32 processors were deployed per investigated problem, which allowed the optimum concurrent job processing. The problem size is generally described in terms of the number of nodes, and, typically, in these cases this was approximately 4 million. This equated to approximately 125,000 nodes per core, requiring approximately 0.5GB of memory per core. If more processors were used, the number of nodes per core was reduced, but this led to a diminishing return due to the increased overheads of communication.

The entire calculations, for all eight cases in the numerical study of this report, consumed a total of over $200,000$ processor hours. This is possibly equivalent to twenty-three years of processing on a single computer, assuming linear parallelized scaling and not accounting for the huge disadvantage of a single I/O bus when processing on an individual chip. The longest continuous spell of processing was done to calculate the velocity average field. This required continuous processing for 144 hours on each case, which was important to maintain accurate numerical values, without round off errors and sequential numerical iterations and was made possible by a special dispensation from CRAG (Computer Resource Allocation Group).

3.4.7 Post-processing

The post-processing requirement is determined by the resolution and the quantity of data needed to isolate interesting behaviour or parameters. Many large-scale CFD calculations have the ability to generate colossal amounts of information, as data can

be made available at any point in space or time. To reinforce this point, if one were to store velocity field data in compressed binary form for every time step in the lid-driven cavity flow problem for a moderate $Re = 1000$, one would need 27.5 GB of space. In reality, this quantity of data is not required and a more selective approach is adopted.

In terms of multibody flows, this study was mainly interested in data collected during one stable flow cycle. The resolution of this data was determined by the rate of change of any quantity being measured within the flow field. In this numerical study, force calculation on multiple bodies and flux through and across defined regions was investigated.

It was decided to use a combination of the different methods which allowed all the essential requirements to be satisfied as follows:

1. Raw data output. This facility allows flow field and mesh data to be dumped to a file at any instant in time and reloaded if required again.

2. Gmsh post-processing. This file is necessary for Gmsh to load and evaluate the flow field. It is limited in that different flow fields cannot be calculated from a single unified flow field. Therefore, for full flexibility, file sizes become bloated by duplicated data.

3. VTK data file stores one instant of the flow field and when loaded into ParaView (a parallel visualization tool) can be interpolated into any flow field. As a result, it is often five times smaller than Gmsh post-processing files.

4. The flow field data log file is a basic binary store of the flow field, used for many time instances. It does not contain positional data, so it is used in conjunction with the mesh file.

5. Parameter data, such as force measurements and field flux on a boundary, are cached locally to memory then flushed to disc when instructed. These variables do not take up much space but are often required at frequent intervals during a single cycle.

Depending on the output format, post-processing is either conducted in Gmsh, ParaView or Matlab. For long, difficult processes, simple executable C# code was found to give superior performance.

3.5 Validation of the numerical code

A critical aspect of code development is its validation against known solutions from other computational codes and published results. There are a number of well-established test cases for two-dimensional Navier-Stokes solvers to test steady state and transient solutions. To ensure fair comparison, the same geometry and boundary conditions were used in all the test cases. Cases I, II and III are shown in Figure 3.8 and correspond to a lid-driven cavity flow, an asymmetrically placed cylinder and a symmetrically placed cylinder. Case I was used to examine convergence to a steady state and validated against Fluent, FEMLAB, OpenFoam and the results of Ghia Ghia et al. [1982], while II and III were used to test the unsteady numerical calculations. Case II was validated against the published bench-mark produced by Schäfer and Turek [1997]. Case III is commonly used and was compared against results from Nithiarasu and Zienkiewicz [2005], de Sampaio et al. [1993], Codina et al. [2004], Ramon [2002], Malan et al. [2002], Nithiarasu [2003]. In particular, this case allows comparison against data from other CBS schemes.

The second element was to test mesh convergence, where progressively more finely resolved meshes are used to show 'mesh' insensivity. The test for mesh insensitivity is quite challenging, since the computational effort quadruples as the mesh size is halved – this is partly due to the time step constraint for the CBS scheme which is set by the smallest element ($\Delta t < L_m/u$), but is mainly set by the number of unknowns, since for a mesh of minimum size L_m, the number of nodes is $N \sim L^2/L_m^2$.

3.5.1 Validation case I: Lid-driven cavity flow

This is a validation for two-dimensional codes in which a square box (of side length L) of incompressible fluid with no-slip walls is driven by a moving lid with horizontal velocity $u_1 = U$ as shown in Figure 3.8a. The pressure needs to be defined at a point to ensure that a solution to step two in the CBS scheme is available. In this case the

pressure is set to be zero at the bottom left hand corner. Care is required to ensure that points on common boundaries are subject to one boundary condition, and, in this case, the nodes at the top left and right corners of the box are prescribed with $u_1 = u_2 = 0$, to ensure there is no flux through the side wall.

The numerical algorithm used (described in §3.3) is a three-step incompressible CBS semi-implicit scheme, solved with a global time step. The flow was calculated for $Re = UL/\nu$=1, 400, 1000 and 5000. The convergence criterion typically used is defined by

$$E = \frac{\sum_{i=1}^{n} \sqrt{\left(|\boldsymbol{u}_{n+1}| - |\boldsymbol{u}_n|\right)^2}}{\sum_{i=1}^{n} \sqrt{\left(|\boldsymbol{u}_{n+1}|\right)^2}}. \tag{3.53}$$

The problem with (3.53) is that it does not take into account the rate of change of the flow field determined by $\partial \boldsymbol{u}/\partial t$. Therefore, an improved measure is

$$E_2 = \frac{\sum_{i=1}^{n} \sqrt{\left(|\boldsymbol{u}_{n+1}| - |\boldsymbol{u}_n|\right)^2}}{\Delta t \sum_{i=1}^{n} \sqrt{\left(|\boldsymbol{u}_{n+1}|\right)^2}}. \tag{3.54}$$

The calculations were assumed to converge when $E_2 < 10^{-6}$. The speed at which this occurs is limited by the size Δt as discussed in §3.3.2. Figure 3.10 shows the progression of stability against iterations (time steps) for $Re = 1$. It is clear that convergence is initially rapid but that this slows towards the steady state solution.

A mesh independence study was carried out for each Re using three different meshes with increasing node numbers, from 1,713 (Figure 3.9a), 6,830 (Figure 3.9b) and 41,600 nodes. As Re increases, the boundary layer on the slipping wall decreases in thickness. The boundary layer thickness is approximately $LRe^{-1/2}$ (Batchelor [1967]), and since we typically require at least 4 nodes across the boundary layer, we estimate that $L^2/(0.25LRe^{-1/2})^2 \sim 16Re$ nodes to *fully* resolve the flow everywhere and for the result to be mesh-size independent. Whilst the accuracy was improved with the 41,600 node mesh, a reasonable result was also achieved with the 6,830

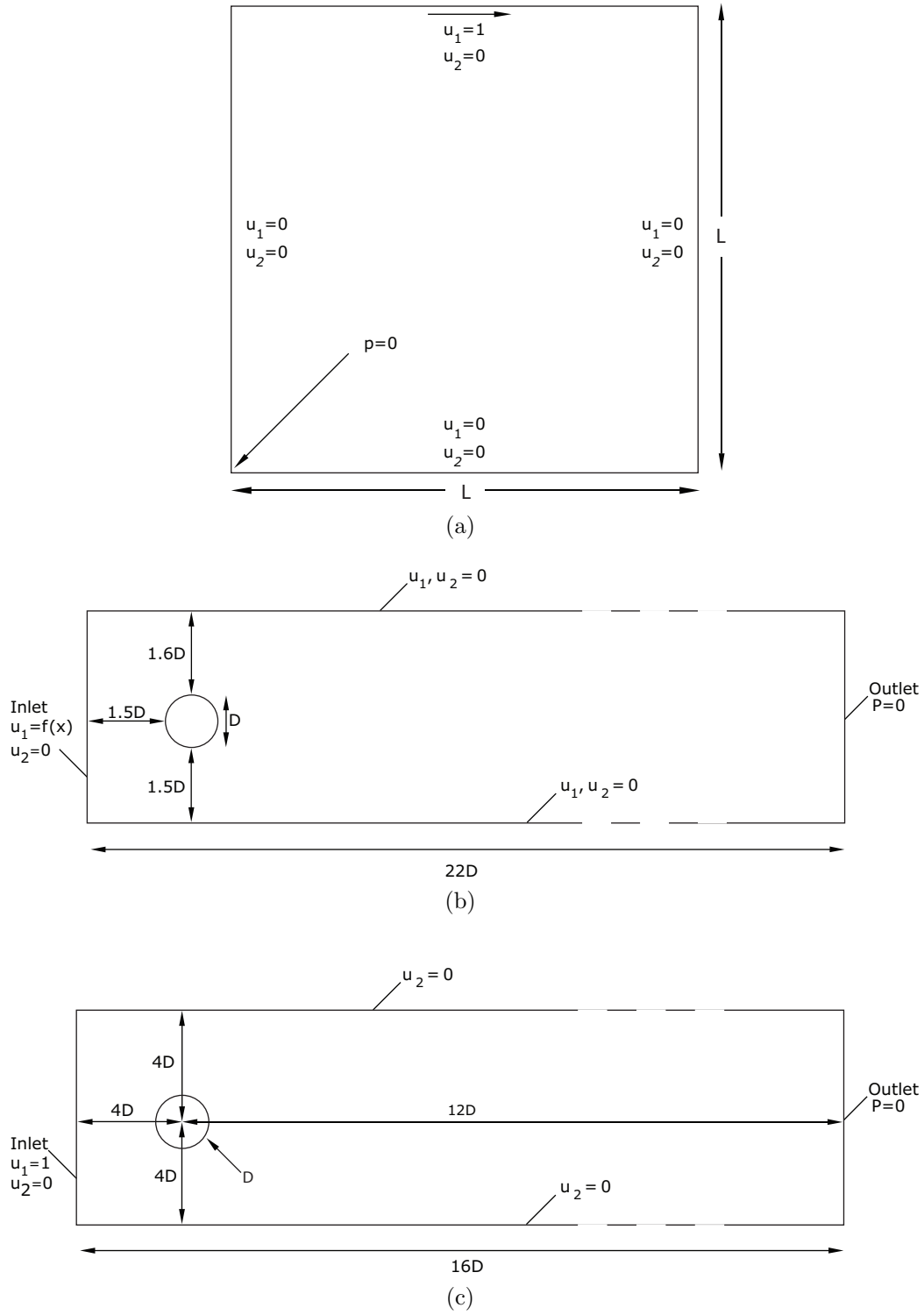

Figure 3.8: Schematic of the test cases used to validate the numerical code. Geometry and boundary conditions are shown for (a) lid-driven cavity flow, (b) asymmetrically placed cylinder and (c) symmetrically placed cylinder.

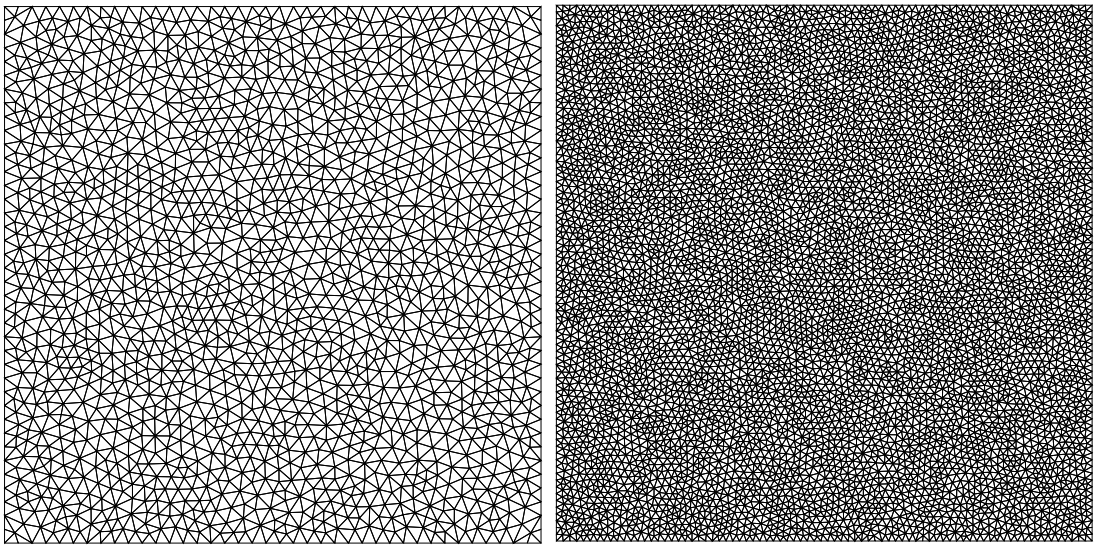

(a) (b)

Figure 3.9: The low and medium resolution meshes used in the lid-driven test cases (Test I). In (a) the number of nodes $N = 1713$, while in (b) $N = 6830$.

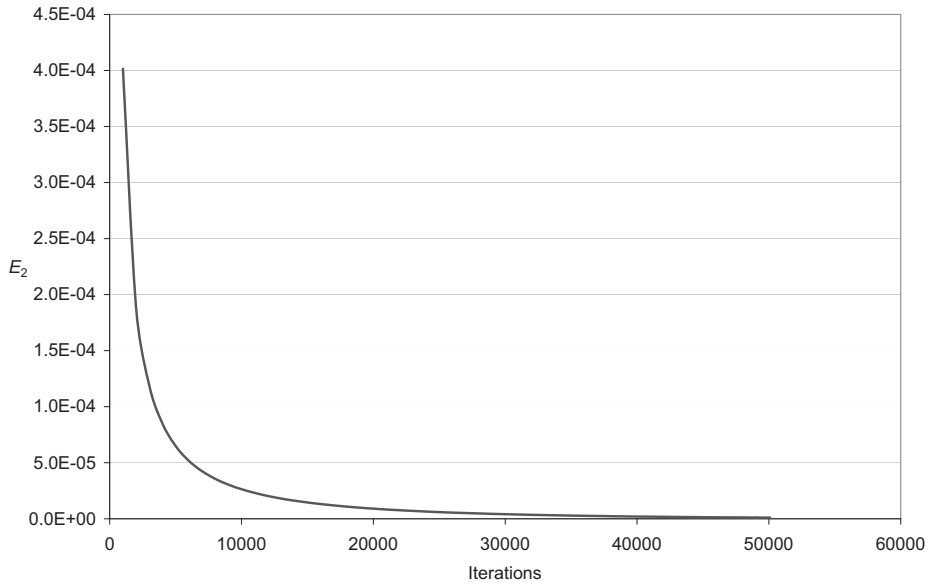

Figure 3.10: Variations of the measure E_2 (3.54) with the number of iterations for $Re = 1$. As the number of iterations increases the solution converges.

node mesh. Based on these estimates, for the highest Reynolds number considered ($Re = 5000$), the medium mesh, while converging, did not capture small detail such as the tertiary eddy in the bottom right corner. It should be noted that the cavity problem has only recently been studied up a maximum of $Re = 4 \times 10^4$ (Erturk et al. [2005]).

Figures 3.11a and 3.11b show the pressure and streamlines for $Re = 1$ and indicate an asymmetrically displaced central vortex near the moving wall boundary. At higher Re, Figures 3.11c and 3.11f show that the center of the main vortex moves into the centre of the domain and secondary vortices grow in size and strength. For $Re = 5000$, pressure and velocity fields also show that a second eddy has formed in the bottom right hand corner – this can only be captured with a higher resolution mesh.

The results were compared against output from commercially available codes (Fluent, Femlab, OpenFoam). For a fair comparison, the mesh density in both the commercial code and the current implementation was chosen to be as close as possible. Ghia et al. [1982] did not publish data for $Re = 1$, which explains why that data set is omitted.

Figure 3.12 shows vertical profiles of the horizontal velocity along the centre line of the cavitational domain for $Re = 1$, 100, 1000 and 5000, which are considered converged to a steady solution. These numerical results show close agreement with results from the other commercial codes and published data. There is a slight variation in the vertical profiles near to the boundary layers, which is believed to be explained by the type of computational scheme used and the different distributions of elements near the walls.

These comparisons provide support for the steady solution and the adequacy of mesh convergence. The presented data is slightly different at higher Re compared to Ghia et al. [1982]. This is not surprising, as higher mesh resolutions were employed than were available to Ghia et al. [1982].

3.5.2 Validating unsteady calculations

As already explained, two test cases were employed to validate the transient flow past a cylinder. One component of the transient analysis is the comparison of the numerical calculation of the unsteady force on the cylinder with other studies. The

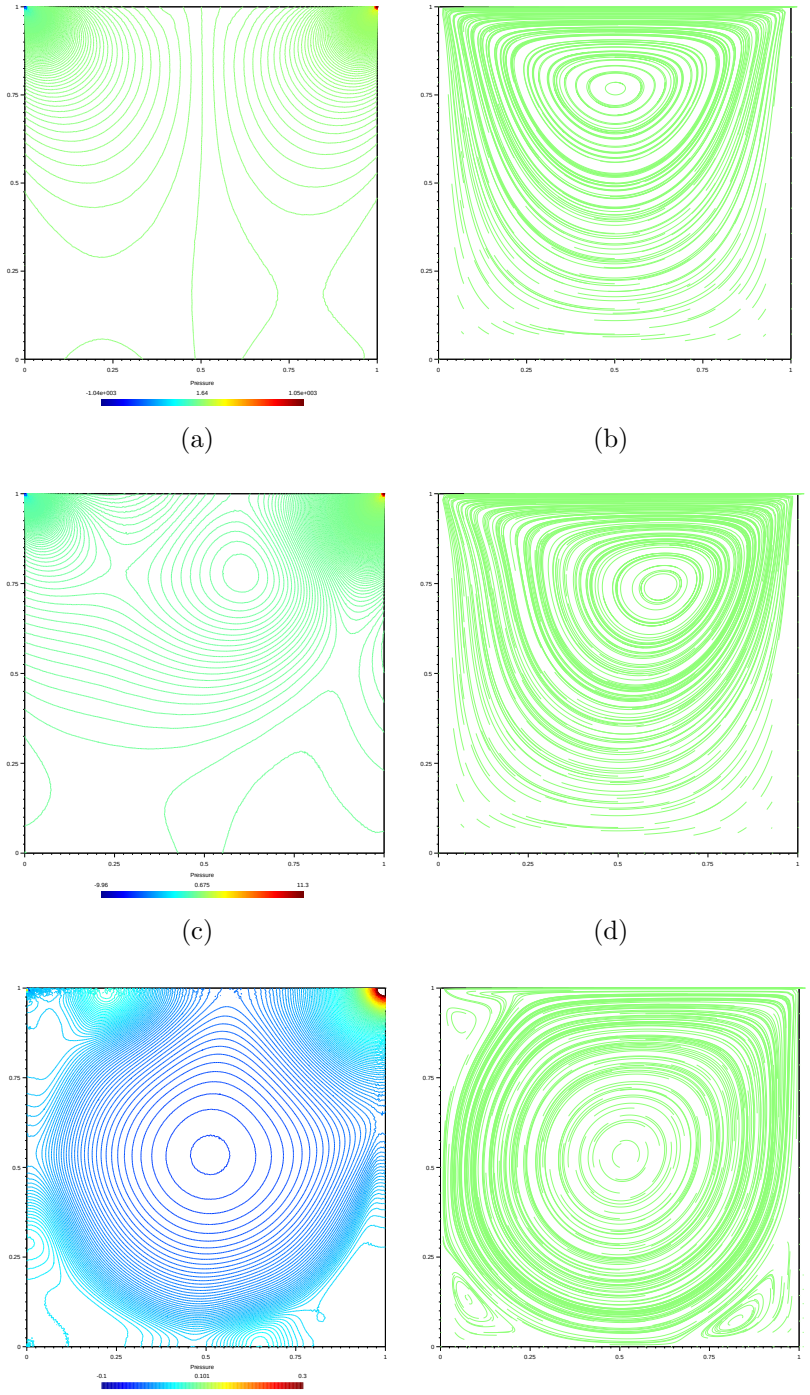

Figure 3.11: Pressure field for the lid driven cavity problem for (a) $Re = 1$, (c) $Re = 100$, and (e) $Re = 5000$ and the corresponding streamlines (b) $Re = 1$, (d) $Re = 100$ and (f) $Re = 5000$.

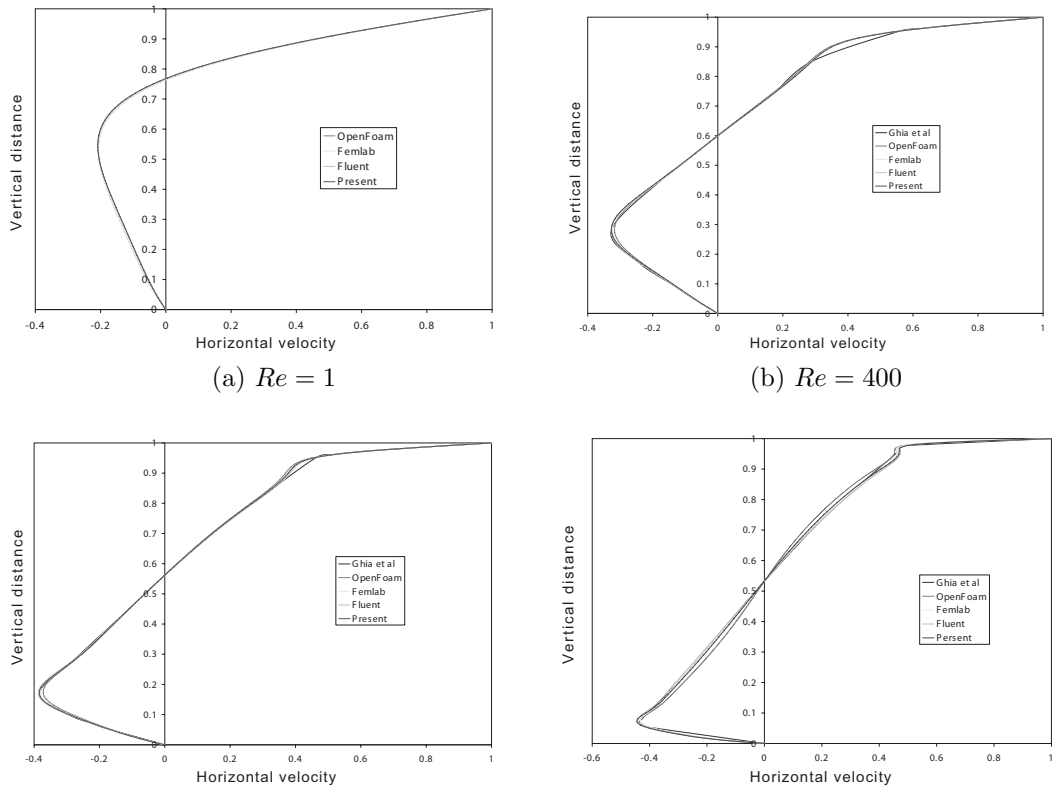

(a) $Re = 1$ (b) $Re = 400$

(c) $Re = 1000$ (d) $Re = 5000$

Figure 3.12: Horizontal profile of u_1 across the middle of the cavity for different Re. (Dr Mark Landeryou generated the OpenFoam data.)

cylinder experiences drag and lift forces. There are two components of the induced lift and drag forces resulting from the pressure and viscous contributions, which are defined by (2.18) and (2.17) respectively.

The pressure contribution is calculated using the pressure values at the nodes on the cylinder's boundary. Therefore, the sum contributions from all the line elements forming the cylinder boundary were used. Each line element is formed by 2 nodes. The pressure at these two nodes is averaged and multiplied by the distance between them. To resolve the direction of this force, the angle of the line element to the force being calculated is factored in. The viscous component is calculated for each triangular element with a face on the cylinder boundary. The shear stress contribution across the element is calculated on the face forming part of the boundary and summed with

the contribution of all elements on the cylinder. As this study focuses on multi-body flow and relies on calculating a large number of drag forces at regular time intervals, cached pointer lists of relative elements are stored to save look-up time.

Drag coefficients, lift coefficients and Strouhal number (St) are defined in Chapter 2 by (2.7), (2.10) and (2.12) respectively. The Strouhal number is inversely proportional to the time between the fluctuating lift coefficient peaks. This is continuously calculated and averaged when calculating lift forces on a body in the code. To ensure the Strouhal number has stabilized, the averaging process only begins when the lift coefficient has settled to a steady peak value. Cylinder wall pressure is normally represented as the variation of pressure coefficient $C_p = (p - p_{ref})/\frac{1}{2}\rho U^2$, with angular displacement around the cylinder, where p_{ref} is the reference pressure at the inlet face.

For steady state problems, it is also possible to compare the pressure difference between the front and rear stagnation points on the cylinder as is done in Case II.

3.5.3 Case II: Transient flow past an asymmetrically placed cylinder

The standard test case adopted by Schäfer and Turek [1997] is shown in Figure 3.8b. The important point is that the cylinder is asymmetrically positioned within the channel, to trip the flow into becoming unsteady earlier in the calculations.

No-slip boundary conditions are applied to the cylinder and walls on either side of the channel with a pressure outlet at the far end of the channel. The inlet flow condition is prescribed to be

$$u_1(0, x_2) = 4U_{max}\frac{(H - x_2)x_2}{H^2}, \qquad u_2(0, x_2) = 0, \tag{3.55}$$

where H is the channel width, x_2 is the distance from the bottom left corner on the inlet face and U_{max} is the maximum inlet velocity. For this problem, the Reynolds number is defined by $Re = 2HU_{mean}/\nu$. In turn, $U_{mean} = 2U_{max}/3$.

To check the sensitivity of mesh size, three meshes were used (see Figure 3.13). The smallest mesh had ($N = 3822$), medium ($N = 11204$) and fine ($N = 17459$). All these meshes used local refinement around the cylinder surface to help resolve the

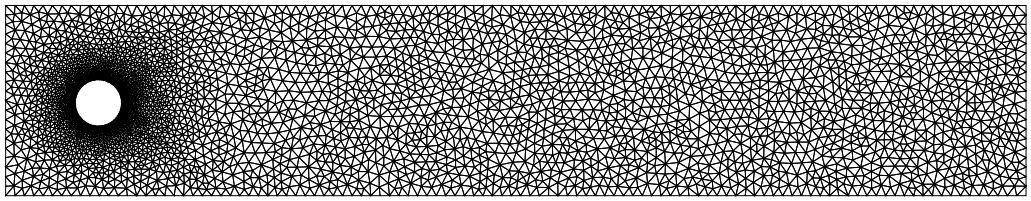

(a)

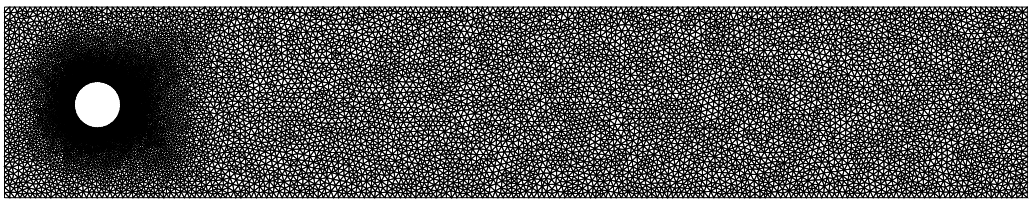

(b)

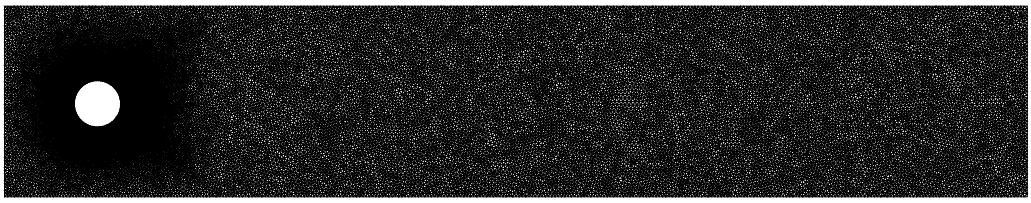

(c)

Figure 3.13: The meshes used for Case II are shown for different resolutions: (a) coarse mesh (3,822 nodes), (b) medium mesh (11,204 nodes) and (c) fine mesh (17,459 nodes).

boundary layer.

Two tests were conducted for this geometry. For $Re = 20$, the flow is steady. Figures 3.14a, 3.14b and 3.14c show the pressure contours and velocity fields for both u_1 and u_2 respectively. From the velocity field, it is possible to observe two opposite rotating eddies trailing the cylinder. These are formed once inertia forces became large enough (e.g. $Re > 0.5$) and result in the boundary layer on the cylinder surface detaching. As the problem is steady, these eddies remain behind the cylinder and form part of the wake which trails the cylinder. While it is difficult to see this in the velocity and pressure Figures, these trailing eddies are asymmetic due to the cylinder's non central alignment. This effect is seen more clearly in Figure 3.14e, where the variation of the lift coefficient against time is plotted but, for a

symmetrically positioned cylinder, the average lift coefficient would be expected to be zero. For an asymmetrically displaced cylinder, C_L is found to be static but either positive or negative.

Figure 3.14d shows the variation of the drag coefficient with time which can be seen to stabilize after two seconds at a value of $C_{D_{max}} = 5.5298$. Also plotted are the viscous and pressure components for total drag. It can be seen that the viscous and pressure forces are of similar magnitude, as is typical for low Re flow past a cylinder. The pressure difference, calculated at steady state between the start and end points of the cylinder, was 0.1176054. All these values compare well with the published data for the same problem which is tabulated in Table 3.2 (more information is provided in Appendix A.2).

Above $Re \sim 46$, these eddies detach sequentially and are then washed downstream. For Case II, when $Re = 100$, a fully formed unsteady wake is present behind the cylinder which can be clearly seen in Figures 3.14a, 3.14b and 3.14c. In Figure 3.14e, which shows the coefficient of lift, a gradually increasing sinusoidal lift coefficient is plotted which reaches a maximum frequency amplitude after approximately $Ut/L = 4.0$. In this Figure, it is clear that most of the induced lift force is due to the pressure component and not viscous stresses, which, at this higher Re, become less important. Again, as the cylinder is asymmetrically placed, the lift coefficient oscillations are slightly offset from zero. The drag coefficient is plotted in Figure 3.14d and shows a slight oscillation which is small compared to its average value. The pressure contribution to drag is approximately ten times that of the viscous term.

For comparison purposes, the presented data uses maximum values for both drag and lift coefficients and these are tabulated in Table 3.2, with the upper and lower boundaries from the average accumulated data which is attached as Appendix A.3. Also tabulated is the changing pressure between reference/stagnation points and the St number, calculated using the time incidence between maximum lift values. While all the data compares well, it does tend to be on the lower side of the lower average boundary. This is due to the mesh being under-resolved.

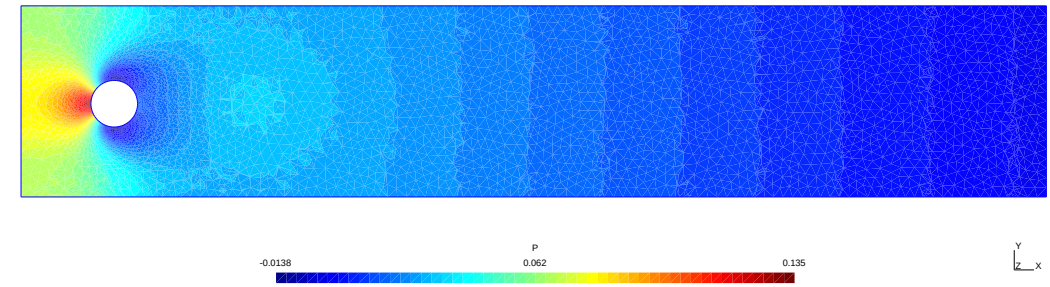

(a)

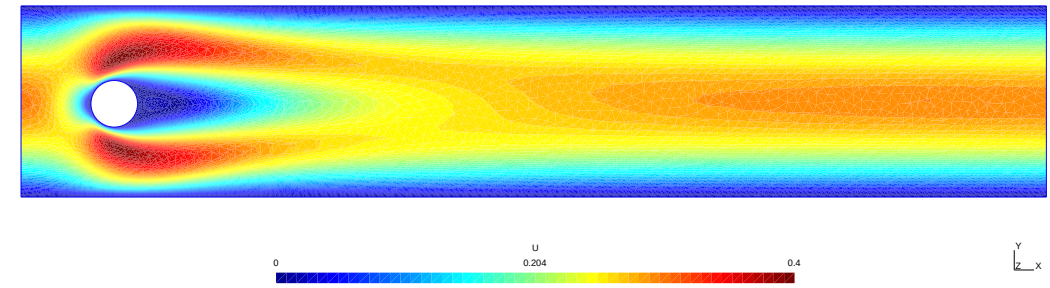

(b)

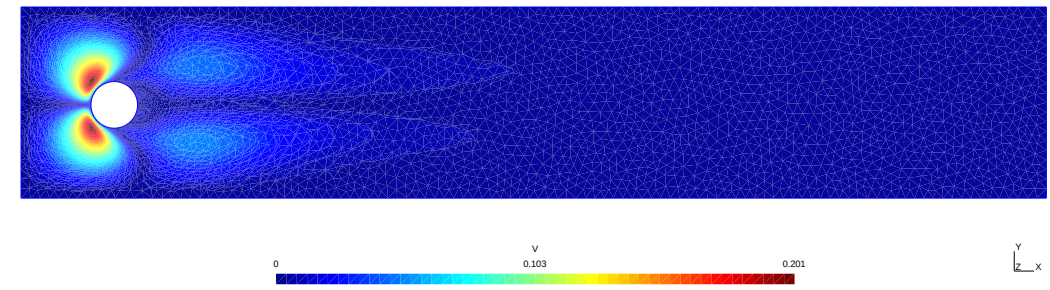

(c)

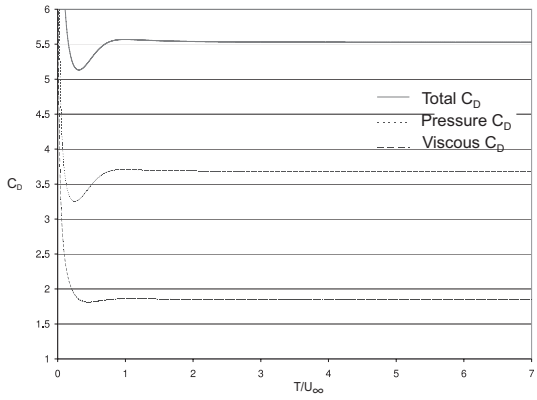

(d)

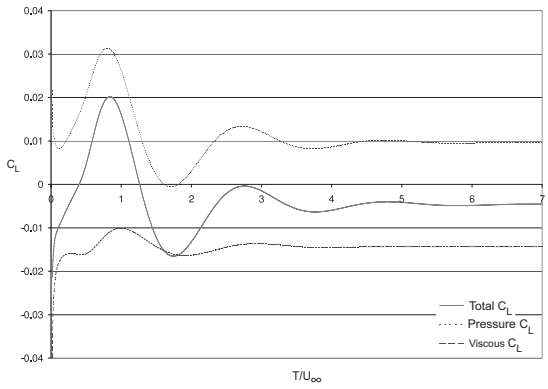

(e)

Figure 3.14: Numerical results for test Case II for $Re = 20$ (a) pressure contour, (b) u_1 contour, (c) u_2 contour, (d) $C_D(t)$ and (e) $C_L(t)$.

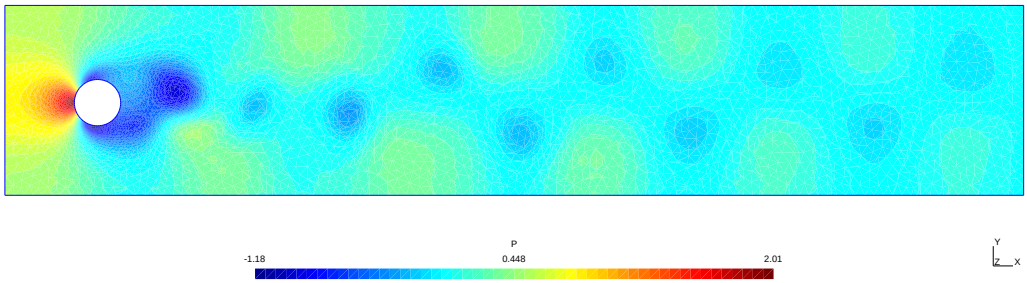

(a)

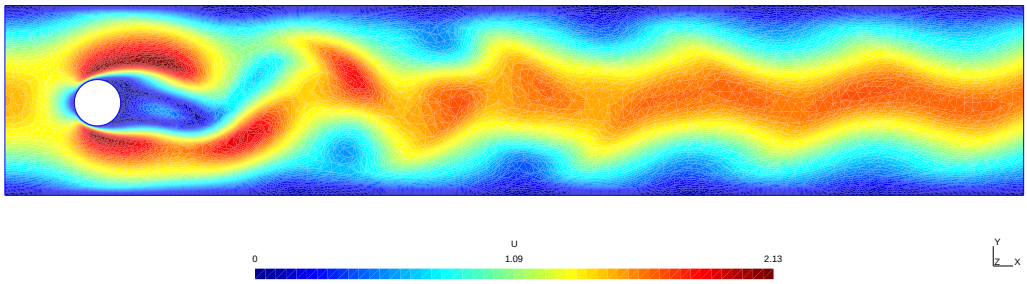

(b)

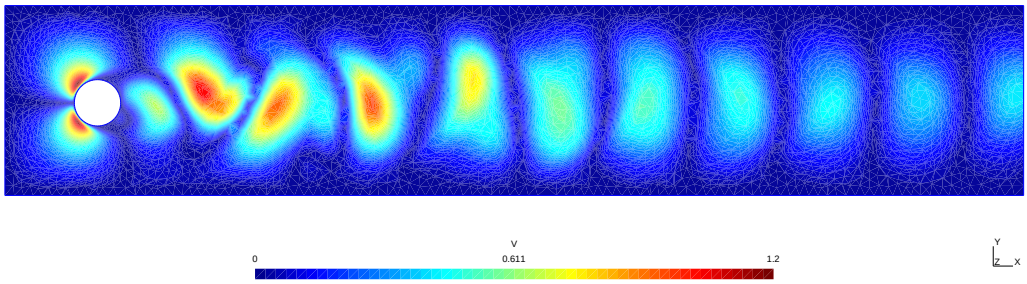

(c)

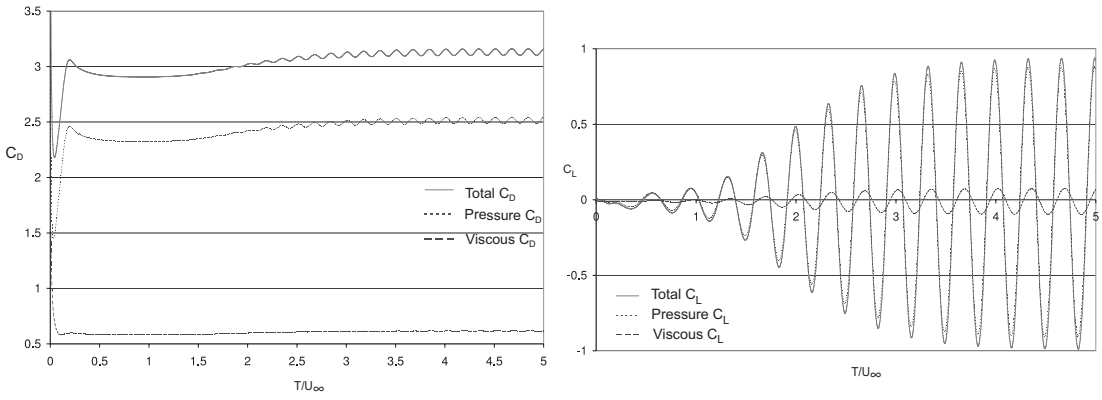

(d) (e)

Figure 3.15: Numerical results for test Case III for $Re = 100$: (a) pressure contour, (b) u_1 contour, (c) u_2 contour, (d) $C_D(t)$ and (e) $C_L(t)$.

FeatFlow Data from Schäfer and Turek [1997]				
State		Average published result		Present calculation
		lower bound	upper bound	
Steady $Re = 20$	$C_{D_{max}}$	5.57	5.59	5.5298
	$C_{L_{max}}$	0.0104	0.0110	0.0063
	ΔP	0.1172	0.1176	0.1176
Unsteady $Re = 100$	$C_{D_{max}}$	3.2200	3.2400	3.1613
	$C_{L_{max}}$	0.9900	1.0100	0.9413
	ΔP	0.2460	0.2500	2.4125
	St	0.2950	0.3050	0.2951

Table 3.2: Comparison between FleatFlow data and the present numerical calculations.

3.5.4 Case III: Transient flow past a circular cylinder symmetrically placed

The transient flow past a circular cylinder is a common test case for code validation. The circular cylinder has diameter D and is placed between two no-slip walls, so that the centre of the cylinder is $4D$ from each wall. An inlet face joins two of the side walls at one end. The cylinder is again $4D$ from this. The outlet face is $16D$ from the inlet face and joins the side walls at the other end. The outlet face boundary condition is set as a pressure outlet $p = 0$ and the inlet face with $u_1 = 1$, $u_2 = 0$. The symmetry walls have the additional force term applied and so no flux travels through them $u_2 = 0$ and they allow slip. Figure 3.8c shows this arrangement. This problem was tested for $Re = 100$ and data for coefficients of lift and drag history against time collected.

There follows an investigation into the previously described geometry which is broken into two parts. Firstly, there is a comparison with published data. Secondly, mesh sensitivity and how parameters are influenced by the mesh resolution are investigated.

Validation against test Case III was used by Codina et al. [2004], Nithiarasu and Zienkiewicz [2005], Ramon [2002], de Sampaio et al. [1993] and Malan et al. [2002], for testing the stability of FEM techniques with particular emphasis on the unsteady

transient flow behaviour. Care must be taken when making comparisons with data from these studies to ensure that a similar mesh is used, as it is believed that the mesh that is commonly employed under-resolves certain parameters by 6%, as described in §3.5.5. Therefore, for the purposes of evaluating the code developed in this research, mesh '2' with 10007 nodes is used (described in Table 3.3). This mesh is believed to exhibit similar properties to that used in the previous publications, most of which do not adequately describe their meshes but seem to reference back to Codina et al. [2004], who, in turn, used a mesh consisting of 19650 elements and 9988 nodes.

As detailed in §3.5.5, describing a mesh in terms of elements and nodes does not really identify its true properties due to possible mesh refinement. However, from the dual step value of 0.1666 quoted, which is identified to be a factor of 50 greater than the critical time step, it can be deduced that their critical $\Delta t = 0.0033$. In this comparison, a mesh with 10007 nodes has been parameterized to achieve a $\Delta t = 0.00459$, which is in the same order, and the mesh consists proportionally of the same number of nodes and elements.

For this mesh, it is found that $St = 0.1833$, $C_{D_{\max}} = 1.520$ and $C_{L_{\max}} = 0.3619$. This data is plotted in Figures 3.17c and 3.17d for lift and drag respectively. Also shown is the pressure field Figures 3.16a, u_1 in Figure 3.15b, u_2 in Figure 3.15c, vorticity field Figure 3.17b and the flow field streamlines in Figure 3.17a. These compare well with Codina et al. [2004] which found an average $C_{D_{\max}} = 1.521$. Separately, Nithiarasu and Zienkiewicz [2005] calculates $St = 0.179$ and a value on $C_{L_{\max}} = 0.36$.

Ramon [2002] found a period of oscillation of 5.7 time units with the OSS formulation and 5.76 time units with ASGS method. de Sampaio et al. [1993], measured the period of oscillation using the velocity at the center of the outlet and found the $St = 6.0$. They employed an initial course mesh which was then adaptively refined. Later work in Malan et al. [2002] achieved the same result. From these results, it is clear that small variations do occur due to the method employed, but, as later concluded, a good comparison is still found when using a similar mesh and time step.

3.5.5 Case III : Mesh independence study

A mesh independence study was conducted to determine whether mesh parameters influenced measured results. Often, with published data, the mesh is quantified in

terms of simple descriptors such as element and node numbers. This study reviews in more detail how different areas of refinement in the mesh can influence the cylinder's behaviour and also whether a single node count is valid.

Eleven different meshes were tested and their characteristics shown in Table 3.3. Two parameters were varied to generate the meshes. The first is the cylinder characteristic lengthscale ($CLS = \frac{\pi D}{N_C}$ where N_C = number nodes on the cylinder boundary) which determines the local resolution around the cylinder. The second variable was the domain characteristic lengthscale ($DLS = \frac{BL}{NB}$ where NB = number nodes on the domain boundary and BL = domain length) which determines the resolution of the downstream and upstream portions of the mesh. Both CLS and DLS were compared independently, although some meshes were used in both comparisons. Two studies for $CLS = 0.01$ and 0.02 were carried out where $DLS = 0.08$, 0.06, 0.04 and 0.02. The second comparison was done varying CLS for values 0.05, 0.025, 0.02, 0.01 and 0.005 while keeping $DLS \approx 0.07$.

The results found for CLS variation on each mesh are shown in Table 3.5. These calculations analyzed the average drag coefficient $\langle C_D \rangle$ and the maximum lift coefficient $C_{L_{\max}}$. St is neglected for reasons which are discussed later. Both $C_{L_{\max}}$ and $\langle C_D \rangle$ show a uniform growth as CLS is reduced. By forecasting what the values would be when CLS approaches zero (effectively an infinitely fine mesh), it is possible to determine the ideal converged solution. These ideal values are tabulated in Table 3.5. From the ideal values, it was possible to calculate percentage error induced by each of the meshes in Table 3.5 and this is tabulated in Table 3.6. This gives a much clearer method of comparison between meshes and it can be seen that the percentage error is reduced to a minimum error of $\langle C_D \rangle = 0.48\%$ and of $C_{L_{\max}} = 0.41\%$ when $CLS = 0.005$. It is worth noting that, in all cases, reducing CLS substantially reduces the error in the viscous stress contribution to both lift and drag forces.

Results from the investigation into DLS are presented in Table 3.4, for CLS fixed at 0.02. It can be seen that both $\langle C_D \rangle$ and $C_{L_{\max}}$ do not substantially change, even though the number of nodes in the domain is increased by a factor of ten. The slight variations in the results are believed to be due to unintentional change of CLS arising from the variation in DLS and the smoothing effect of the transition from the domain to the fine mesh surrounding the cylinder. This conclusion is supported by

Mesh	Nodes	Element	CLS	DLS
1	27872	55314	0.05	0.05
2	10007	19736	0.025	0.09
3	13232	26132	0.02	0.08
4	22511	44596	0.02	0.06
5	46175	91786	0.02	0.04
6	142199	283668	0.02	0.02
7	16772	33056	0.01	0.08
8	27565	54548	0.01	0.06
9	54336	107952	0.01	0.04
10	163239	325584	0.01	0.02
11	22865	44926	0.005	0.08

Table 3.3: Characteristics of the eleven meshes used in the mesh independence study.

Varying DLS with $CLS = 0.02$					
Mesh	DLS	$\langle C_D \rangle$	$C_{L_{\max}}$	St	Δt
3	0.08	1.5330	0.3679	0.18394	0.0024
4	0.06	1.5339	0.3691	0.18438	0.0023
5	0.04	1.5341	0.3686	0.18548	0.0024
6	0.02	1.5364	0.3696	0.18954	0.0017

Table 3.4: Mesh sensitivity results: varying DLS.

the tabulated minor changes in Δt.

The second element analysed was the influence of element size on the truncation numerical errors. The truncation error due to using basis functions of order p is $O(h^p)$ where h is a measure of element size. In this problem, linear triangular basis functions were applied, giving an error proportional to h. This is confirmed in Table 3.6, where as the mesh becomes finer, the ratio of the error in $\langle C_D \rangle$ to CLS tends to a constant value of 1.5.

It can be seen that most parameters are stable, however St does increase with the domain resolution which shows the necessity of resolving the downstream wake. This was also the case when varying DLS with a different $CLS = 0.01$. This explains the rationale for not presenting St in tables 3.5 and 3.6.

Varying CLS							
Mesh	CLS	$\langle C_D \rangle$	$C_{L_{\max}}$	$\langle C_{DP} \rangle$	$C_{LP_{\max}}$	$\langle C_{DV} \rangle$	$C_{LV_{\max}}$
1	0.05	1.4717	0.3088	1.1383	0.2821	0.3331	0.0319
2	0.025	1.5204	0.3596	1.1641	0.3262	0.3565	0.0392
4	0.02	1.5339	0.3691	1.1722	0.3330	0.3617	0.0422
8	0.01	1.5480	0.3765	1.1754	0.3372	0.3726	0.0454
11	0.005	1.5538	0.3797	1.1745	0.3383	0.3793	0.0472
∞	0.00	1.5613	0.3812	1.1759	0.3383	0.3853	0.0494

Table 3.5: Mesh sensitivity results: the effect of varying CLS.

Percentage error when varying CLS							
Mesh	CLS	$\langle C_D \rangle$	$C_{L_{\max}}$	$\langle C_{DP} \rangle$	$C_{LP_{\max}}$	$\langle C_{DV} \rangle$	$C_{LV_{\max}}$
1	0.05	5.74	18.99	3.19	16.62	13.56	35.53
2	0.025	2.62	5.66	1.01	3.57	7.47	20.69
4	0.02	1.75	3.17	0.31	1.56	6.13	14.58
8	0.01	0.85	1.23	0.04	0.34	3.29	8.17
11	0.005	0.48	0.41	0.12	0.01	1.56	4.39

Table 3.6: Mesh sensitivity results: the percentage error caused by varying CLS.

3.6 Three-dimensional cavity flow

To illustrate the full potential of the object oriented approach used in the code, the code was applied to a three-dimensional example. This example is included to demonstrate the code's flexibility and was done with useful input from Christian Klettner, who implemented the tetrahedron class and rewrote the FEM formulation to convert the two-dimensional formulation into three dimensions. Figure 3.19 shows the velocity vectors of the three-dimensional cavity case which was run with this code, using a 146,220 node mesh. The results were compared with other publications and found to be in good agreement.

3.7 Roll out onto a supercomputer

During the final stage of this thesis, UCL acquired a new supercomputer, Legion. This provided potential for a more instructive test of the code and the resources to run at a resolution two or three orders of magnitude greater than the test cases described. It was during this period that Legion was going through acceptance trials which limited runs to 24 hours. Most initial testing, apart from speed evaluation, was conducted using meshes with less than $200k$ nodes. For larger simulations, such as the eight high-resolution cases in this investigation, a systematic approach to running the numerics was essential with running times extending to twenty days for each case. The full solution to each case can not be run in one processing session and require re-submission to the Legion job queue every 24 hours. To cater for this, in the investigated cases the code uses a script file which is automatically generated with the geometry for each case. The automatic generation of this script file reduces the chance of error when using thousands of tagged boundaries.

The script file also allows easy refinement and adjustment of the programme without requiring re-compiling. Different diagnostics are triggered when certain critical values are achieved. An example of the script file used to set up C_{20} is shown in Appendix A.14. This file can additionally load other script files which give instructions for solving, running diagnostics and determining the output format. An example of a typical script file for conducting the solve and monitoring the force routine is included in Appendix A.15.

To control the solve progress, loop objects are nested within one another, which allow routines to be run at different times or intervals. The loops can be set to monitor any global variable by use of a limit name flag specified by the user. In the example shown in Appendix A.15, the routine ensures that the code stops in under 24 hours by the use of the system global variable called $system\_current\_run\_time$, thus adhering to cluster resource allocation limits. When all the loops have been backed out, the code then performs a safe shut-down, backing up the current processed position ready for the next stage of processing.

All eight cases solve simultaneously using all the processors. Those processors finishing first are redeployed to unfinished cases during the restart. Solutions are run until the lift and drag forces indicate a uniform wake. This is not always regular, but is run until it maintains a level average of magnitude and frequency over time. For C_1, this occurs very quickly as only one lengthscale is involved. Other cases, like C_{39}, take much longer to settle, due to the slow formation of the wake behind the group.

For future diagnostics, the steady state solution is saved. It can then be reloaded to allow processing to start from a fully developed flow field. Because of the size of the data sets, most diagnostics are first run within the code and the results presented in CSV format for manipulation and plotting using MATLAB. To save time in generating flow field Figures, additional libraries are incorporated into the numerical code which allows specified regions to be 'downgraded' into a png picture format for presentation.

3.8 Conclusion

The purpose of this chapter is to describe the development of a numerical code required to accurately and efficiently solve unsteady two-dimensional multi-body flows. Commercially available codes were initially implemented but were finally judged to give poor interface capabilities. Therefore it was decided, as a component of this thesis, to write a code specific for the task. This new code implements a three step CBS (Characteristic-Based-Scheme) FEM formulation. This involves solving the momentum equation (without the pressure forcing), the intermediate pressure field and the velocity correction to force the intermediate velocity field to be sinusoidal. The implementation of the CBS scheme was achieved by writing a platform independent

C++ programme, which utilizes MPI libraries to ensure positive scaling for any sized problem. A demonstration of this flexibility was its application to a three-dimensional flow domain which required only the implementation of a few additional call functions.

Two numerical libraries, PETSc and MKL, were evaluated, but the final evaluation pointed to full implementation of PETSc along with ParaMETIS to ensure interconnect overheads were minimized on large, sparse, memory-intensive matrices. The code was written using object oriented techniques so that implementation and flexibility was assured, facilitating the type of work required in this research.

The results from the code were validated against standard sets of geometries, specifically lid-driven cavity flow and asymmetrically/symmetrically placed cylinders in a channel flow. The range of Re from $1-1000$ was tested for an unsteady flow and from $1-5000$ for steady flows. In conclusion and based on the validation exercise, results from the new code have been shown to compare well with values from other published data and comparable output from commercial programs using a variety of other numerical schemes. The numerical truncation error associated with using linear basis functions gives an error proportional to grid size (as confirmed numerically). The error associated with time integration gives again an error proportional to Δt; since the underlying flow tends to be either steady or oscillatory the numerical error associated with truncation with time is not compounded.

As shown in §3.5.5, the choice of mesh plays an important part in calculating accurate values from a flow simulation. It has also been shown that it is possible to compute convergent values of C_D and C_L making it possible to calculate the percentage error for under-resolved meshes. Because of the considerable work involved in a full mesh independence study, it is helpful to be able to reliably estimate the maximum number of nodes required to calculate a grid independent (and probably over-resolved) solution beforehand.

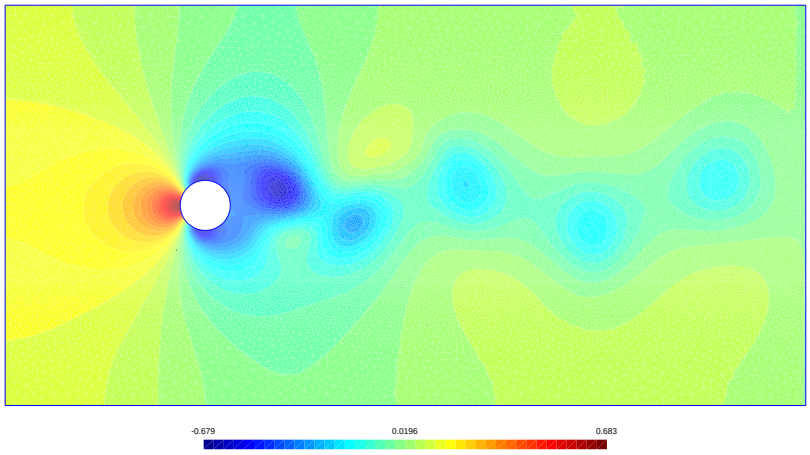

(a)

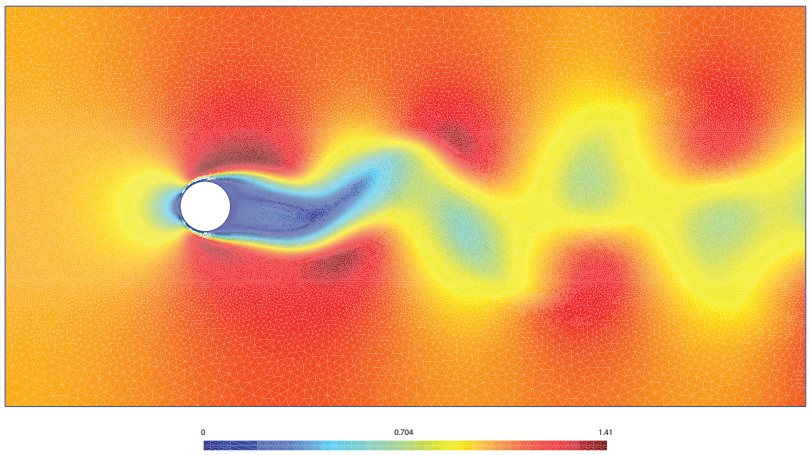

(b)

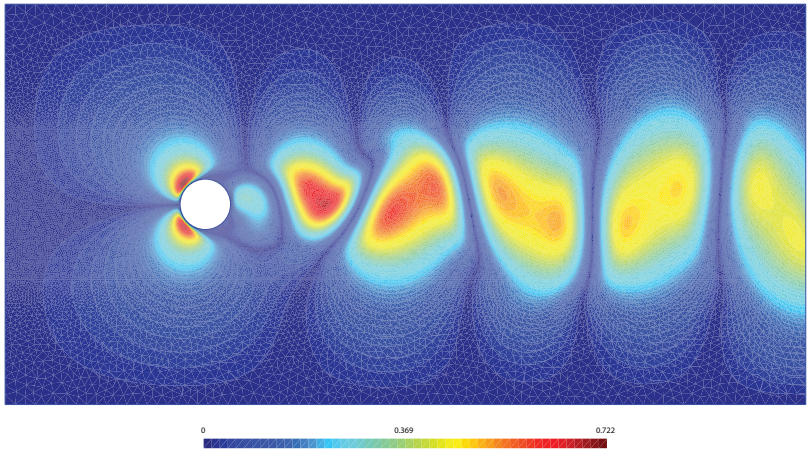

(c)

Figure 3.16: Case III for $Re = 100$ gives: (a) pressure contour, (b) u_1 and (c) u_2.

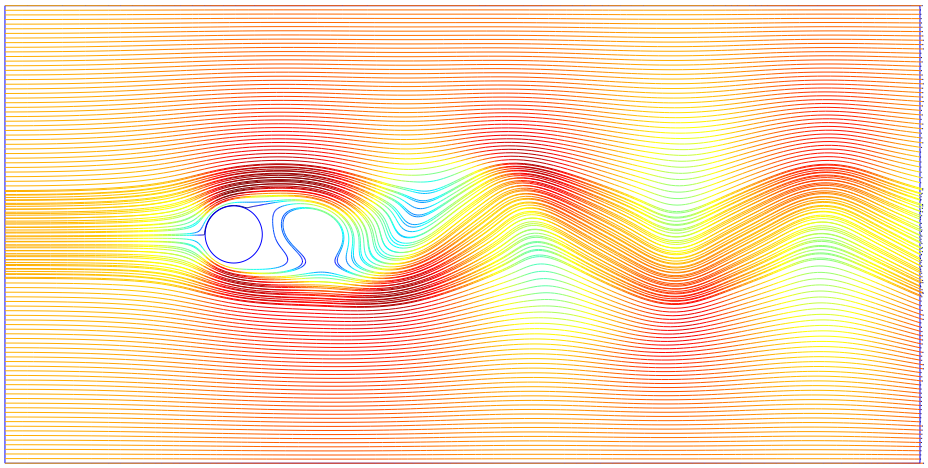

(a)

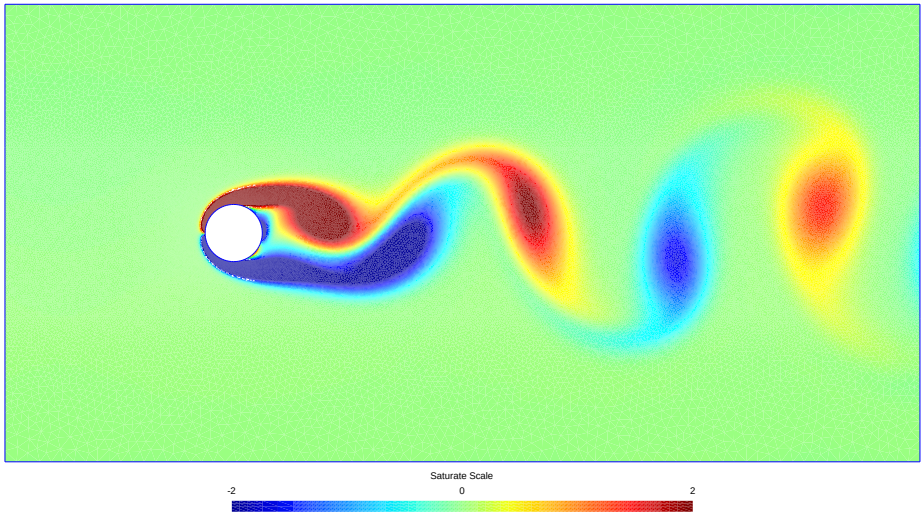

(b)

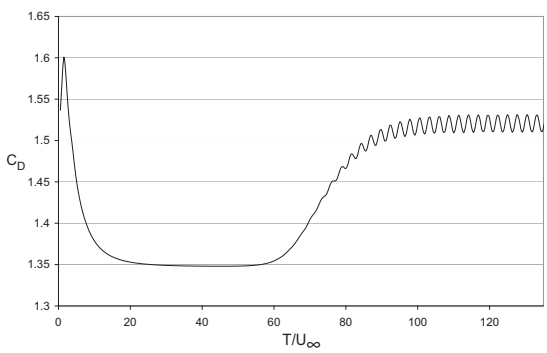

(c)

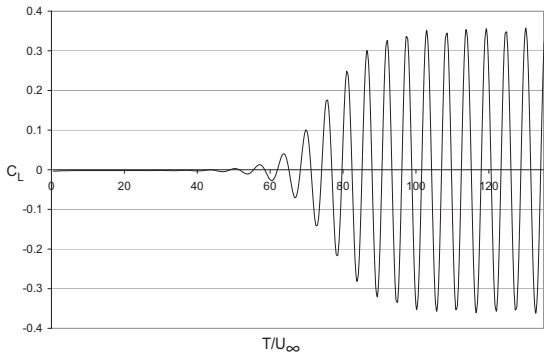

(d)

Figure 3.17: Case III $Re = 100$ gives: (a) instantaneous streamlines, (b) vorticity, (c) $C_D(t)$ and (d) $C_L(t)$.

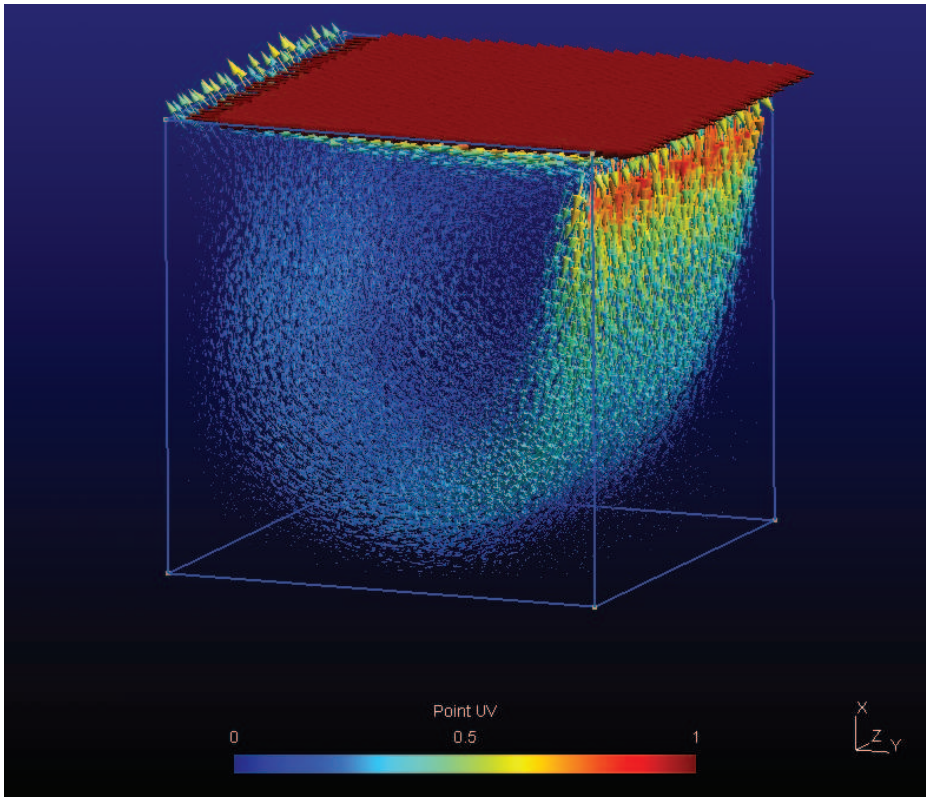

Figure 3.18: Velocity vectors for a three-dimensional cavity flow problem at $Re = 100$. The length, height and traction velocity are all unity.

Chapter 4

Design of experimental apparatus

4.1 Experimental considerations

There are clear computational limitations to what is currently achievable in high-resolution studies of fluid mechanical problems (as discussed in Chapter 3.1). This applies particularly in the range $Re > 1000$ and for groups of bodies with complex bounding geometry. This experimental study extends and expands on the companion numerical study of flow through and around individual and groups of bodies.

As discussed in §2.6, the aims of this experimental component were, in a uniform flow, to be able to:

1. measure the instantaneous and average drag and lift forces on any specific individual body within a group and on the overall group.

2. measure the velocity deficit profile across the wake at various distances and time intervals downstream from the group of cylinders across the flow.

3. identify flow blockage and wake regimes through visualization of the flow field.

A typical method for measuring an unsteady force in engineering flows is to use accelerometers. This approach is useful for measuring forces which are constantly changing. This is partially true for lift forces resulting from body shedding vortices, but does not account for steady drag forces. Strain gauges can be used to measure

steady forces. In terms of accuracy, the size of body is also quite important – small bodies experience smaller lift and drag forces, but the range of possible Re is wider.

In terms of facilities and apparatus available, the Department of Mechanical Engineering at UCL has one wind tunnel and a single water flume. Based on their dimensions and specifications, the maximum flow rates achievable in the wind tunnel and water flume were 25 m/s and 1 m/s respectively, with the water flume giving the widest operating envelope of Re. The recirculating flume available at UCL is a newly-installed tank 25 m long $\times$ 1 m deep $\times$ 1 m wide. This flume does not have a quietening section, so the flow is entirely turbulent with longitudinal vortices which seem to extend over its entire length. To undertake experiments in this tank, a settling and turning section would need to be constructed at one end of the flume to manage the flow. In this flume, PIV is also difficult because of lack of accessibility. The flume is constructed of glass on three sides, but access from below and from one side is limited. The presence of a free surface limits what can be done from above.

Apparatus to measure forces on individual bodies and the group of bodies as a whole was not available and it was quickly realized that this would need to be purpose-built. A final decision on whether to use the wind tunnels or the existing flume at UCL was deferred until the exact apparatus requirements had been considered.

Chapter 2 has already presented arguments for the shape of the bodies and group. Different circular arrays of cylinders were chosen because they provided a means of understanding the processes that occur as the void fraction increases from low values and the available space fills until the array eventually equates to a solid cylinder. To reduce the number of experimental parameters, it had been decided that the overall size of the array should be fixed. A wide range of Re was to be investigated for different void fractions.

Flow field visualization methods include:

1. Dye injection, which can be used to identify stream lines, flow through and the divergence around groups of bodies. It can also be used for 'time-of-flight' measurements.

2. Hot wire method, which can be used to interrogate at points the flow field by measuring the heat flux away from a wire which is proportional to the local flow.

3. PIV (Particle Image Velocimetry) which works by forming a laser sheet into a clear liquid and taking pairs of images. The velocity field is calculated from the correlation distance of intensity fields in small sub-regions. This method is not invasive and ideal for capturing velocity profiles across the stream.

It should be noted that, while imaging techniques can quantify the velocity profile, they cannot easily determine the force exerted on bodies in the flow. The requirements for and design/construction of the apparatus are considered in the sections below.

4.2 Apparatus development and solution

The significant constraints were recognized to be:

1. Time (to construct, design and conduct experiments).
2. Equipment and facilities available.
3. Space (in the Environmental Fluids Laboratory).
4. Financial constraints.
5. Health and safety compliance.

It was decided that the experimental facility required the following:

1. Optical access on all sides.
2. Settling section to remove large-scale turbulence.
3. Porous grids to reduce small-scale turbulence.
4. Straining of inlet flow to elongate small-scale turbulence causing it to rapidly decay.
5. Controllable flow rate.
6. No free surface.

7. Open access to the apparatus without time constraint.

8. Fully computerized integrated control.

9. Achieve $Re = 100 - 7000$ based on the flow past an isolated cylinder.

The wind tunnel satisfied 2, 3, 4, 5, and 6. The flume only satisfied 5 and 9.

Given that neither the wind tunnel nor the existing flume satisfied certain important requirements, it was decided that the way forward was through a purpose-designed recirculating flume with suitable instrumentation designed to capture the specific data required (the forces on individual bodies and the group as a whole and sample data about the flow field). The experimental work therefore included design, manufacture, testing and commission of this apparatus as a main objective. As a secondary element, it was intended that as much time as possible should be devoted to experimental work to gain a useful body of comparative data. Based on tests during the initial stages, it was decided that visualization should focus on dye injection and PIV should be deferred to future work.

Key design parameters were identified and fixed which allowed design, build and testing to happen simultaneously. Computational simulations using finite element analysis of loaded structures (using COSMOS) and CFD (using Fluent) were employed to help short-cut the design process. The design was sequentially progressed in the following order (there were inevitable overlaps of certain aspects):

1. Pump selection, §4.3. The pump is the most costly component and determines many other parameters. A pump was selected to give maximum flow rate within budget constraints and this had to achieve up to $Re = 7000$. This flow rate was effectively a key parameter on which the rest of the design depended.

2. Cylinder group arrangement, §4.4. In order to have adequate data, four void fractions were specified, within the group of cylinders. The group was confined to a fixed overall width determined by the blocking ratio based on the channel width (defined in §4.6.2) and adjusted to facilitate uniform distributions of the cylinders.

3. Instrumented cylinder design, §4.5. Cylinder dimensions were established as a function of pump performance and experimental requirements. Cylinder design facilitated accurate drag and lift force measurements in experimental work.

4. Flume design, §4.6. The flume was designed to keep turbulence to a minimum in the space available, whilst working to a budget. Manufacturing was kept as simple as possible.

5. Data logging, §4.7. An electronic solution was developed around discrete components with the ability to log data in real time at the sample rates required.

4.3 Pump selection

The defining parameter for the size and design of a flume is the performance of the pump used to drive the fluid through the channel section. The pump selected must satisfy the following requirements:

1. Variable speed requirement to allow flow to be adjusted in order to achieve $Re = 100 - 7000$, at intervals of 100.

2. Powered by electricity at 2 or 3 phase with maximum rating of 415V at 32A.

3. Computer controlled.

4. Steady flow rate.

5. In-line fitting to reduce footprint area and fit in the Environmental Fluid Mechanics Laboratory.

6. Minimum noise and vibration.

7. Pump medium – water.

The major constraint on the pump selection was financial. A single manufacturer, Lowrana, was chosen because they appeared to be competitive across their wide range of models and their pumps were easy to source. In common with the other main manufacturers, they have a comparison table of their models (Appendix A.4).

Appendix A.5 shows the pump operating envelope according to pressure head and flow volume. The pump in the Lowrana range that was best suited and within the cost allocation was FCS4-150-200-203, which incorporates the option of a four pole motor which reduces motor speed by 50% to 1400 rpm. This assists in reducing vibration and noise. Compensating for the lower motor speed, the pump comes equipped with an oversized, cast iron, 203 mm impellor. From this, a flow rate of 200 m^3/hr is achievable, against a pressure head of 4.7 m. It works at supply frequency of 50 Hz and consumes 5.5 kW (at maximum load) using a 3 phase AC motor, which relies on the frequency of its power supply to determine its speed. By altering this frequency using a digital AC inverter FSD650, it is possible to accurately vary the motor speed from $10 - 1,400$ rpm. These parameters were used to progress the design of the flume. Two subsequent checks were necessary:

1. To calculate the pressure drop through the flume design against the pump's operating envelope.

2. To ensure that the design prevented pump cavitation.

4.3.1 Pressure drop calculations

This section shows these calculations incorporating data derived from the flume design section below and expressed in terms of the head of water, rather than Pa. This is because most of the data sheets are expressed in this format, although it is simple to convert between both sets of units.

The pressure drop encountered in a flume consists of two components – the pressure drop in the flume itself (including settling tanks and working channel) and the return pipework connecting the pump. The pressure drop across the flume was calculated using a CFD analysis of the flume flow. This showed that, because of the relatively large cross-sectional area of the channel and the even flow angles, there was a small pressure drop ≈ 0.3 m. This also assumed a worst case situation, where the channel contained a dense array of cylinders with a blocking ratio of 3. The pipework has a much smaller cross section and its pressure drop is higher. In total, there needed to be 7.2 m of piping with 3 direction changes of 90° degrees, as shown in the flume layout in Figure 4.1.

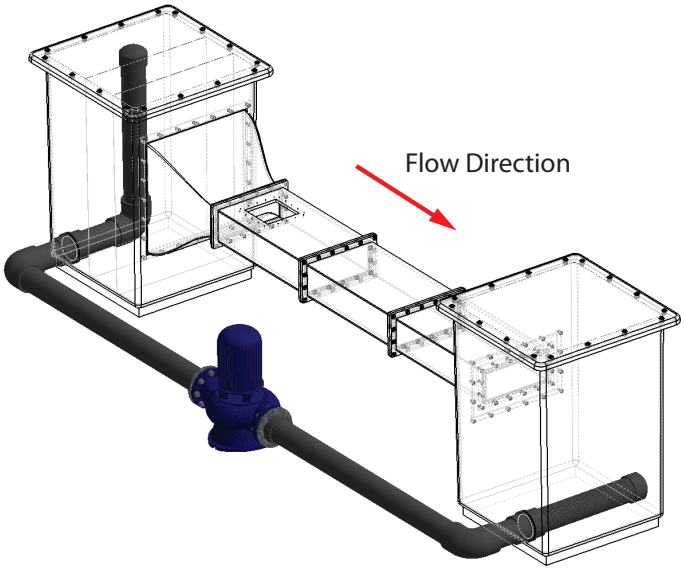

Figure 4.1: CAD image showing the path of the pipework for the recirculating flume and the location of the pump. There are three 90° bends with a total pipe length of about 7.2 m.

The piping selected is Durapipe ABS. This was available in the required diameter of 150 mm, matching the pump inlet/outlet. The manufacturer provides data sheets (Appendix A.6) for calculating pressure drop on their piping systems. At maximum flow rate of 200 m^3/hr, the head loss for a 7.2 m of pipe, was estimated to be 0.36 m. The direction changes were achieved by 90° tight elbow bends. Durapipe provides tables of pressure loss coefficients for bends which allow an approximate equivalent pipe length to be calculated. Three 90° elbows gave a head loss of $(3 \times 4.5 \times 5 \div 100) = 0.675$ m. A wider radius bend is available, which reduces the head loss (by 50%), but the benefit was not cost-effective. This improvement, while substantial, was not required, as the pump was adequately powerful. Therefore, the total pressure drop across the pump was estimated to be 1.035 m head of water, which fell well within the operating range of the pump.

4.3.2 Cavitational test calculations

Cavitation in a centrifugal pump may take place on the impeller blades. Small voids form which, in the extreme, can damage the impeller's surface, cause pressure fluctuations, poor efficiency, vibration and, in the worst case, pump failure. Factors which adjust the point at which cavitation forms are fluid type e.g. water, liquid temperature (estimated to be 20°) and elevation above sea level (presumed to be negligible). Ensuring that the pump will not cavitate is best done by checking the operating parameters against pump literature. This provides working envelopes within which cavitation can be avoided. To be safe and avoid cavitation, the $NPSH$ (net positive suction head) required for cavitation ($NPSH_r$) must be larger than the net position section head available ($NPSH_a$).

The parameters used to calculate the extreme flow conditions are:

Water temperature	$T = 20°$ C
Water density	$\rho = 9983$ kg/m^3
Vapour pressure of water	$h_{vp} = 0.2337$ m
Absolute pressure	$h_p = 10$ m
Suction supply head	$h_z = +1.5$ m
Pumps rated $NPSH$ from data sheets	$NPSH_r = 2.5$
Flow resistance in the suction pipe	$h_f = \frac{1.035}{2.0} = 0.5175$ m
Head safety factor	0.5 m

The measures are $NPSH_a = h_p + h_z - h_f - h_{vp} = 10.7$ m, while $NPSH_r = 2.5 + 0.5 = 3.0$ m. This showed that cavitation was unlikely to occur in the experimental study since $NPSH_r < NPSH_a$

4.4 Geometry of cylinder group

When investigating flow through and around a group of bodies, the following parameters with respect to the group's signature can be varied:

1. Shape and size of the group of bodies.

2. Void fraction of group of bodies.

3. Distribution of bodies within the group.

The aim of the proposed series of experiments was to examine the individual and collective forces acting on individual and groups of bodies fixed in a uniform flow. The parameter range of the experiments was limited to groups of cylinders, which occupy a circular array. A minimum of four void fractions was necessary in order to draw any firm conclusions from the study.

The dispersal of the cylinders within the arrays was simplified by equally spacing cylinders from one another. Cylinders were distributed in concentric circles with one cylinder at the center. The densest circular group contained four concentric circles of cylinders. To maintain the structural integrity of the mounting plates, the distance between cylinders was required to be at least $D/4$. This places a constraint on the densest cylinder arrangement, which had a width of 9 cylinder diameters and consisted of 64 cylinders. Figure 4.2 shows the different cylinder arrangements employed for the circular groups. There was no need to instrument all the cylinders. The construction time for each instrumented cylinder was about one machining day and each required an additional day to build and mount the bespoke electronic circuity. The design required the potential to interchange instrumented/non-instrumented cylinders, as necessary, during experimental work.

As not all the cylinders were instrumented, the total force on the group could not be measured by aggregating individual forces on cylinders on the larger arrays. The total force was, therefore, measured from the force transferred by all the cylinders to the support plate to which they were all attached. Force on the support plate was measured using calibrated load cells. An independent check was performed for the total aggregate force but only by using all instrumented cylinders on the smallest array.

4.5 Instrumented cylinder design

As discussed above, some of the individual cylinders had the potential to be separately instrumented to measure drag and lift forces, in addition to the total forces on the group being measured. Individually measured cylinders are referred to as 'instrumented cylinders'. Section 4.4 identifies that 15 instrumented cylinders would

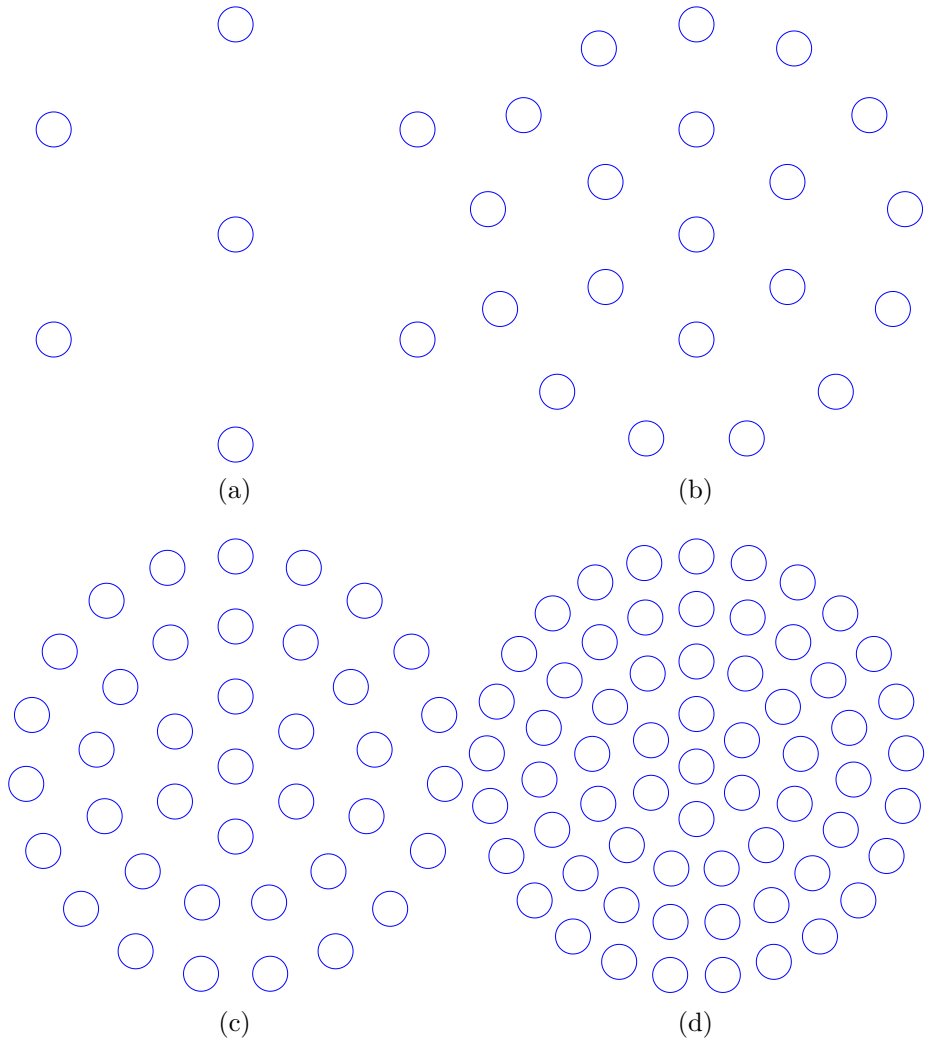

Figure 4.2: The cylinder configurations for a circular group of bodies are shown in (a) to (d), for increasing numbers of cylinder (N_C). These correspond to (a) $N_C = 7$, (b) 20, (c) 39, and (d) 64.

ultimately be needed to give adequate data for evaluation of the experiments against theory.

The cylinder dimensions were derived using parameters already set and two equations, as shown below:

Pump flow volume (Pump Selection § 4.3)	$F_r = 200\text{m}^3/\text{hr} = 0.055\text{m}^3/\text{s}$
Maximum Re for an individual cylinder	$Re = 7000$
Cylinder diameter	$D = unknown$
Channel width (Group Design § 4.4)	$W = 39D$
Channel velocity	$U_\infty = unknown$
Cross channel area	$A = unknown$
Channel depth	$L_C = unknown$

As indicated previously, the limiting range of Re, and the sensitivity needed to measure forces accurately, placed a constraint on the cylinder diameter. From the pump flow rate and channel cross-sectional area, two restraining equations are formed

$$U_\infty = \frac{F_r}{A}, \qquad A = L_C W = 39 D L_C, \tag{4.1}$$

which after elimination gives:

$$U_\infty D = F_r / 39 L_C \tag{4.2}$$

Having set the channel width to be $W = 3 \times 13D = 39D$. Eliminating $U_\infty D$, it is found that the channel depth is $L_C \sim 0.2\text{m}$. The cylinder drag force is:

$$F = C_D \frac{1}{2} \rho U_\infty^2 D L_C. \tag{4.3}$$

The experimental study is being undertaken in water up to $Re = 7000$. From the definition of Re,

$$U_\infty D = \nu Re. \tag{4.4}$$

Thus:

$$U_\infty D \sim 0.007(\text{m}^2/\text{s}), \tag{4.5}$$

giving:

$$F = \frac{0.0049}{D} \quad \text{(N)}. \tag{4.6}$$

As the cylinder diameter is reduced, the drag force on the cylinder increases. The compromise was a small cylinder which would produce a measurable drag force, but not so small that turbulence became an issue. A load cell which is rated for a load of 0.5 N was found to give reliable readings so the cylinder diameter was determined for $F = 0.4$ N to allow for overload caused by accelerating flow. Therefore

$$D = \frac{0.0049}{0.4} = 0.01225(\text{m}), \tag{4.7}$$

Thus the optimum cylinder diameter was determined to be 13 mm with channel width $W = 39 \times 0.013 \approx 0.5$ m and the channel depth $L_C = 0.2$ m.

4.5.1 Force measurement of instrumented cylinders

One requirement of the experiments was to measure the force on the cylinder in two mutually perpendicular directions. A typical way of measuring force is to measure the strain in the supporting member using strain gauges. These can be incorporated into a pre-manufactured load cell which, in this case, could also have been used to support the cylinders and group of cylinders. By calibrating the response of the strain gauge with an applied load, it was possible to determine the force applied to the cylinder. With the correct amplification and data logging, such a load cell can be accurate to a resolution of $30,000$ divisions, with a load capacity of 0.5 N. Pre-manufactured load cells would be the most practical, but it was soon realized that these would require more mounting space than was available. This was resolved by integrating a *purpose-designed* load cell into the cylinder construction. This load cell measured the force transferred from the surface of the cylinder to its mounting plate in the channel through a machined aluminium supporting beam incorporating a strain gauge or gauges.

Different instrumented cylinder design strategies were explored before deciding which to use. The initial concept was to use cylinders supported at both ends, before refining the design to a cylinder supported at one end.

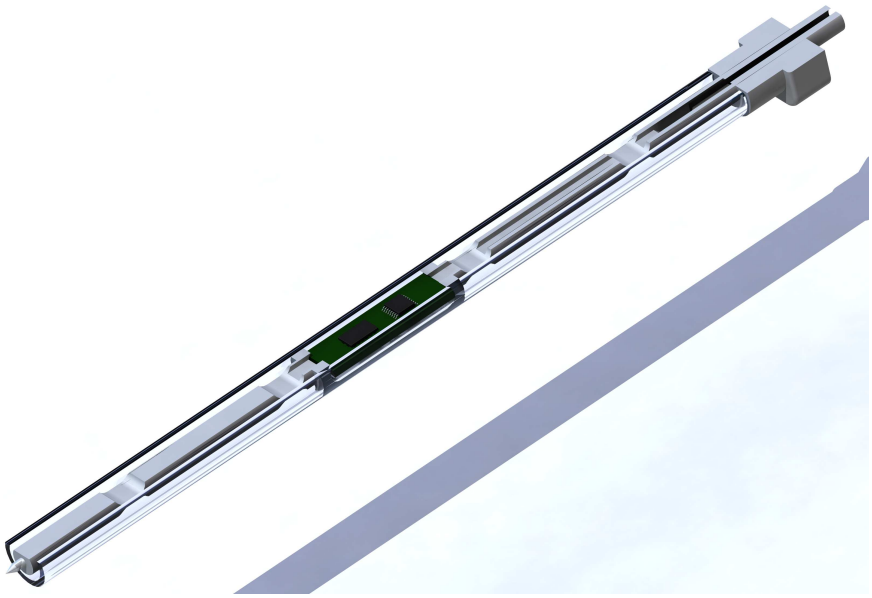

Figure 4.3: CAD image of an instrumented cylinder supported from two ends. This was the first design concept tested.

4.5.2 Instrumented cylinders support at both ends

A CAD representation of a cylinder supported at both ends is shown in Figure 4.3 and design drawings are in Appendix A.7. The cylinder is held rigid on the floor of the flume by a tapered pin and at the top end by a square plug which is integral to the cylinder and rests within the top location plate. The square plug arrangement facilitated the reorientation of the cylinders through 90° to allow the strain gauge in each cylinder to separately measure force in the x_1 and x_2 directions. The plug formed a waterproof joint in the top mounting plate of the channel. Each cylinder comprised an outer Perspex sleeve with an overall diameter of 13 mm and wall thickness of 1.5 mm, supported on an inner machined aluminium beam. The outer Perspex sleeve was attached to the inner support beam at the mid point, as shown in the designs. Encapsulated strain gauges were attached on the four hinged sections, either side of where the Perspex sleeve was attached, which facilitated sensing of uneven loads. These sections were weakened so that flexing takes place, locally concentrating the load in the location of the strain gauges. Supporting the cylinders

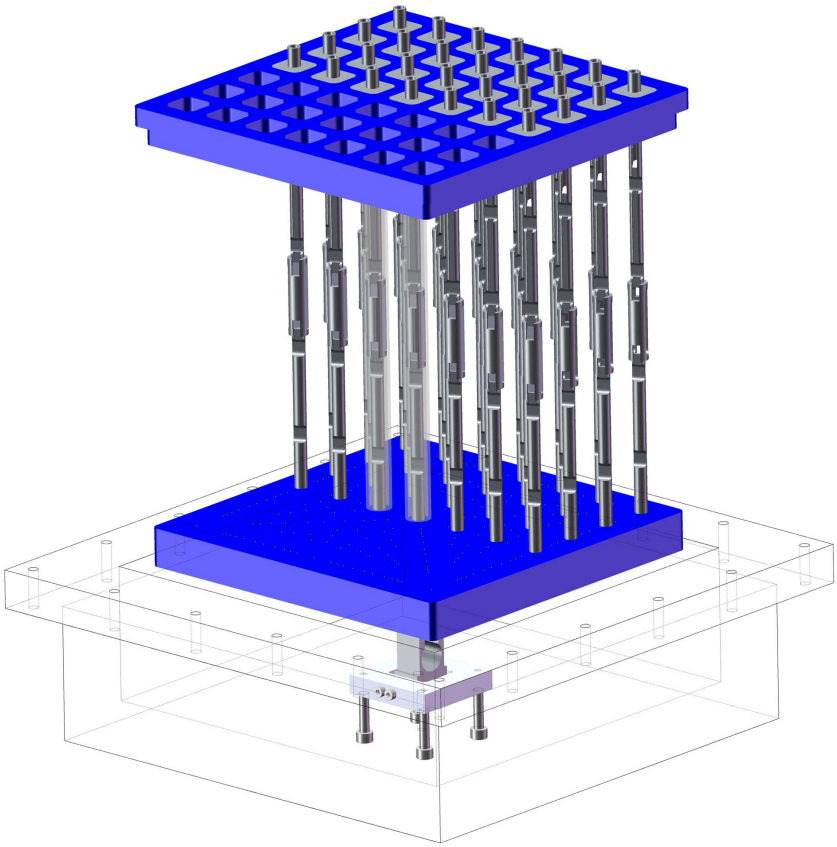

Figure 4.4: CAD image showing the configuration for an array of cylinders supported from two ends.

at both ends facilitated quick and easy rearrangement of the group of cylinders into different patterns and allowed positions of instrumented/non-instrumented cylinders to be interchanged. It also meant that the cylinders could be held by a fixed top location mounting plate which reduced the chance of movement. The other end of the cylinders could be used to measure the total group drag force. This force (measured at the one end) represented 50% of the overall load from the group, assuming that the force was equally distributed along the cylinders at an instant in time. Figure 4.4 shows how the instrumented cylinders were incorporated. The final engineering designs are shown in Appendix A.11.

This concept was initially evaluated with a test beam (Figure 4.5a) which assessed whether small-scale deflections generated by such a beam could be measured. This

trial was carried out by point supporting both ends of the beam and loading the central region, while recording the strain gauge output (Figure 4.5b). Figure 4.5c shows that the signal from the strain gauges changed proportionately and with adequate sensitivity to the load applied, in the force range under investigation.

A finite element analysis of the instrumented cylinder deflection showed that the method of supporting the cylinder beam ends was critical to the deflection resulting in the hinged sections. With only one hinged section at each end, the beam was bent in an 'S' shape which resulted in a cancellation of stresses in the strain gauges, as illustrated in Figure 4.6a. To solve this problem, two additional hinging sections were incorporated into the beam, which allowed the sensing hinging sections to bend uniformly as in Figure 4.6b. The cylinder design went through many revisions which were mainly geared to facilitating manufacture. Some of these design revisions are shown in Appendix A.8 to A.10.

A study was carried out to determine the optimum load cell hinge section thicknesses. This was in order to minimize displacement along the beam from its original position, while maximizing the measurable strain signals. This was studied using finite element analysis to test the effect of different hinge thicknesses, using the software package COSMOS 2007. Figure 4.7 shows the maximum displacement of the cylinder against strain at the hinge sections, indicating that the optimum hinge section was > 0.40 mm. If the thickness was reduced beyond this point, the increase in strain was substantial but displacement also rapidly increased which resulted in an unduly flexible load cell.

Figures 4.8a and 4.8b show the displacement and levels of strain on an aluminium supporting beam with 0.6 mm hinged sections, when an even load of 0.5 N was applied along the length of the cylinder. It can be seen that the displacement of the central region was 1.81×10^{-4} m.

The strain was uniform across the hinged sections and the average surface displacement measured by the attached strain gauges was 2.13×10^{-4} m. Figures 4.9a and 4.9b show the effects of unevenly loading the cylinder at either end with 0.5 N. This is an extreme example, but does illustrate how it is possible to measure uneven distribution of drag across the cylinder, by measuring the force independently on both hinged sections.

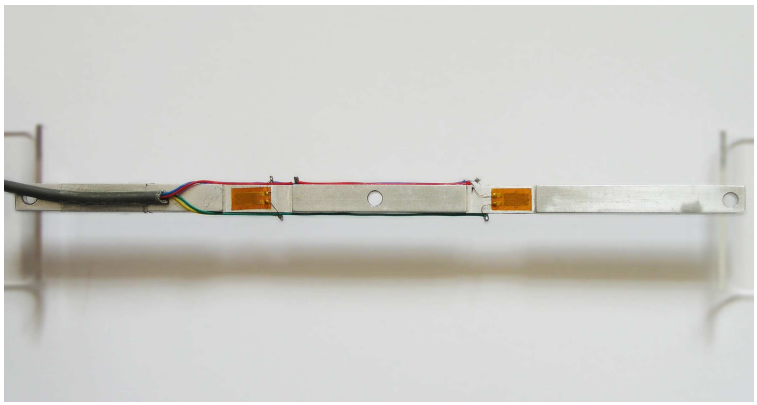

(a)

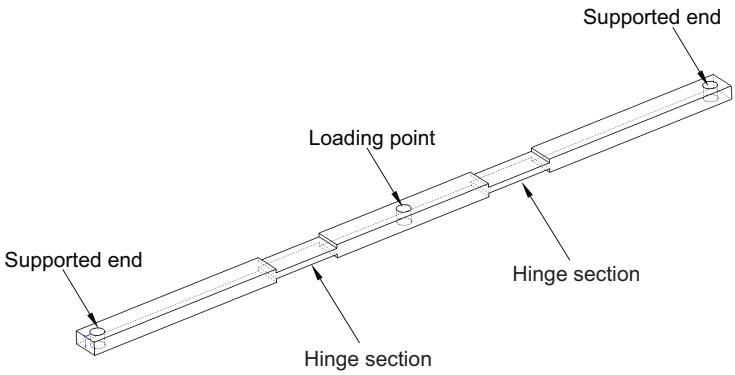

(b)

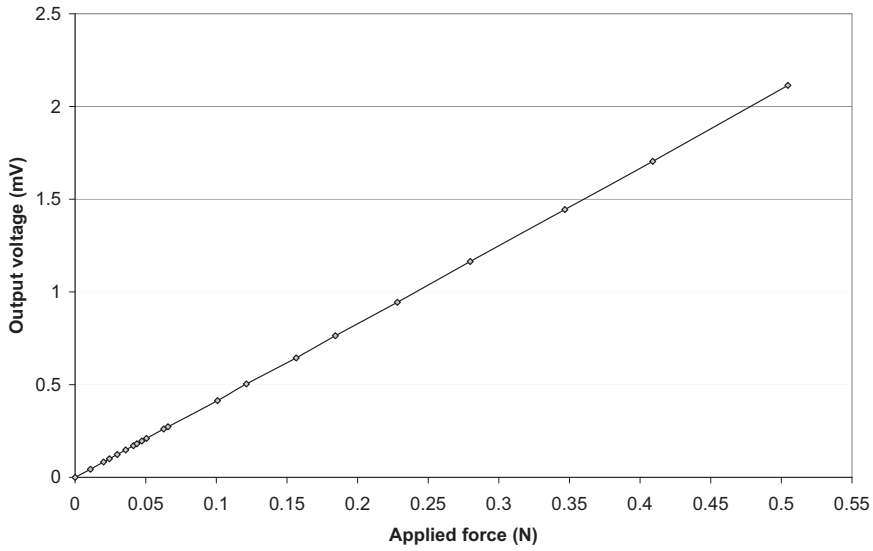

(c)

Figure 4.5: (a) Photograph of initial beam constructed. (b) Schematic of a beam used to test the strain gauge sensors on a simulated section. (c) Measurement of the amplified voltage signal versus a force applied at the loading point.

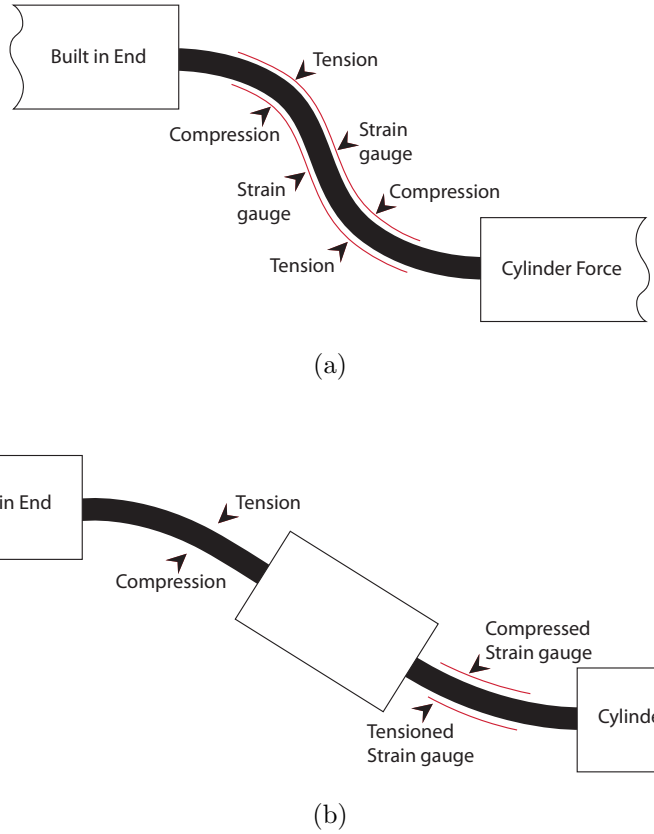

Figure 4.6: Hinged section concept for instrumented cylinder: (a) load is cancelled in the strain gauges and (b) uniformly loaded strain gauges.

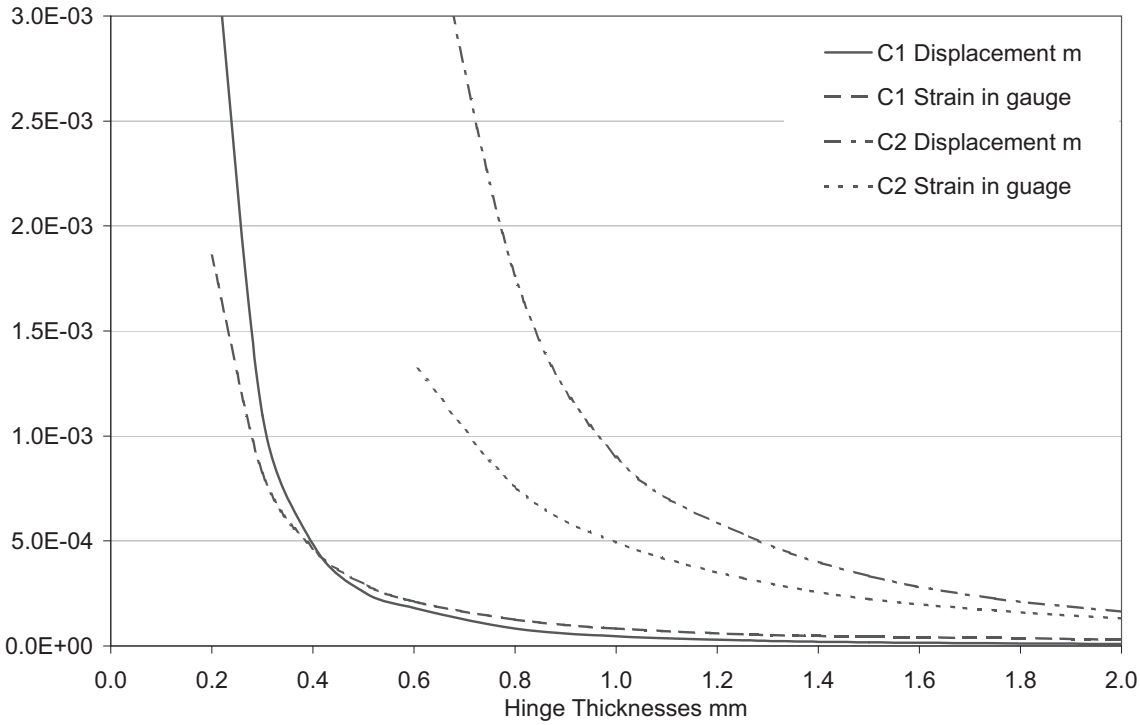

Figure 4.7: Numerical results from an FEA study of the strain at the sensing surface of an instrumented cylinder, held at two (C1) and one (C2) end versus the hinge thickness.

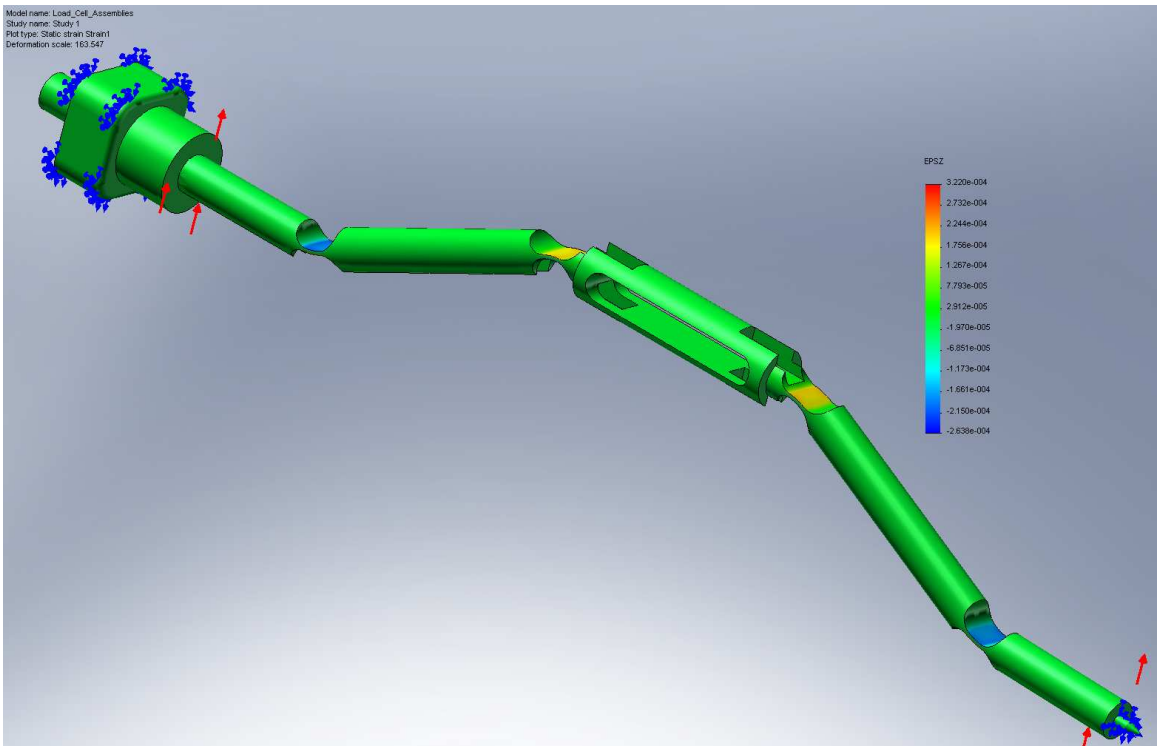

(a)

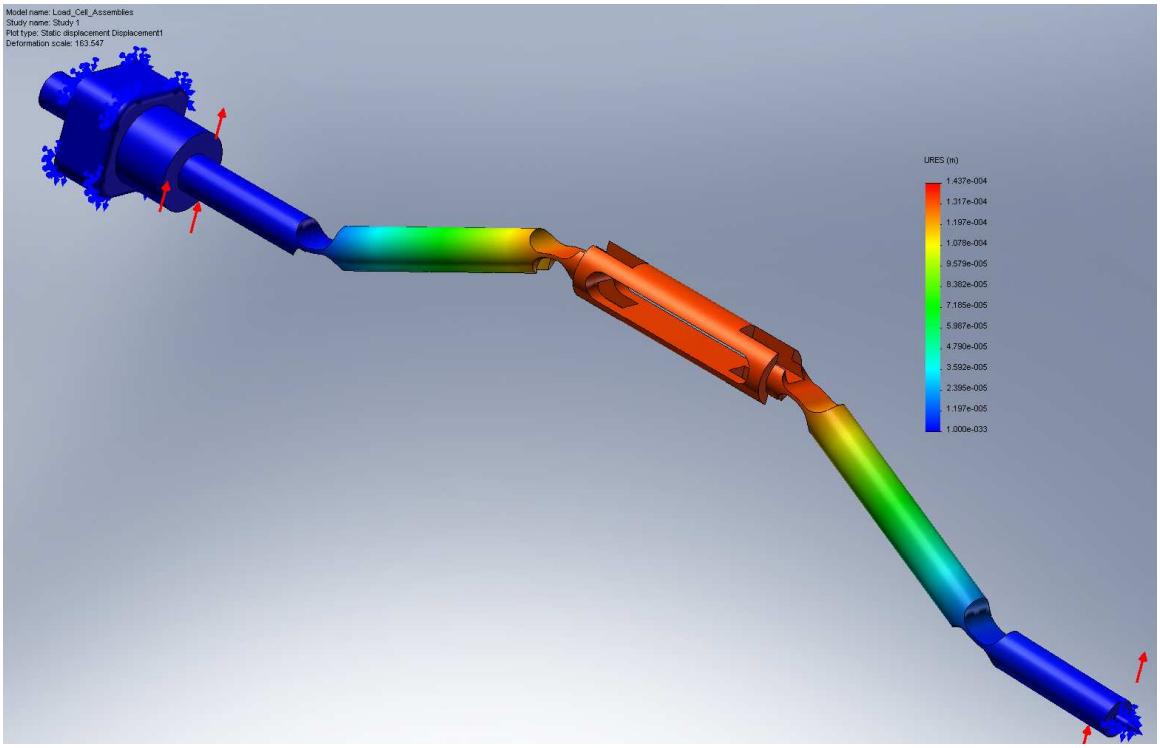

(b)

Figure 4.8: Results from an FEA calculation of the (a) strain and (b) displacement of the integrated load cell on an instrumented cylinder. The displacements are magnified to enable the displacement field to be viewed.

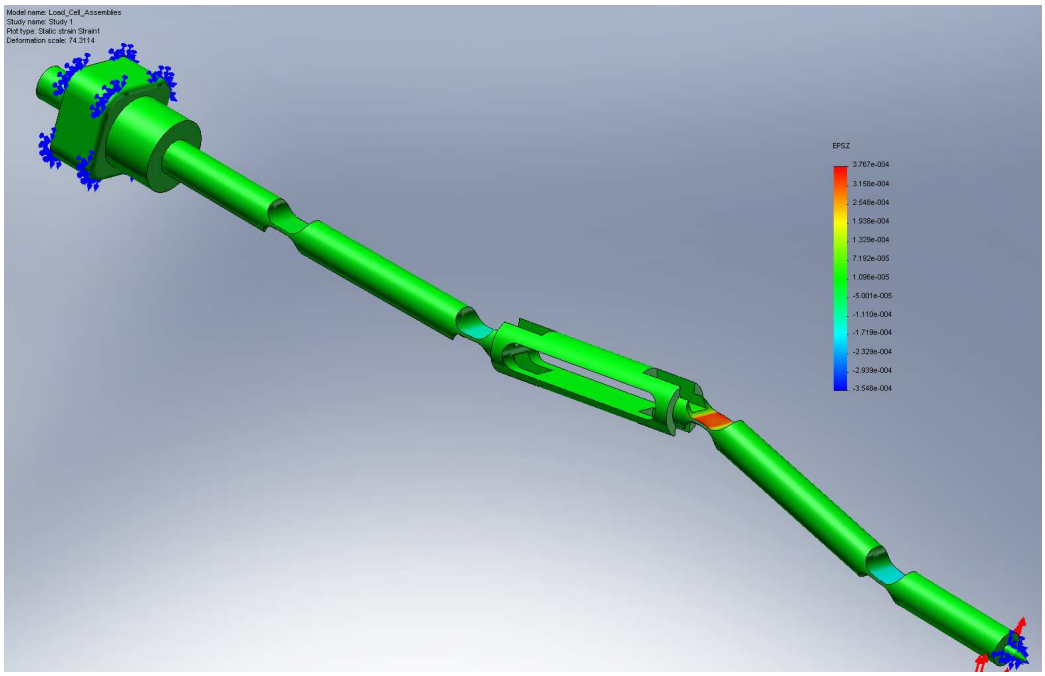

(a)

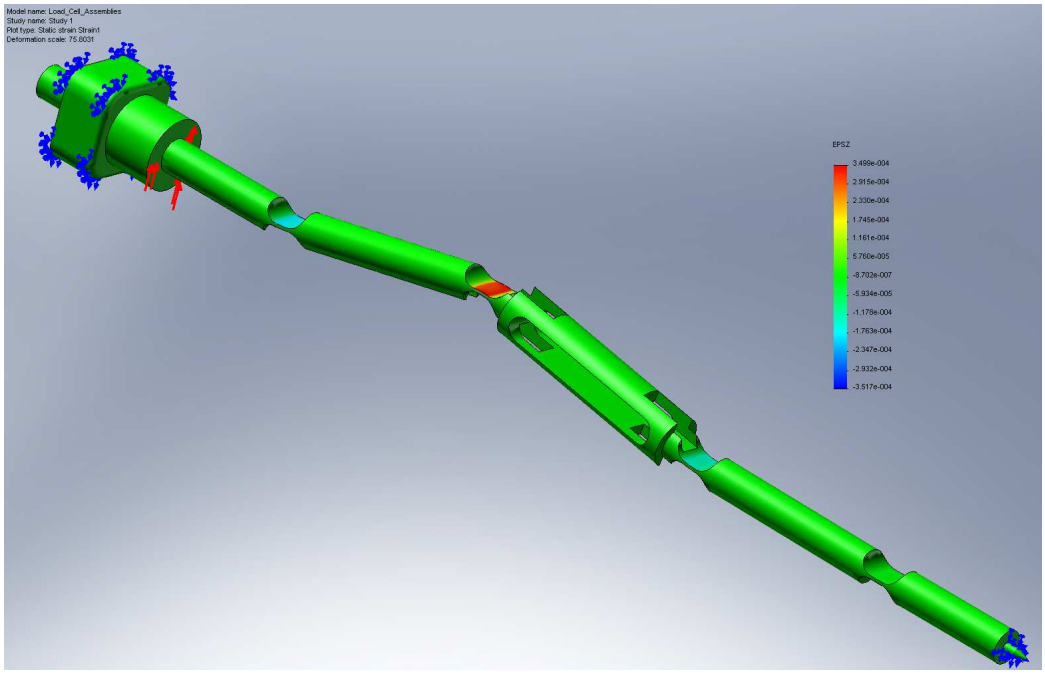

(b)

Figure 4.9: FEA results showing the strain on the hinged sections for an unevenly applied force. (a) and (b) correspond respectively to the case when the force is applied to the bottom or top of the cylinder.

Figure 4.10b shows two plots of force against Re. The first plot was produced by measuring the signal on the prototype instrumented cylinder (shown in Figure 4.10a), using a small flume producing a steady flow measured by a calibrated paddle wheel. The second plot is the ideal force induced on a two-dimensional cylinder calculated for different values of Re using the equation $F_D = \frac{1}{2}\rho D U_\infty^2 C_D$ and a constant drag coefficient of 1.0.

This exercise was designed to determine whether adequate signal resolution could be achieved within the design concept of the instrumented cylinder. For this, the cylinder was not independently calibrated against a known force, as would normally be expected. Instead, it was linearly corrected to one point on the theoretical curve. As can be seen, this gave a remarkably good correlation, considering many assumptions were made but, most obviously, that the drag co-efficient between the range $Re = 500 \rightarrow 2500$ was equal to 1.0.

The method of supporting the cylinder at both ends, while having advantages, reduced the low amplitude signals from the strain gauges, requiring considerable amplification with increased noise and error introduction. This reduction was because the hinging sections on either side of the supporting ends could only measure half the moment along the beam. As already discussed, reducing the thickness of the hinge sections below 0.6 mm was not feasible. Therefore, signal strength would always be limited, using this design concept.

4.5.3 Instrumented cylinders supported at one end

The alternative approach investigated was to support the cylinder at just one end. The significant difference here was that this gave rise to greater moments about the hinge sections which were now placed near the top of the supporting beam. These increased moments translated into significantly larger output signals from the strain gauges.

Figure 4.11 shows the design of the modified beam and drawings can be found in Appendix A.12. Unlike the double-end supported cylinder which displaces evenly along its length, this design, being fixed at one end allowed the unattached end to freely displace in the direction of the force (seen in Figure 4.13a). It was therefore important, at a preliminary stage, to calculate the maximum displacement and this

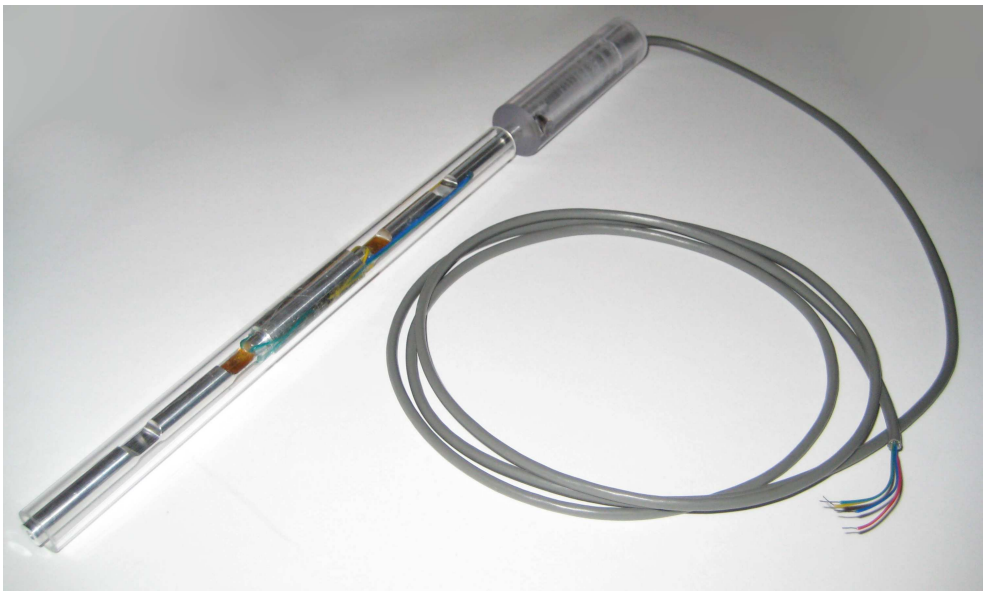

(a)

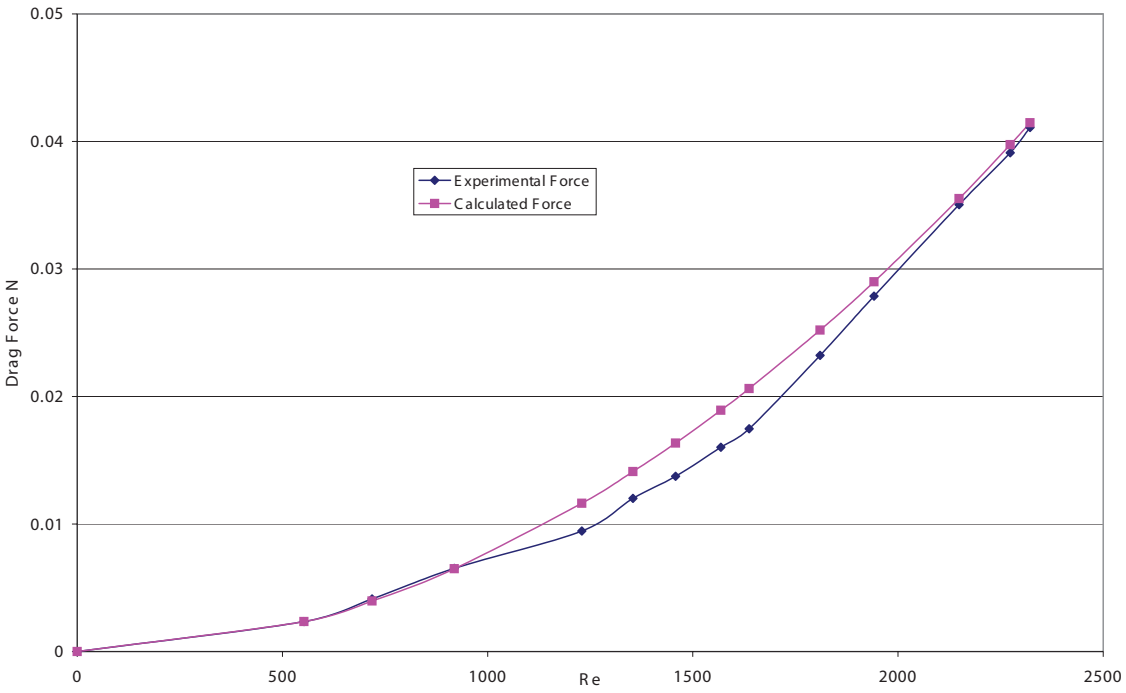

(b)

Figure 4.10: (a) Photograph of a prototype instrumented cylinder. (b) Experimental measurements of the force acting on the prototype instrumented cylinder, versus Reynolds number (blue triangles), which are compared with the predictions (pink squares).

(a) (b)

Figure 4.11: (a) CAD image showing the final design of the instrumented cylinder with a single supported end. (b) Photograph of a manufactured instrumented cylinder.

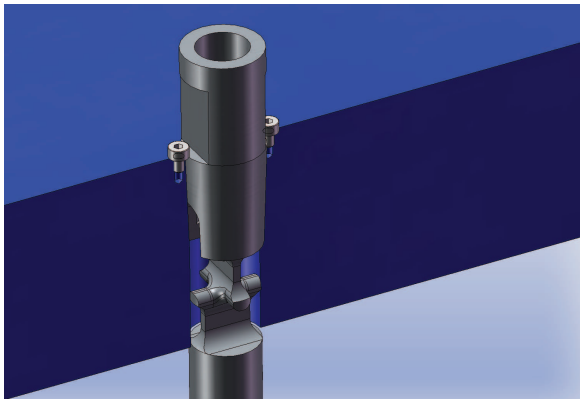

Figure 4.12: Fixing arrangement for the final instrumented cylinder held at one end.

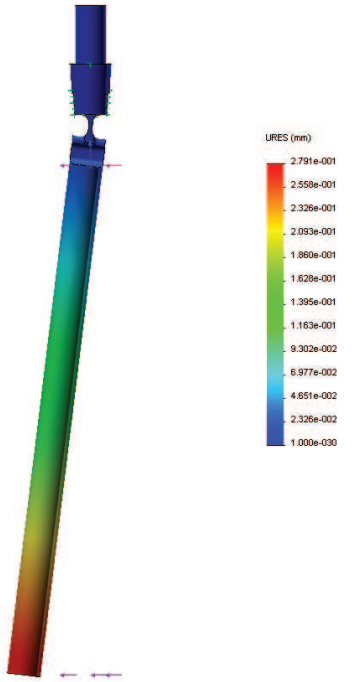

(a)

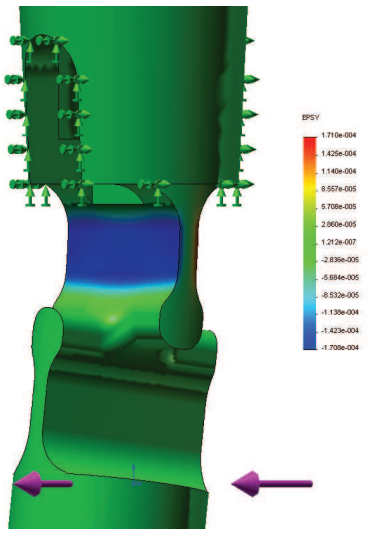

(b)

Figure 4.13: Results from an FEA calculation of (a) displacement and (b) strain of the instrumented cylinders held at one end with a hinge thickness of 0.6 mm.

was done using finite element analysis.

Figure 4.7 shows the effect of changing the hinge section thickness on the free end displacement of the cylinder and the resultant measured strain induced in the hinge section. It was found that the maximum displacement for the hinge thickness used was 0.279 mm or 2.14% of cylinder diameter which was small enough not to have a significant effect. The single-ended cylinder produced a signal many times greater, for a much thicker hinge section, than the double-end supported cylinder which is also plotted for comparison. It was also clear from the graph that the hinge thickness offered scope for tuning to ensure that strain level was adequate for measurement.

The detailed design of the cylinder with the single-ended support differs in that the cylinder, its support and the hinged sections were all constructed out of one piece of aluminium bar. Working dimensions of the cylinder were identical. The hinge section was CNC'd into the top of the cylinder bar. These sections were located within the cylinder bar where it passed through the top supporting plate, so that the bottom end of the hinged section was flush with the channel roof, as shown in Figure 4.12. The top end of the cylinder was tapered to locate in the supporting plate above the hinged section. There was sufficient clearance around the hinged section to allow free movement of the hinged section. The cylinder was locked in place by tensioning screws.

The cylinder above the hinged section was machined out to house the electronics. The electronics could measure the force acting on the cylinder in two mutually perpendicular directions (usually lift and drag). This was accomplished by incorporating two hinging sections within the beam, set at 90° to each other. Two full Wheatstone Bridges were used to separately collate data. This was an improvement, as it allowed force measurements to be made simultaneously in two directions without the need to disassemble and re-orient the cylinder. The disadvantage was that the effect of uneven vortex shedding along the length of the cylinder was no longer measurable. However, when measuring static drag, this was overcome by time averaging the output data. Figures 4.13a and 4.13b show displacement and strain analysis for this cylinder when a force of 0.5 N was applied along its length in the stream flow direction. This shows that only one hinge point reacted to this force, confirming the independence of the load cells in measuring forces in two directions.

The single-end supported cylinders only required attaching to a top mounting plate, so group drag force needed to be deduced from this plate. (For the double-ended support cylinders there was a second supporting platform on the channel floor.) The top mounting plate was, therefore, floated on a gantry which was supported by Vichey 1004 load cells to independently measure both total group drag and lift. This required four load cells on each axis. The load cells were orientated such that they would support the considerable mass of the cylinders and the support plate, but not induce distorted readings in the sensing elements. A reasonably complicated structure was required, which is shown in Figure 4.14.

To ensure that the load cells used in the supporting gantry were correctly rated and no unforeseen forces would affect the arrangement, finite element analysis was again used to check both the independence of the strain in the gauges induced by load on each axis and the resultant displacement is shown in Figure 4.15. Figure 4.16 also shows that both x_1 and x_2 arranged strain gauges reacted when a combined lift and drag force was applied.

4.6 Flume Design

The flume design was required to:

1. Produce laminar flow in the working section of the flume.
2. Allow easy adaptation to present and future experiments.
3. Allow optical access to the flow sections.
4. Fit into available space.
5. Be controllable.

Key parameters have been set with reference to previous sections which deal with what is practically needed for successful experiments with this cylinder group. Therefore:

1. Pump capacity was fixed at 200 m^3/hr maximum.

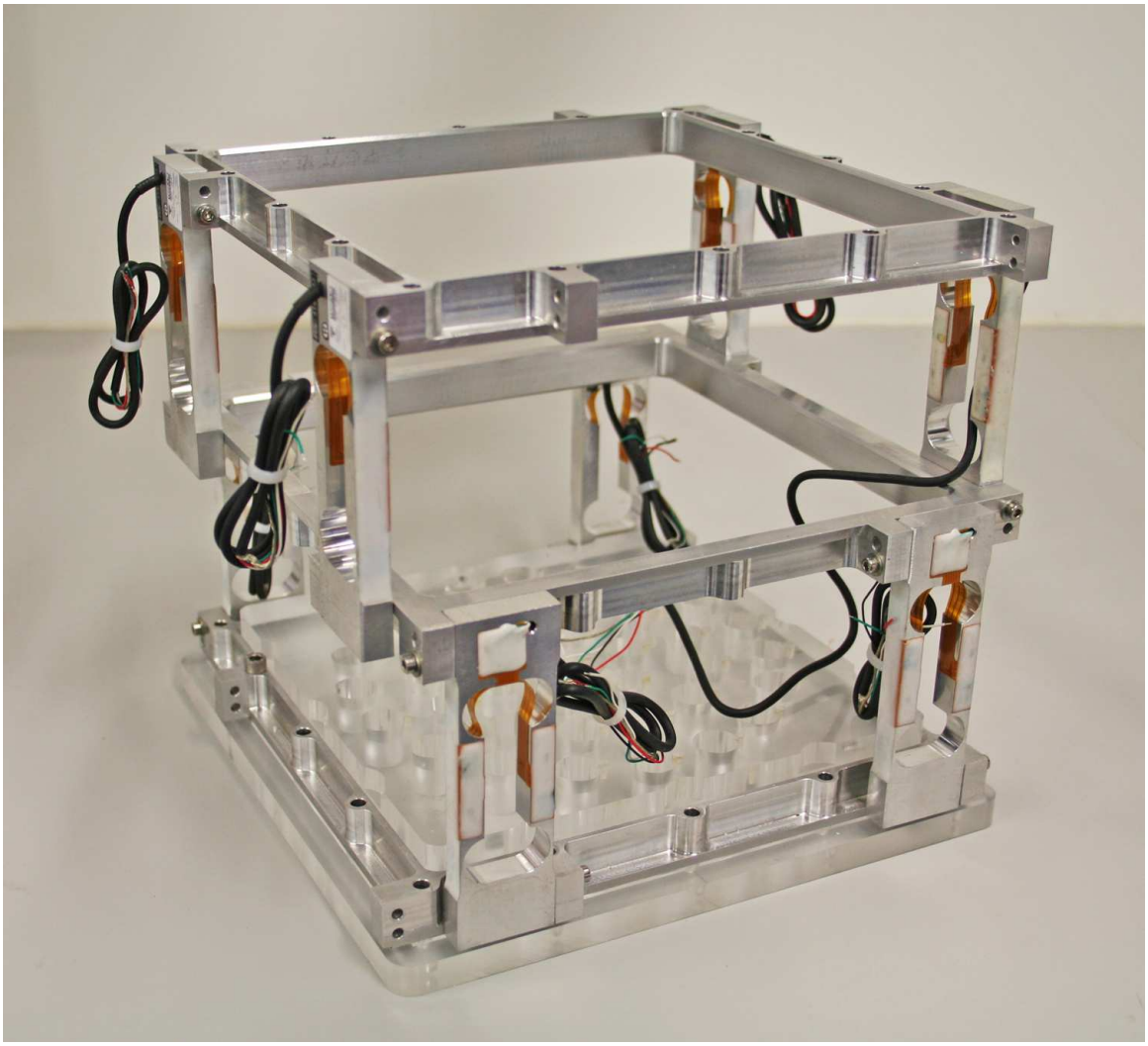

Figure 4.14: Photograph of the manufactured gantry used to hold and measure the total lift and drag on the group of single-end supported cylinders.

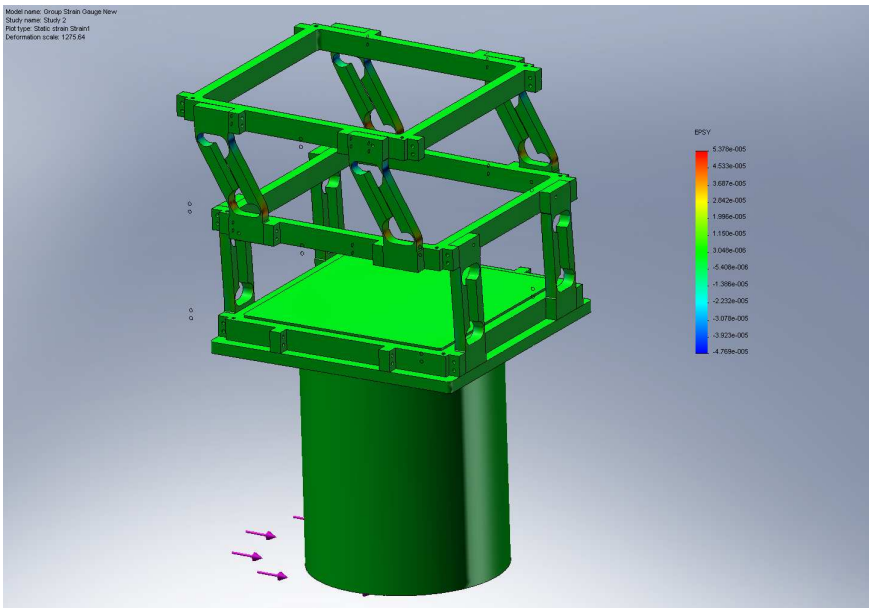

(a)

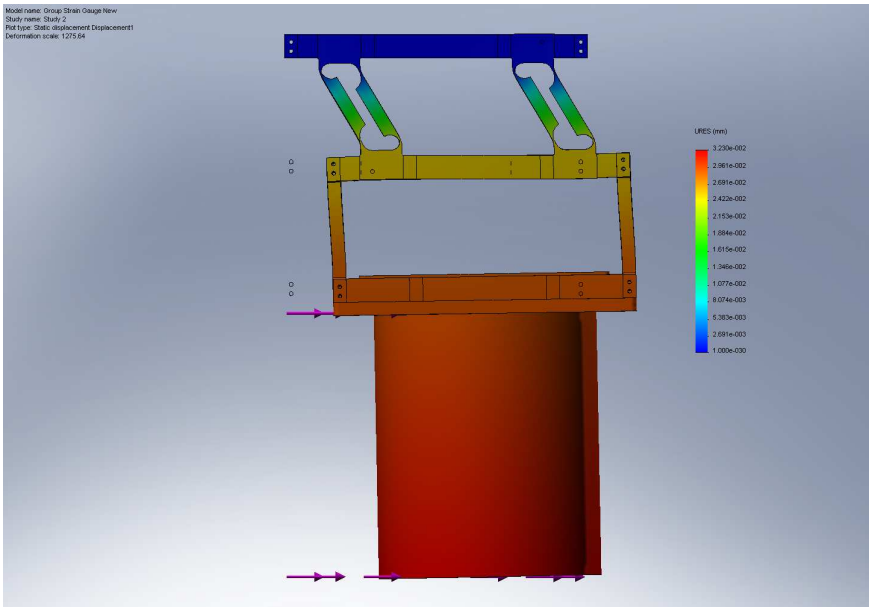

(b)

Figure 4.15: FEA results of the gantry system which is used to measure the total force on the group of bodies. The applied force is one direction. (a) Shows the strain field and (b) the displacement field.

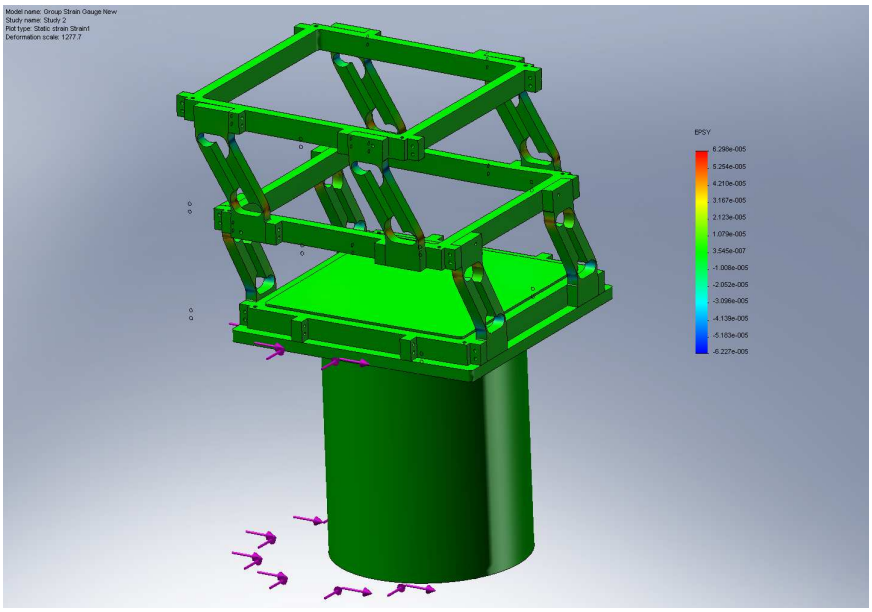

Figure 4.16: FEA results showing the displacement field of the support gantry which is forced in two directions. The displacements are magnified to enable the deformation of the instrumented cylinder to be seen.

2. Channel cross section was 39 times the cylinder diameter and workable channel dimensions were computed to be width 0.5 m and depth 0.2 m.

3. Head loss across the flume was not to exceed 3 m.

The final design of the flume shown in Appendix A.13 and Figure 4.17 is a three-dimensional isolinear view of the flume. The design incorporates a channel bridged between two settling tanks with an inline pump on the return pipework. The overall assembly is 5.8 m long, 1.6 m high with a minimum width of 2 m.

4.6.1 Turbulence Reduction

A key factor in the flume design was to reduce spatial gradients in the mean flow and flow unsteadiness or turbulence. Components within the design are labelled as shown in Figure 4.18. The in-line pump accelerated the flow through the return pipe to 4 m/s which was reduced to the channel velocity. This flow was also highly turbulent and required settling before entering the test section. The pump, while being controllable,

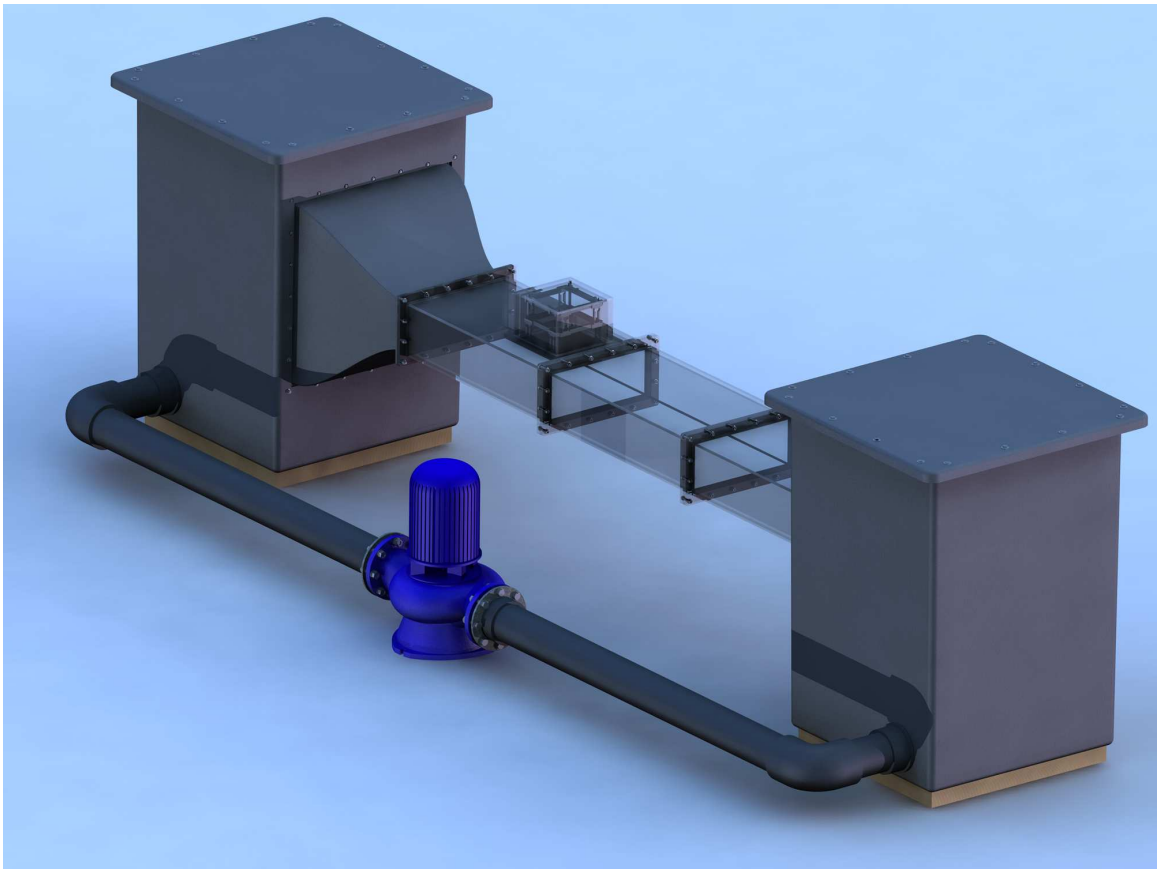

Figure 4.17: CAD image showing the entire flume configuration, including the instrumented array (see labels on Figure 4.18).

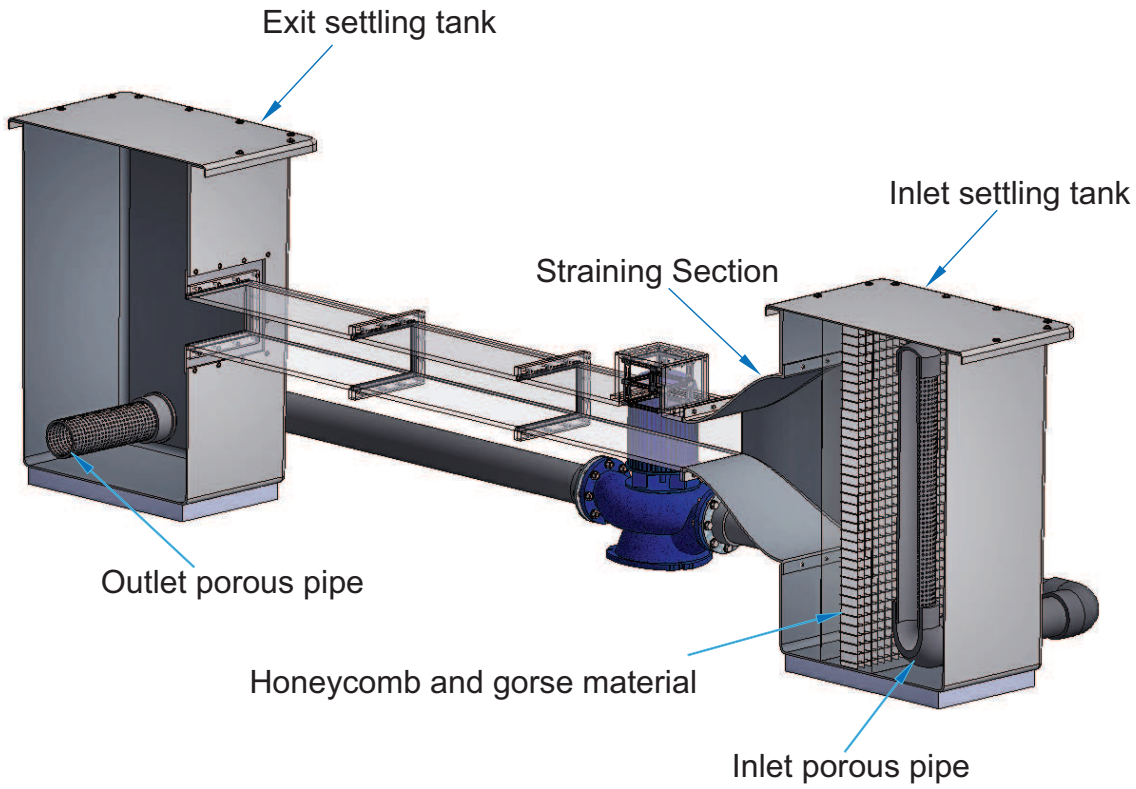

Figure 4.18: CAD drawing of the flume showing the turbulence reduction stages.

inevitably caused slight fluctuations in the flow rate which needed to be smoothed. To address this, settling sections were needed at each end of the tank. The structure was joined with high tolerances in order to prevent turbulence in the channel through misalignment. The tanks were supported on metal frames allowing their height and angle to be slightly adjusted, compensating for unevenness in the floor in the Fluids Laboratory.

Turbulence reduction was achieved in stages. Settling sections are normally staged to slowly degrade turbulence. Firstly, large-scale turbulence was removed using a porous inlet pipe which evenly introduced flow into the settling tank. The settling tanks slowed the flow, acting like a diverging section. The larger the tank, the lower the flow rate achieved in the tank. The size of the settling tanks was, however, limited by available space. Dimensions chosen were 1 m $\times$ 1 m $\times$ 1.5 m high. This height enabled the flume to be sufficiently suspended above the floor to allow optimal access from all sides.

To make the source settling tank more effective, a honeycomb structure was positioned across the central region, made from PVC Coroflute, with 4 mm channels. The thickness of the honeycomb structure was chosen to be 200 mm and again this was limited by cost. To accelerate the flow between the settling tank and the test section, a converging section was used, which reduces to the width and depth of the flume. This had two effects – it evenly accelerated the flow as it entered the channel and it elongated any small-scale turbulence, causing it to dissipate. This section had a complex three-dimensional shape which was accurately produced using CNC. This former was used to construct a moulding plug which could then be fibre-glassed forming a smooth interior surface for the straining section. The designs for this are shown in Figure 4.19b.

4.6.2 Channel design

The dimensions of the channel are set as stated above. The channel section is illustrated in Figure 4.19a. The channel was split into three 1 m long sections which could be bolted together. It was constructed from 20 mm acrylic sheet and, to ensure accurate flange jointing and uniform flow, the edges were CNC milled with grooved jointing.

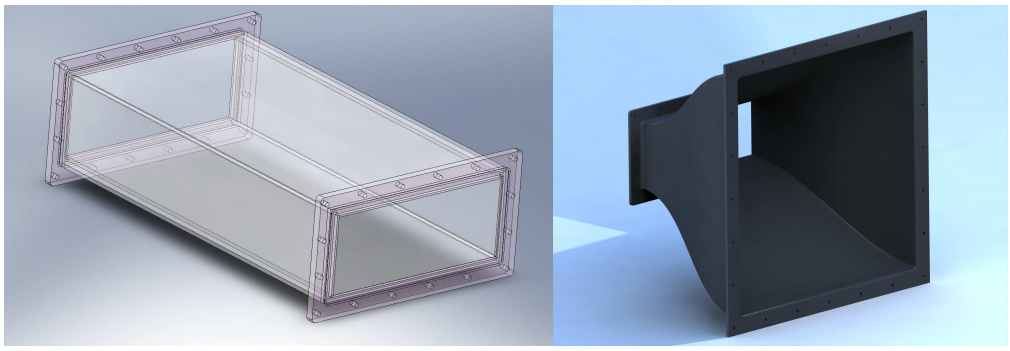

(a) (b)

Figure 4.19: CAD images showing the structural elements of the flume. (a) is the horizontal channel section and (b) the straining inlet section.

Typically, flumes have a free surface which allows easy access to the flume channel. However, this normally results in the free surface interacting with the experiments. It is not useful here to have any free surface as this is just a complicating factor, which requires taking account of channel flow profile changes. Additionally, the cylinders were required to imitate infinitely long cylinders so both the top and bottom edges of the cylinders were bounded. For this reason, an enclosed channel was more appropriate.

4.7 Data logging and electronic circuity

The challenge of this research was to log forces simultaneously on up to 40 discrete loaded elements, at sampling rates over 500 samples per second and where force values measured were so small that they were easily degraded by external electrical noise or mechanical vibration. The high sampling rates and the space constraints made it impossible to mount data logging equipment near the strain gauges for noise limitation.

Off the shelf data loggers also present problems (quite apart from cost) as most of these share a single ADC and rely on multiplex switching of the signal from different signal sources. This means that sampling rates achievable are, in practice, lower than those advertised or that there is inadequate time for electrical settling given the speed

of sampling.

The solution to address all these issues included measuring the forces using strain gauges in a full Wheatstone Bridge. This arrangement improved temperature and signal management. Dedicated 24 bit ADCs were set alongside each active Wheatstone Bridge, eliminating settling time constraints and minimizing electrical noise, as the ADC was integrated into the instrumented cylinder right next to the strain gauges.

With so many channels of source data and the irregular sampling periods, logging and handling the data was a key consideration. In raw data terms, 120 kb of data was collected, every second equating to 20000 samples per second. To achieve this a PIC micro-controller with a dedicated USB bus was programmed to collect from each ADC buffer when ready, storing and time stamping the data locally on a one gig flash memory chip. This was then loaded back across the USB to the host computer for long term storage.

4.8 Conclusion

A detailed assessment of the existing facilities in the Fluids Laboratory showed that modification and use of the available wind tunnels or flumes to undertake the experimental study proposed in Chapter 1 was not practical. The main factors governing this decision were controllability (of the flow and level of turbulence) and accessibility (optical access and time). This chapter has described the procedure for designing a new flume facility to undertake a specific detailed study of the forces and flows around collections of bodies (see Figure 4.17 and Appendix A.13).

The design criteria were set to satisfy a specified range of Re, cross sectional geometry of the bodies and the shape of the groups of bodies. Along with these fixed criteria, the incident flow was required to have a very low level of turbulence. The first step was to choose a suitable pump and controller. The loading on the pump was calculated using a commercial CFD package (Fluent) which uses a parameterization for the turbulence so that the pressure drop across the flume could be estimated. The additional component from the pipework was obtained from the manufacturer's catalogue. Calculations showed that cavitation on the impeller blade was not likely to

occur. The maximum pump volume flux and highest *Re* criterion enabled the channel width to be determined. Geometrical constraints enabled the cylinder diameter to be calculated. The flume was powered by a single three phase 5.5 kW Lowrana pump which circulated water between the two GRP settling tanks via 150 mm ABS pipe. Inside the source tank, a honeycomb structure reduced large-scale turbulence. A straining section was employed to accelerate the flow into the 0.5 m wide and 0.2 m deep channel which was 3 m long and constructed of Perspex. The major limitation was space. The experiments needed to be contained within a closed space in order to enable its future use with laser diagnostics which precluded its installation in the main fluids area.

Two solutions were proposed for the instrumented cylinders, either to be held at one or both ends. A stress/strain analysis of the induced forces acting on an instrumented cylinder showed that the optimal fixing and sensing point would be at one end of the cylinder. Groups are based on 15 instrumented cylinders each with a dedicated integrated analogue to digital converter (ADC) which is connected to a microcontroller which allows real-time data logging into a 1GB SDM RAM. Additionally, depending on the grouping, there are up to 49 dummy cylinders which are not instrumented.

A major part of the effort in design was the instrumentation of the cylinders and group of cylinders, especially the electronic data retrieval. The final system which was designed involves simultaneous measurement for lift/drag on 15 instrumented cylinders at a resolution capable of measuring small forces induced at low Reynolds numbers, and at frequency high enough to capture vortex shedding ($\sim$ 200 Hz). A major factor in the experimental diagnostics was that the cylinders were quite closely placed and there were many of them. The only practical solution was to integrate the force sensors with the cylinders themselves, including the data acquisition devices. The strain-gauge signal was logged locally on a purpose-built integrated circuit consisting of an ADC connected to an external central processor which stores, time stamps and then transmits data to the external device. On completion of a sample period, time logged data can be read via a .net C# webform interface back into the PC for analysis.

The new aspects of this experimental design project are the ability to:

1. Rearrange bodies within a group.
2. Examine different group shapes.
3. Achieve simultaneous force measurements on individual and total drag on large collections of bodies in a group.
4. Create a controllable flume with data acquisition from a single access point.
5. Have an effective series of quietening sections for accurate flow control.

Most of the apparatus had to be constructed in the department. Measuring small fluctuating forces meant that high machining tolerances were specified for the experimental section. The electronics and interfacing software had to be individually designed and manufactured as part of this study, as the design is specific to the investigation. In Chapter 6, experimental results are described using this apparatus.

Chapter 5

Numerical Computations

5.1 Introduction

Previous numerical studies on inertial dominated flows past groups of rigid bodies have either concentrated on a small number of bodies (usually < 4) in an unbounded flow or used symmetry constraints for bounded flows, for example in heat exchangers. This chapter describes a numerical study of the flow and force induced on individual bodies, interacting in a well-defined large group and over a range of void fractions. The major computational challenge is the wide range of flow lengthscales that must be resolved, in the boundary layer, both close to the bodies and in the downstream wake. Numerically resolving both of these length scales requires considerable computational resources and explains the, hitherto, limited research in this area. However, recent increases in computer power and the availability of high performance clusters with low latency interconnects, now enables large scale, fully resolved computations to be undertaken. This investigation makes use of the new high performance supercomputer at University College London, called Legion, using purpose built code written for this problem (described in Chapter 3). This allows parallelized real solution time diagnostics on the entire flow field.

5.2 Problem definition

The key domain variable in this study was the void fraction (ϕ), for cylinders set in a circular array. Each array offered a different value of void fraction by increasing the number of cylinders, while fixing other parameters. Eight cases were investigated, consisting of six discrete arrays of cylinders and two control cases. The number of cases studied was limited by computational time (each case study took approximately $23,000$ processor hours). The manner in which the void fraction within the arrays was varied is discussed in §5.2.1.

The Reynolds number for the arrays was fixed at $Re_G = D_G U_\infty/\nu = 2100$, which corresponds to $Re = DU_\infty/\nu = 100$ for an isolated, individual cylinder, which is in the range where a von Karman street is generated. $Re = 100$ for the individual cylinders was chosen because previous work in Chapter 3 used this value for the validation of the numerical scheme and code, as well as mesh sensitivity evaluation.

This numerical investigation has allowed characterisation and quantification of the flow field, including the effect of blocking and straining between individual bodies and the overall contribution of these to the force on the flow (which induces a velocity deficit downstream of the group). The later part of the chapter is structured as follows. In §5.2, the numerical problem is defined in more detail, including mesh properties, run times and convergence properties. The diagnostic tools applied to interpret the numerical results are defined in §5.3. A mathematical model is described in §5.4 to provide a basis for comparison and interpretation of the numerical results. This model, proposed developed by Dr Ian Eames, is based on a linear superposition of the effect of many isolated bodies and included the additional effect of the wake and source terms, neglected in the earlier inviscid treatment of Eames *et al.* (2004). The numerical results are presented in §5.5, compared with the mathematical model and interpreted. Finally, §5.6 concludes this section.

5.2.1 Geometry

As already discussed, the array had the same circular geometry as its constituent bodies, namely that of a circular cylinder. Therefore, as the void fraction (ϕ) within the array approached unity, the geometry of the array became similar to or the same

as its constituent cylinders. The cylinder is a common geometry in engineering and has been well studied. It also allows resolution of the shedding of vortices, even for moderate Re.

To enable the void fraction to be varied over a significant range, the diameter of the array D_G was chosen to be considerably larger than the diameter of the constituent components D. The number of cylinders in the array was $N_C = \phi(D_G/D)^2$ and this increases significantly with D_G/D (for fixed ϕ). The intention was to limit computations to $N_C \sim 100$ and this required the ratio D_G/D to be about 20. To maintain an uniform void fraction throughout the array, cylinders were equally spaced from each other.

The array geometry of the eight test cases considered is shown in Figure 5.1 and they are referred to as C_1, C_7, C_{20}, C_{39}, C_{64}, C_{95}, C_{133} and C_{S1}, with the subscripts denoting the number of cylinders in each array.

In the investigated cases, the distribution of cylinders was not chosen to be random, as this could have had an undue bias on the results, when N_C was small. To maintain the overall circular array, cylinders were arranged in concentric rings (starting from the circumference of the array) and filling inwards, with an additional cylinder at the centre. The separation between the concentric rings and between the cylinders on each ring was the same. It can be seen in Figure 5.1 that the resultant geometries in the free stream direction were irregular (neither aligned nor staggered) due to the uneven number of cylinders in each concentric row. The specific choice of $D_G/D = 21$ for the numerical study was through the optimisation of the arrangements of cylinders in the arrays. In the experimental work, design and manufacturing constraints meant that D_G/D was limited to 13.

(C_1) determined properties of an individual cylinder of diameter D at $Re = 100$, using a mesh resolution determined from the mesh independence study in Chapter 3. This mesh resolution was shown to give an error no greater than 1.23% for $\langle C_L \rangle_{\max}$ and 0.08% for $\langle C_D \rangle$. The second control case (C_{S1}), employs a cylinder of diameter $D_G = 21D$, which corresponds to $Re_G = 2100$. The C_{S1} cylinder is used to compare with an array of bodies of the same diameter, when the void fraction of that array approaches 1.

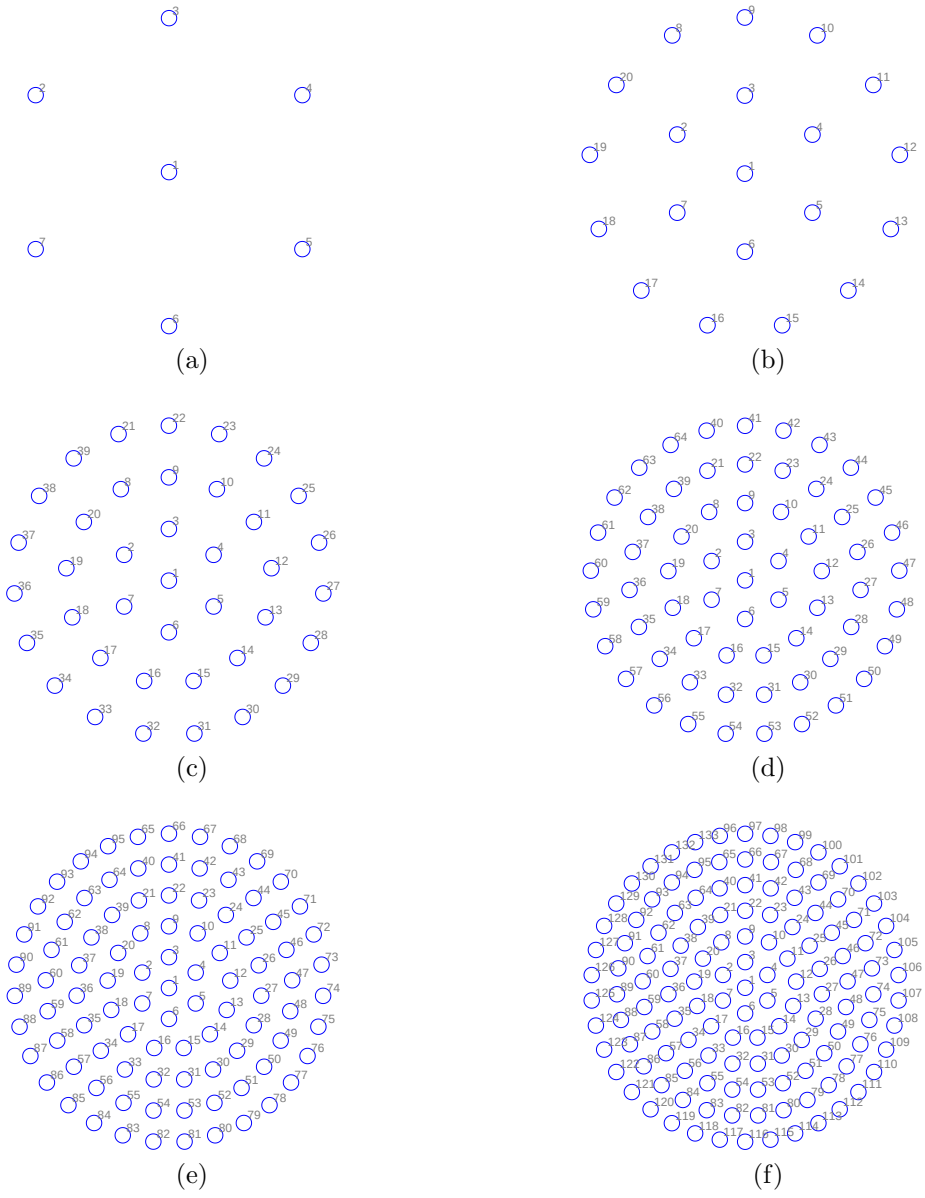

Figure 5.1: Cylinder configuration for cases (a) C_7, (b) C_{20}, (c) C_{39}, (d) C_{64}, (e) C_{95} and (f) C_{133}.

Case	C_1	C_7	C_{20}	C_{39}	C_{64}	C_{95}	C_{133}	C_{S1}
N_C	1	7	20	39	64	95	133	1
ϕ	0.0023	0.0159	0.0454	0.0884	0.1451	0.2154	0.3016	1
Rows	0	1	2	3	4	5	6	NA
Low resolution mesh								
Nodes	0.064m	0.098m	0.102m	0.101m	0.099m	0.096m	0.093m	0.130m
Elements	0.133m	0.201m	0.212m	0.215m	0.216m	0.217m	0.218m	0.270m
BL	$0.075D$							
CLS	$0.1D$							
DLS	$1.0D$							
FFLS	$4.0D$							
High resolution mesh								
Nodes	3.29m	3.73m	3.76m	3.76m	3.76m	3.75m	3.74m	3.34m
Elements	6.58m	7.48m	7.54m	7.53m	7.55m	7.54m	7.53m	6.68m
BL	$0.005D$							
CLS	$0.02D$							
DLS	$0.1D$							
FFLS	$3.0D$							

Table 5.1: Description of cylinder arrays investigated and information about mesh quality.

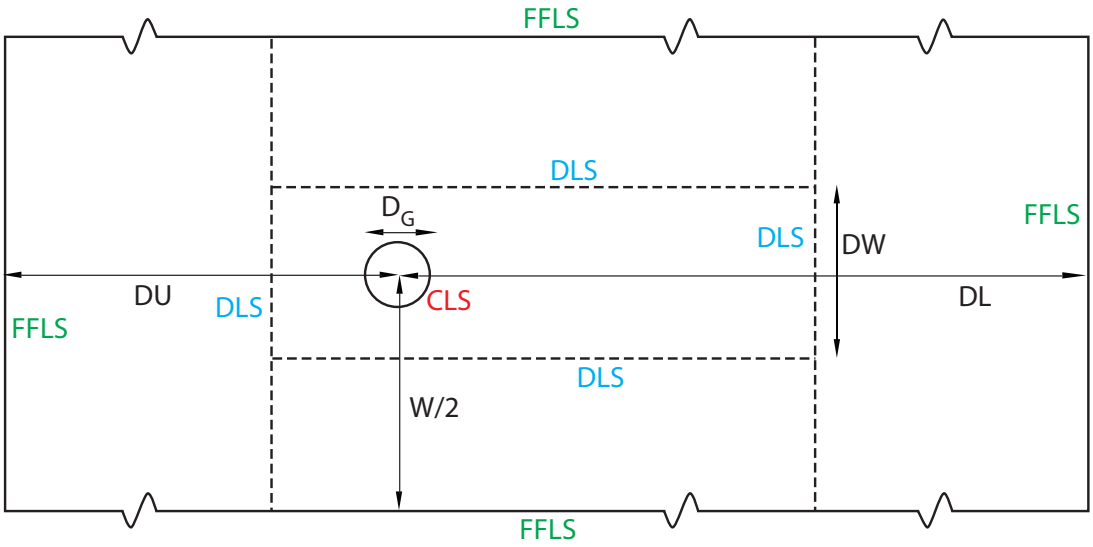

Figure 5.2: Schematic of the whole computational domain. The inlet is on the left-hand side of the domain. The dimensions are shown in Table 5.1.

The geometry of the outer computational domain had fixed shape, size and boundary conditions and is shown schematically in Figure 5.2. To reduce the influence of the inlet, outlet and wall effects, the array was centred a distance $950D$ ($45.2D_G$) from the inlet and on the centre-line of the channel. The channel had a width $W = 500D$ ($23.8D_G$) and channel length from the centre of the group to the channel outlet of $2500D$ ($119D_G$). The effective blocking ratio of array was less than $D_G/W = 0.042$. As discussed in Chapter 2, the blocking has a negligible effect on the calculated force and does not require numerical correction.

A no-slip boundary condition was applied on the surface of the cylinders. A shear free condition was applied on the sides of the channel walls ($u_2 = 0$ and $\partial u_1/\partial x_2 = 0$, where $x_2 = \pm W/2$). On the inlet boundary, $u_1 = U_\infty$, $u_2 = 0$ and the pressure was set to $p = 0$ on the outlet.

5.2.2 Mesh specification

The computational domain was meshed using Gmsh (see Chapter 3) which generates high quality, unstructured, triangular meshes, whose resolution is specified in the mesh script file. To prevent over-resolving the problem and increasing the run-time of

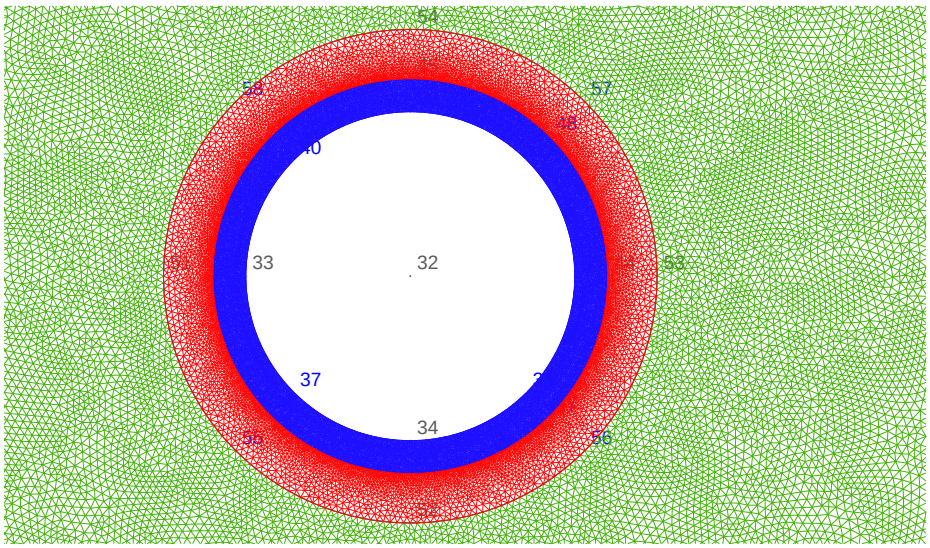

Figure 5.3: Local mesh around an individual cylinder showing the refinement regions. The blue region represents the mesh used in the boundary layer and the red is the region where the mesh stages up to the surrounding array region (shown in green).

the code, the mesh resolution was varied across the computational domain. Adjacent to the surface of the cylinders, the boundary layer must be fully resolved and the estimates in Chapter 3 provided an idea of mesh size (typically $0.005D$). In the range of Re_G considered, vortex shedding was evident and the slow decay of the shed vortices (from the array and individual cylinders) required the resolution to be maintained far downstream. Adjacent to the wake region and far upstream, the flow was irrotational, so that the gradient of the velocity was weak and, in this region, it was possible to use a much coarser mesh.

The computational mesh domain was, therefore, broken into three specific regions: (identified in Figure 5.2):

1. Diagnostic region: Most of the diagnostic analysis was done in this region. The mesh resolution was uniform in order to fully resolve the shear layer and shed vortices. The mesh length scale of this region is labelled, DLS.

2. Array region: This contains boundary layers that required the finest mesh used in the investigation and a gradual staging up to the surrounding array mesh resolution. This staging could be implemented using a gradient property (in Gmsh)

but this led to complications when dealing with different meshing boundaries within a group cylinders. To overcome this, two sub-regions were created around the cylinder, as illustrated in Figure 5.3. The first was the boundary layer (blue) of resolution length scale BL and the second (red) formed a transition to the surrounding area of length scale CLS. This maintained an even mesh resolution in the boundary layer and a uniform transition to open-stream flow.

3. Far-field region: In this region a primarily concern was with reducing the effect of the boundary blocking by displacing them as far away as necessary from the investigated region. As flow in these regions was uniform with only small fluctuations in any property, there was no need for a fine mesh. The mesh was gradually made coarser as it moved towards the domain boundaries, which have a length scale FFLS.

To allow initial testing of diagnostics and code, a low resolution mesh was produced for each test case. A summary of the high and low resolution meshes is presented in Table 5.1.

5.3 Diagnostics

The diagnostic tools needed to be defined at the outset due to the processing requirements. The scale of the computations meant that the diagnostics had to be computed on the supercomputer, in real time. A range of diagnostic tools were used which measured the forces on individual bodies as well as interpreted the near- and far-field components of the flow.

5.3.1 Flow diagnostics

To understand why the flow signature created by an individual body in the array decays quickly (either through local straining of the wake or wake intermingling), diagnostic tools need to be applied to distinguish between straining and vortical regions.

However, there are more comprehensive approaches, for instance those applied to turbulent flows that provide measures of the relative strength of the symmetric and non-symmetric components of the velocity gradient tensor defined by

$$\boldsymbol{\Sigma} = \frac{1}{2}(\nabla \boldsymbol{u} + (\nabla \boldsymbol{u})^T), \qquad \boldsymbol{\Omega} = \frac{1}{2}(\nabla \boldsymbol{u} - (\nabla \boldsymbol{u})^T). \tag{5.1}$$

For a two-dimensional flow, these tensors are explicitly defined by

$$\boldsymbol{\Sigma} = \begin{bmatrix} \frac{\partial u_1}{\partial x_1} & \frac{1}{2}(\frac{\partial u_1}{\partial x_2} + \frac{\partial u_2}{\partial x_1}) \\ \frac{1}{2}(\frac{\partial u_1}{\partial x_2} + \frac{\partial u_2}{\partial x_1}) & \frac{\partial u_2}{\partial x_2} \end{bmatrix}, \qquad \boldsymbol{\Omega} = \begin{bmatrix} 0 & -\frac{1}{2}\omega \\ -\frac{1}{2}\omega & 0 \end{bmatrix}. \tag{5.2}$$

A usual measure of the magnitude of these tensors is $||\Sigma||^2 = \Sigma_{ij}\Sigma_{ij}$ and $||\Omega||^2 = \Omega_{ij}\Omega_{ij}$. The second invariant of the velocity gradient tensor is

$$Q = \frac{1}{2}\left(||\Sigma||^2 - ||\Omega||^2\right). \tag{5.3}$$

Various measures have been proposed and are summarized in Jeong and Hussain [2006] to assess turbulent flows, including the sign of Q which signifies when local strain is larger than local vorticity. Truesdell [1955] has used

$$\frac{||\Omega||}{||\Sigma||}, \tag{5.4}$$

which is a measure of quality of rotation. The diagnostic used here is the dimensionless ratio

$$E = \frac{||\Sigma||^2 - ||\Omega||^2}{||\Sigma||^2 + ||\Omega||^2}. \tag{5.5}$$

From this definition, E is bounded between -1 and 1 (Davidson [2004, p. 41]). To understand this measure, three different flow fields are considered. For a local shearing flow parallel to the x_1-axis, $\boldsymbol{u} = (U_\infty + \alpha x_2, 0)$. The strain and rotation matrices are

$$\boldsymbol{\Sigma} = \begin{bmatrix} 0 & \alpha/2 \\ \alpha/2 & 0 \end{bmatrix}, \qquad \boldsymbol{\Omega} = \begin{bmatrix} 0 & \alpha/2 \\ -\alpha/2 & 0 \end{bmatrix}. \tag{5.6}$$

so that $E = 0$. For a vortical flow, the velocity field is $\boldsymbol{u} = (U_\infty - \alpha x_2, \alpha x_1)$. The strain and rotation matrices are

$$\boldsymbol{\Sigma} = \begin{bmatrix} 0 & 0 \\ 0 & 0 \end{bmatrix}, \qquad \boldsymbol{\Omega} = \begin{bmatrix} 0 & \alpha \\ \alpha & 0 \end{bmatrix}, \tag{5.7}$$

so that $E = -1$. For an irrotational flow, (expressed in terms of a velocity potential ϕ as $\boldsymbol{u} = \nabla\phi$), then $\boldsymbol{\Omega} = \mathbf{0}$ and $E \equiv 1$. It is also clear that when $E = 1$, then from the definition (5.5), $\boldsymbol{\Omega} = \mathbf{0}$ and the flow is irrotational.

5.3.2 Force diagnostics

The drag and lift forces on an individual body are usually expressed in terms of the local velocity, as if the body was not present. Since there are a large number of cylinders, the flow in the vicinity of an individual cylinder is not uniform and, indeed, may vary with time. It is, therefore, more relevant to define the lift and drag coefficients, in relation to the flow incident on the array U_∞. The drag and lift coefficients characterising the force on the i-th cylinder ($1 \leq i \leq N_C$) are defined by

$$C_{Di}(t) = \frac{\boldsymbol{F}_i \cdot \hat{\boldsymbol{x}}_1}{\frac{1}{2}\rho D U_\infty^2}, \quad C_{Li}(t) = \frac{\boldsymbol{F}_i \cdot \hat{\boldsymbol{x}}_2}{\frac{1}{2}\rho D U_\infty^2}, \tag{5.8}$$

where the force on the i-th cylinder is

$$\boldsymbol{F}_i = \int_{S_b} (p\boldsymbol{I} - \boldsymbol{\tau}) \cdot \hat{\boldsymbol{n}} \mathrm{d}S. \tag{5.9}$$

From (5.8), time averaged drag coefficient for an individual cylinder over a long period T from an initial time t_0 is defined by

$$\langle C_{Di} \rangle = \frac{1}{T} \int_{t_0}^{T+t_0} C_{Di} \mathrm{d}t. \tag{5.10}$$

The average maximum lift coefficient, $\langle C_{Li} \rangle_{\max}$ (over a period from t_0 to $T + t_0$) is obtained by averaging the local maximum of the lift coefficient over the number of cycles.

The drag and lift coefficients of the array are defined as

$$C_{DG}(t) = \frac{\sum_{i=1}^{N_C} \boldsymbol{F}_i \cdot \hat{\boldsymbol{x}}_1}{\frac{1}{2}\rho U_\infty^2 D_G}, \qquad C_{LG}(t) = \frac{\sum_{i=1}^{N_C} \boldsymbol{F}_i \cdot \hat{\boldsymbol{x}}_2}{\frac{1}{2}\rho U_\infty^2 D_G}, \tag{5.11}$$

where D_G is the array diameter. From (5.11), time averaged drag coefficient for the array is defined as

$$\langle C_{DG} \rangle = \frac{1}{T} \int_{t_0}^{T+t_0} C_{DG} \mathrm{d}t. \tag{5.12}$$

The average maximum lift coefficient, $\langle C_{LG} \rangle_{\max}$ (over a period from t_0 to $T + t_0$) is obtained by averaging the local maximum of the lift coefficient over the number of cycles.

5.3.3 Average Lagrangian and Eulerian velocity

Due to the unsteady nature of the velocity field, it is useful to visualize the flow domain using the averaged velocity field in the region of the array, which is defined in §2.5 as

$$\langle \boldsymbol{u} \rangle = \frac{1}{T} \int_{t_0}^{T+t_0} \boldsymbol{u} \mathrm{d}t, \tag{5.13}$$

where T is the period of time that includes all unsteady operating conditions. The period (T) was set on a case-by-case basis, taking into account both the eddy shedding cycle of the array and any additional cycles that effect the wake formation. In the computations, Δt varied with each time step, so that, computationally, the time average was computed by summing the vector array $(T\langle \boldsymbol{u} \rangle)(t + \delta t) = (T\langle \boldsymbol{u} \rangle)(t) + \delta t \boldsymbol{u}(t)$ over the period t_0 to $t_0 + T$. It is useful to discuss the value of T for each case individually:

1. C_1: Is characterised by a well-defined shedding frequency. To improve the accuracy of the averaging over time, T was chosen to be 13 oscillation cycles.

2. C_7 and C_{20}: Both cases exhibit an irregular lift force, as can be seen later in the chapter. However, over a long period of time ($T = 300D/U_\infty$), the lift force follows a recurring pattern. The data for this average velocity field compares well with data captured over a period $T = 600D/U_\infty$ velocity time steps, with a deviation of less than $0.001U_\infty$. Therefore, ($T = 300D/U_\infty$) was used.

3. C_{39} and C_{64}: The flow near the array is particularly stable and a shorter time frame is required to produce a deviation of less than $0.001U_\infty$. In these cases,

$T = 100D/U_\infty$ was used.

4. Cases C_{95} and C_{133}: These have regular, periodic and large velocity fluctuations in the flow field. To allow for this, T was set to 20 lift oscillations.

5. C_{S1}: This has large velocity fluctuations in the flow field. However, the lift force does not oscillate uniformly. It has a slight secondary oscillation resulting in a positive/negative bias which oscillates at a 1/20 of the frequency of the vortex shedding. To allow for this, T was set to 100 lift oscillations.

The streamlines through the array were calculated by releasing $N_p = 10^3$ marked fluid elements (from x_{1k}, x_{2k}, where $k = 1, ..., N_p$) at a distance $\frac{1}{2}D_G + D$ from the origin of the array and integrating the coupled equations

$$\frac{\mathrm{d}x_{1k}}{\mathrm{d}t} = \langle u_1 \rangle (x_{1k}, x_{2k}), \qquad \frac{\mathrm{d}x_{2k}}{\mathrm{d}t} = \langle u_2 \rangle (x_{1k}, x_{2k}), \tag{5.14}$$

with respect to time. The initial positions of the particles are

$$x_{1k} = (D_G/2 + D) \cos \frac{2\pi k}{N_p}, \qquad x_{2k} = (D_G/2 + D) \sin \frac{2\pi k}{N_p}. \tag{5.15}$$

The history of the particle positions $(x_{1k}(t), x_{2k}(t))$ gives the streamline through the average velocity field. The second piece of information which is tracked is the time it takes for the fluid elements to be advected through the array (T_k), measured from when they are within a distance $D_G/2$ from the origin to when they leave the array. In addition, the entry and exit points of the fluid elements are stored, providing the horizontal distance L_k. The fluid elements were released outside the array to prevent any local bias caused by their release in the boundary layer of the constituent cylinders. Following the definition of Eames et al. [2007], the Lagrangian average horizontal velocity of a fluid element is L_k/T_k, where the integration is over the space between the cylinders. The placement of the release point of the fluid elements was close to the array, so a large fraction passed through, but some proportion did not and were ignored. The horizontal Lagrangian velocity is defined by

$$\langle u_1 \rangle_L = \left\langle \frac{L_k}{T_k} \right\rangle, \tag{5.16}$$

where the average is taken over the fluid elements which enter the array (Eames et al. [2004]).

The Eulerian average velocity is the spatial average of the velocity field over the array of bodies (Eames et al. [2004]) defined as

$$\langle u_1 \rangle_E = \frac{1}{V(1-\phi)} \int_{V-V_b} \langle u_1 \rangle \mathrm{d}V. \tag{5.17}$$

This is calculated from the average velocity field within the circular perimeter formed around the array. Numerically, the Eulerian average velocity is calculated for each triangular element within the perimeter and its contribution scaled by its area:

$$\langle u_1 \rangle_E = \frac{\sum_{e \in V-V_b} \frac{1}{3}(u_{1i} + u_{1j} + u_{1k}) A_e}{\sum_{e \in V-V_b} A_e}, \tag{5.18}$$

where the sum is over all the elements (e) within the region $V - V_b$.

5.3.4 Maximum vorticity

The rate of vorticity annihilation is a feature of a body's wake and is measured along the x_1-axis. Upstream of the body, vorticity is $\omega \approx 0$ and, therefore, only measured between $x_1 = 10.5D$ and $x_1 = 1000D$. Vorticity is unevenly shed in x_2-axis and time t and therefore:

$$\Omega_{max}(x_1) = \max_{\substack{|x_2| < 125D \\ 0 < t < T}} \left| \omega(x_1, x_2, t) \right|. \tag{5.19}$$

5.4 Mathematical model

A mathematical model was developed to provide a framework to interpret the numerical results. The basis of the model is a linear superposition of the effect of blocking, drag and downstream velocity deficit on the ambient flow. Since there are no dynamics in this model, the flow field is steady. The numerically calculated average drag forces are used to provide a closure for certain terms (specifically the force term and the velocity deficit).

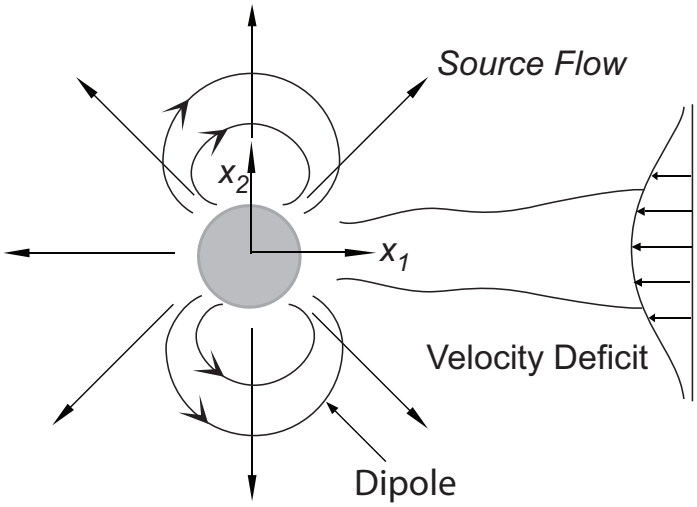

Figure 5.4: Schematic of the steady unbounded flow past a rigid body.

5.4.1 Flow field

As shown in Figure 5.4, the steady flow past an isolated body, located at the origin, can be modelled (for laminar wakes) by summing the contributions from the incident uniform flow, dipole (blocking component), monopolar (wake source component) and the wake deficit:

$$\boldsymbol{u}(x_1,x_2) = \underbrace{U_\infty(1,0)\hat{\boldsymbol{x}}_1}_{\text{uniform}} + \underbrace{\frac{Q(x_1,x_2)}{2\pi(x_1^2+x_2^2)}}_{\text{source}} + \underbrace{\frac{\mu}{2\pi}\frac{(-x_1^2+x_2^2,-2x_1x_2)}{(x_1^2+x_2^2)^2}}_{\text{dipole}} \\ \underbrace{-(1,0)H(x_1)\frac{Q}{\sqrt{4\pi\nu x_1/U_\infty}}\exp\left(\frac{-x_2^2U_\infty}{4\nu x_1}\right)\hat{\boldsymbol{x}}_1}_{\text{wake}}\,. \quad (5.20)$$

The above contributions are well-known and for instance, are listed in Eames et al. [2007], as equations (7.4), (7.9a) and (7.9b).

The wake component is weighted with the heavyside step function, $H(x_1) = 0$ for $x_1 < 0$ and 1 for $x_1 > 0$. For an unbounded flow, the drag force on the body is related to the volume flux through:

$$Q = \frac{F_D}{\rho U_\infty} = \frac{1}{2}\langle C_D \rangle DU_\infty, \tag{5.21}$$

([Batchelor, 1967, p. 351], equation 5.12.15). The dipole moment is set to be equal to the inviscid value,

$$\mu = \frac{1}{2}U_\infty \pi D^2, \tag{5.22}$$

corresponding to a cylinder (e.g.from Eames et al. [2007, equation 7.9]). A first order analysis can be obtained by summing up the contributions from the bodies located at (x_{1i},x_{2i}) $(i = 1, ..., N_C)$.

$$\begin{aligned}\boldsymbol{u}(x_1,x_2) = \underbrace{U(1,0)\hat{\boldsymbol{x}}_1}_{\text{uniform}} + \sum_{i=1}^{N_C} \Bigg(& \underbrace{\frac{Q_i(x-x_i, x_2-x_{2i})}{2\pi((x_1-x_{1i})^2+(x_2-x_{2i})^2)}}_{\text{source}} \\ & + \underbrace{\frac{\mu_i}{2\pi}\frac{(-(x_1-x_{1i})^2+(x_2-x_{2i})^2, -2(x_1-x_{1i})(x_2-x_{2i}))}{((x_1-x_{1i})^2+(x_2-x_{2i})^2)^2}}_{\text{dipole}} \\ & \underbrace{-(1,0)H(x-x_i)\frac{Q_i}{\sqrt{4\pi\nu(x_1-x_{1i})/U_\infty}}\exp\left(\frac{-(x_2-x_{2i})^2U}{4\nu(x_1-x_{1i})}\right)\hat{\boldsymbol{x}}_1}_{\text{wake}} \Bigg),\end{aligned} \tag{5.23}$$

where

$$Q_i = \frac{1}{2}\langle C_{Di}\rangle DU_\infty, \tag{5.24}$$

the effect of the domain being bounded means that the integral of the velocity deficit across a streamline plane is zero. The monopolar contribution to the flow, decays slowly with the distance. The effect of the bounding channel walls was included, using conformal mapping. The superposition model can be applied to estimate the Eulerian averaged velocity within the array. From (5.17),

$$V(1-\phi)\langle u_1\rangle_E - V(1-\phi)U_\infty = \int_{V-V_b} (\langle u_1\rangle - U_\infty)\,\mathrm{d}V. \tag{5.25}$$

The right-hand side of (5.25) describes the integral over the fluid within the array and

this can be rewritten as the sum of the integral over the wake and non-wake region:

$$\int_{V-V_b} (\langle u_1 \rangle - U_\infty)\,\mathrm{d}V = \int_{in \quad wakes} (\langle u_1 \rangle - U_\infty)\mathrm{d}V + \int_{outside \quad wakes} (\langle u_1 \rangle - U_\infty)\,\mathrm{d}V. \tag{5.26}$$

The contribution to the integral over the wake regions from the i-th body is

$$\int_{in \quad wakes} (\langle u_1 \rangle - U_\infty)\mathrm{d}V = -\int_0^{L_{Wi}} Q_i \mathrm{d}x_1, \tag{5.27}$$

since from (2.23),

$$Q_i = \int_{wake} (U_\infty - \langle u_1 \rangle)\mathrm{d}x_2. \tag{5.28}$$

The length $L_{Wi} = \sqrt{D_G^2/4 + x_{2i}^2} - x_{1i}$ corresponds to the length of the wake within the array from the i-th body and is shown schematically in figure 5.5. The flow outside the individual wake regions is irrotational. The total contribution from the source flow terms is zero by cancellation between diametrically opposite cylinders within the array. Eames et al. [2004, equation 4.5] showed that, for an inviscid dipolar flow past an array of cylinders in a circular array,

$$V(1-\phi)\langle u_1 \rangle_E - V(1-\phi)U_\infty = 0. \tag{5.29}$$

Combining the above equations,

$$(1-\phi)\langle u_1 \rangle_E - (1-\phi)U_\infty = -\frac{\sum_{i=1}^{N_C} \int_0^{L_{Wi}} Q_i \mathrm{d}x_1}{V}. \tag{5.30}$$

The right-hand side expression can be written as

$$\frac{\sum_{i=1}^{N_C} \int_0^{L_{Wi}} Q_i \mathrm{d}x_1}{V} = \frac{N_C}{V}\overline{\int_0^{L_{Wi}} Q_i \mathrm{d}x_1} = \frac{\phi}{V_{bi}}\overline{\int_0^{L_{Wi}} Q_i \mathrm{d}x_1}, \tag{5.31}$$

where V_{bi} is the volume of an individual body in the array. This term was first identified in a study of interstitial velocity fields by Eames et al. [2007, equation

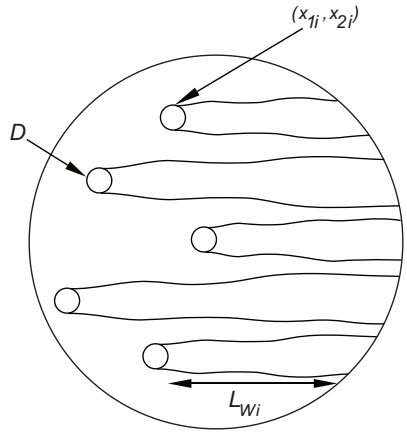

Figure 5.5: Schematic showing wake length in the array for a individual cylinder.

7.49]. From (5.20), Q_i is constant along the wake length so that

$$\frac{\sum_{i=1}^{N_C} \int_0^{L_{Wi}} Q_i \mathrm{d}x_1}{V} = \frac{\sum_{i=1}^{N_C} L_{Wi} Q_i}{V}. \tag{5.32}$$

In combination, an estimate of the Eulerian mean velocity within the array is

$$\frac{\langle u_1 \rangle_E}{U_\infty} = \frac{1 - \phi - \dfrac{\sum_{i=1}^{N_C} L_{Wi} Q_i}{V}}{1 - \phi}, \tag{5.33}$$

which can be evaluated numerically using results for Q_i and the cylinder positions. Eames et al. [2004] showed that for inviscid flow through a circular group of cylinders, the Lagrangian mean velocity is $\langle u_1 \rangle_L = (1 - \phi) U_\infty$, which is less than the Eulerian mean ($\langle u_1 \rangle = U_\infty$). The mean Lagrangian velocity was not calculated using the model of the flow (5.20) due to the complexity of tracking fluid elements along streamlines.

5.4.2 Vorticity field

A linearised analysis of the vorticity equation can provide insight into the physical processes that occur in the types of flow where the approximation of linearisation is invalid. The irrotation components of (5.20) do not contribute to the vorticity field. The vorticity field is dominated by cross-stream variations of the streamwise velocity in the wake region (*i.e.* $\omega \sim -\partial u_1/\partial x_2$). The vorticity field associated with (5.20) is

$$\omega(x_1, x_2) = H(x_1)\frac{QU_\infty x_2}{2\nu x_1}\left(\frac{U_\infty}{4\pi\nu x_1}\right)^{\frac{1}{2}} \exp\left(-\frac{U_\infty x_2^2}{4\nu x_1}\right). \tag{5.34}$$

The maximum vorticity magnitude occurs at a distance $x_2 = (2\nu x_1/U_\infty)^{\frac{1}{2}}$ from the centerline and is

$$\Omega_{max}(x_1) = (QU_\infty \exp(-1/2)/\sqrt{2\pi})/(2\nu x_1). \tag{5.35}$$

The interaction between the positive and negative components of vorticity leads to a x_1^{-1} decay of the maximum vorticity. This decays is rapid because opposite signed vorticity are intermingling and being annihilated (Hunt and Eames [2002]). Now proceeding to consider the interaction of the wake from the individual bodies. This is estimated by adding together the contributions from all the bodies to give

$$\omega(x_1, x_2) = \sum_{i=1}^{N_C} H(x_1 - x_{1i})\frac{Q_i U_\infty (x_2 - x_{2i})}{2\nu(x_1 - x_{1i})}\left(\frac{U_\infty}{4\pi\nu(x_1 - x_{1i})}\right)^{\frac{1}{2}} \exp\left(-\frac{U_\infty (x_2 - x_{2i})^2}{4\nu(x - x_i)}\right). \tag{5.36}$$

The above model is valid when the flow is steady. When discrete vortices are shed into the ambient fluid, the vortical lumps of positive and negative vorticity are well-separated so that vorticity annihilation does not occur. Instead, the vorticity decays slowly due to the growth of the size of the vortex patches. The circulation is $\Gamma = \lambda\Omega_m\pi R_p^2$, where R_p is the radius of the vortex patch. Since Γ is conserved, and R_p^2 increases linearly due to diffusion, then $\Omega_m \sim \Gamma/\lambda(R_{p0}^2 + 2\nu x_1/U_\infty)$, where R_{p0} is the initial radius of the patch. Even further downstream, the vortex patches intermingle when they have grown sufficiently with diffusion that they can interact. The vortices

are separated by a distance D. Beyond a downstream distance of $x_1 \approx D^2 U_\infty / \nu \approx DRe$, the vorticity field consists of positive and negative components adjacent to one another and vorticity annihilation.

5.5 Numerical results

Results for each diagnostic are presented, discussed and (where appropriate) compared with the mathematical model in the following order:

1. Forces acting on individual cylinders in the array are defined in §5.3.2. This is examined by case using scatter plots to show force magnitude and direction and discussed in §5.5.1.

2. Aggregate forces on an array are defined in §5.3.2 and discussed in §5.5.2.

   (a) Both time dependent and average approaches are tabulated and plotted on a case by case basis.

   (b) Scatter plots are used for visual comparison.

3. Observations of the flow field are defined in §5.3.1 and discussed in terms of

   (a) vorticity (§5.5.3),

   (b) straining (§5.5.4),

   (c) vortex structures identified by a ratio of vorticity to straining (§5.5.5).

4. Lagrangian and Eulerian average velocities are defined in §5.3.3. Comparison of numerical and mathematical velocity values for flows within the array's boundary are discussed in §5.5.6.

5. Upstream velocity reduction. Both numerical and mathematical models of the upstream region are irrotational and a maximum deficit plot is used for comparison. A velocity deficit plot is also included for each case. These are discussed in §5.5.7.

6. Decay of maximum vorticity is defined in §5.3.4. Vorticity decay in the wake is compared for each case and the mathematical model used to explain the mechanisms involved. These are shown in comparative plots and discussed in §5.5.8.

5.5.1 Forces acting on individual cylinders in the array

Lift and drag forces are stored, as a function of time, for individual cylinders. This aids the understanding of the importance of forces in different regions of the array. Presenting this data in a meaningful way can only be achieved graphically and, therefore, the approach used is a scatter plot for each individual cylinder within the array. This gives an indication of magnitude (when appropriately scaled), mean direction and, in the case of lift force, the range of angles of the lift force.

Figure 5.6 shows the force scatter plot for the six array cases. For comparison, in Figure 5.9, the same approach is presented for the control cases C_{S1} and C_1. The position and size of each cylinder is plotted in grey and the red region radiating from the centre of the cylinder is the scatter plot of the dimensionless force ($|\boldsymbol{F}|/\rho U_\infty^2 D$) on that cylinder. To allow comparison between all the cases, a red line is plotted for each scatter plot that shows the scale. The length of this line represents a drag coefficient of unity. In this discussion, when explicit reference is made to a specific cylinder, its label (C) is described, which is shown in Figure 5.1.

Discussion by case:

1. C_7 is shown in Figure 5.6a and shows a weakly interactive group of cylinders. The two cylinders that are upstream ($C = 2$ and 7) show force scatter plots similar to that seen for the isolated cylinder C_1, which was shown in Figure 5.9a. This is expected, as the subjecting flow was unobstructed and uniform, and the closest cylinder downstream was $10D$ away.

   The cylinders along the centre line of the array ($C = 1$, 3 and 6) again exhibit a similar magnitude of force to an isolated cylinder. The lift force fluctuation is, however, slightly greater, due to the proximity of these cylinders to the wake generated by the two upstream cylinders. Phase coupling is likely, as the upstream cylinder wake will be the dominant timing force.

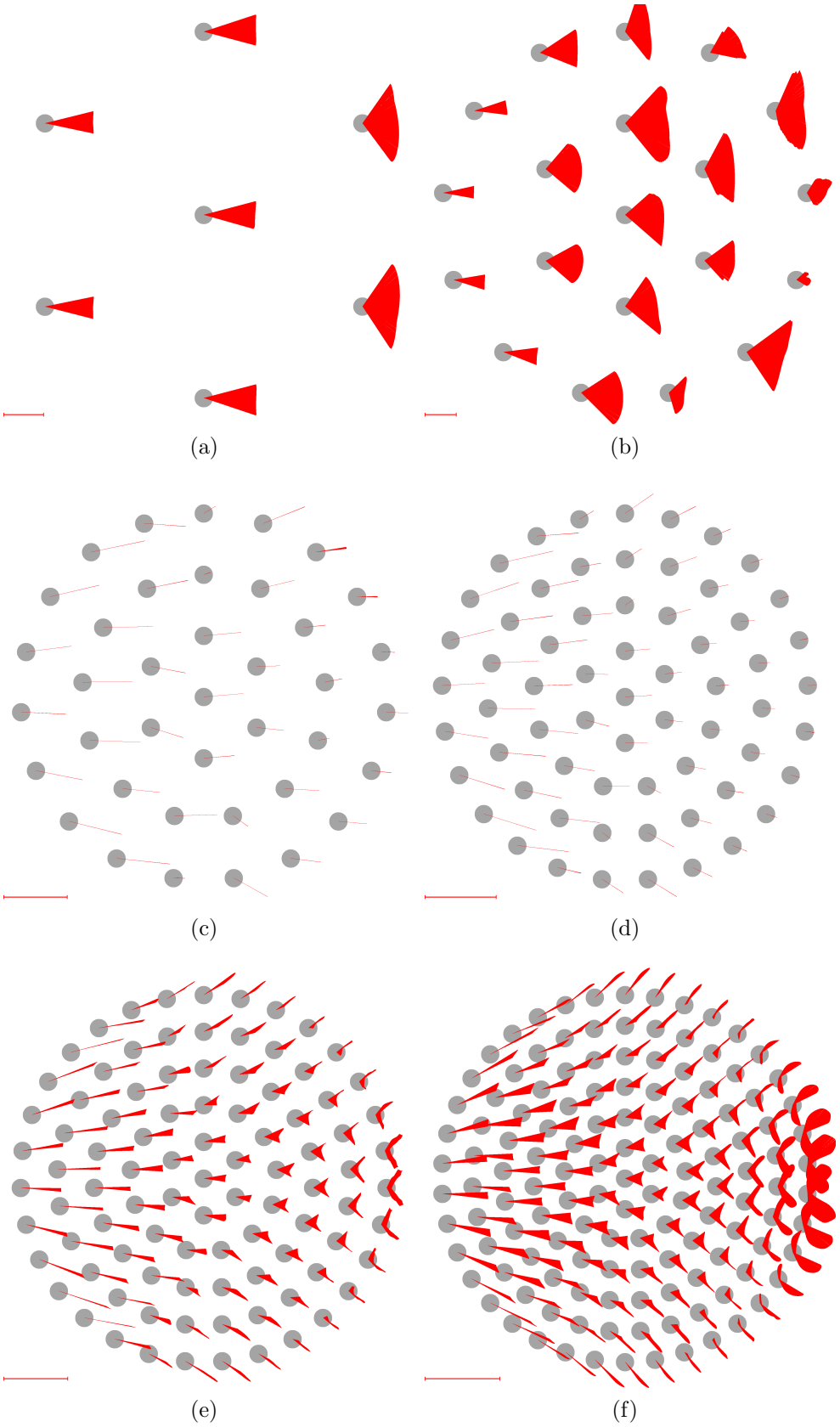

Figure 5.6: Diagram illustrating individual cylinder force scatter plots for cases (a) C_7, (b) C_{20}, (c) C_{39}, (d) C_{64}, (e) C_{95} and (f) C_{133}. The line bottom left indicates C_{DG} =unity

The two downstream cylinders ($C = 4$ and 5) exhibit an angular oscillation of more than double the magnitude seen with an isolated body. This is due to the fluctuating upstream cylinder wakes switching between states. The drag force magnitude on these cylinders is slightly reduced, influenced by their position in the wake of the upstream cylinders.

2. In C_{20} (Figure 5.6b), cylinders are far closer together and, therefore, the interactive forces are stronger. Upstream cylinders (those between $C = 17$ and $C = 20$) exhibit a drag force similar to that of an isolated body, but the lift force, while still relatively small, is determined by the position of the cylinders downstream.

   Those cylinders positioned downstream of other cylinders (ie across the middle of the array) experience larger drag and lift forces as a result of the accelerated flow induced between the upstream bodies. Cylinders are still far enough apart that vortex shedding occurs, even though this is strongly coupled in some cases.

   It should be noted that the entire array does not have a single small scale shedding frequency and, as discussed later, the overall array has a strongly suppressed group wake lift force.

3. In C_{39} and C_{64} (Figures 5.6c and 5.6d), the variation in the lift force, as a function of time, is extremely small. In effect, there is no lift force on either individual cylinders or on the group as a whole. The separation between the cylinders is small enough that vortex shedding is suppressed. The wake bubbles behind the cylinders are trapped. The mean flow through the array has been reduced below the critical value for wake shedding. Later discussion shows that the mean flow within the array is $\langle u_1 \rangle_E / U_\infty \sim 0.4 - 0.5$. The effective Re describing the flow past the individual cylinders is now $40 - 50$, sufficiently low that shedding does not occur (see discussion in Chapter 2 about flow regimes). The aggregate drag force on the array is dominated by the contributions from the first two rows of upstream cylinders. The force magnitude on each of these cylinders is comparable to that of a single cylinder. The mean force on each cylinder is primarily horizontal, indicating the flow is largely through the array, rather than around.

Case	C_1	C_7	C_{20}	C_{39}	C_{64}	C_{95}	C_{133}	C_{S1}
$\langle C_{Di} \rangle = \frac{\langle C_{DG} \rangle}{N_C}$	0.0619	0.0530	0.0408	0.0249	0.0173	0.0173	0.0133	*
$\langle C_{DG} \rangle$	0.0619	0.3707	0.8155	0.9694	1.1063	1.6460	1.7678	1.6497
$\langle C_{Li} \rangle_{max}$	0.0145	0.0065	0.0079	0.0001	0.0000	0.0038	0.0055	*
$\langle C_{LG} \rangle_{max}$	0.0145	0.0453	0.1581	0.0006	0.0000	0.3604	0.7278	1.7353
$\langle St_G \rangle$	3.5503	3.3695	2.8897	1.1297	0.0000	0.2542	0.2547	0.2430

Table 5.2: Summary of the drag and lift coefficient and metrics for the cases investigated.

4. In C_{95} and C_{133} (Figures 5.6e and 5.6f), the most pronounced effect seen is that the mean force on the upstream cylinders has a significant cross-stream component, indicating that the flow diverges, as it passes through the front of the array. The reduction in the streamwise force on the upstream portion of the array is due to significant blocking by the array, causing the incident flow to pass around it. The second interesting point is that the scatter plot of the force on the downstream cylinders has an unusual butterfly-wing shape. This is entirely due to the downstream influence of a recirculating wake (which is being shed) and switches between one state and another (ie being shed from the left / right sides of the array). The effect of increasing the void fraction (from C_{95} to C_{133}) leads to a slight increase in the scatter of the forces on the upstream cylinders and significantly increases the magnitude of the forces on the downstream cylinders. The scatter of the forces on the upstream cylinders increases because the wake is stronger and now has a greater influence on the flow past interior cylinders.

5.5.2 Aggregate force on an array

Figures 5.7a and 5.7b show the variation of the array drag and lift coefficients with time. Table 5.2 tabulates the average drag and lift coefficients, in addition to the Strouhal number St_G, defined in terms of the group diameter. These tabulated values of average drag and lift coefficients are also plotted in Figures 5.8a and 5.8b for all the cases, against void fraction. Additionally, to aid visualization, scatter plots are

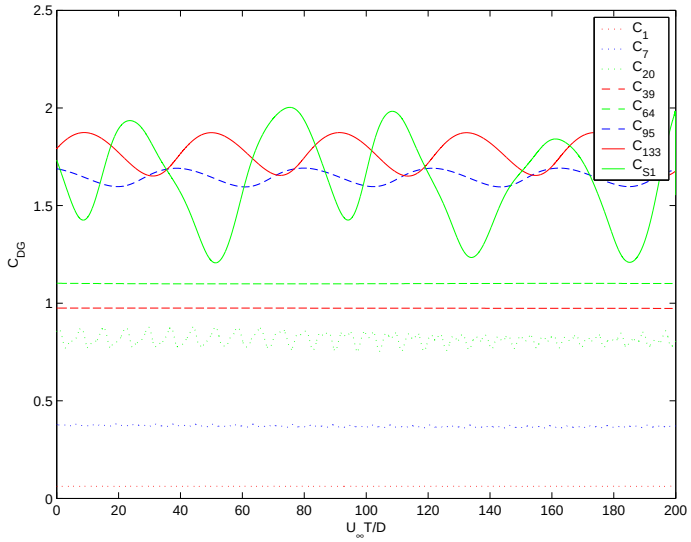

(a)

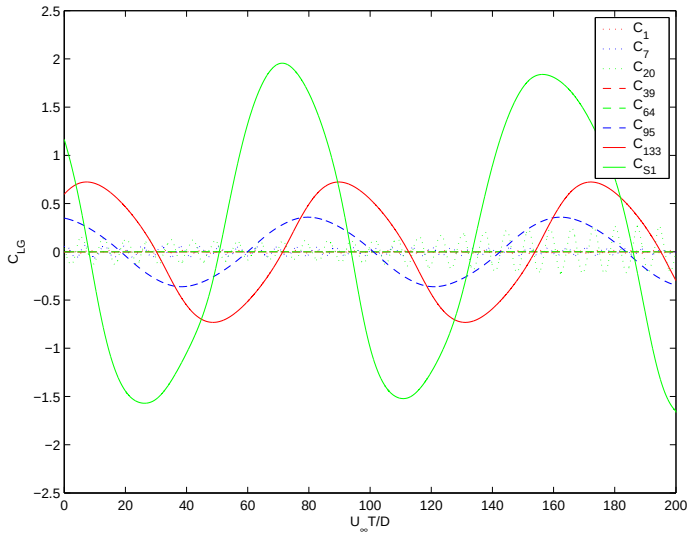

(b)

Figure 5.7: Variation of (a) $C_{DG}(t)$ and (b) $C_{LG}(t)$ with time after initial start-up.

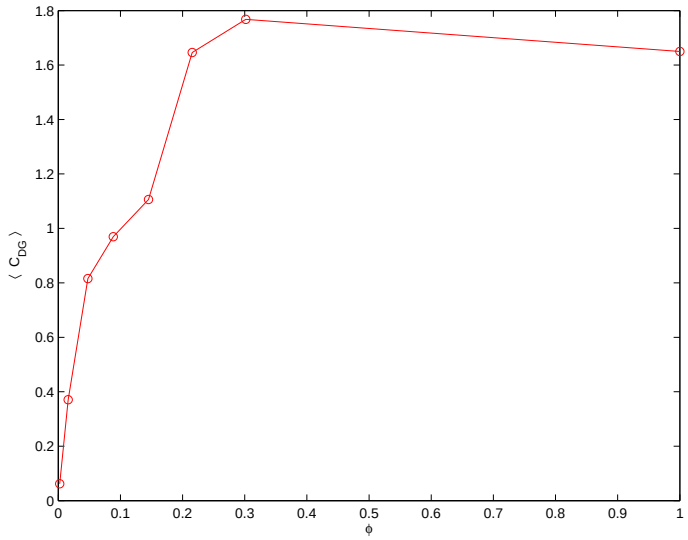

(a)

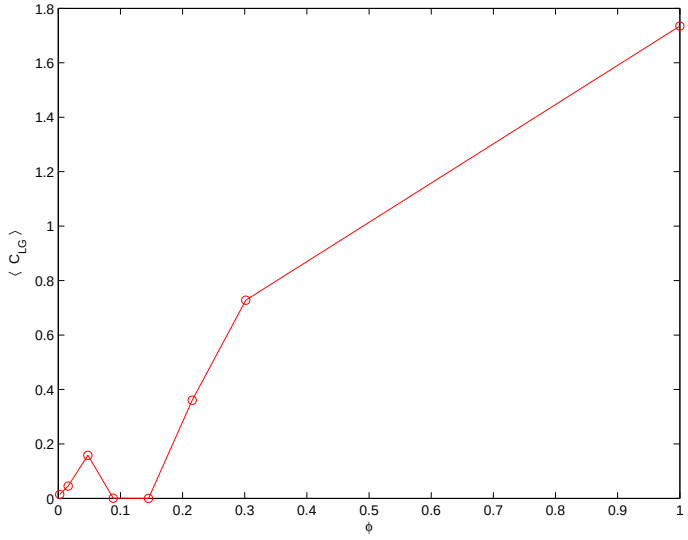

(b)

Figure 5.8: Variation of (a) $\langle C_{DG} \rangle$ and (b) $\langle C_{LG} \rangle_{max}$ with the void fraction (ϕ) within the array.

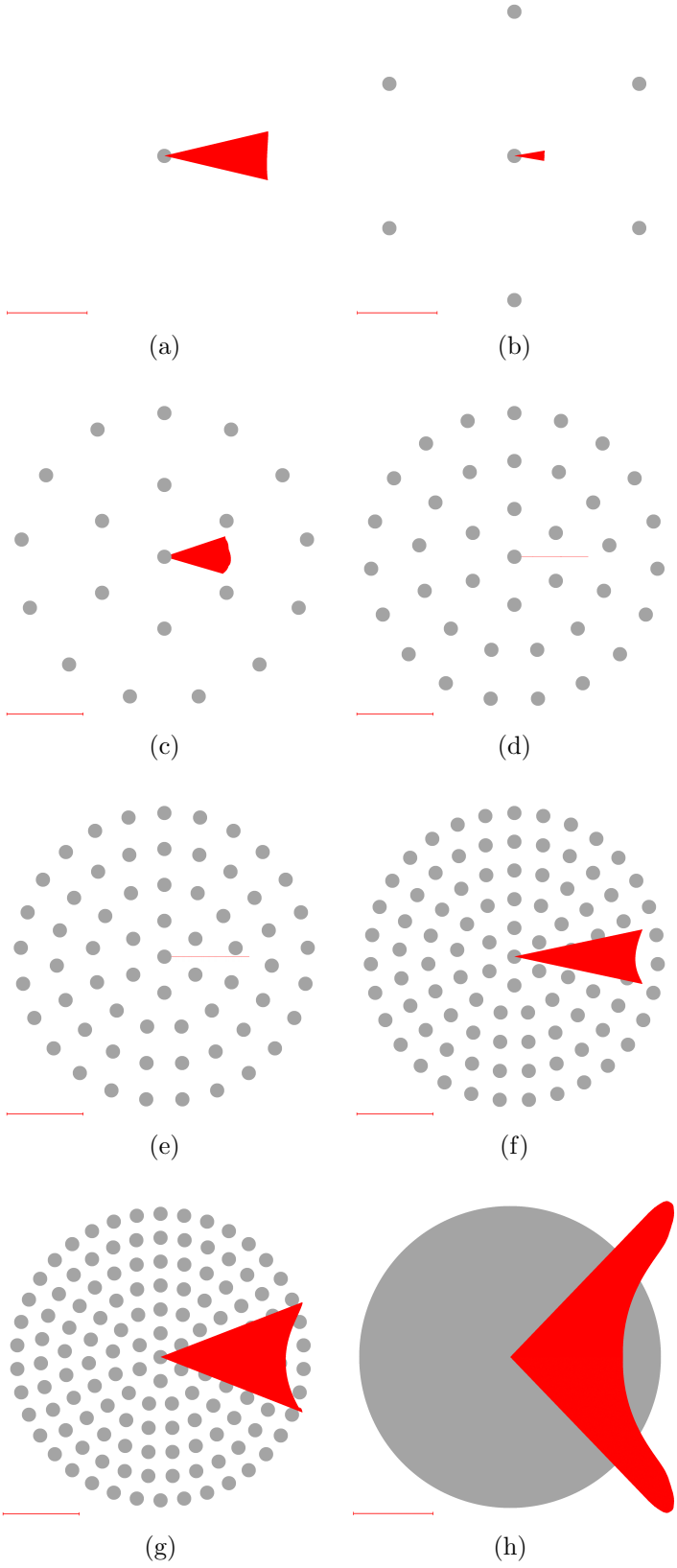

Figure 5.9: Diagram illustrating individual cylinder force scatter plots for cases (a) C_1, (b) C_7, (c) C_{20}, (d) C_{39}, (e) C_{64}, (f) C_{95}, (g) C_{133} and (h) C_{S1}.

used for the individual cylinders (Figure 5.9). To allow comparison between all the cases, a red line is plotted for each scatter plot that shows the scale. The length of this line represents a drag coefficient of unity.

The eight numerical investigations can be broken into three characteristic groups, each exhibiting similar group force behaviour. Each of the above groups are discussed further:

1. C_7 and C_{20} show loosely coupled arrays. There is no single dominant overall wake formation and the fluctuation in $C_{DG}(t)$ with time (Figure 5.7a) is very small, mainly caused by individual wake patterns coalescing at alternate frequencies. In Figure 5.7b, a very distinctive lift force perturbation can be identified which indicates two lift force mechanisms at work operating at different frequencies. In C_{20}, the overall group's lift force fluctuation is proportionately larger than that in C_7 (comparing in Figures 5.9b and 5.9c). While the group lift coefficient increases, the average lift coefficients in C_7 and C_{20} are comparable.

2. C_{39} and C_{64} show arrays with a stabilizing influence on the wake regime. The lift force on the entire array is zero and does not register in Figure 5.7b, while the drag force is steady (Figure 5.7a). The resultant scatter plots for C_{39} and C_{64} (Figures 5.9d and 5.9e) give single lines in the direction of the drag force which are almost parallel to the flow, save for the slight deviation caused by the lack of symmetry in the array geometry.

3. C_{95} and C_{133} show arrays where the void fraction is sufficiently high that the wake pattern begins to exhibit similar properties to those seen in the solid body C_{S1}. In both arrays, a clear uniform sinusoidal lift force can be seen (Figure 5.7b). The magnitude of this lift force increases with the void fraction towards that seen in C_{S1}. Neither, however, exhibits the same instability that was seen in the lift force in C_{S1}, where the magnitude of this fluctuated erratically by up to 50%. This erratic behaviour is also evident in the drag force for C_{S1} shown in Figure 5.7a. The drag force on C_{95} and C_{133} fluctuates at twice the frequency of the lift force but with a regular amplitude.

   The erratic behaviour seen in C_{S1} is a feature of two dimensional high Re cylinder flow and results from instabilities separating the boundary layer on

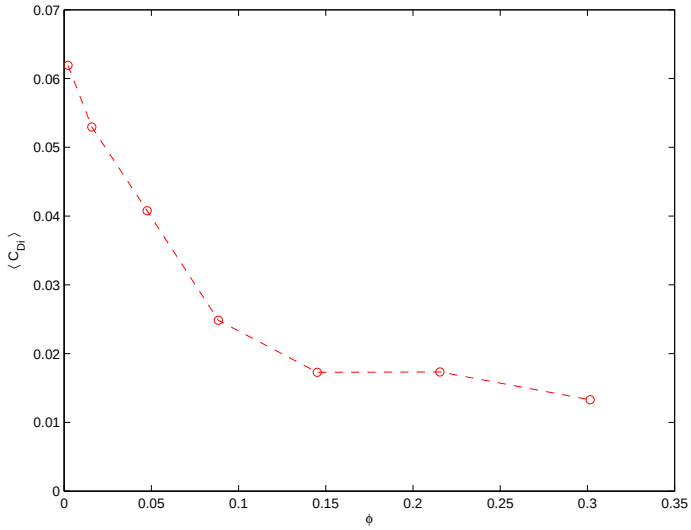

Figure 5.10: Individual cylinder drag force $\langle C_{Di} \rangle$ with ϕ.

the wall of C_{S1}. This obviously can not occur in C_{95} and C_{133} because of the absence on a unifying wall.

Figure 5.10 shows $\langle C_{Di} \rangle$ data from Table 5.2. $\langle C_{Di} \rangle$ can be seen to reduce rapidly with increase ϕ before stabilizing at higher ϕ. This reflects the difficulty in using the freestream (U_∞) when calculating the average $\langle C_{Di} \rangle$, as it would imply a contradiction with the more reliable information in Figure 5.8a.

In C_1, $St_G = 3.5503$ which, in the context of an isolated body $St = (D/D_G)St_G \sim 0.169$. This value compares well with published data presented in Figure 2.3. The St_G for C_7 and C_{20} is of similar magnitude which indicates that loosely coupled, low void fraction arrays, exhibit similar behaviour to their constituent bodies. C_{39} and C_{64} exhibit negligible lift and the St_G is insignificant. C_{95} and C_{133}, with unified wakes exhibit a St_G similar to that seen for C_{S1}. This reflects that high void fraction groups quickly come to represent a solid body.

5.5.3 Vorticity field

To provide a starting point to discuss the flow structures generated by the array, the instantaneous vorticity field is considered. From an analysis of the numerical results, the time-averaged vorticity field tended to smear out important information

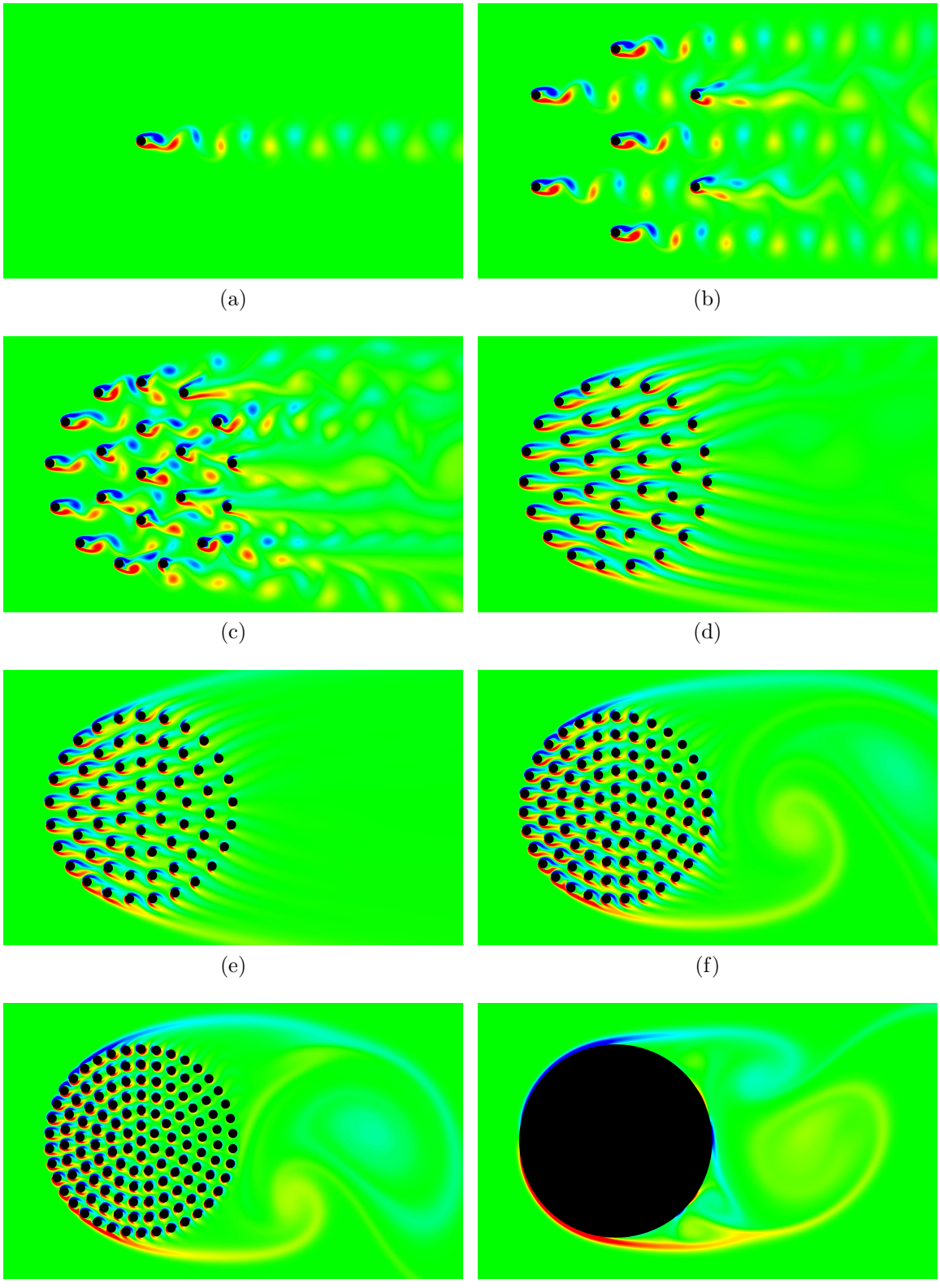

(a) (b) (c) (d) (e) (f) (g) (h)

Figure 5.11: Vorticity field for cases (a) C_1, (b) C_7, (c) C_{20}, (d) C_{39}, (e) C_{64}, (f) C_{95}, (g) C_{133} and (h) C_{S1}.

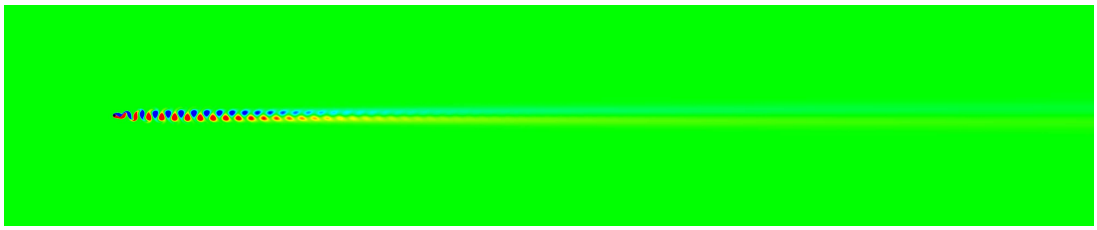

(a)

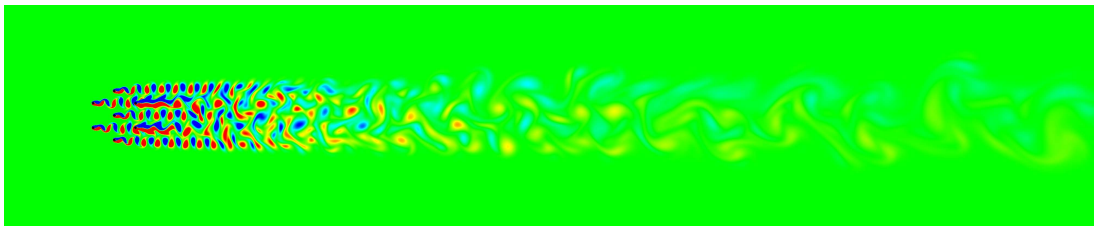

(b)

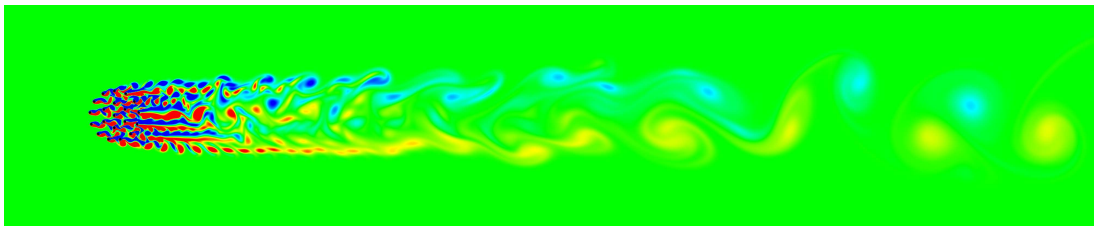

(c)

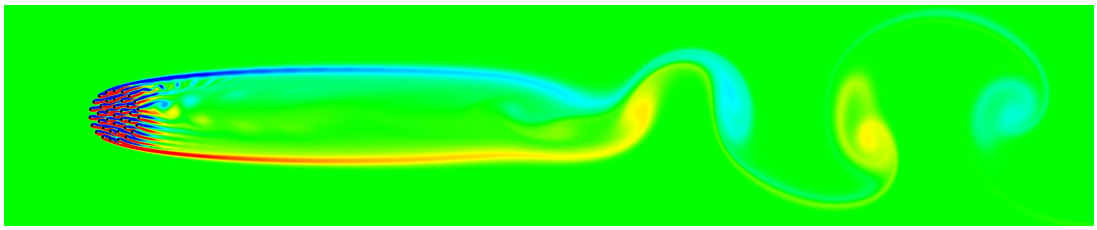

(d)

Figure 5.12: Vorticity field for cases (a) C_1, (b) C_7, (c) C_{20} and (d) C_{39}.

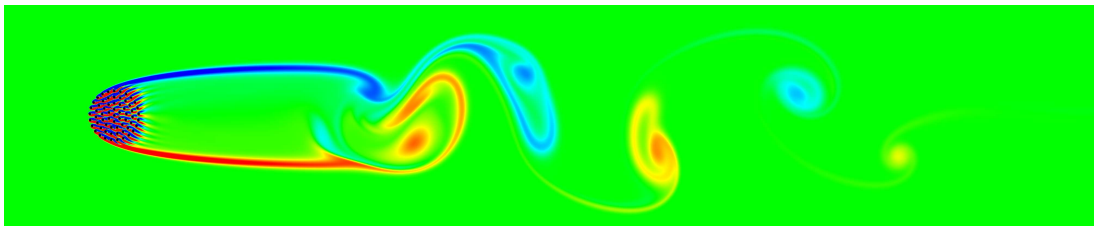

(e)

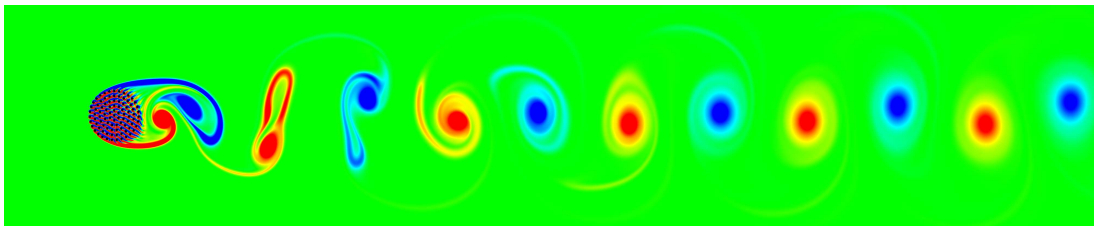

(f)

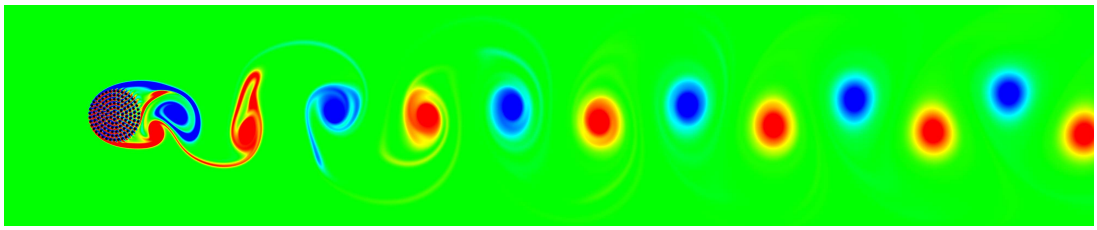

(g)

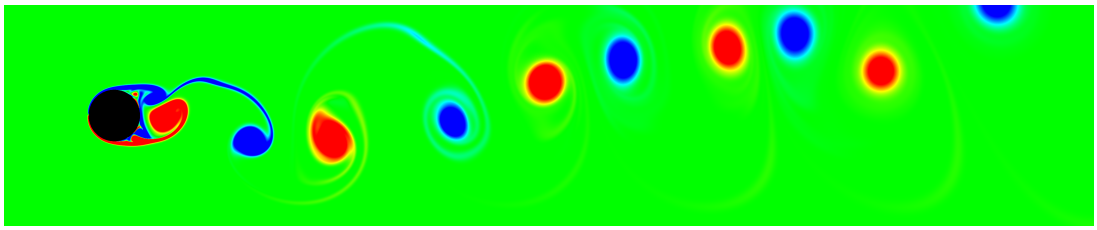

(h)

Figure 5.12: Vorticity field for cases (e) C_{64}, (f) C_{95}, (g) C_{133} and (h) C_{S1}.

about the structure of the flow, particularly the attached wakes. The action of a two-dimensional body in a uniform flow is to create a source and sink of vorticity, that has positive and negative components. Upstream of a rigid body in a uniform flow, the flow is irrotational. Unlike passive material, vorticity can be cancelled out if positive and negative components are brought together in equal measure. Two instantaneous vorticity plots are used for subsequent discussions about the vorticity field. Figure 5.11 shows the near-field in the region around the array to enable visualization of an individual body's vorticity. Figure 5.12 shows the far-field for discussion of the advection of vorticity downstream.

1. Case C_1: Close to the individual cylinder, positive and negative vortices are shed alternately and are then advected downstream. For this calculation, $Re = 100$, and the downstream calculations were extended sufficiently far downstream, that the vortices diffuse and finally generate a laminar planar wake. As can seen from Figure 5.11a, beyond a distance of $x_1/D \sim Re = 100$, the coherent and distinct lumps of positive and negative vorticity are lost and then consist of strips of positive and negative vorticity adjacent to one another.

2. Cases C_7 and C_{20}: Vortices are shed from each cylinder and advected downstream in a region of width D_G. The individual vortices shed by each cylinder merge and rapidly cancel, broadly over the same distance as in C_1. Beyond a distance of 500D, the vorticity appears to organise into coherent lumps of positive and negative vorticity.

3. Cases C_{39} to C_{64}: The vorticity field outside the array is characterised by two intense stable vortex sheets (of opposite sign). Beyond a critical distance downstream, the street is unstable and a von Karman vortex street is created further beyond this. The critical distance seems to be determined by the blocking effect arising from the void fraction of the array and can be seen to reduce for higher ϕ. While the vorticity created by the individual cylinders is intense, their vorticity signature does not survive as the flow passes through the array and is rapidly attenuated. This local mechanism is likely to be due to vorticity annihilation caused by wake interactions (see Hunt & Eames 2004).

4. Cases: C_{95} to C_{S1}: C_{95} and C_{133} have sufficiently high void fractions that the detached vortex layers become unstable immediately behind the array, in the same manner as seen in C_{S1}. This results in a very close region of vorticity behind the array, which totally dominates any vorticity generated within the arrays (in C_{95} and C_{133}). The areas of vorticity behind the arrays become so strong relative to the base bleed flow that they result in an almost negligible horizontal flux from within the arrays, due to the suction of material into this region. The formation of positive/negative vorticity lumps, behind the arrays in C_{95} and C_{133}, becomes more rapid between cases as the void fraction increases. This reduces the vorticity annihilation between positive and negative regions, as these vorticity lumps can only diffuse around their perimeter, which is shielded by a region of irrotational fluid. In both these cases, a clear stable von Karman vortex street is produced, which is similar to that of a solid body at lower Re. On the other hand, C_{S1} produces an unstable vortex street of very intense lumps which can be seen to be ejected behind the body at different positive/negative intensities and result in a vortex street which tends to oscillate. This ejection mechanism is highly sensitive to previous events, which causes it to have long periods of oscillation.

5.5.4 Straining field

The straining field is characterized by $||\Sigma||$. In the far-field, $||\Sigma||$ is negligible, so attention is focussed on the near field region where the strain rate (shown in figure 5.13) varies rapidly. Instantaneous straining is measured as a positive value from zero. Zero strain is shown in blue and the most intense straining value is shown in red. This diagnostic, described in Section §5.3.1, is useful for identifying regions of strain, which cannot always be seen using the flow diagnostics presented later, because irrotational flow and straining are often identified together. The strain occurs mainly where the flow is irrotational (for instance upstream of the array) and in attached shear layers. Where the flow is purely vortical (for instance in the downstream vortices), the strain field is negligible.

In C_1 (Figure 5.13a), straining occurs upstream of the cylinder and within the

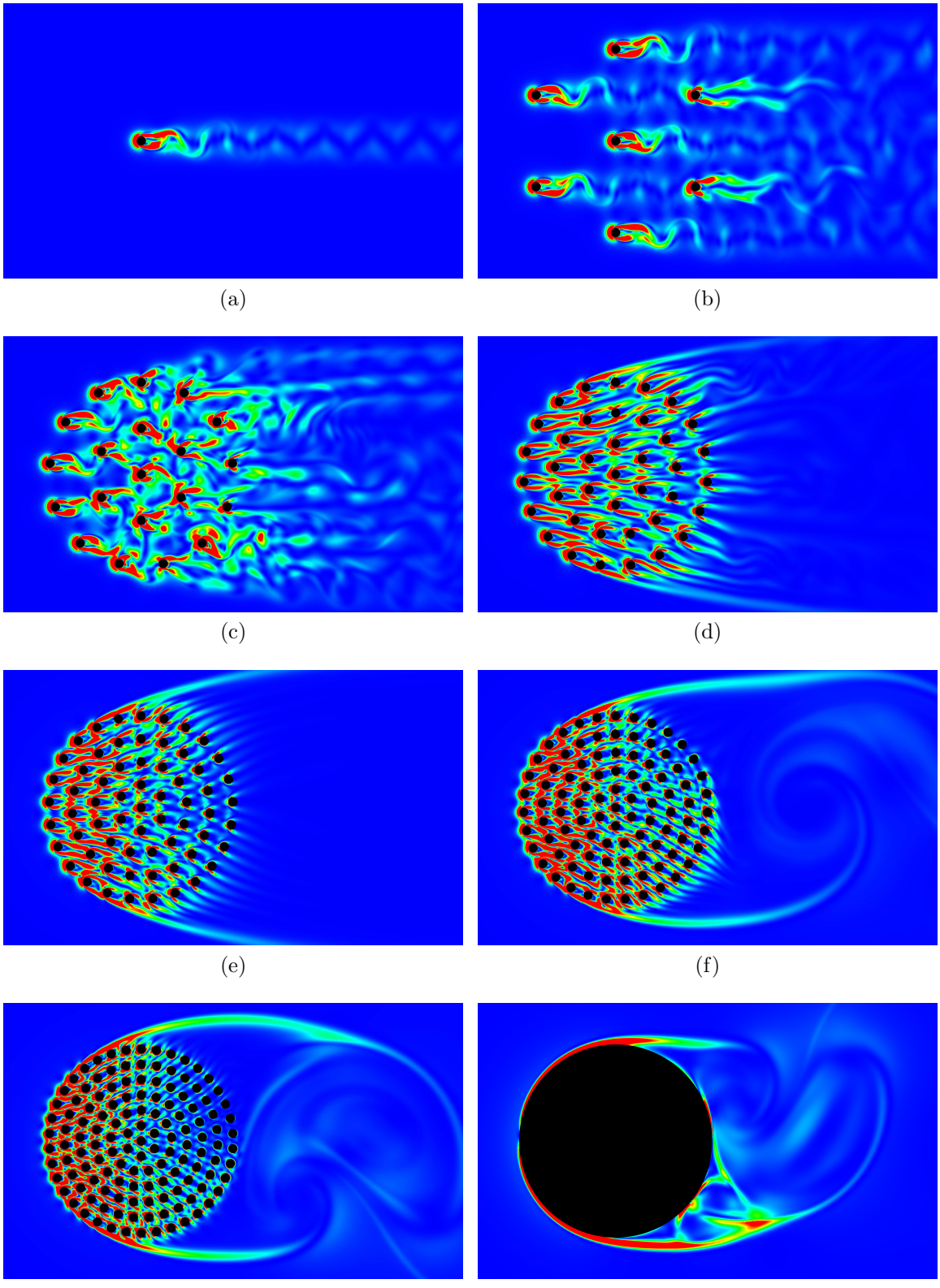

(a) (b) (c) (d) (e) (f) (g) (h)

Figure 5.13: Strain field $||\Sigma||$ for cases (a) C_1, (b) C_7, (c) C_{20}, (d) C_{39}, (e) C_{64}, (f) C_{95}, (g) C_{133} and (h) C_{S1}.

boundary layer. The strain in the irrotational upstream flow scales as U_∞/D. Adjacent to the sides of the cylinder are two attached shear layers which periodically break off to generate vortex lumps. The strain within the shear layer, which scales as U_∞/D, is clearly seen. Downstream, where the flow consists of a von Karman vortex street, the strain field is zero within the vortices and small between the vortices.

A picture emerges in C_7 (Figure 5.13b). There is still sufficient separation between the cylinders that straining fields, similar to that seen in C_1, are seen for each of the individual cylinders within the array.

In C_{20} (Figure 5.13c), cylinders are now sufficiently close that interaction has started to take place. On the surface of the upstream cylinders, a separate region of straining can be identified, but inside the array, any areas of straining are highly time dependent and form because of divergence around the cylinders, as well as between wake vortex interactions. Straining regions also persist in the unstable wake region behind the array, caused by interactions between individual cylinder wakes. The intensity of straining in these regions can be equal to that seen in the shear layers attaching to individual bodies.

In C_{39} and C_{64} (Figures 5.13d and 5.13e), the flow through the array has stabilised, with upstream wakes pinned on downstream bodies. The flow through the array is still sufficient that all the individual cylinders exhibit a shear layer on their upstream face. Because of the stabilizing wake formation inside the group, extended shear layers now form and this leads to the first signs of a group shear layer.

In C_{95} and C_{133} (Figure 5.13f and 5.13g), the flow in the upstream portion of the array is almost entirely dominated by straining. The shear layer, in the wake of the array as a whole, has intensified and regions of straining can now be identified between the entrapped trailing vortices.

In C_{S1} (Figure 5.13h), the largest contribution to the strain field is generated in the attached boundary layer. The shear in the boundary layer scales as $D_G/Re_G^{1/2}$, so that the strain rate in this region is $U_\infty/(D_G Re_G^{-1/2}) \sim 2.2U_\infty/D$, which is comparable to irrotational straining upstream of a single cylinder. The strain rate caused by the upstream irrotational flow around C_S1 scales as $U_\infty/D_G \sim 0.05U_\infty/D$, and this explains why it is not evident in figure 5.13h.

5.5.5 Flow diagnostic

A useful flow diagnostic, described in Section §5.3.1, is a dimensionless measure E of the second invariant of the velocity gradient tensor. It gives a measure of whether the flow is vortical, shearing or irrotational, but does not discriminate in terms of magnitude. These flow forms correspond respectively to $E = -1$, 0 and 1, or in terms of figure 5.14, blue, green and red regions.

Figure 5.14a, shows a single cylinder (C_1) in a domain of irrotational flow. A clear vortex street can be seen, with areas of pure vorticity at the centre of the vortices. Upstream of the cylinder, the flow is irrotational and, because of blocking, the straining region can no longer be seen. (It should be noted that this is a common feature of this diagnostic in all cases). A shear layer can be seen extending from the shoulders of the cylinder, which is encompassed by vorticity.

In Case C_7 (Figure 5.14b), the void fraction is still sufficiently low that irrotational flow transfers, undisturbed, through the array, and is enveloped in the wake of the array. The wake is formed from regions of vorticity shed by the individual cylinders into the wake. These vorticity regions are separated by irrotational flow, but can be seen to amalgamate into larger areas of vorticity.

In C_{20} (Figure 5.14c), the void fraction is increased and less irrotational flow travels through the array. Regions of vorticity are now closely packed representing a higher proportion of the wake, indicating that there is now shear present. Compared with C_7, the formation of larger vortices seems to be faster, indicating a higher rate of annihilation.

C_{39} (Figure 5.14d) is the first case in which a group wake is fully established. It is possible to see an entrapped region of shear flow, bounded by a thin layer of vorticity. A remarkable feature of this case is the extent of the areas of vorticity and shear flow within the wake region, which can only be formed through annihilation and accumulation of vorticity. Within the array, thin dividing regions of irrotational flow form between each individual body's shear layers and these can also only be formed through a process of annihilation, as cylinders are sufficiently closely packed that their wakes comprising vorticity would consume the array's entire void region.

C_{64} (Figure 5.14e) shows similar features within the array to those in C_{39}, however, the wake regime is more uniformly developed. The entire wake attaching to the array

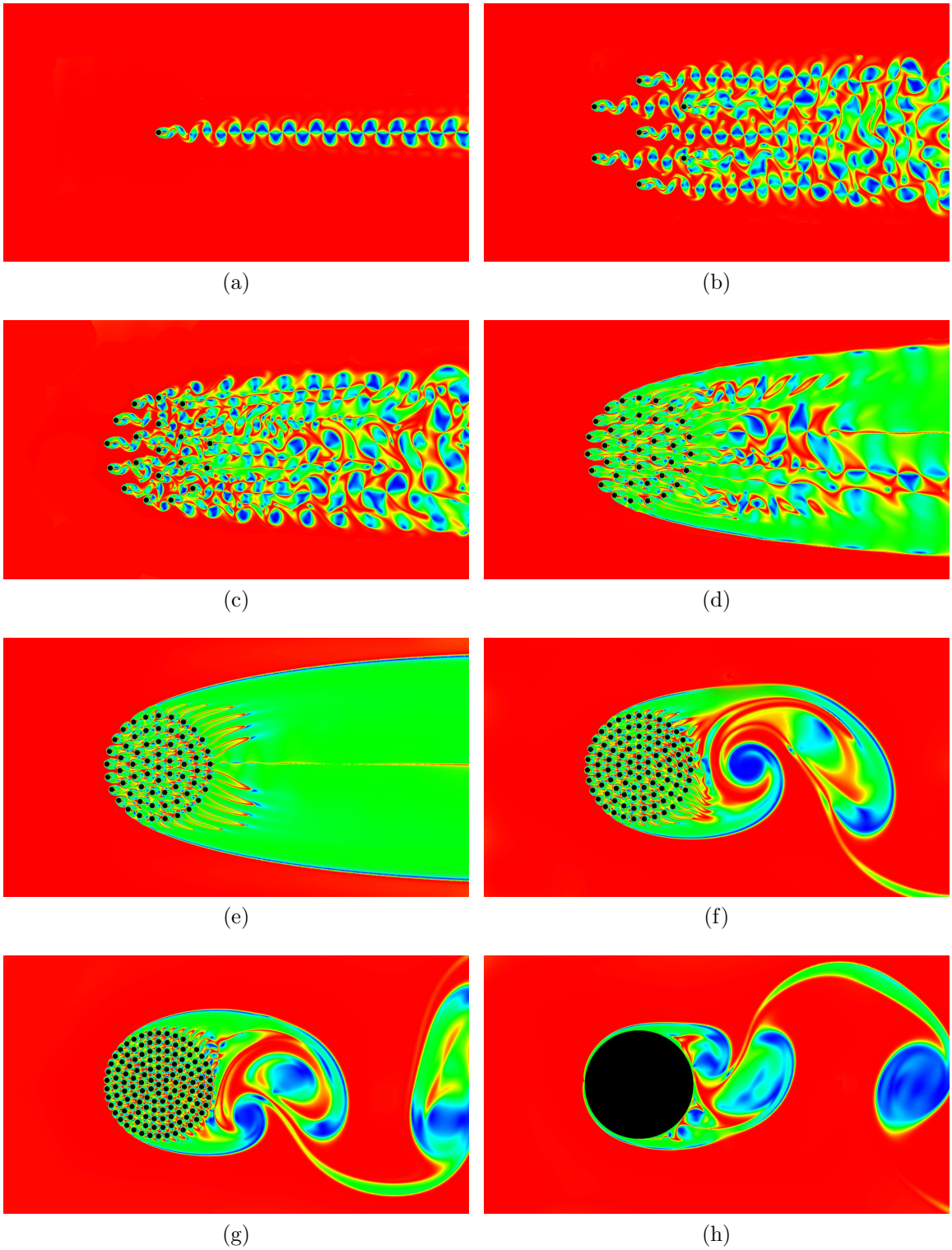

Figure 5.14: Flow diagnostic for cases (a) C_1, (b) C_7, (c) C_{20}, (d) C_{39}, (e) C_{64}, (f) C_{95}, (g) C_{133} and (h) C_{S1}.

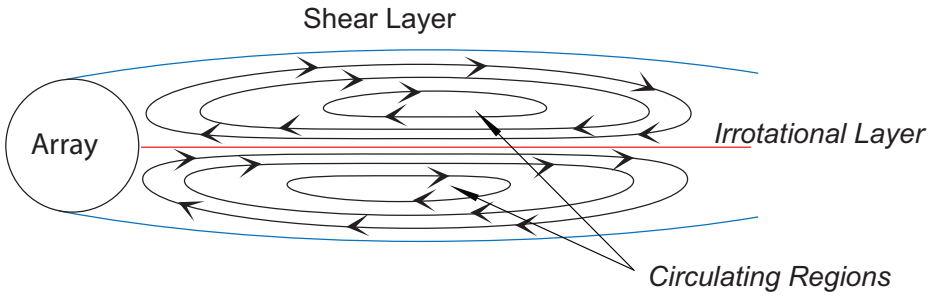

Figure 5.15: Case C_{39} circulating region in the wake.

is bounded by a coherent, thin vortex sheet, which is indicative of a uniform flow near its boundary edges. The flow, within the wake, is now represented in solid green, apart from an almost symmetrical, thin, irrotational, dividing region on the centre line. This indicates that there is uniform circulation within the wake, with a shear velocity gradient through this region of equal strength to the circulation. To help with the explanation Figure 5.15 illustrates the flow pattern, identifying areas of interest. Two counter-rotating vortices, either side of the irrotational separating layer, draw fluid back towards the array. This irrotational layer effectively acts as a wake stabilizer. While these circulating regions are vortices, they also have a velocity gradient across them indicated by the presence of strain, as the energizing force acts around their perimeter. This means that, at the centre of the circulation, fluid is circulating at a slower rate.

Downstream cylinders produce finger like shear layers extending from the array for approximately $7D$ down the wake. These shear layers are surrounded by an irrotational boundary, which indicates that they are being quickly reduced by annihilation across this boundary and into the much larger array wake. The generation of vorticity at the end of these individual wakes is formed by approximately perpendicular contact with the larger circulating regions, which draw the base bleed flow around the edges of the wake.

Cases C_{95}, C_{133} and C_{S1} (Figure 5.14f, 5.14g and 5.14h), can be viewed as typical of what would also be expected from a solid body. The attached circulating regions behind these arrays entrain irrotational flow from the surrounding field, causing the isolated roll-up of intensive vortex lumps, which are advected downstream. From the shoulders of the arrays, a shear layer separates which is bounded by a thin vorticity

region. For the solid body (C_{S1}), a shear layer is formed from the stagnation point, which is, in effect, within the boundary layer. This grows, as a function of $D_G/Re^{1/2}$ around the body, until separating into a shear layer at the shoulders of the cylinder.

5.5.6 Lagrangian and Eulerian average velocity

Flow velocities within irregular and closely packed arrays of bodies are difficult to interpret, so a useful set of diagnostics were suggested by Eames et al. [1994]. These diagnostics are described in §5.3.3 and measure Lagrangian and Eulerian velocity derived from the average velocity field within each arrays circular perimeter.

The Eulerian average is based on particle transition time, which is found from the streamlines through the array. These streamlines are illustrated in Figure 5.16. As the streamlines are released upstream, the lines do not tend to become enveloped in the boundary layer, and, therefore, diverge around, and converge behind the individual cylinders. The enveloped region is a circulating region, where fluid travelling through the array, does not enter. As discussed later, these regions can effectively be considered as part of the void fraction.

The streamlines in Figure 5.16 are colour coded by the velocity magnitude and scaled from the free stream velocity (shown in yellow), through to zero velocity or stagnation (shown as dark blue). Red regions denote where the flow rate is greater than in free stream, typically seen in areas of straining.

Commenting on the individual cases:

1. C_7 (Figure 5.16a): The majority of streamlines through the array are horizontal and have a flow rate of a magnitude equal to free-stream. As the streamlines approach individual bodies, they slow, before then accelerating past and re-converging at a distance of $2D$ downstream.

2. C_{20} (Figure 5.16b): Streamlines still tend to pass through the array horizontally but preferential channels of flow start to emerge, where flow can pass more easily. Upstream cylinders still have a stagnation region in their wake, of approximately $2D$ length, but cylinders further downstream can be seen to have stagnation regions of up to $4D$ length. This corresponds to what would be seen for cylinders

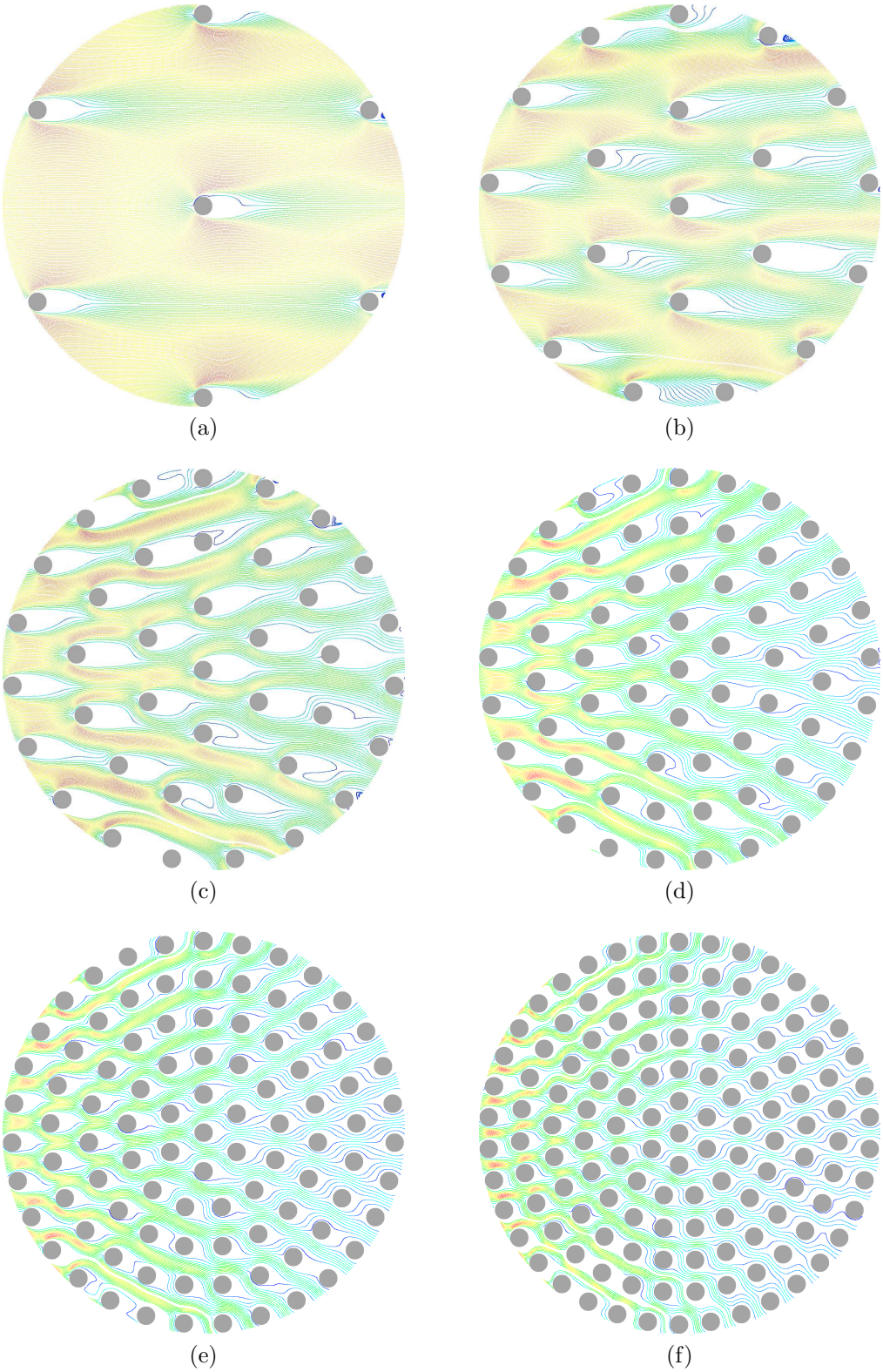

Figure 5.16: Stream lines though Group of Bodies using the average flow field for (a) C_7, (b) C_{20}, (c) C_{39}, (d) C_{64}, (e) C_{95} and (f) C_{133}. Flow is from left to right.

at a lower Re and indicates that the freestream flow at certain points in the array is substantially lower.

3. C_{39} (Figure 5.16c): Streamlines within this array are starting to diverge from the side of the array and the majority of the bodies now exhibit stagnation regions of greater length than $2D$ and up to $4D$. Cylinders on the front surface of the array also have longer wake regions than those seen in earlier cases, which indicates that the inviscid blocking from the array is causing a lower flow rate through the array, with the flow instead diverging around the entire array.

4.C_{64} (Figure 5.16d): This case marks the transition, where individual cylinders are packed sufficiently closely together that the wake regions are now restricted by downstream bodies. Most stagnation region lengths are equal and proportional to the spacing of the cylinders. A large proportion of the streamlines entering the array leave from the sides of the array.

5. C_{95} and C_{133} (Figures 5.16e and 5.16f): These become very tightly packed. The wake region behind individual bodies, becomes almost entirely suppressed. A majority of the flow leaves from the sides of the array and, by C_{133}, flow has been substantially suppressed in the rear half of the array. In this case, the role of the individual cylinder has become completely subordinated to the impact of the array as a whole.

Figure 5.17a is a comparison of flow within the array showing the numerically calculated Eulerian and Lagrangian velocities and the mathematical model prediction of the Eulerian average. The mathematical prediction is based on Equation 5.33 which uses the numerically calculated $\langle C_{Di} \rangle$ for each cylinder and a simple approximation of wake length L_{Wi} according to the cylinder position. The Eulerian velocity field is less than the Lagrangian measure. This was predicted in the inviscid analysis done by Eames et al. [2004] who showed that circular or spherical groups of bodies were special cases and that the Eulerian mean for these cases was

$$\langle u_1 \rangle_E = U_\infty \left(\frac{1 - (1 + C_m)\,\phi + (1/d)(1 + C_m)\phi}{1 - \phi} \right), \tag{5.37}$$

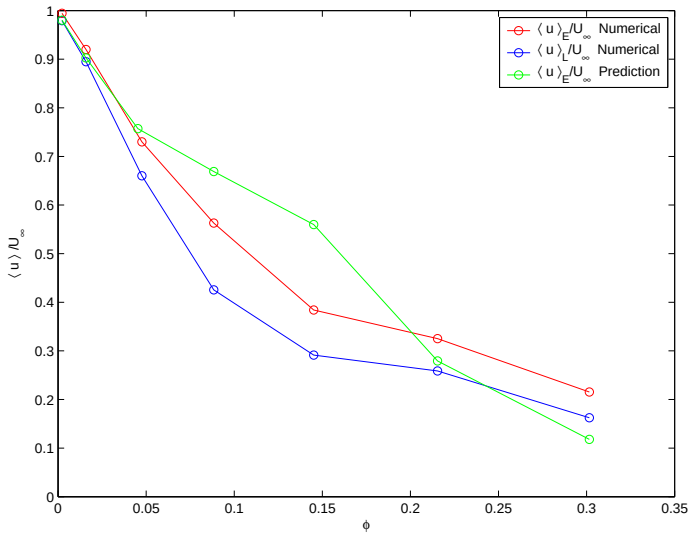

(a)

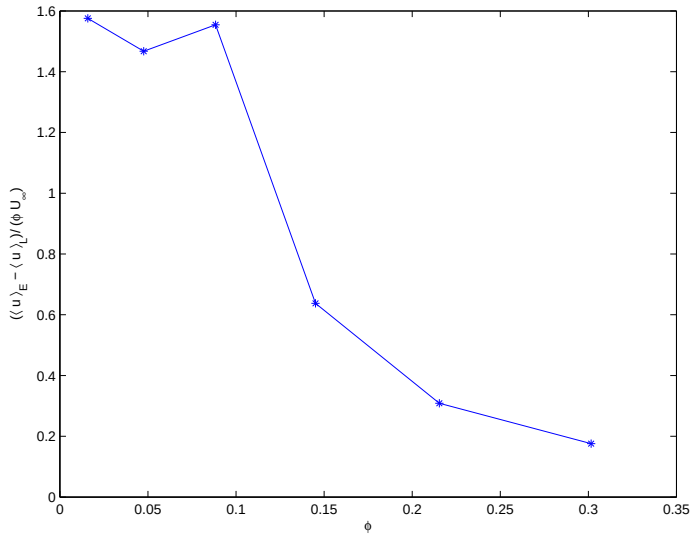

(b)

Figure 5.17: (a) Variation of Eulerian and Lagrangian average velocity with void fraction and (b) Difference between numerically calculated Eulerian and Lagrangian average velocities in terms of void fraction.

(Eames et al. [2004, equ. 4.5]) and the Lagrangian mean was

$$\langle u_1 \rangle_L = U_\infty (1 - \phi C_m) \tag{5.38}$$

(Eames et al. [2004, equ. 4.6]) where for two-dimensional flow $d = 2$ and for a circular array $C_m = 1$. This leads to an under-prediction of approximately $(1 + C_m)\phi/d$. This equates to ϕ. From the numerical work, the difference was found to be 1.6ϕ, where the void fraction was low in C_7, C_{20} and C_{39} but the difference rapidly reduces for higher void fractions as seen in Figure 5.17b. The reliability of the model is also indicated in Figure 5.17a where the mathematical model predictions are very good at low void fractions but are also in reasonable agreement at higher ϕ.

5.5.7 Upstream velocity perturbation

Figure 5.18a shows the centerline streamwise velocity (u_1), upstream of the array, for varying void fractions. The flow is irrotational and slows down, due to the blocking effect of the entire array and the drag force from the bodies. Within a distance $\sim D$ of the front of the array, the flow is influenced by the placement of individual cylinders and tends to accelerate as it enters the array. For case C_{S1}, the flow is completely blocked at $x = -D_G/2$, as a consequence of the kinematic condition applied on the surface of the cylinder.

Figure 5.18b shows the model predictions of the streamwise velocity, based on using the numerical calculations of the individual drag coefficients on the cylinders in the array. Also plotted for comparison is the minimum velocity upstream of the array (Figure 5.19). This gives a broad measure of the blocking influence of the array on the incident flow. The model gives a very good comparison for small ϕ as for C_7 and C_{20} but for higher ϕ it under-predicts on C_{39} and C_{64} and over-predicts on C_{95} and C_{133}. The discrepancy seen between the numerical and model results for high ϕ cases and for the solid cylinder (C_{S1}) is due to the model being a point force and bipolar representation, which is only valid at distances greater than D_G from the bodies. Therefore, for large diameters, the bodies are close to $x_1 \approx -D_G/2$, where the velocity minimum occurs, and will result in a discrepancy.

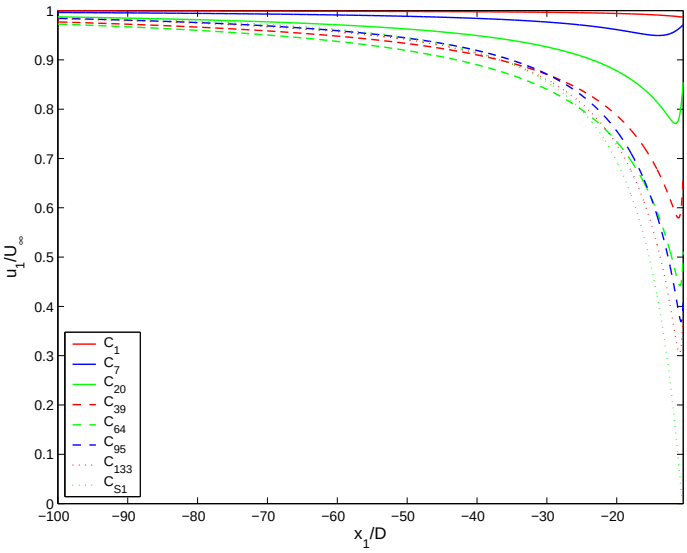

(a)

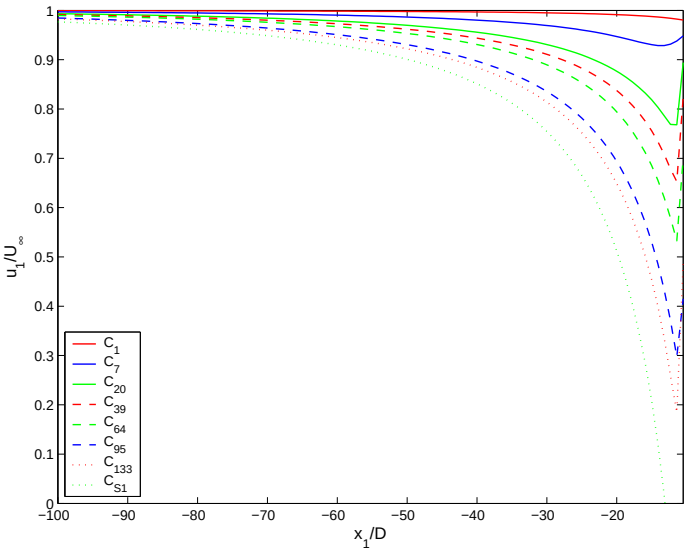

(b)

Figure 5.18: Variation of centreline velocity with distance upstream of the array. Numerical and predicted profiles are plotted in (a) and (b) respectively.

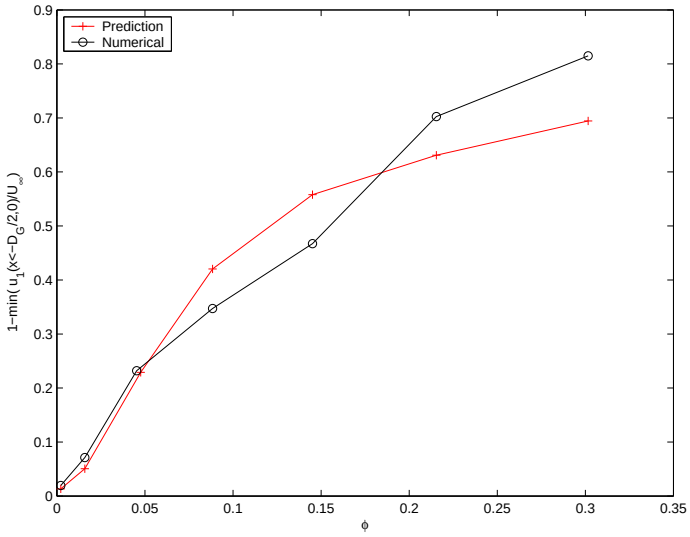

Figure 5.19: Variation of the minimum upstream centreline velocity as a function of void fraction.

5.5.8 Vorticity decay within the wake

A useful measure of the intensity of a body's wake and the rate at which this reduces downstream of the body can be found by measuring the value of maximum vorticity, as described in §5.3.4. The variation of Ω_{max} with downstream distance is shown in Figure 5.20. The two main processes which lead to the Ω_{max} decreasing with downstream distance are (a) diffusion which causes Ω_{max} to decay as $x_1^{-1/2}$ and (b) vorticity annihilation caused by positive and negative vorticity intermingling causing Ω_{max} to decay rapidly as x_1^{-1}. To enable the numerical results to be interpreted, Figure 5.20 includes two lines with gradients -1/2 and -1. The specific rate for either process is largely governed by the surface area of the interface in which each process operates. The cases investigated in this study are grouped into four categories defined according to the characteristics that they exhibit and the processes involved.

1. Figure 5.20a shows maximum vorticity for C_1. (C_{S1}, which has a different flow regime, is plotted for comparison and discussed later). Figure 5.20a starts $10D$ behind the cylinder in case C_1 and, at this point, there is already a fully developed von Karman vortex street. Because of the low Reynolds number ($Re = 100$), positive and negative vortex lumps are shed at a much higher

frequency which results in them being much closer. These are closely packed oppositely signed vortices, so the maximum vorticity decays rapidly with distance. At $40D$ downstream, the vortex lumps form into positive and negative vortex sheets, representing the initial bias in the von Karman vortex street. The intensity of the vorticity in the sheets reduces at a rate of x_1^{-1} because of the large interface area and combined annihilation and rapid diffusive processes.

2. C_7 and C_{20} (Figure 5.20b) are low void fraction cases, which retain the individual wake signatures of the bodies in the array. There is no overall group wake with an identifiable single positive or negative vortex. It is rather composed of identifiable individual wakes, each consisting of multiple positive and negative vortices. Behind the array, these are restrained by the flow around the array into a region of very compressed oppositely signed vorticity, which rapidly annihilates, at a rate of x^{-1}. As can be seen in Figure 5.20b, this process of annihilation continues along the wake at a uniform rate. In C_{20}, at $100D$ down-stream, vorticity can be seen to form into weak vortex lumps, which then diffuses at a slower rate.

3. Both C_{39} and C_{64} (Figure 5.20c) have a shear layer that separates from the shoulders of the array and continues downstream, until it becomes unstable and rolls up into a von Karman vortex street. In the initial region, the stable shear layers are separated from one other by a region of enclosed irrotational flow. This prevents annihilation and means that there is only diffusive reduction from the shear layers, leading to a $x_1^{-1/2}$ decay in Ω_{max}. This, however, is considerably more rapid than the diffusion on vortex lumps, because the shear layer presents a large surface area from which to diffuse the intensive region of vorticity. At a distance downstream of $3D_G$ (C_{39}) or $5D_G$ (C_{64}), the rate of diffusion reduces as the vortex sheets roll up into more slowly diffusing discrete vortex lumps.

4. C_{95} and C_{133} (Figure 5.20d) are compared with the solid cylinder C_{S1}. These cases exhibit wakes similar to the solid cylinder, in that a shear layer separates from the shoulders of the array (as with the single cylinder C_{S1}) and forms two oppositely signed vortices, of approximately D_G in length, which are attached downstream behind the array/cylinder.

The intensity of these periodically switches and they eventually detach creating positive or negative vortical lumps which are advected down-stream. The radii of the shed vortices are much larger than the diffusive lengthscale (as seen in figures 5.12f, 5.12g and 5.12h) and so the maximum vorticity decays more slowly than $x_1^{-1/2}$.

For a distance of D_G behind the arrays/cylinder , the vorticity reduces at a faster rate depending on ϕ. This is particularly noticeable in C_{S1}, where the rate of reduction is indicative of rapid annihilation between the trailing vortices. In C_{95} and C_{133}, the rate of annihilation is less rapid, as the vortices are separated from the array's base bleed by a region which is effectively irrotational and acts as a barrier.

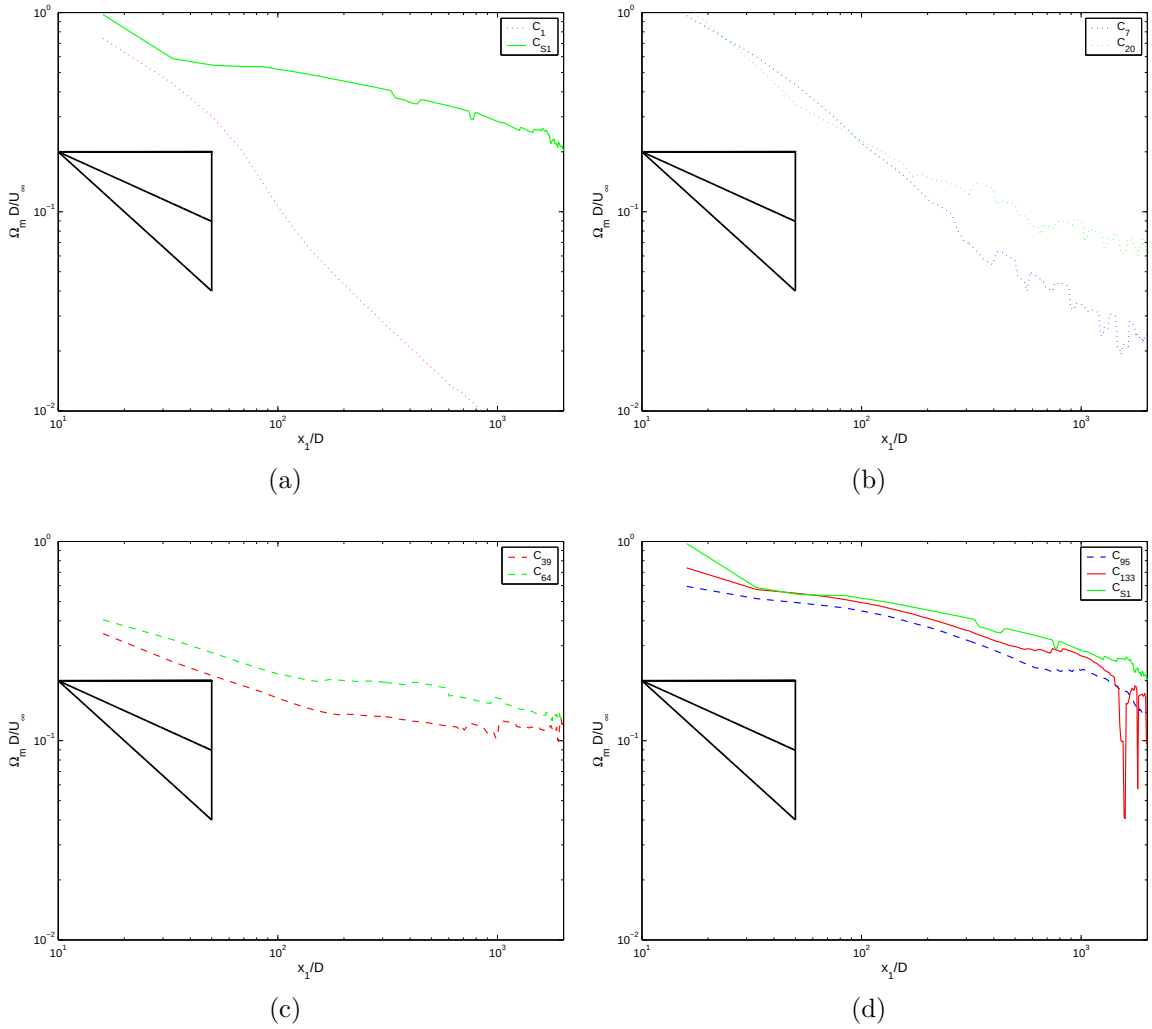

Figure 5.20: Maximum vorticity downstream (a) C_1 and C_{S1}, (b) C_7 and C_{20}, (c) C_{39} and C_{64} (d) C_{95}, C_{133} and C_{S1}.

5.6 Conclusion

In this chapter, numerical data for six different void fraction cases have been presented, alongside two control cases. All have been successfully processed on the new UCL Legion supercomputer. Each case was run using direct numerical simulation, with no turbulence modelling or time marching acceleration techniques. The mesh used to discretize the domains was evaluated through a mesh independence study and possible errors predicted for the investigated $Re = 100$. Mesh refinement regions used boundary layers with controlled gradient transitions to regions needing less refinement. In total, approximately $200,000$ processor hours were required, which allowed for long simulation times of approximately $3000D/U_\infty$.

A number of diagnostic techniques have been applied to determine flow characteristics and array behaviour. Each diagnostic is targeted at a specific property but because of the coupled nature of multibody flows, a combination of diagnostics can usefully be employed to interpret particular patterns of behaviour. Three distinct wake regimes have been identified from the cases studied:

1. At low ϕ, individual bodies within an array exhibit similar wake and force characteristics to those seen for an individual body. The wake of the group is composed of the identifiable individual wakes of the bodies making up the group. These rapidly dissipate through an annihilation process, as they are advected along down the stream.

2. At moderate ϕ, there is a stable wake in the near-field behind the array, giving zero lift force on the array. The lift and drag forces on individual cylinders are steady with time. The flow within the array is totally filled by individual body wakes and there are signs of annihilation between these wakes. The overall group wake is formed between two shear layers and is characterised by two circulating regions, which contain both strain and vorticity.

3. At high ϕ, the total drag force is comparable or greater than that seen for the fully filled array. The forces on identifiable groupings of individual cylinders within the array are uniform and depend on the position of these groupings within the array. However, the majority of the flow goes around the array and

forms a von Karman vortex street, as if the array were a solid body. The street can be seen to diffuse at a very slow rate, due to its small interface area and the surrounding irrotational flow.

Each average velocity field was calculated in a continuous 6 day, 32 processor stint, which allowed accurate time independent calculation of the average Eulerian and Lagrangian values for the flow within the array. As expected this flow reduces with increased ϕ and this shows in both Eulerian and Lagrangian measures. The mathematical model also showed a reduction and accurately predicted the Eulerian value at low ϕ. Eames et al. [2004] anticipated the Lagrangian would have a lower value than the Eulerian and for low ϕ the difference between these measures compares surprisingly well with the inviscid analysis done by Eames et al. [2004], especially considering the sensitivity of the measure. For higher ϕ, there is a considerable difference, as would be expected.

The effective blocking upstream of the array was measured numerically by finding the minimum values of u_1 along the centre line leading upstream of the arrays. This was compared to the mathematical model, which was found to predict well for $\phi > 0.05$. However, for higher values of ϕ, the model does not seem to take account of transitions between wake regimes.

Measurements of the vorticity field downstream from the array have shown different mechanisms by which vorticity is either diffused or annihilated. Where annihilation is identified it results in a rapid decline in vorticity at a rate of x_1^{-1}. In the von Karman vortex street, a more gradual reduction through diffusion is identified at a rate of $x_1^{-\frac{1}{2}}$. This slower degradation of large well spaced vorticity lumps is because the diffusion occurs across a very small region.

Chapter 6

Experimental study and results

6.1 Introduction

The aims and objectives of the experimental study, set out in Chapter 4, were to develop a capability to investigate the effect of high Re_G, three-dimensional flows on groups of cylinders. This is not possible using numerical techniques and this means that the results of this work can not be directly compared to the numerical study in Chapter 5. However, experimental work provides a useful physical context in which to understand the effect varying void fractions on such flows. This component required the design, manufacture, commissioning and testing of a purpose built flume, incorporating an instrumented platform for measuring and visualizing the complex interactions in these multibody flows.

The innovative nature of the experimental apparatus required a significant input from the technical staff in the workshop of the Department of Mechanical Engineering. The final apparatus is composed of over ten thousand individual components, of which approximately one thousand involved machining (some of which took a week). Despite huge efforts on everyone's part, integrating this project into workshop schedules meant a two year manufacture time and about sixteen months of technician time. Time constraints meant that the scope of the actual experimental investigations undertaken was limited to the measurement of the force on groups of bodies and dye contrast imagery. This was successfully achieved. The measurement of forces on individual cylinders is now targetted for future work as detailed in §7.

The two diagnostic tests used, demonstrated the functionality of the apparatus for future work. The first, discussed in §6.5.1, related to the overall induced drag force on an array. The second used dye contrast imagery to streamlines, and is discussed in §6.5.4. The results from these initial experiments are discussed in §6.6.

6.2 Problem definition

In line with the main numerical component of the broader study described in Chapter 4, the experimental apparatus was designed to enable the void fraction in an isolated group of bodies to be varied, while also using a range of Re_G flows, from $9000 - 24000$, all of which were of a higher order than was achievable in the numerical study in Chapter 5.

To summarize the earlier discussions in Chapters 1 and 4, the individual bodies were formed from identical circular cylinders (diameter $D = 13$ mm and length $L_C = 200$ mm) in the same way as for the numerical work. The array was also taken to be a circular cylinder shape. To maintain an even void fraction throughout the array, cylinders were equally spaced from each other. Since the number of cylinders (N_C) was relatively small, a random distribution was not chosen, as this could have given an undue bias to the results. To maintain the overall circular group shape, cylinders were arranged in concentric rings (starting from the circumference of the array) and moving inwards, with an additional cylinder at the centre. The separation between the concentric rings and between the cylinders on each ring was the same. As can be seen in Figure 4.2, the resultant geometries in the free stream direction were irregular (neither aligned nor staggered).

The overall group diameter was linked to $D_G = 169$ mm (based on design limitations) giving $D_G/D = 13$ (compared to $D_G/D = 21$ for the numerical study in Chapter 5) and this made it possible to investigate four void fractions consisting of $N_C = 7$, 20, 39 and 64 cylinders, as proposed in Chapter 4. These cases are referenced E_7, E_{20}, E_{39} and E_{64}, where the subscript denotes the number of cylinders (N_C). Two additional control cases were considered; the first referred to as E_1, was a single individual cylinder, and the second referred to as E_{S1}, was a solid cylinder, representing a full array where the $\phi = 1$. These cases are tabulated in Table 6.1 and

Case	E_1	E_7	E_{20}	E_{39}	E_{64}	E_{S1}
N_C	1	7	20	39	64	1
ϕ	0.0059	0.0414	0.1243	0.2308	0.3787	1
Rows	0	1	2	3	4	NA

Table 6.1: Description of cylinder arrays investigated.

the cylinder arrays are shown in Figure 4.2.

The centre of the array was positioned 1.75 m from the inlet channel and 1.25 m from the outlet along the centre line of the channel. The channel width and depth were $W = 0.5$ and $L = 0.2$ m respectively, giving an effective blocking ratio of $0.169/0.5 = 0.338$ for E_{S1}. The latter was expected to show the greatest difference when compared to unbounded flows. For smaller cylinder numbers, the effect of blocking was much weaker. The results between cases are comparable and while correction techniques could reduce the difference between bounded and unbounded flows, these were not applied here, as only E_{S1} needed a correction.

6.3 Description of the apparatus

After initial feasibility studies and prototype testing, described in Chapter 4, the apparatus was then designed using computer aided design software (IDEAS) to produce a full set of working drawings for manufacture in the Department of Mechanical Engineering workshop. This work utilized a four-axis CNC machine for manufacture and the expertise of Phil Jeavons.

As was inevitable, during the manufacturing phase, changes were incorporated to take account of manufacturing considerations and perceived improvements. The final flume is shown in the photographs in Figures 6.1 and 6.2 and can be compared with the initial CAD rendering in Figure 4.17. In these photographs, the flume contains a single solid cylinder (E_{S1}), positioned in the channel. The instrument gantry section can be seen to be positively pressured with air to displace any water ingress but the electronics were waterproofed to IP67 (using epoxy resin) to withstand full immersion in water.

Figure 6.1 shows the pump controller mounted on the wall to the left of the

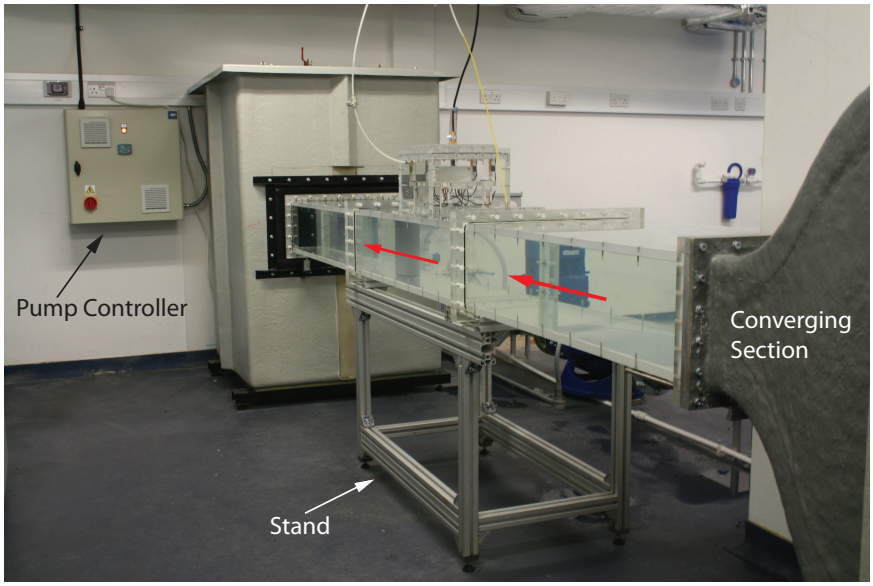

Figure 6.1: Flume view along the flow direction which is denoted by the red arrow. This should be compared with Figure 4.17.

Figure 6.2: Flume view towards inlet with E_{S1}.

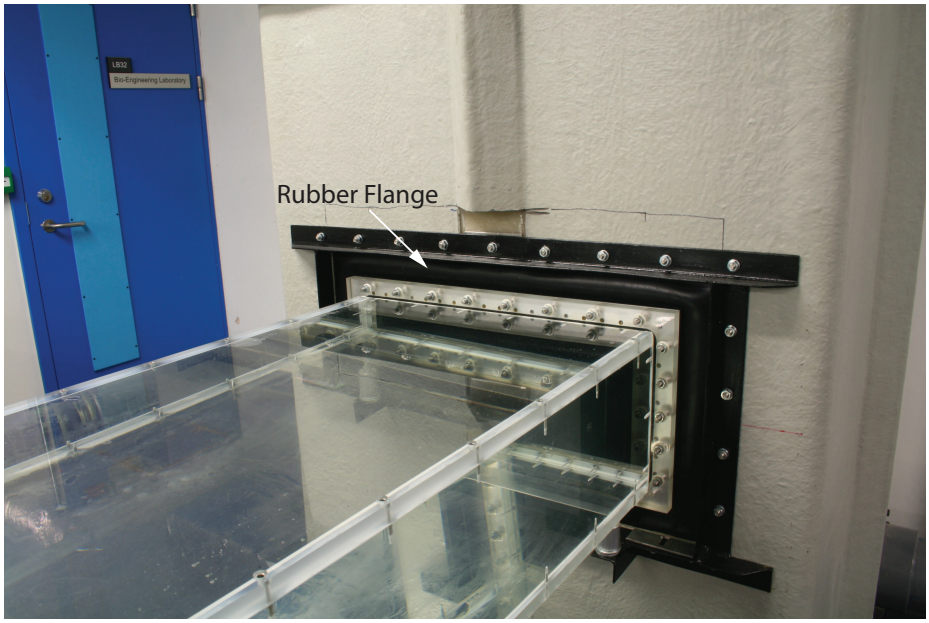

Figure 6.3: Rubber outlet flange to aid channel alignment.

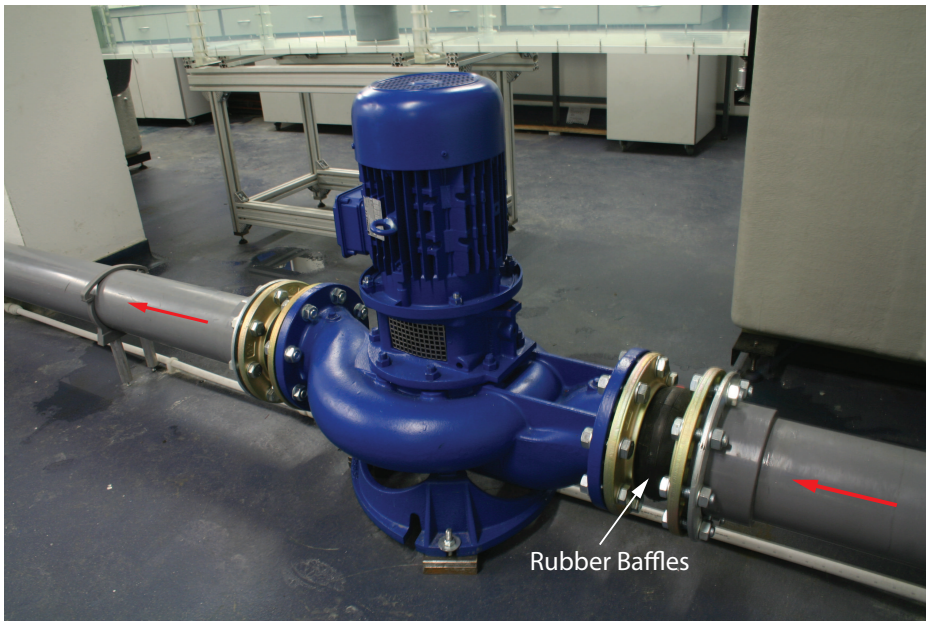

Figure 6.4: Lowrana centrifugal pump used to circulate flume with rubber alignment / damping baffles. The red arrow denotes the direction of the flow.

receiving tank. Figure 6.3 shows the outlet rubber mounting which allowed for any slight misalignments between the two supporting tanks. Figure 6.4 shows the Lowrana centrifugal pump attached to the pipework with rubber baffles to dampen any residual vibration. This inclusion alongside the pump type meant that vibration was not a factor when the pump was working at the required flow rates. Indeed, it produced less noise than the cooling fan for the controller.

Figure 6.5 shows the instrumentation gantry with the solid cylinder (E_{S1}) attached to the bottom of the gantry, via the mounting plate. On the top of the gantry, the hatch lid forms a seal to the enclosed channel. The instrumentation connections feed through a pipe which attaches to this lid and is sealed with an elastic sealant. The instrumentation cable has 25 cores, terminating in a D-socket computer connection. There is a junction box in the centre of the gantry to which each of the load cells is connected.

Each arrangement plate consists of precisely positioned tapered mounting holes onto which cylinders could be located and fixed - as shown in Figure 6.10c. These hole arrangements were described in Chapter 4 and are designed to be used to mount both the instrumented and non-instrumented cylinders, which are shown in Figures 6.10a and Figure 6.10b respectively. As instrumental cylinders had to be aligned with the flow to correctly distinguish lift and drag forces, an alignment bolt was used to lock them in place (as shown in Figure 6.10b).

The loaded arrangement plate bolts to the base of the gantry (Figure 6.5). To reduce the number of arrangement plates, E_{S1} had a special tensioning bolt to support the single solid cylinder onto the arrangement plate for E_7. Holes on this plate which were not populated had blanking plugs inserted. Each of the plates can be seen standing upright in Figure 6.8. In Figure 6.9, the cylinders have been colour coded to show the concentric rings whose colours are described in the legend.

To load the gantry into the channel, the flume water level had to be reduced to prevent spillage. The up-stand on the instrument cell allowed for 70% of the water content to be retained. The flume was refilled to the level predetermined during the calibration of the flow rate and this was automated by using a ball valve assembly.

The instrumented gantry was precisely held in the channel by a water-tight hatch lid, secured by 20 bolts spaced at 25 mm. The forces transferred through the gantry

were measured using the incorporated load cells. All eight load cells were connected in parallel and attached to a power supply, set to provide a 10 V stabilized supply. The signal from the integrated load cells Wheatstone bridge has an output differential range of 20 mV.

6.4 Calibration of the flow

Older flumes normally rely on a spill gate or flow control mechanism to control the flow rate within the channel. However, by using a modern AC inverter, it is now possible to directly and precisely control the pump speed. This flume was designed to provide a repeatable flow velocity for a given water level. The motor controller was restrained by parameter $par2$ in its firmware, which limited the pump frequency to a maximum of 26.8 Hz. In these experiments, the flow was calibrated against the percentage of the maximum (imposed) rotation rate of the circulating pump. The percentage of the maximum pump speed was indicated by a digital output on the controller.

The channel flow rate was compared with motor speed settings using a Nortek Vecrino Velocimeter. This sensor is a four arm Acoustic Doppler Velocimeter (ADV) downlooking sensing probe, which consists of a transmitter in the stem and four receivers on the pick-up arms at 90° to each other. The arms are angled downwards so they measure the velocity of a sample volume approximately 50 mm beneath the transmitter. This distance was taken into account in mounting the probe to ensure that the sample volume was at mid-channel depth. The probe was mounted on the top of the channel surface, through a mounting formed by two semi-circular plates, which ensures a watertight seal around the ADV probe's stem. Figure 6.6 shows the access port for the ADV probe. The probe sampled at a rate of 25 Hz and the sample region length was set to 6 mm.

The data from the probe was collected using the proprietary software (Vectrion version 1.00) and firmware version 1.27. The software corrects for water temperature, which was measured to be 15.02°C at the time of calibration.

The readings from the probe are generated by bouncing sound waves off suspended particles within the flow medium and measuring the delay of the re-bounding signals

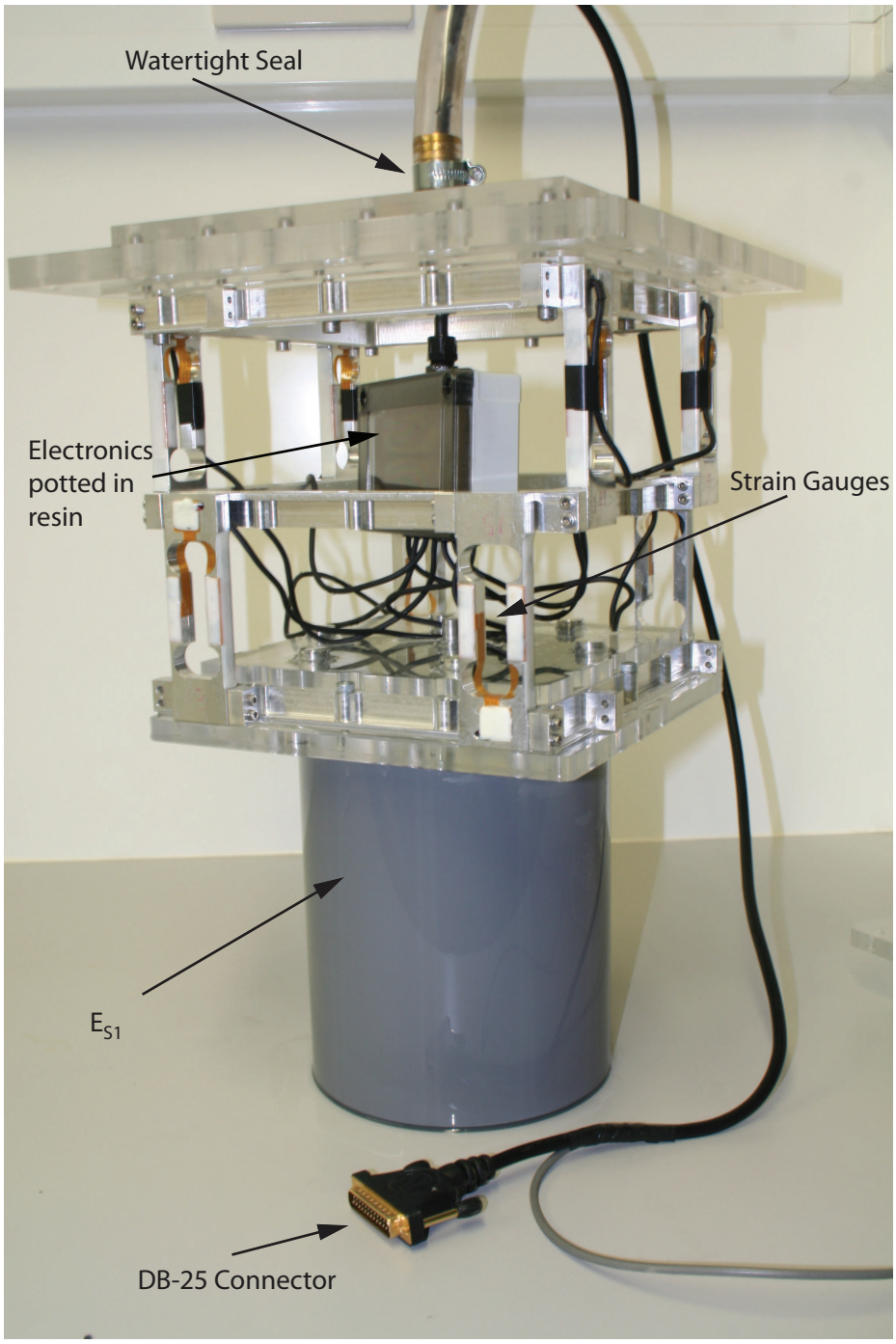

Figure 6.5: Instrumentation gantry set up for Case E_{S1}.

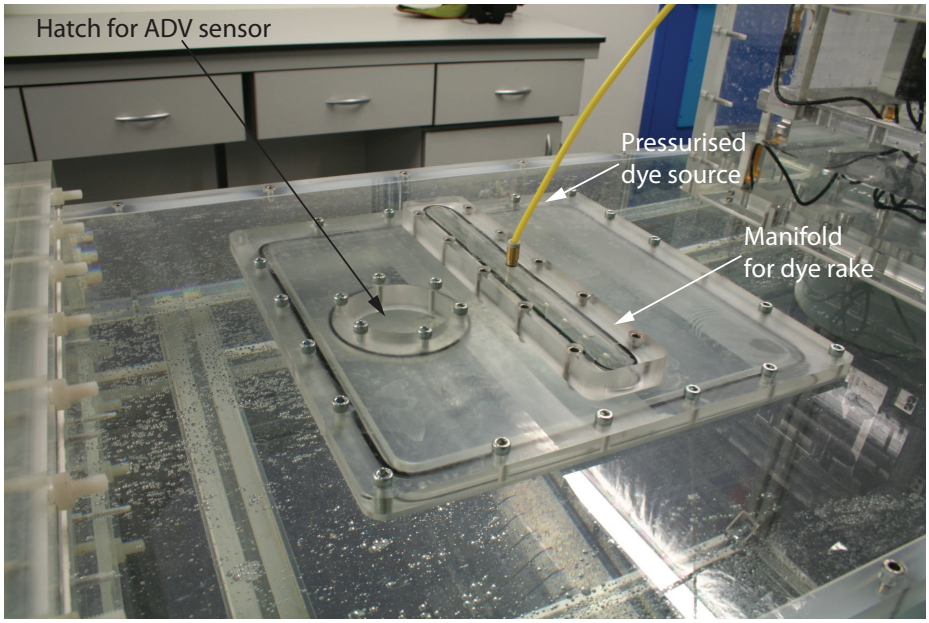

Figure 6.6: Channel hatch used for mounting dye rake and ADV instruments.

on each receiver. The water in the flume was initially filtered to prevent biofilms but this reduced the particulate loading below the level needed by this instrument - just 10 counts per sample were obtained which was well below the 50 counts specified for a reliable reading. For the calibration tests, the flow was, therefore, seeded with spherical 110P8 hollow glass microspheres, at a concentration of 10ppm, which produced a uniform suspension allowing a count to be maintained above 80 per sample. This reduced the standard deviation of results to an acceptable level, as can be seen in Figure 6.7.

The probe was set to measure a range of mean streamwise flow velocities $\overline{u_1}$ up to 0.3 m/s. The flow velocities were measured at regular intervals determined by reference to the percentage of restrained maximum pump speed. The percentage motor speed is a proxy measure of the angular velocity of the motor. Figure 6.7 shows the mid-channel mean velocity against the motor percentage speed. The mean velocity is indicated in m/s to enable the percentage rms to be plotted on the same graph.

The recorded velocity can be seen to vary linearly with the pump motor supply frequency, other than when the flow velocity exceeds 0.171 m/s, when an anomaly

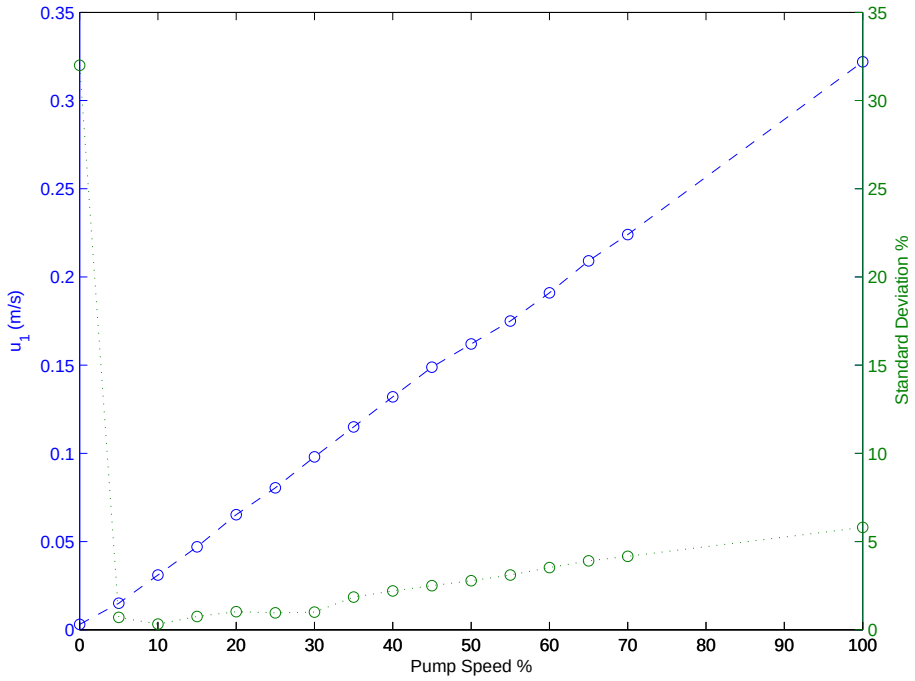

Figure 6.7: The variation of the mid channel average streamwise velocity $\overline{u_1}$ (measured by the ADV) with percentage (of the imposed maximum) pump speed is shown by the dashed curve. The percentage standard deviation $\sqrt{\overline{u_1'^2}}/\overline{u_1}$ of these results is shown by a dotted curve.

is seen. This is almost certainly due to the spilling over of water in the upstream settling tank. This flow velocity is outside the range used in this study and so is not an issue here.

6.5 Experimental results and observations

The experimental apparatus was designed for force measurements on arrays of bodies, individual bodies within the array and visualization of the flow around and through the array. As already explained, measurements of force on individual instrumented cylinders has been deferred to future work. The full range of experiments covering group drag/lift measurements and visualization is described below.

6.5.1 Group drag and lift measurements

This set of experiments investigated the group drag (F_{DG}) and group lift (F_{LG}) for each array of cylinders at different void fractions and four values of $Re_G = (9527; 14320; 19289; 23672)$. The forces induced on the arrays were measured using the supporting gantry load cells. The void fraction was changed by populating the four arrangement plates with different numbers and configurations of cylinders.

6.5.2 Force measurement procedure

For each cylinder arrangement, the apparatus needed to be set up and force measurements taken to calibrate the gantry. The flume was run until the temperature of the circulating water reached $15°\mathrm{C} \pm 1$, which was maintained during all measurements. The pump was then stopped and the flume was allowed to settle in order to calibrate the gantry load cells when $\overline{u_1} = 0$. The calibrated data from the load cells was averaged and this value was deducted from the subsequent force measurements. This was important, because each time the gantry was set up, different tensions were introduced in the load cells which probably arose from tightening the hatch lid and gantry bolts, as well as the varying mass of the cylinder arrangements.

A Picoscope 16 channel, 24 bit data logger was used to record the signals from the load cells. This logger relied on a single ADC, with multiplex switching of signals

(a) (b)

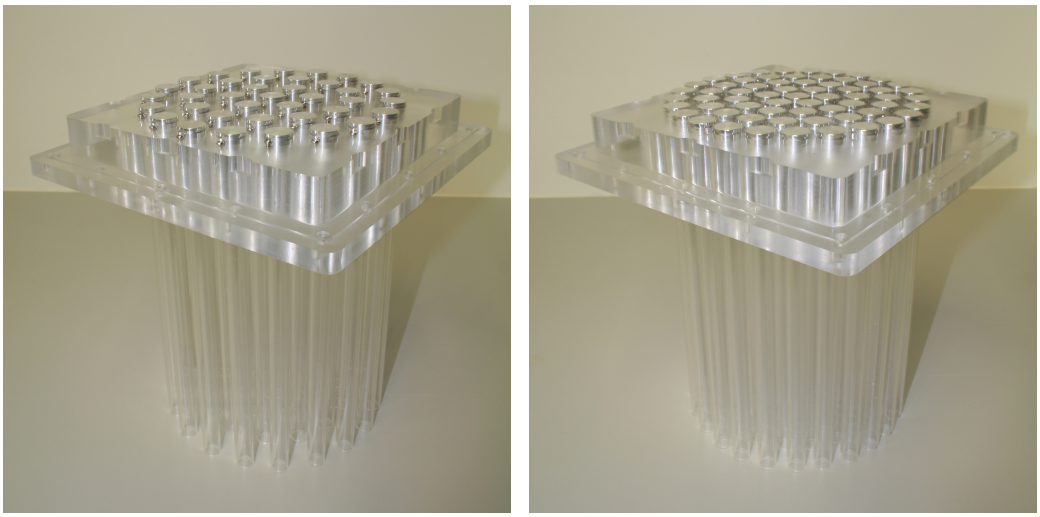

(c) (d)

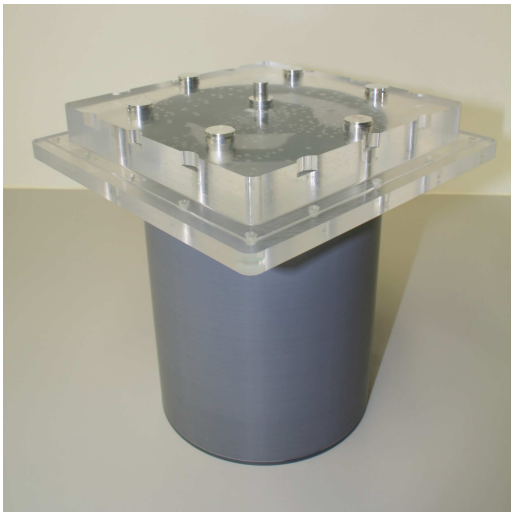

(e)

Figure 6.8: Photograph of the arrangement plates for cases (a) E_7, (b) E_{20}, (c) E_{39}, (d) E_{64} and (e) E_{S1}. The blanks inserted in these plates can also be seen in case E_{S1}.

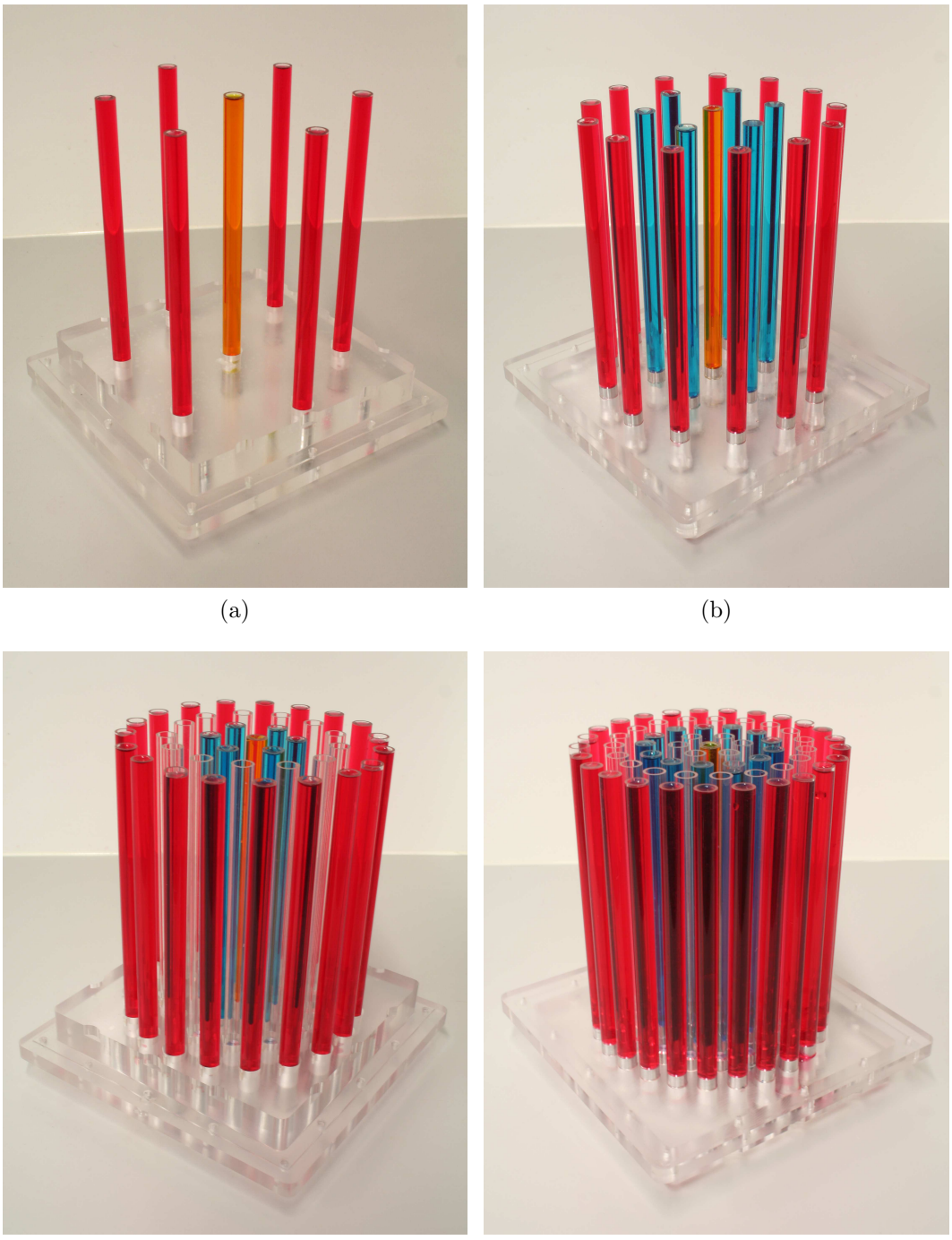

(a) (b)

(c) (d)

Figure 6.9: Photograph showing colour coded cylinder rows in arrangement plates for cases (a) E_7, (b) E_{20}, (c) E_{39} and (d) E_{64}. The orange cylinder is located at the centre, with red cylinders on the outside; interior cylinders are blue. This visualization of the cylinders was achieved by inverting the cylinders and filling them with coloured dye.

between channels. This was not ideal for unsteady loading, as the sample period was below that required to fully interpret the time dependent lift forces. To improve sample time and resolution, only a single load cell in each x_1/x_2 direction was monitored and the signal was amplified for each load cell using an Analog Device instrument amplifier model AD620 to increase the signal to 2.5 V and reduce the differential output to a single channel. In this way, the sample delay was reduced to 100 ms, but the bit resolution was improved from 15bit to 19bits.

After the initial calibration settling time, the flow rate was increased initially to $\overline{u_1} = 0.0652$ m/s and again allowed to settle for 10 minutes. Force measurements were then logged simultaneously for lift and drag over 600 seconds and saved to a computer. The flow rate was then gradually increased to $\overline{u_1} = 0.098$, 0.132 and 0.162 m/s and the procedure repeated at each increment.

6.5.3 Results

Readings from the Picoscope data logger were logged in a text file that was read into Matlab 13.1 for data processing and plotting. Sample data for E_{S1} is presented in Figures 6.11a and 6.11b for drag and lift respectively. As a signal to force measurement has not been calibrated, results are given in mV as read by the data logger and calibrated to a zero force load cell condition. This was shown to be a valid approach in Chapter 4, as load cells produce a linear response within their working range.

Figure 6.11a shows the drag force for different Re_G numbers with sampling points represented by + symbols. It can seen, that for higher Re_G numbers, the drag force becomes progressively less stable because of the large wake fluctuations. Figure 6.11b shows the lift force at $Re = 14320$. Again sample points are shown by + symbols. The lift force can be seen to oscillate about zero, but the amplitude of the oscillations varies greatly. This is consistent with the two-dimensional numerics elsewhere in this study which show an irregular shedding amplitude at high Re_G.

In E_{S1}, the sample frequency was only just adequate, so for arrays of bodies with a lower void fraction where shedding frequencies are more erratic and at higher frequency, this was not adequate to form a trace line following the lift. This was, of course, not unexpected and, in Chapter 4, purpose-built electronics were designed to address this issue.

Over a long period of time, adequate samples of data can be obtained, which give a useful rms value for lift, as shown in figure 6.12. In this figure, rms values of the approximately measured value of $C_{LG(rms)}$ reduces in E_{39} and E_{64} and is substantially less than that found for the solid cylinder E_{S1}. It is probable that this is the same effect seen in numerical studies of C_{39} and C_{64} (shown in Figure 5.8a), where the wake rolls up far downstream, and, as a result, the induced lift force on these arrays is quite small.

To compare the mean drag force between cases, a scaling value was calculated for each Re_G from E_{S1}, which was itself scaled to $\langle C_D \rangle = 1$ for plotting purposes. This drag coefficient was chosen as this is the expected value in flow regime TRSL1 (Zdravkovich [1997]). These standardized values are plotted in figure 6.13a, where it can be seen that $\langle C_{DG} \rangle$ increases with void fraction (ϕ) and, in E_{64}, overshoots the drag coefficient for the solid cylinder (E_{S1}). This is the same situation as was found in numerical work, where an array of bodies can induce more drag on the ambient flow than a solid body with the same perimeter size.

E_{64} demonstrates that a transition occurs when the drag coefficient starts to reduce with increasing Re_G; at lower void fractions, it increased with Re_G. This does not mean that the drag force is less for higher flow rates. It merely reflects a change in the mechanism causing the induced drag. The same data is plotted in Figure 6.13b, but in this case, the force is plotted in the form of mV.

6.5.4 Flow visualization

The flow visualization component was added after preliminary tests had been successful. To allow for this type of visualization, the channel was supported in mid-air, giving unobstructed visual access to all sides of the working channel. This is important when using light boxes or laser sheets, where the camera often needs to be positioned at 90° to the lightsheet and some distance away. In these experiments, dye injection contrast imaging was used. The slightly rough machine surfaces and ambient lighting acted as a diffuse light source.

6.5.5 Imaging procedure

Dye injection involves using thin filaments of dye to continuously mark the flow field or more precisely individual streamlines within the flow field. This is similar to the wind tunnel smoke technique, but, in this case, dye was released into the flow from a dye rake upstream from the instrumental cell. The rake is shown in Figure 6.14 and incorporates ten, 1.5 mm, stainless steel hypodermic tubes which release a dye filament in line with the flow. The dye rake was positioned across the flow and fed from a single manifold as shown in figure 6.6. The manifold was connected to a large dye reservoir which was hydrostatically balanced with the flume to ensure that a stable filament of dye entered the channel. A solenoid valve was used to rapidly switch the supply to the manifold on and off.

To capture the images of the dye, a mirror was positioned 500 mm under the channel, at 45° to the horizontal. A Dolphin F-145B Allied Vision Technologies camera, with a 36 mm lens, was positioned 1.5 m from the mirror (to reduce parallax distortion which would otherwise be caused by using a wide angle lens). Differential digital images were used. In order to calculate the time sequenced flow, first a clear picture with no dye was used to highlight the contrast differences between frames. Images of the dye moving though the arrays were captured at 4 frames per second, $ISO200$ and resolution 1280×960. Image processing was done on a frame by frame basis. The diagnostic visualization was enhanced by using existing diffused light coming from above and switching other lights off. Using a calibration image without dye (I_c), contrasts with images with dye (I_d) could be highlighted using the algorithm $I = log(I_c/I_d)$. Each frame (I) was written in turn to file and stitched together using ImageMagick into a video AVI file, which employed Matlab image processing software. This technique provided an unusually good visualization of the movement of dye through the array.

6.5.6 Discussion of visualization

Figure 6.15 shows a single contrast enhanced frame for each case, when a steady state flow pattern had been achieved. The images focus on the near-field of the array, but upstream divergence of the streamlines and the resulting wake in the near-field behind

the array are also visible. As previously shown in the numerical work, three types of wake regime can be identified using this technique, depending on the void fraction of the array.

1. The first wake regime exhibited behind the array is found at low void fractions, as in E_7 and E_{20}, (Figures 6.15a and 6.15b). There is little divergence of the dye filaments around the array, indicating a weak blocking effect. Dye filaments pass through the array and intercept with individual bodies in the array, rolling up into discrete identifiable wake signatures for each body.

   In E_{20}, upstream cylinder wakes become redirected by downstream bodies but they still maintain their identity. In E_7 and E_{20}, the overall wake of each array is the accumulation of all the individual wakes generated from bodies within the array. It can also be seen that filament lines exit the arrays approximately in line with their entry.

2. For E_{39}, which has a higher void fraction, the effect of blocking results in divergence of the outer two filament lines around either side of the array. These filaments are then compressed into the shear layer released from the side of the array. Dye filaments, which enter into the array, flow along the path of least resistance and tend to exit the array at 110° to the stagnation point. This is some distance further downstream from the shear layer separation point, which can be seen at approximately 80° from the stagnation point. Due to the relatively large individual body sizes in these experiments (compared to the group size), the exact initialising surface of these angles is likely to be influenced by the positioning of the outer-most individual cylinders. This explanation is supported by the asymmetric nature of these points. The filament line released from the centre of the rake passes through the centre of the array and exits at approximately the downstream stagnation point. At this point, the filament can be seen to form a clearly identifiable and stable wake component behind a perimeter cylinder - which is within the overall group's wake. This indicates that the wake regime, at this void fraction, is not the same as would be expected from a bluff body. This is the same behaviour as was shown on the numerical two dimensional studies on C_{39} and C_{64}. These numerical cases were, of course,

run at a much lower Re_G. The void fraction was also approximately 50% of the experimental case for the same number of bodies.

3. As the void fraction of the array approaches full blocking ($\phi \rightarrow 1$), it will, at some point, exhibit similar characteristics to a solid bluff body. This is found in E_{64}, where the outer three dye filaments can be seen to diverge around each side of the array and filaments which enter the array are again drawn along the path of least resistance and tend to exit much closer to the separation point of the shear layer, on the shoulder sections of the array. One noticeable difference between E_{64} and the lower void fraction cases is the total annihilation of individual cylinder wakes behind the array. This is also seen in E_{S1} and indicates that the base bleed rates, through the array, are so small that the wake region behind the array is dominated by the bluff body wake of the array as a whole. Unlike E_{S1}, E_{64} exhibits a wide wake region downstream of the array, similar to that found in E_{39}. This effect seems to be present despite the bounded nature of the flow.

   Figure 6.15e shows E_{S1} which represents an array with $\phi = 1$. This flow is expected to represent the behaviour of a solid cylinder at $Re_G = 2191$. As there is no base bleed at all through the array, the wake's width immediately behind the body can be seen to be equal to or slightly less than the cylinder diameter. In freestream flow, the wake's width would be expected to grow as a function of distance. The secondary upstream flow caused by a body in the incident shear flow is clearly visible. The dye lines lie quite close to the top channel wall and are reversed by the secondary flow.

   Upstream dye filaments can be seen to diverge around the array. However, dye filaments near the stagnation point seem to 'disappear'. This is an optical illusion created because the base of the cylinder is closer to the camera, thus appearing larger and obstructing the view of the region where the dye transverses around the cylinder. The boundary layer on the cylinder can be seen to detach at 90° to the stagnation point and forms a narrow vortex street. However, due to the zero base bleed, the vortex layers wrap up much closer behind the body and dye can be seen to transfer much quicker into the region immediately

behind the cylinder. This was also as seen in E_{64}.

One anomaly was noted. A dye region can be seen in front of the cylinders which look like a 'bow wave'. This was found to be due to the dye having slight positive buoyancy and travelling up inside the boundary layer on the cylinder wall and into the boundary layer on the top channel wall.

6.6 Conclusion

The apparatus has successfully demonstrated its ability to carry out force measurements on groups of bodies, as well as allowing the simple concept of flow imagery to be revitalised, using modern equipment and image processing.

The flume itself performed as predicted during design and the following points are made:

1. The suspended clear channel section allowed excellent visibility. Uniquely, it was possible to see the working channel from all directions. Three-dimensional wake structures were visible. This gave superior access when compared to typical flumes with free surfaces.

2. The pump and controller allowed precise control of the flow rate. Cavitation only became an issue when the pump exceeded the prescribed experimental flow rates (opening the inlet pipe would allow an increase in the possible flow rate).

3. The source settling tanks successfully reduced the turbulence from the distributing inlet pipe. The honeycomb section plays an important part.

4. The flow in the working section of the channel was very steady at experimental flow rates, as seen in the dye filament visualisation. This demonstrated that the straining section generated an even flow.

5. The gantry load cell arrangement very precisely supported cylinders in the channel. Flow and force measurements derived from it were successfully logged and are presented here.

6. The dye rake produced stable dye filaments which were easily identifiable using contrast imagery.

7. The channel flowrate was successfully measured using an ADV and, with the aid of seeding, very accurately measured the flowrate.

Experimental time was limited, so the focus of the work was to demonstrate and confirm that the apparatus and methods were useful as diagnostic and research tools. This work has successfully measured the drag force on each array for different Re_G numbers and this has been scaled by a solid body to allow comparison between each case. As also seen in the numerical work, the high void fraction case (E_{64}) had a larger drag force as a whole than that of the solid body. The lift force rms value does not uniformly increase to that of a solid cylinder, which indicates that the base bleed initially suppressed the wake roll up, moving it further downstream.

The effect of channel blockage has not been investigated for different void fractions. It is likely that blockage is a product of both channel width and cylinder group void fraction and thus the regime transitions are likely to be affected. For low void fraction cases, the effect of blockage will be substantially less than case E_{64} and E_{S1}.

Using dye contrast visualization, it was possible to identify flow regimes similar to those found in the two-dimensional numerical study of Chapter 5. Transitions in the wake patterns, between cases, have shown the point at which coupling occurs and the effect on individual wake signatures immediately downstream of the array. Wake annihilation within this region has been identified as a predominate feature of higher void fraction arrays, when their wakes come to represent that of a solid body. It is possible to see that the wake width behind the arrays was considerably wider than that for a solid body, which is a consequence of the higher base bleed factor at the relatively low void fractions tested.

The major limitation in the experimental study was time. The design, construction and testing of the apparatus was successful. While the intention was to measure forces on individual bodies using bespoke electronics for each instrumented cylinder, this would have taken an additional three months work. The current work has successfully demonstrated the potential for this to succeed.

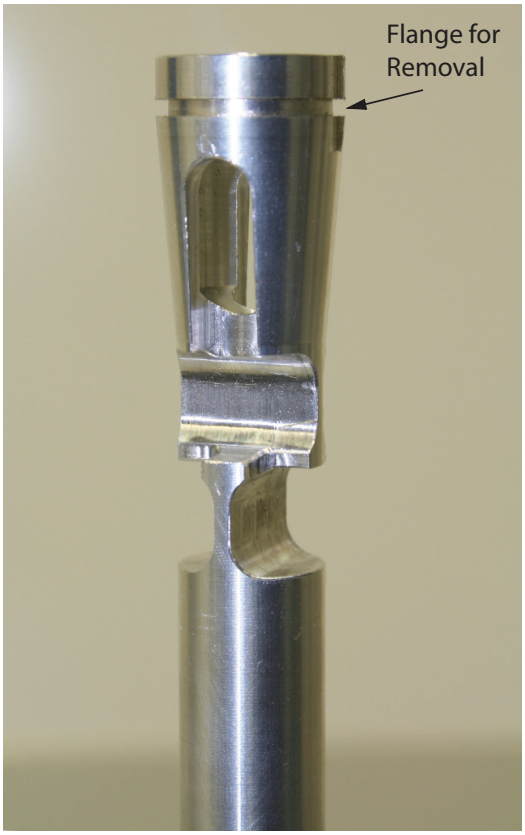

(a)

(b)

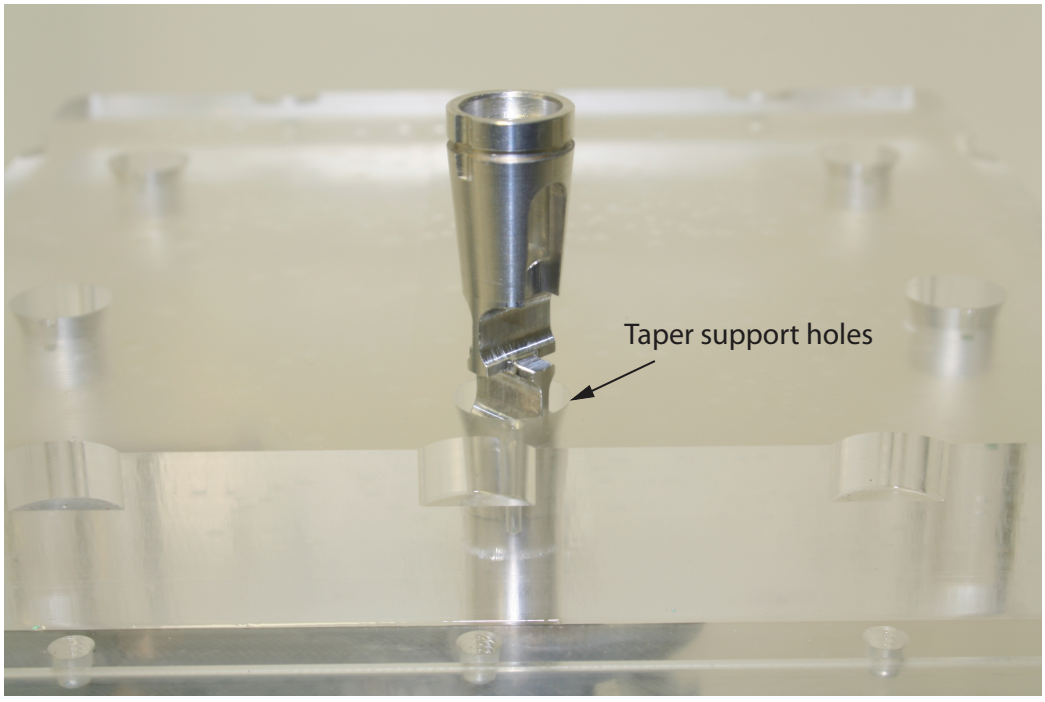

(c)

Figure 6.10: (a) Instrumented cylinder aluminium body. (b) Non instrumented cylinder. (c) Arrangement plate with cylinder partially loaded from above.

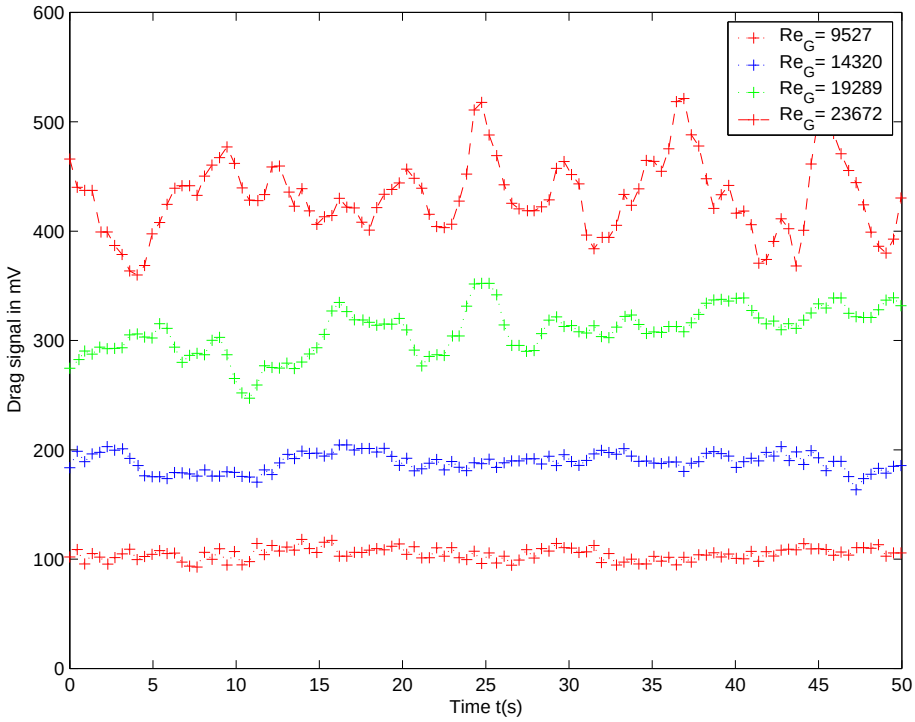

(a)

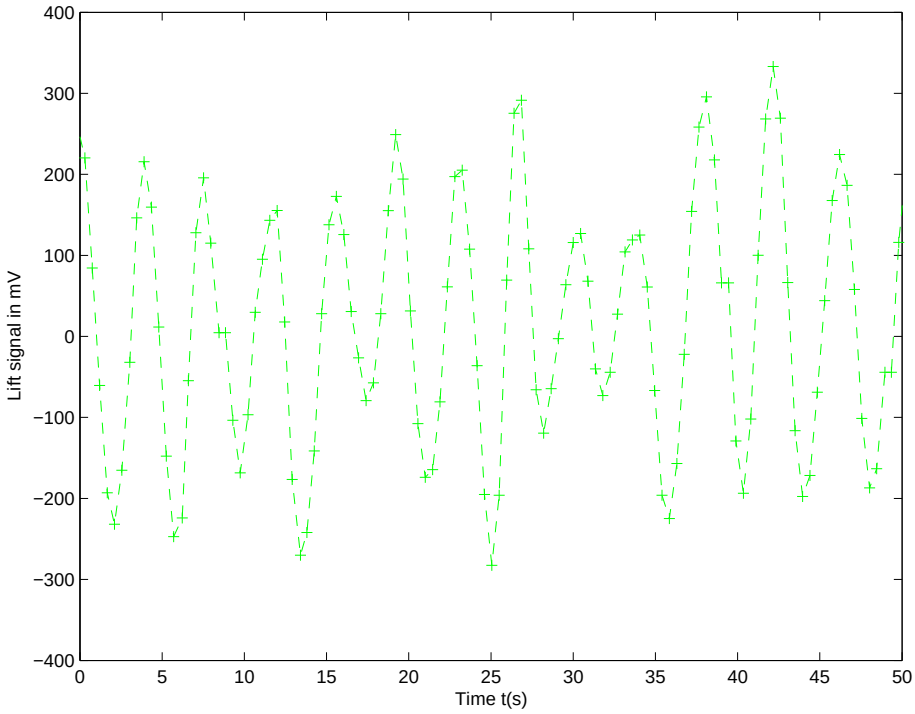

(b)

Figure 6.11: (a) Amplified voltage signal from the strain gauge for the drag on E_{S1} for four different Re_G. (b) Amplified voltage signal from the strain gauge for the lift force for E_{S1} for $Re_G = 19,289$.

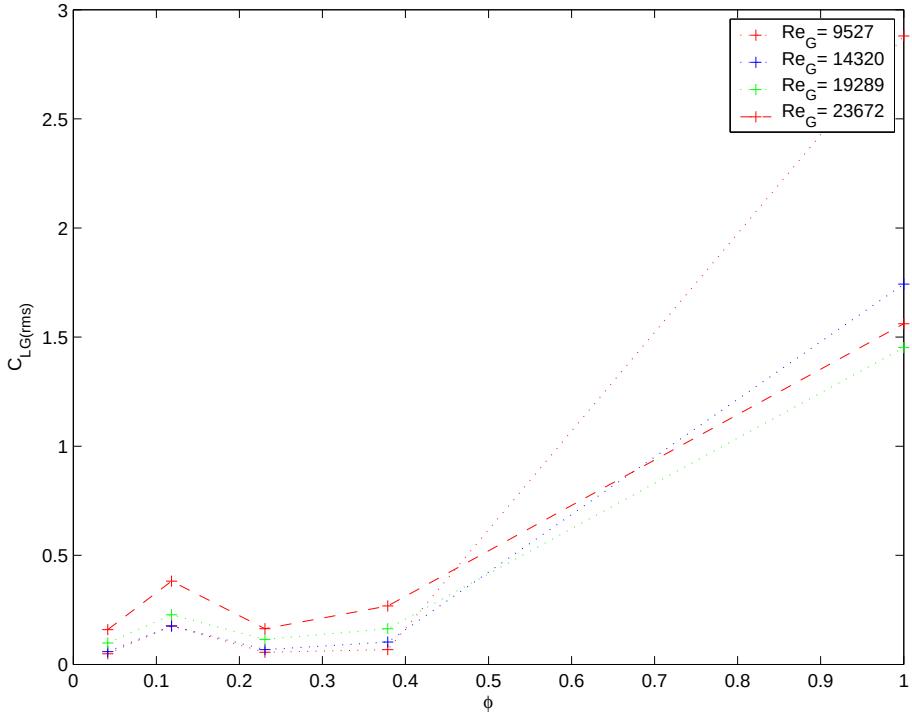

Figure 6.12: Experimentally measured rms lift force normalized by E_{S1} against void fraction for four different Re_G.

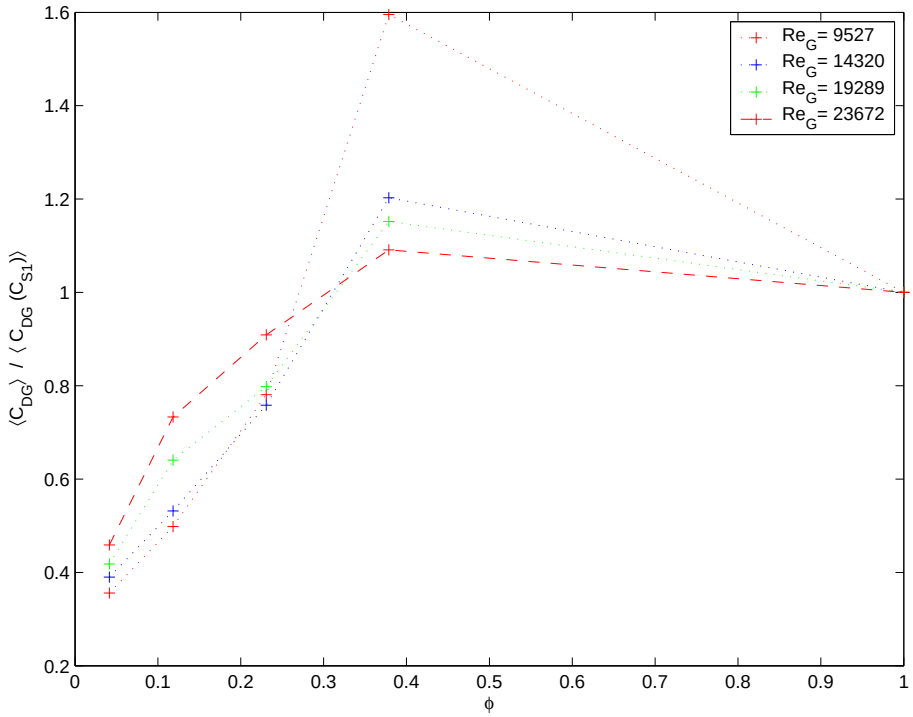

(a)

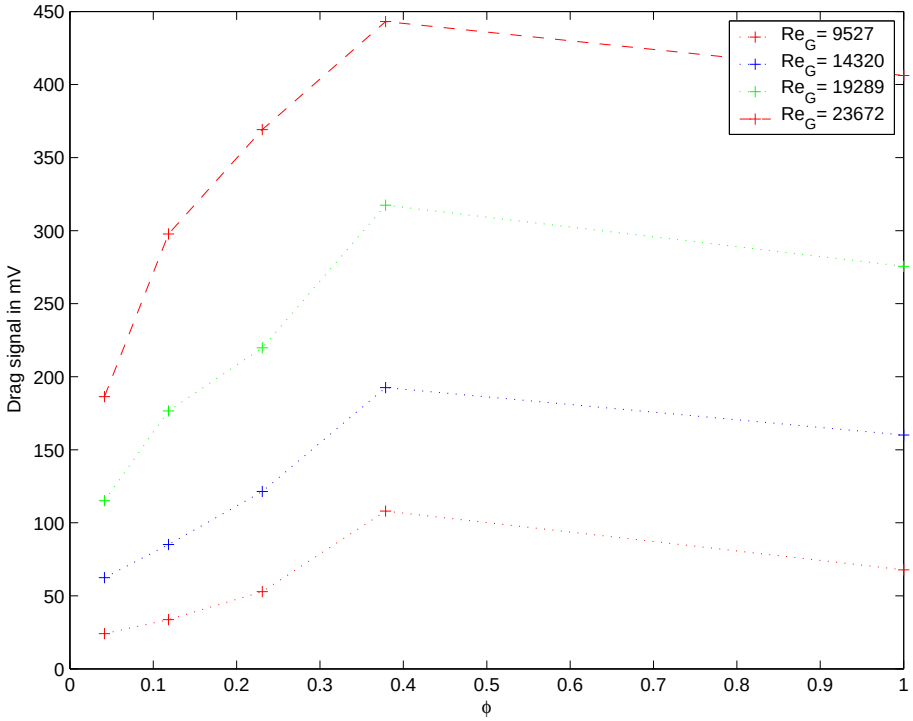

(b)

Figure 6.13: (a) Experimentally measured average drag force normalized by E_{S1} against void fraction for four different Re_G. (b) Experimentally measured average drag force in mV against void fraction for four different Re_G.

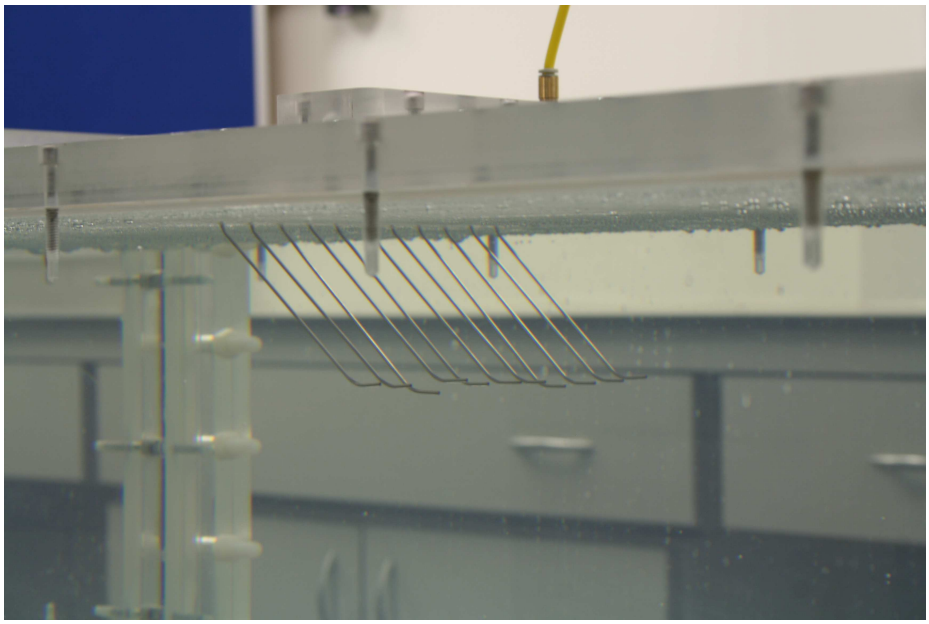

Figure 6.14: Photograph of the dye rake viewed through the channel.

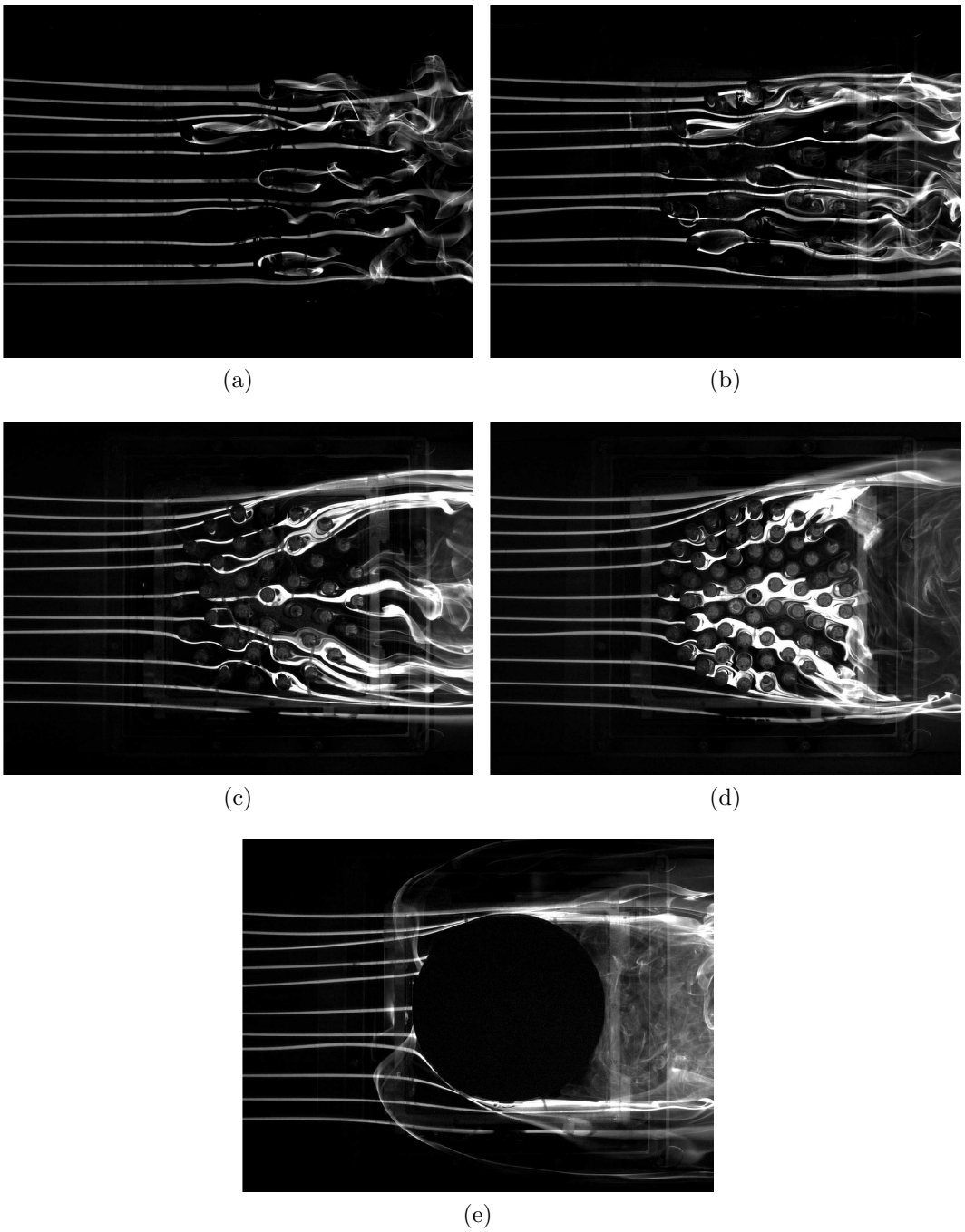

(a) (b) (c) (d) (e)

Figure 6.15: Post-image processing showing dye streamlines for developed flow in (a) E_7, (b) E_{20}, (c) E_{39}, (d) E_{64} and (e) E_{S1}.

Chapter 7

Conclusion and future work

Flow through and around groups of bodies is not well understood and there is little useful comparative research material available. Experimentally, it has been difficult to investigate the interactions within larger groups of bodies, as this required quantification of the flow field which was often impractical. Numerical investigations have been, and indeed still are, limited by the 'development frontier' of the processing power available. Computations are inherently complex, especially in the area of simultaneously resolving substantially different length scales. The objectives of this work, as set out in Chapter 1, were to address both of these issues by developing experimental and numerical approaches designed to harness and utilize the latest technology in both apparatus and computational resources. The former has involved manufacture of custom designed, high precision instrumentation, incorporating multichannel, simultaneous, computer based data capture. The latter required writing an unstructured numerical code, based on a FEM CBS formulation to make use of large scale, distributed memory, parallelized, computational environments.

The work identified a key characteristic that can be used to define a group of bodies, irrespective of its bounding geometry or the constituent geometry of the bodies making up the group. This was determined to be the void fraction (ϕ) and this work concentrates on the range of $0.0159 \leq \phi \leq 0.3787$, whilst simplifying other geometries and the flow regime. The group's perimeter and individual bodies in the group were represented by a circular cylinder and the flow regime was a steady uniform flow.

Numerical investigations

Numerical work focused on the properties of the flow field for six void fractions $\phi = 0.0159$, 0.0454, 0.0884, 0.1451, 0.2154 and 0.3016. Each case was formed from an array of equally spaced cylinders, organized in concentric rings. The number of cylinders in these arrays was $N_C = 7$, 20, 39, 64, 95 and 133.

The main objective of the numerical investigation was to carry out an accurate study of the two-dimensional flow through the six study cases and to compare results with observations from a fully filled array. Reference data was also calculated for a single isolated body.

The method solved the Navier-Stokes equation of incompressible flow in two dimensions. A FEM CBS formulation was employed to conduct DNS calculations on a highly resolved, unstructured mesh consisting of approximately 4 million nodes and 8 million triangular elements. The mesh was developed for each case and based on a mesh independence study for an individual cylinder at the same $Re = 100$. A numerical code was written to carry out the calculations and specifically targeted for the cluster architecture of the Legion supercomputer. The code was written to ensure the highest performance on large problems by decomposition of the domain into regions for parallelization. The code was based on the PETSc numerical library. Domain decomposition was achieved using ParaMETIS. During the development phase, code and numerical validation was conducted using well-known steady and unsteady cases, which were successfully solved to a high degree of accuracy. Parallelized diagnostic tools become increasingly necessary with larger simulations and were developed alongside the numerical code.

The numerical investigation has demonstrated that three flow regimes exist for increasing values of ϕ. These regimes mainly relate to the nature of the wake formation behind the arrays and aspects of this have been investigated using different diagnostic techniques. The conclusion to the numerical work is in §5.6.

Experimental work

The experimental work investigated the properties of the flow field with particular focus on induced drag. Four arrays were selected, each presenting a different void fraction. The values of ϕ for the arrays were $\phi = 0.0414$, 0.1243, 0.2308 and 0.3787 and the number of cylinders in each array was $N_C = 7$, 20, 39 and 64. Experiments

were conducted at $Re_G = (9,527; 14,320; 19,289; 23,672)$. Practical issues limited the domain width and these were taken into account in the investigation planning.

A precision flume was designed and constructed to allow flow visualization and force measurements on interchangeable arrays of bodies. The design also allowed force measurements on individual bodies in the array, by means of an integrated load cell within individual instrumented cylinders. A proto-type instrumented cylinder with an integrated ADC was tested and resolved the two-dimensional forces at 24 bits and 500 samples per second. The data from the ADC was collected and stored by a purpose programmed PIC micro-controller which connected to a computer through a USB bus interface. Manufacture time and project constraints meant that experimental use of the instrumented cylinders has been deferred to future work.

The experiments demonstrated that the apparatus performed successfully on the array experiments over the specified range of void fractions and Reynolds numbers. The conclusion to the experimental work is in §6.6.

7.1 Future work in relation to this project

Future numerical work will include:

1. Conducting a study to determine the effect of blocking.
2. Increasing the number of cylinders used in the array by expanding the value of D_G.
3. Conducting a study at higher Re numbers and possibly using three-dimensional flow.
4. Investigating different group shapes and individual body geometries.
5. Calculating Lagrangian and Eulerian velocities for instantaneous flow within the group of bodies.
6. Improving the code by:
   (a) Conducting in depth comparison of different solvers and their convergence properties. Relating this to use with different pre-conditioners.

(b) Conducting an in depth optimization study, including using pre-fetching algorithms to improve vectorization for matrix inserts.

(c) Determining optimum Blas and LaPack libraries.

(d) Implementing MPI IO for disc operations.

(e) Refining the intercommunication network to match the hardware topology of Legion.

Future experimental work will focus on:

1. Experiments measuring forces on individual cylinders and using the instrumented cylinders. This will provide an insight into the flow field through the array and the effect of blocking upstream from the array.

2. PIV visualization of the upstream flow approaching the array will give another useful measure of the effect of blocking. PIV visualization downstream will allow a more definitive evaluation of which wake regime is operating.

3. Further experiments with dye contrast imaging, including residence time measurements (the time that the dye is within the array) which can be used to calculate experimental Lagrangian values.

4. The apparatus was designed to allow for other array shapes and different individual constituent body shapes. Future work on these will give insight into their importance to the overall flow profile.

5. Minor changes can be made to the experimental apparatus, which will improve its future use as follows:

   (a) Adding extra length to the flume channel would improve stability at higher flow rates as the settling distance of 1.75m will not be adequate if rates are increased.

   (b) It is often useful to have low flow rates for visualization, especially when using dye imagery. These are not achievable with the current Lowrana pump and it is suggested that a second smaller pump should made available

in parallel. This could be used as an alternative and run from the same controller via a two way, break-before-make switch.

(c) The honeycomb gauze material should be changed from a felt to a thicker, less dense medium to reduce the pressure drop across it. The honeycomb section should be raised by 100 mm to reduce chances of spill over.

(d) Tuning vanes should be installed in the settling tank to even out the exit flow.

(e) A water level indicator should be installed on one of the tanks to facilitate filling operations.

(f) The supporting table of the channel should be re-designed to reduce its impact on visualization of the floor.

(g) Three-phase chokes should be installed as the rectifiers generate unnecessary electrical noise.

7.2 Closing statement

Numerical investigations may generally be the 'cheapest' and most flexible fluid investigation tool, but their limitations mean that experimental work still has a useful and complimentary role where numerical investigation is not possible. This study, by using both approaches, has allowed different diagnostics to be utilized. The structuring of the investigations has taken these into account. It has used simplified case studies and experiments to test and demonstrate new platforms which can be used in future multibody research.

Given that the main aim and objective was to develop and test new multibody methodologies, a measure of reality and restraint was always needed in terms of the number of test cases/experiments which should be undertaken at this stage. The results have, however, identified specific and detailed features of the flow field and allowed three distinct regimes to be identified. All the main objectives set out in §1.1 have been met. The major advancement from previous research is the level of resolution that has been achieved.

Appendix A

A.1 Appendix

```
Run: jobbot Set_Value -value-name=mesh-dir     -value-string='-root-dir',/
Run: jobbot Set_Value -value-name=results-dir  -value-string='-root-dir',/results/
Run: jobbot Set_Value -value-name=problem-name -value-string=Cavity

Run: jobbot UseJobBot -timer=1 -file-name='results-dir','problem-name',_logfile.txt

Run: exe Build_Domain -name=Domain
Run: Domain Setup  -gmsh-file='mesh-dir',Cavity60node.msh

// Domain node
Run: jobbot Set_Value -value-name=DOMAIN_NODES -value-int=0
Run: Domain Group_Elements -g-tag='DOMAIN_NODES' -element-type=1 -domain-tag=6

// Domain elements
Run: jobbot Set_Value -value-name=DOMAIN_ELEMENTS -value-int=1
Run: Domain Group_Elements -g-tag='DOMAIN_ELEMENTS' -element-type=3 -domain-tag=6

// Setup U=1
Run: Domain Group_Elements -g-tag=2 -element-type=1 -domain-tag=3

// Setup U=0
Run: Domain Group_Elements -g-tag=3 -element-type=1 -domain-tag=1,2,4

// Setup V=0
Run: Domain Group_Elements -g-tag=4 -element-type=1 -domain-tag=1,2,3,4

// Setup P=0
Run: Domain Group_Elements -g-tag=5 -element-type=1 -element-tag=1

Run: exe Connect_DL -name=dl_module -dl-file-name='-root-dir',/Solver_2d.so
Run: dl_module CBS_Direct_Solver_3D -name=Solver  -mesh=Domain

Run: Solver Add_Wall -g-tag=2 -b-tag='U' -value=1.0
Run: Solver Add_Wall -g-tag=3 -b-tag='U' -value=0.0
Run: Solver Add_Wall -g-tag=4 -b-tag='V' -value=0.0
Run: Solver Add_Wall -g-tag=5 -b-tag='P' -value=0.0
Run: Solver Set_Pramiters -viscosity=0.001 -density=1.0

Run: jobbot Set_Value -value-name=v1_limit -value-double=0
Run: jobbot Set_Value -value-name=v2_limit -value-double=100

Run: exe Build_Loop -name=fast_loop
Run: fast_loop Add  -object=Solver -function=Solver
Run: fast_loop Add  -object=jobbot -function=Set_Value -value-name=v1_limit -value-
add-double=1;

Run: fast_loop Run -loop-count=0 -code-time=0.0 -loop-time=0.0 -limit-1='v1_limit',
<,'v2_limit'

Run: Domain Write_File  -pos-file-name='results-dir','problem-name',.pos

Run: exe Exit
```

A.2 Appendix

Table 3: Results for steady test case 2D-1

	Unknowns	c_D	c_L	L_a	ΔP	Mem.	CPU time	MFlop rate
1	200607	5.5567	0.0106	0.0845	0.1172	15	788	1600 PEAK
	51159	5.5567	0.0106	0.0843	0.1172	4	273	
	13299	5.5661	0.0105	0.0835	0.1169	1	144	
3a	10800	5.6000	0.0120	0.0720	0.1180	2.5	121	75 PEAK
4	297472	5.5678	0.0105	0.0847	0.1179	137	31000	445 LINP
	75008	5.5606	0.0107	0.0849	0.1184	73	8000	
	19008	5.5528	0.0118	0.0857	0.1199	57	2000	
6	1314720	5.8190	0.0110	0.0870	0.1230	40	80374	13 LINP
	332640	5.7740	0.0030	0.0830	0.1230	10	10461	
	85140	5.7890	-0.0060	0.0870	0.1230	2.6	1262	
7a	294912	5.5846	0.0106	0.0846	0.1176	75	192	13 LINP
	73728	5.5852	0.0105	0.0845	0.1176	19	47	
	18432	5.5755	0.0102	0.0842	0.1175	5	13	
8a	20487	5.5760	0.0110	0.0848	0.1170	9.0	2574	8.3 LINP
	6297	5.5710	0.0130	0.0846	0.1160	2.9	362	
	2298	5.4450	0.0200	0.0810	0.1110	1.3	109	
9a	240000	5.5803	0.0106	0.0847	0.1175	53	9200	34 LINP
	60000	5.5786	0.0106	0.0847	0.1173	10	1400	
	15000	5.5612	0.0109	0.0848	0.1166	2.5	200	
10	2665728	5.5755	0.0106	0.0780	0.1173	350	677	90 LINP
	667264	5.5718	0.0105	0.0770	0.1169	89	169	
	167232	5.5657	0.0102	0.0730	0.1161	22	52	
	42016	5.5608	0.0091	0.0660	0.1139	5	18	
12	32592	5.5069	0.0132	0.0830	0.1155	18	1796	5.5 LINP
	26970	5.5125	0.0056	0.0827	0.1154	15	1099	
	22212	5.6026	-0.0031	0.0815	0.1167	13	3437	
13a	25410	5.6145	0.0159	0.8315	3.0002	4	14203	90 LINP
	12738	5.6114	0.0169	0.8224	2.9943	2	3018	
	6562	5.7377	0.0514	0.8107	3.2277	1		
14a	3077504	5.6323	0.0137	0.0782	0.1159	214	15300	6.6 LINP
	768704	5.6382	0.0102	0.0775	0.1156	53	5490	
	191840	5.5919	-0.0009	0.0750	0.1143	13	2800	
14b	30775296	5.5902	0.0108	0.0853	0.1174	5340	1534	1334 LINP
	7695104	5.6010	0.0110	0.0844	0.1174	1341	400	
	1922432	5.6227	0.0113	0.0833	0.1172	338	119	
14c	797010	5.5708	0.0167	0.0837	0.1168	460	8000	334 LINP
	363457	5.5598	0.0142	0.0835	0.1166	230	3290	
	176396	5.5106	0.0046	0.0835	0.1150	110	2560	
15a	432960	5.5602	0.0329	0.0730	0.1054	4.4	179986	7.4 LINP
	108240	5.6300	0.0751	0.0720	0.1037	1.1	13593	
	27060	5.7769	0.2085	0.0680	0.0998	0.3	688	
17	111342	5.5610	0.0107		0.1170	87	2568	8.3 LINP
	60804	5.5520	0.0102		0.1168	47	1092	
	19416	5.5160	0.0099		0.1158	15	373	
	lower bound	5.5700	0.0104	0.0842	0.1172			
	upper bound	5.5900	0.0110	0.0852	0.1176			

A.3 Appendix

Table 4: Results for time–periodic test case 2D-2

	Unknowns								
	Space	Time	c_{Dmax}	c_{Lmax}	St	Δ P	Mem.	CPU time	MFlop rate
1	267476	67	3.2224	0.9672	0.2995	2.4814	—	—	1600 PEAK
	267476	34	3.2030	0.9223	0.2941	2.4664	—	—	
	267476	18	3.1605	0.8026	0.2901	2.4466	—	—	
	68212	67	3.2171	0.9591	0.2995	2.5009	—	—	
	17732	68	3.2168	0.9295	0.2979	2.5573	—	—	
3	12800	34	3.2200	0.9720	0.2960	2.4700	2.5	789	75 PEAK
4	297472	670	3.2460	0.9840	0.2985	2.4900	137	6600	445 LINP
	297472	338	3.2710	0.9800	0.2959	2.4870	137	3400	
	297472	172	3.3200	0.9720	0.2907	2.4810	137	1700	
	75008	670	3.2410	0.9910	0.2985	2.5020	73	2350	
	19008	674	3.2320	1.0260	0.2967	2.5320	57	1350	
6	332640	12000	4.1210	1.6120	0.3330	3.1420	10	10086	13 LINP
	85140	6000	4.7330	2.0600	0.3380	3.4300	2.6	1259	
7a	294912	36	3.2358	1.0069	0.3003	2.4892	75	6167	13 LINP
	294912	19	3.2356	1.0000	0.2973	2.4871	75	6391	
	294912	10	3.2152	0.9028	0.2881	2.4715	75	4994	
	73728	36	3.2443	1.0261	0.2994	2.4929	19	1946	
	18432	36	3.2706	1.0695	0.2968	2.5035	5	445	
8a	29084	66	3.2240	1.0060	0.3020	2.4860	11	4992	8.3 LINP
	29084	33	3.2470	1.0740	0.3030	2.5010	11	3777	
	29084	16	3.2900	1.2500	0.3130	2.5700	11	3217	
	8764	66	3.1740	0.9640	0.3000	2.4630	3.6	1000	
	2978	70	2.8920	0.5540	0.2890	2.2870	1.5	339	
9a	240000	5000	3.2267	0.9862	0.3017	2.4833	53	32500	34 LINP
	60000	10000	3.2232	0.9830	0.3012	2.4773	10	8550	
	60000	5000	3.2232	0.9832	0.3012	2.4773	10	4500	
	60000	2500	3.2232	0.9836	0.3012	2.4773	10	3400	
	15000	5000	3.2058	0.9651	0.2994	2.4587	2.5	3240	
10	667264	612	3.2314	0.9999	0.2973	2.4707	128	8545	90 LINP
	667264	204	3.2351	1.0123	0.2957	2.4734	128	2850	
	667264	68	3.2771	1.1205	0.2997	2.4961	128	1065	
	167232	188	3.2498	1.0081	0.2927	2.4410	32	655	
	42016	164	3.2970	0.8492	0.2713	2.3423	8	147	
13b	25410	6755	3.1822	1.0692	0.2960	2.6066	5.1	44710	90 LINP
	25410	3877	3.1895	1.0883	0.2968	2.6057	4.8	27175	
	25410	1678	3.2043	1.1268	0.2979	2.5307	4.7		
	12738	6799	3.1945	1.1233	0.2941	2.6140	2.9	13045	
	6562	7223	3.1317	1.2961	0.2768	3.0253	1.8		
15a	432960	7790	3.0804	0.7256	0.2778	2.1330	4.4	108844	7.4 LINP
	108240	4003	3.1677	0.6880	0.2646	2.0954	1.1	34876	
	108240	3859	3.1096	0.8249	0.2841	2.1105	1.1	58003	
	27060	1985	3.2544	0.5658	0.2336	1.9727	0.3	3796	
	27060	1670	3.1759	0.7656	0.2740	1.9961	0.3	4188	
	lower bound		3.2200	0.9900	0.2950	2.4600			
	upper bound		3.2400	1.0100	0.3050	2.5000			

A.4 Appendix

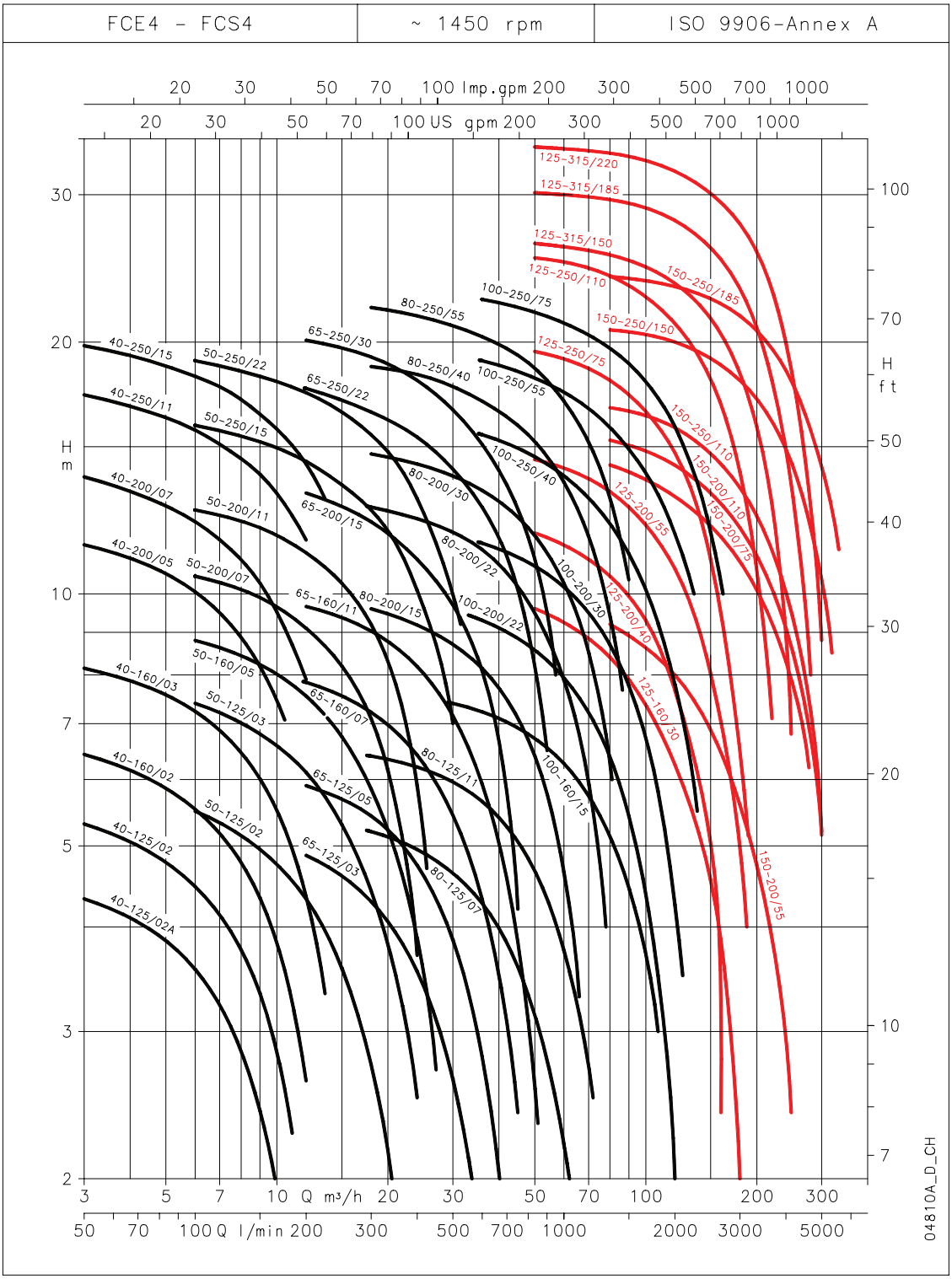
FCE4 – FCS4
~ 1450 rpm
ISO 9906-Annex A
20 30 50 70 100 Imp.gpm 200 300 500 700 1000
20 30 50 70 100 US gpm 200 300 500 700 1000
H m
H ft
Q m³/h
Q l/min
125-315/220
125-315/185
125-315/150
125-250/110
150-250/185
100-250/75
80-250/55
150-250/150
125-250/75
65-250/30
80-250/40
100-250/55
40-250/15
50-250/22
65-250/22
40-250/11
50-250/15
150-250/110
100-250/40
80-200/30
125-200/55
150-200/110
150-200/75
40-200/07
50-200/11
65-200/15
80-200/22
100-200/30
125-200/40
40-200/05
50-200/07
65-160/11
80-200/15
100-200/22
125-160/30
50-160/05
40-160/03
65-160/07
50-125/03
80-125/11
100-160/15
40-160/02
65-125/05
50-125/02
150-200/55
40-125/02
65-125/03
80-125/07
40-125/02A
04810A_D_CH

A.5 Appendix

ITT Lowara

FCS4 SERIES
OPERATING CHARACTERISTICS AT 50 Hz, 4 POLES

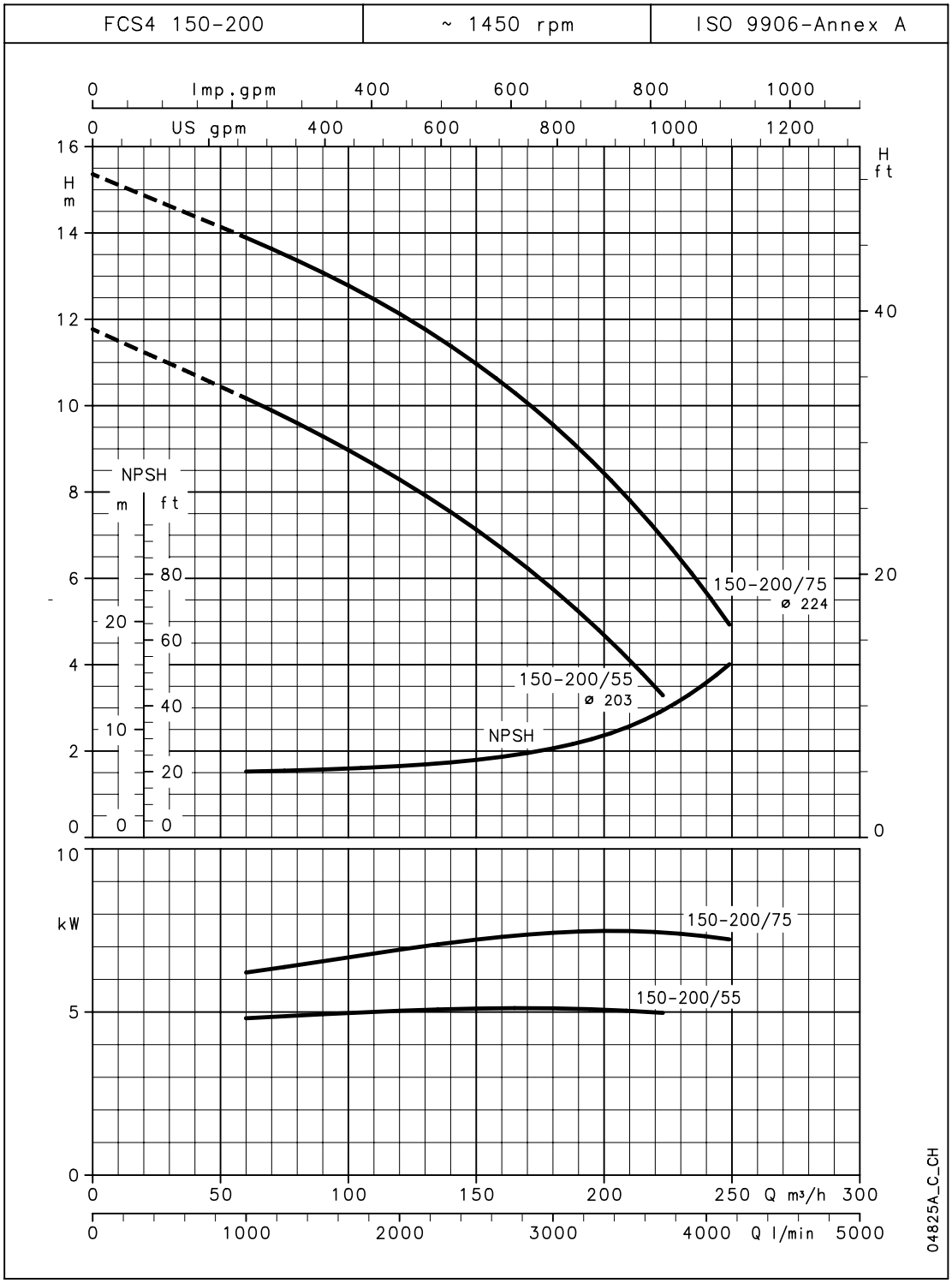

The declared NPSH values are laboratory values: for practical use we suggest increasing these values by 0.5 m.
The declared performances are valid for liquids with density $\rho = 1{,}0$ kg/dm ^{3} and kinematic viscosity $\upsilon = 1$ mm ^{2}/s.

A.6 Appendix

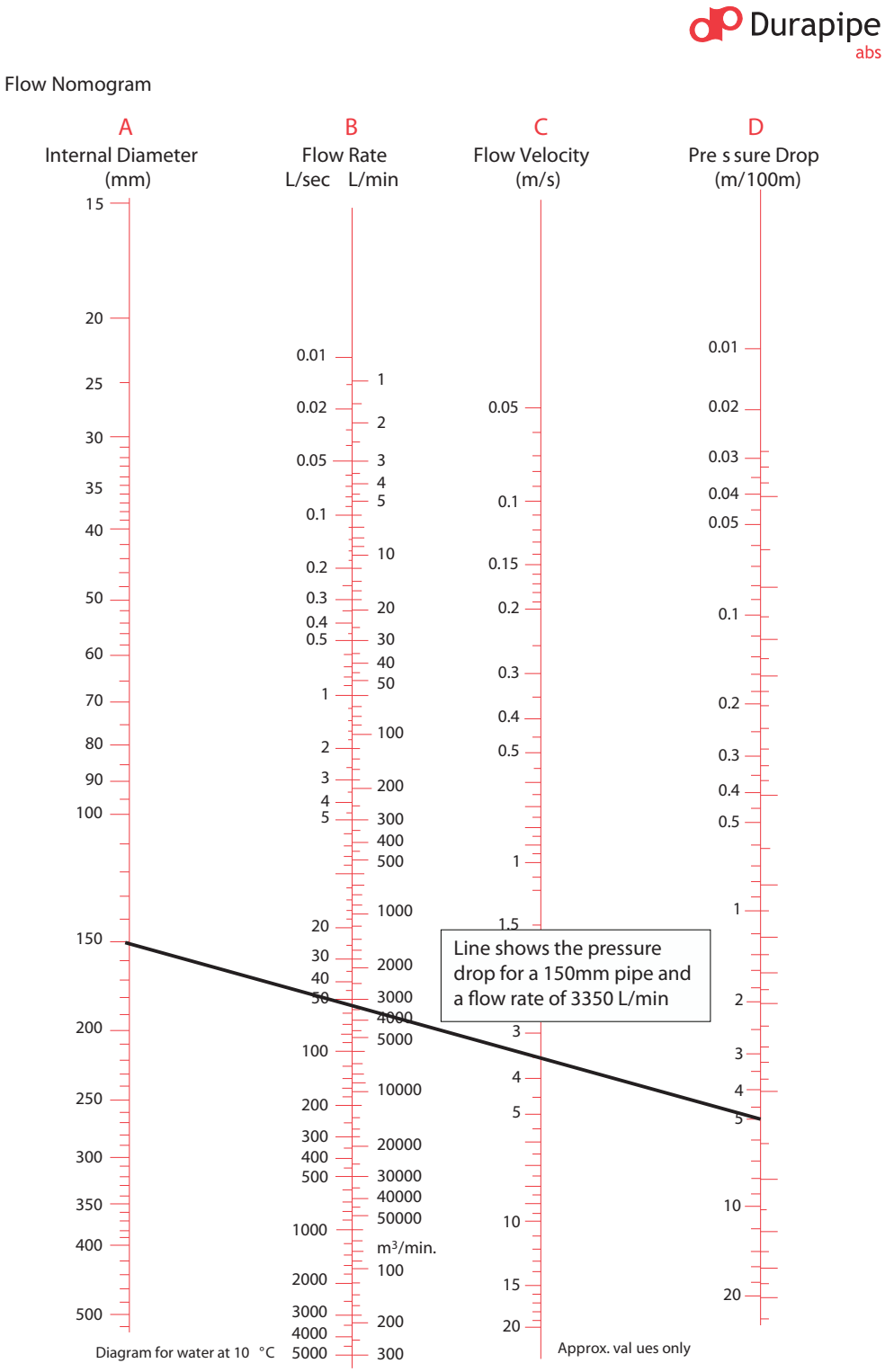
Durapipe
abs
Flow Nomogram
A
Internal Diameter
(mm)
B
Flow Rate
L/sec L/min
C
Flow Velocity
(m/s)
D
Pre s sure Drop
(m/100m)
Line shows the pressure drop for a 150mm pipe and a flow rate of 3350 L/min
m³/min.
Diagram for water at 10 °C
Approx. val ues only

A.7 Appendix

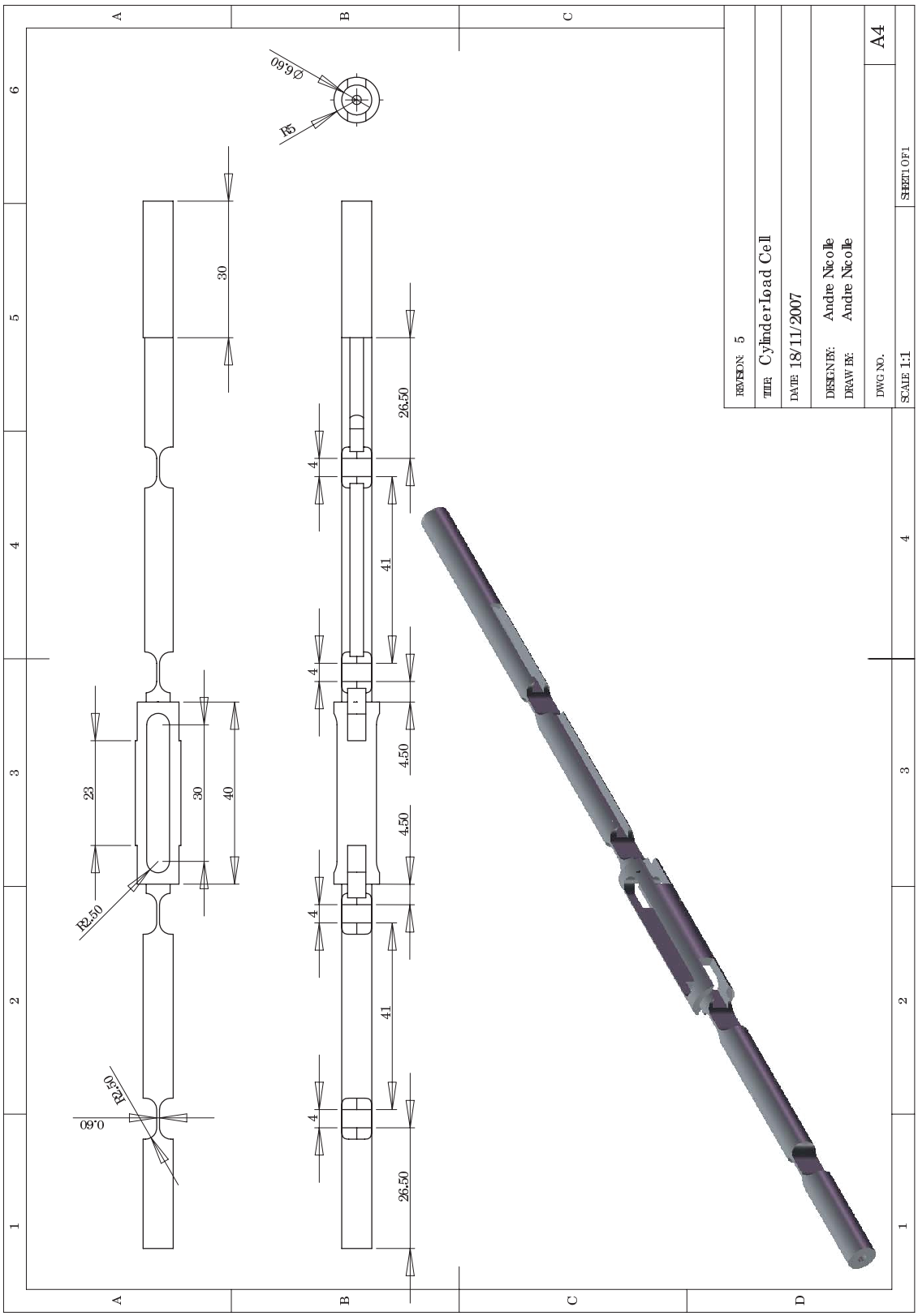
Ø6.60
R5
30
26.50
4
41
4
4.50
4.50
4
41
4
26.50
23
30
40
R2.50
R2.50
0.60
REVISION 5
TITLE Cylinderload Cell
DATE 18/11/2007
DESIGN BY: Andre Nicolle
DRAWN BY: Andre Nicolle
DWG NO.
A4
SCALE 1:1
SHEET 1 OF 1

A.8 Appendix

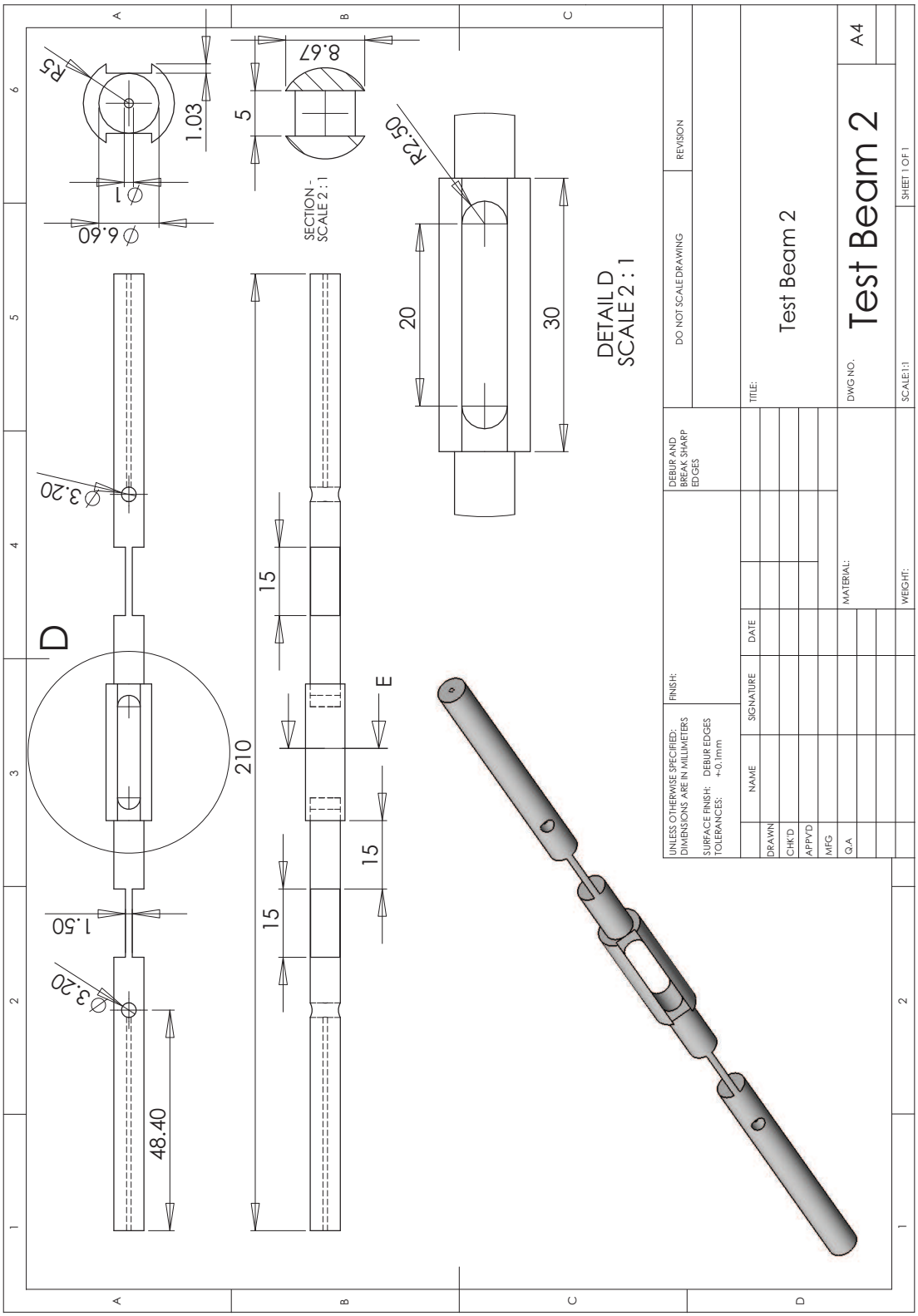
R5
1.03
8.67
5
SECTION -
SCALE 2 : 1
R2.50
20
30
DETAIL D
SCALE 2 : 1
Ø6.60
Ø1
Ø3.20
D
210
15
15
15
E
1.50
Ø3.20
48.40
DEBUR AND BREAK SHARP EDGES
FINISH:
UNLESS OTHERWISE SPECIFIED:
DIMENSIONS ARE IN MILLIMETERS
SURFACE FINISH: DEBUR EDGES
TOLERANCES: +-0.1mm
NAME
SIGNATURE
DATE
DRAWN
CHK'D
APPV'D
MFG
Q.A
MATERIAL:
WEIGHT:
DO NOT SCALE DRAWING
REVISION
TITLE:
Test Beam 2
DWG NO.
Test Beam 2
A4
SCALE:1:1
SHEET 1 OF 1

A.9 Appendix

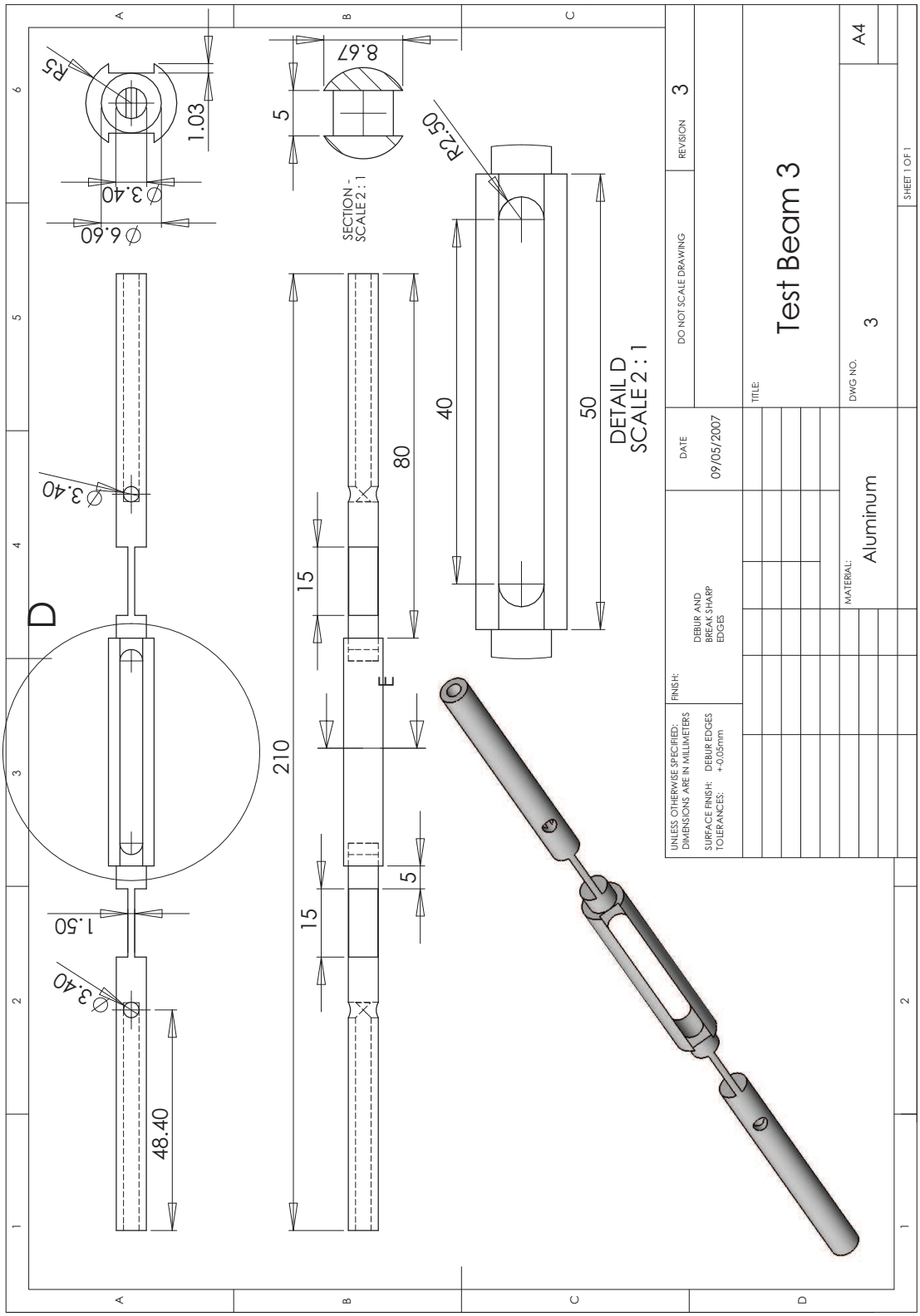
Test Beam 3
A4
Aluminum
DO NOT SCALE DRAWING
09/05/2007
REVISION 3
DWG NO. 3
SHEET 1 OF 1
DEBUR AND BREAK SHARP EDGES
DETAIL D
SCALE 2 : 1
SECTION -
SCALE 2 : 1
R5
R2.50
8.67
5
1.03
Ø3.40
Ø6.60
210
80
40
50
15
15
5
48.40
1.50
Ø3.40
Ø3.40
D
E

A.10 Appendix

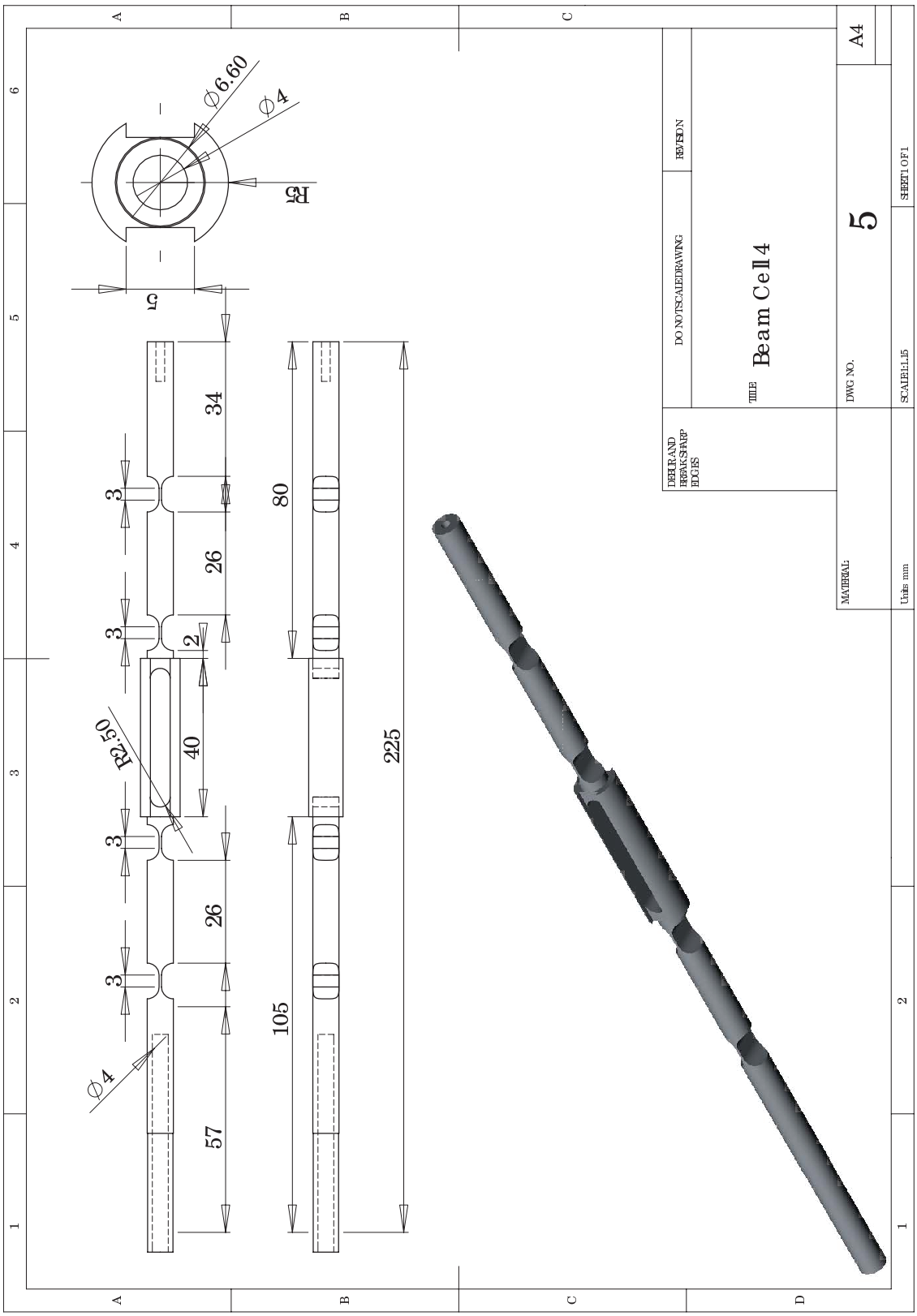

A.11 Appendix

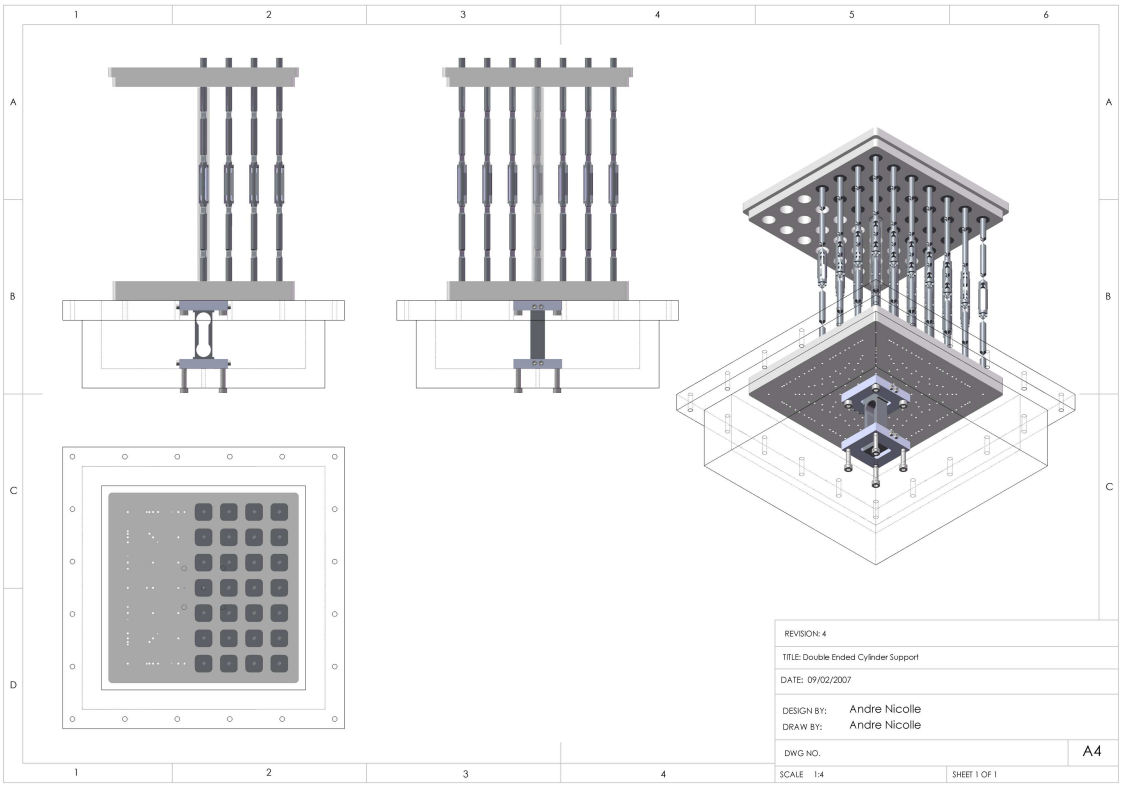

A.12 Appendix

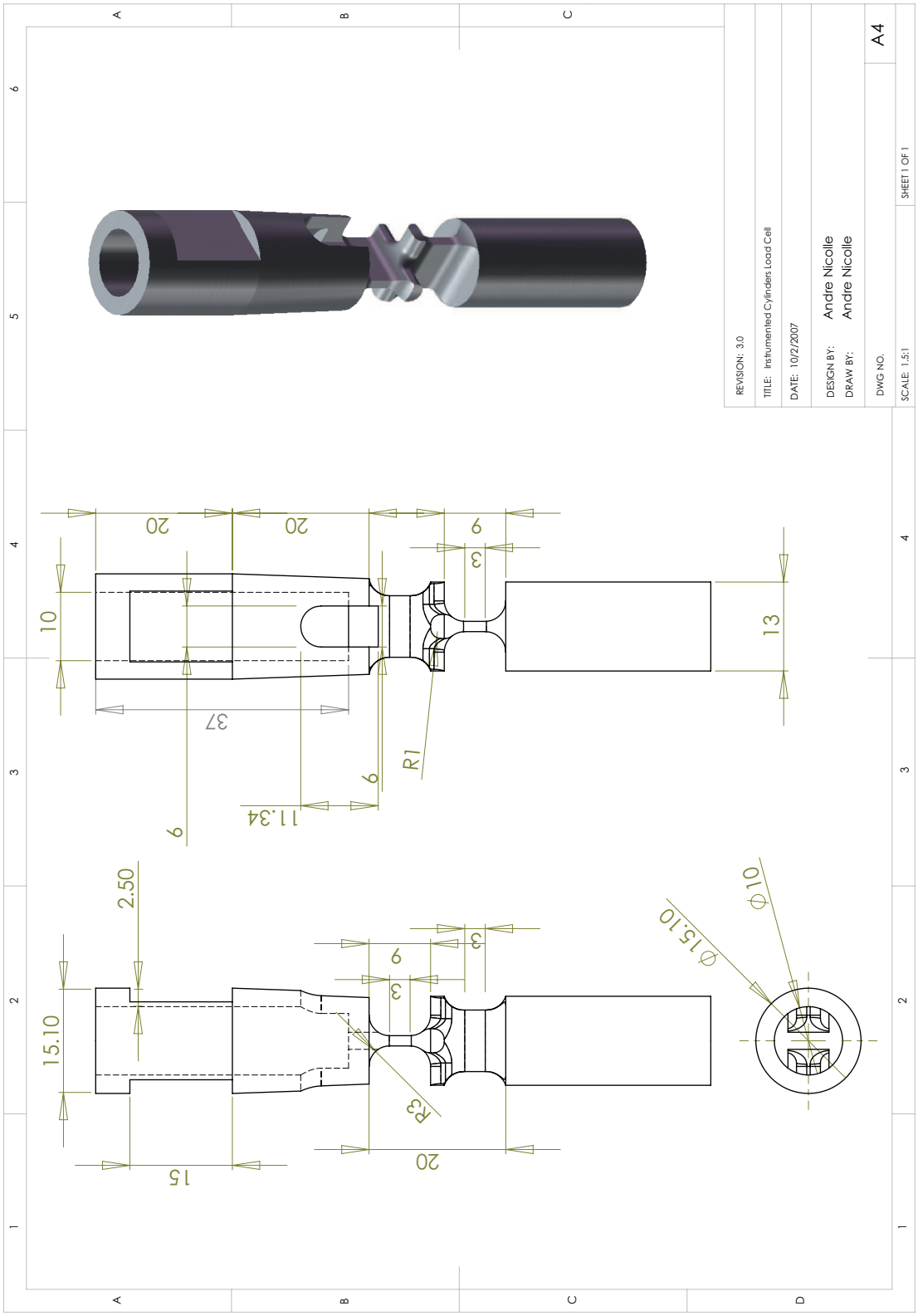

A.13 Appendix

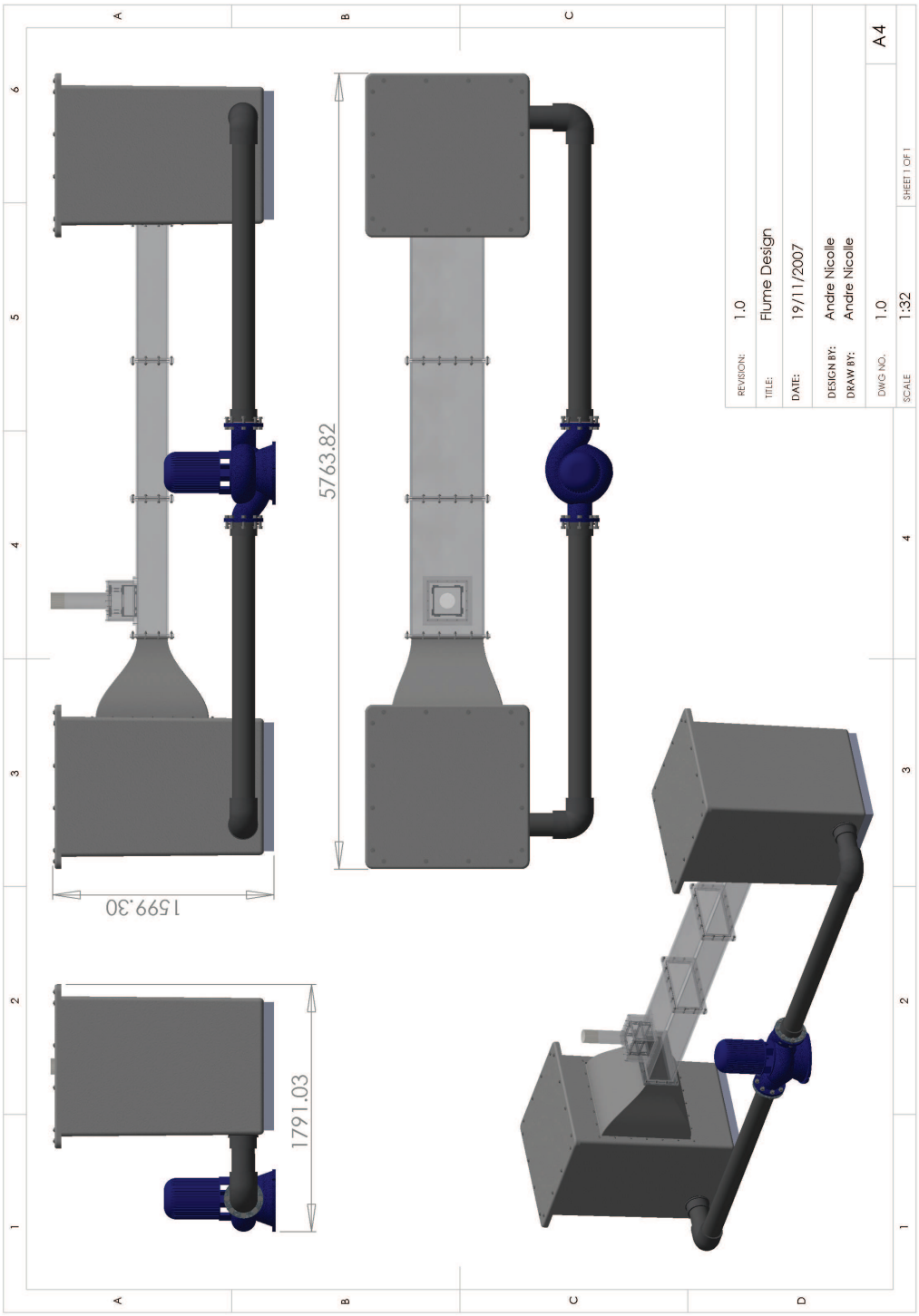

A.14 Appendix

```
Run: exe Load_Command -file-name=dir.txt

Run: jobbot Set_Value -value-name=problem-name -value-string=C_07
Run: jobbot Set_Value -value-name=code_run_time -value-double=165600  //1 day 22 hour

Run: jobbot UseJobBot -timer=0 -file-name='results-dir','problem-name',_logfile.txt

Run: exe Build_Domain -name=Domain
Run: Domain Setup  -gmsh-file='mesh-dir','problem-name',_data.msh

// Domain node
Run: jobbot Set_Value -value-name=DOMAIN_NODES -value-int=0
Run: Domain Group_Elements -g-tag='DOMAIN_NODES' -element-type=1 -domain-tag=
1,2,3,33,38,67,68,97,98,127,128,157,158,187,188,217,218,247,248

// Domain elements
Run: jobbot Set_Value -value-name=DOMAIN_ELEMENTS -value-int=1
Run: Domain Group_Elements -g-tag='DOMAIN_ELEMENTS' -element-type=3 -domain-tag=
1,2,3,33,38,67,68,97,98,127,128,157,158,187,188,217,218,247,248

// Setup U=1
Run: Domain Group_Elements -g-tag=2 -element-type=1 -wall-tag=35

// Setup U=0
Run: Domain Group_Elements -g-tag=3 -element-type=1 -wall-tag=
44,45,46,47,74,75,76,77,104,105,106,107,134,135,136,137,164,165,166,167,194,195,196,19
7,224,225,226,227

// Setup V=0
Run: Domain Group_Elements -g-tag=4 -element-type=1 -wall-tag=
35,21,25,29,31,34,36,44,45,46,47,74,75,76,77,104,105,106,107,134,135,136,137,164,165,1
66,167,194,195,196,197,224,225,226,227

// Setup P=0
Run: Domain Group_Elements -g-tag=5 -element-type=1 -wall-tag=30

// Setup slip
Run: Domain Group_Elements -g-tag=6 -element-type=2 -wall-tag=
35,30,21,25,29,31,34,36,44,45,46,47,74,75,76,77,104,105,106,107,134,135,136,137,164,16
5,166,167,194,195,196,197,224,225,226,227

Run: exe Build_Boundray_Data -name=Boundary -mesh=Domain
Run: Boundary Add_Wall -g-tag=2 -b-tag='U'  -value=1.0
Run: Boundary Add_Wall -g-tag=3 -b-tag='U'  -value=0.0
Run: Boundary Add_Wall -g-tag=4 -b-tag='V'  -value=0.0
Run: Boundary Add_Wall -g-tag=5 -b-tag='P'  -value=0.0
Run: Boundary Add_Wall -g-tag=6 -b-tag=7    -value=0.0
Run: Boundary Setup

Run: exe Build_Body_Force -name=Wall_Force  -mesh=Domain
Run: Domain Group_Elements -g-tag=7 -element-type=2  -wall-tag=44,45,46,47
Run: Wall_Force SetupSurface -g-tag=7 -tag-number=0
Run: Domain Group_Elements -g-tag=8 -element-type=2  -wall-tag=74,75,76,77
Run: Wall_Force SetupSurface -g-tag=8 -tag-number=1
Run: Domain Group_Elements -g-tag=9 -element-type=2  -wall-tag=104,105,106,107
Run: Wall_Force SetupSurface -g-tag=9 -tag-number=2
Run: Domain Group_Elements -g-tag=10 -element-type=2 -wall-tag=134,135,136,137
Run: Wall_Force SetupSurface -g-tag=10 -tag-number=3
Run: Domain Group_Elements -g-tag=11 -element-type=2 -wall-tag=164,165,166,167
Run: Wall_Force SetupSurface -g-tag=11 -tag-number=4
Run: Domain Group_Elements -g-tag=12 -element-type=2 -wall-tag=194,195,196,197
Run: Wall_Force SetupSurface -g-tag=12 -tag-number=5
Run: Domain Group_Elements -g-tag=13 -element-type=2 -wall-tag=224,225,226,227
Run: Wall_Force SetupSurface -g-tag=13 -tag-number=6

Run: exe Load_Command -file-name=solver.txt
```

A.15 Appendix

```
Run: exe Build_Solver -name=Solver -mesh=Domain -boundary=Boundary
Run: Solver Set_Pramiters -viscosity=0.01 -density=1.0 -file-priority=1

Run: exe Build_Loop -name=fast_loop
Run: fast_loop Add  -object=Solver     -function=Solver
Run: fast_loop Add  -object=Wall_Force -function=Calculate

Run: exe Build_Loop -name=slow_loop
Run: slow_loop Add  -object=fast_loop  -function=Run -code-time='run_time' -loop-time=
3600
Run: slow_loop Add  -object=jobbot         -function=Print_Value
Run: slow_loop Add  -object=Wall_Force -function=Write_File  -file-type=csv
Run: slow_loop Add  -object=Domain     -function=Write_File  -msh-file-name=default

Run: slow_loop Run -code-time='code_run_time'

Run: Wall_Force Write_File -file-type=csv
Run: Domain Write_File -msh-file-name=default

End:
```

Bibliography

DJ Acheson. Elementary fluid dynamics. Oxford University Press, 1990.

P. Anagnostopoulos and G. Iliadis. Nonlinear dynamics and pattern formation in turbulent wake transition. International Journal for Numerical Methods in Engineering, 22:1061–1074, 1996.

D.j. Ball and C.D Hall. Drag of yawed pile groups at low reynold number. ASCE J.Roy. Aero. Soc, 90:128–38, 1980.

Dwight Barkley and Ronald D. Henderson. Three-dimensional floquet stability analysis of the wake of a circular cylinder. Journal of Fluid Mechanics, 322:215–241, 1996.

G.K. Batchelor. An introdution to fluid dynamics. Cambridge University Press, 1967.

A. Betz. A method for the direct determination of profile drag. Z. Flugtechn. Motorluftschiffahrt., 16, 1925.

S. Bhattacharyya, S. Dhinakaran, and A. Khalili. Fluid motion around and through a porous cylinder. Chemical Engineering Science, 61(13):4451–4461, 2006.

H.M. Blackburn. Effect of blockage on critical parameters for flow past a circular cylinder. International Journal for Numerical Methods in Fluids, 50:987–1001, 2006.

H.M. Blackburn. Effect of blockage on spanwise correlation in a circular cylinder wake. Journal Experiments in Fluids, 18:134–136, 1994.

M. Susan. Bloor. The transition to turbulence in the wake of a circular cylinder. Journal of Fluid Mechanics, 19:290–304, 1964.

C. Camichel, P. Dupin, and M. Teissie-Solier. Sur làpplication de la loi de similitude aux aux pèriode de formation des tourbillons alternès de bènard-kàrmàn. C. R. Acad. Sci., 185:15561559, 1927.

B.S. Carmo, S.J. Sherwin, P.W. Bearman, and R.H.J. Willden. Wake transition in the flow around two circular cylinders in staggered arrangements. Journal of Fluid Mechanics, 597:1–29, 2008.

Chien-C Chang, Shih-Hao Yang, and Chin-Chou Chu. A many-body force decomposition with applications to flow about bluff bodies. Journal of Fluid Mechanics, 600:95–104, 2008.

R. Codina, R. Vasquez, and O.C. Zienkiewicz. A general algorithm for compressible and incompressible flows. part iii. the semi-implicit form. International Journal for Numerical Methods in Fluids, 27:13–32, 1998.

R. Codina, H. Coppola-Owen, P. Nithiarasu, and C-B. Liu. Numerical comparison of cbs and sgs as stabilization techniques for the incompressible navier-stokes equations. In European Congress on Computational Methods in Applied Sciences and Engineering, 2004.

A. Crespo, J. Hernàndez, and S. Frandsen. Survey of modelling methods for wind turbine wakes and wind farms. Wind Energy, 2:1–24, 1999.

P.A. Davidson. Turbulence: an introduction for scientists and engineers. Oxford University Press, USA, 2004.

P.A.B. de Sampaio, P.R.M Lyra, K. Morgan, and N.P. Weatherill. Petrov-galerkin solutions of the incompressible navier-stokes equations in primitive variables with adaptive remeshing. Computer Methods in Applied Mechanics and Engineering, 106:143–178, 1993.

S. Dong and G.E. Karniadakis. Dns of flow past a stationary and oscillating cylinder at $re = 10000$. Journal of Fluids and Structures, 20:519531, 2005.

I. Eames, SE Belcher, and JCR Hunt. Drift, partial drift and Darwin's proposition. Journal of Fluid Mechanics Digital Archive, 275:201–223, 1994.

I. Eames, J.C.R. Hunt, and S.E Belcher. Inviscid mean flow through and around groups of bodies. Journal of Fluid Mechanics, 515:371–389, 2004.

I. Eames, V. Roig, J.C.R. Hunt, and Belcher S.E. Vorticity annihilation and inviscid blocking in multibody flows. In Nato Meeting Ukraine May, volume 69, 2007.

E. Erturk, T.C. Corke, and C. Gokcol. Numerical solutions of 2-d steady incompressible driven cavity flow at high reynolds numbers. International Journal for Numerical Methods in Fluids, 48:747–774, 2005.

A. Fage. On the two-dimensional flow past a body of symmetrical cross-section mounted in a channel of finite dreadth. Brit. Aero. Res. Council, 1223, 1929.

JJ Finnigan and SE Belcher. Flow over a hill covered with a plant canopy. Quarterly Journal of the Royal Meteorological Society, 130(596), 2004.

Sten Frandsen, Rebecca Barthelmie, Sara Pryor, Ole Rathmann, Soren Larsen, and Jorgen Hojstrup. The necessary distance between large wind farms offshore - study. Technical report, Ris National Laboratory Roskilde Denmark, 2004.

M. Gaster. Vortex shedding from circular cylinders at low reynolds numbers. Journal of Fluid Mechanics, 46:749–759, 1971.

M. Gaster. Vortex shedding from slender cones at low reynolds numbers. Journal of Fluid Mechanics, 38:565–576, 1969.

Detlev Gerich and Helmut Eckelmann. Influence of end plates and free ends on the shedding frequency of circular cylinders. Journal of Fluid Mechanics, 122:109–121, 1982.

J.H. Gerrard. The wakes of cylindrical bluff bodies at low reynolds numbers. Mathematical and Physical Sciences, 288:351–382, 1978.

U. Ghia, K.N. Ghia, and C.T. Shin. High re solutions for incompressible flow using the navier-stokes equations and a multigrid method. Journal of Computational Physics, 48:387–411, 1982.

R.D. Henderson. Nonlinear dynamics and pattern formation in turbulent wake transition. Journal of Fluid Mechanics, 352:65–112, 1997.

Ronald D. Henderson. Details of the drag curve near the onset of vortex shedding. Physics of Fluids, pages 2102–2104, 1995.

JCR Hunt and I. Eames. The disappearance of laminar and turbulent wakes in complex flows. Journal of Fluid Mechanics, 457:111–132, 2002.

J. Jeong and F. Hussain. On the identification of a vortex. Journal of Fluid Mechanics Digital Archive, 285:69–94, 2006.

CNH Lock. The interference of a wind tunnel on a symmetrical body. R. & M, 1275, 1929.

A.G. Malan, R. W. Lewis, and P. Nithiarasu. An improved unsteady, unstructured, artificial compressibility, fnite volume scheme for viscous incompressible flows: Part ii. application. International Journal for Numerical Methods in Engineering, 54: 715–729, 2002.

N. Massarotti, F. Arpino, R.W. Lewis, and P. Nithiarasu. Explicit and semi-implicit cbs procedures for incompressible viscous flows. International Journal for Numerical Methods in Engineering, 66:16181640, 2006.

B.S. Massey. Mechanics of fluids. Taylor & Francis, 1998.

S. Mittal. Computation of three-dimensional flows past circular cylinder of low aspect ratio. Physics of Fluids, 13:177, 2001.

V J Modi and S.E. El-Sherbiny. A free-streamline model for bluff bodies in confined flow. ASME, Transactions, Series I-Journal of Fluids Engineering., 99:585–592, 1977.

P. Nithiarasu. An efficient artificial compressibility (ac) scheme based on the characteristic based split (cbs) method for incompressible flows. International Journal for Numerical Methods in Engineering, 56:18151845, 2003.

P. Nithiarasu and C.B Liu. Steady and unsteady incompressible flow in a double driven cavity using the artificial compressibility (ac)-based characteristic-based split (cbs) scheme. International Journal for Numerical Methods in Engineering, 63:380–397, 2005.

P. Nithiarasu and O.C. Zienkiewicz. Analysis of an explicit and matrix free fractional step method for incompressible flows. Computer Methods in Applied Mechanics and Engineering, 195:5537–5551, 2005.

P. Nithiarasu, J.S. Mathur, N.P. Weatherill, and K. Morgan. Three-dimensional incompressible flow calculations using the characteristic based split (cbs) scheme. International Journal for Numerical Methods in Fluids, 44:1207–1229, 2004.

C. Norberg. An experimental investigation of the flow around a circular cylinder : influence of aspect ratio. Journal of Fluid Mechanics, 258:287–316, 1994.

H.H. Pearcey, S. Sing, R.F. Cash, and R.B Matten. Interference effects on the drag loading for groups of cylinders in uni-directional flow. Feltham UK Rep NMI R130, 1982.

Oliver. Posdziech and Roger. Grundmann. Numerical simulation of the flow around an infinitely long circular cylinder in the transition regime. Journal Theoretical and Computational Fluid Dynamics, 15:121–141, 2001.

Anil Prasad and C.H.K. Williamson. The instability of the shear layer separating from a bluff body. Journal of Fluid Mechanics, 333:375–402, 1997.

Codina Ramon. Stabilized finite element approximation of transient incompressible flows using orthogonal subscales. Computer Methods in Applied Mechanics and Engineering, 191:4295–4321, 2002.

V. Roig and Larue de Tournemine. Measurement of interstitial velocity of homogeneous bubbly flows at low to moderate void fraction. Journal of Fluid Mechanics, 572:87–110, 2007.

A. Roshko. On the development of turbulent wakes from vortex streets. Technical report, NACA Report 1191, 1954.

M. Schäfer and S. Turek. Benchmark computations of laminar flow around a cylinder. Physics of Fluids, 13:177, 1997.

F. Shakib. Finite element analysis of the compressible euler and navier-stokes equations. Phd thesis, 1988.

Sadatoshi. Taneda. Experimental investigation of the wall-effect on a cylindrical obstacle moving in a viscous fluid at low reynolds numbers. Journal of the Physical Society of Japan, 19:1024–1030, 1964.

P.H. Taylor. Current blockage: reduced force on offshore space-frame structures. In Offshore Technology Conference, volume 69, 1991.

D.J. Tritton. Experiments on the flow past a circular cylinder at low reynolds numbers. Journal of Fluid Mechanics, 6:547–567, 1959.

C. Truesdell. The kinematics of vorticity. Bull. Amer. Math. Soc. 61 (1955), 356-358. DOI: 10.1090/S0002-9904-1955-09945-2 PII: S, 2(9904):09945–2, 1955.

L.J. Vermeera, J.N. Sorensen, and A. Crespo. Wind turbine wake aerodynamics. Progress in Aerospace Sciences, 39:467–510, 2003.

C.Y. Wen, C.L. Yeh, M.J. Wang, and Lin C.Y. On the drag of two-dimensional flow about a circular cylinder. PHYSICS OF FLUIDS, 16, 2004.

G.S. West and C.J. Apelt. The effects of tunnel blockage and aspect ratio on the mean flow past a circular cylinder with reynolds numbers between $l0^4$ and $l0^5$. Journal of Fluid Mechanics, 114:361–377, 1982.

C.M. White. The drag of cylinders in fluids at slow speeds. Mathematical and Physical Sciences, 189:472–479, 1956.

C.H.K. Williamson. Vortex dynamics in the cylinder wake. Annual Reviews Fluid Mech, 28:477–539, 1996.

C.H.K Williamson. Defining a universal and continuous strouhalreynolds number relationship for the laminar vortex shedding of a circular cylinder. Physics of Fluids, 31, 1988.

C.H.K Williamson. Three-dimensional wake transition behind a cylinder. Journal of Fluid Mechanics, 1995.

C.H.K. Williamson. Oblique and parallel modes of vortex shedding in the wake of a circular cylinder at low reynolds numbers. Journal of Fluid Mechanics, 206: 579–627, 1989.

M.M. Zdravkovich. Flow around circular cylinders: applications Vol 1. Oxford University Press, 1997.

M.M. Zdravkovich. Flow around circular cylinders: applications Vol 2. Oxford University Press, 2003.

O.C. Zienkiewicz and R. Codina. A general algorithm for compressible and incompressible flow - part i. the split, characteristic-based scheme. International Journal for Numerical Methods in Fluids, 20:869–885, 1995.

O.C. Zienkiewicz, K. Morgan, B.V.K. Satya Sai, R. Codina, and R. Vasquez. A general algorithm for compressible and incompressible flow - part ii. tests on the explicit form. International Journal for Numerical Methods in Fluids, 20:887–913, 1995.

O.C. Zienkiewicz, R.L Taylo, and P. Nithiarasu. The Finite Element Method for Fluid Dynamics, Sixth Edition. Elsevier Butterworth Heinemann, 2005.